Max-Planck-Institut für Metallforschung
Stuttgart

Atomistic and Continuum Studies of Deformation and Failure in Brittle Solids and Thin Film Systems

Markus J. Buehler

Dissertation
an der
Universität Stuttgart

Bericht Nr. 147
Mai 2004

Atomistic and Continuum Studies of Deformation and Failure in Brittle Solids and Thin Film Systems

Von der Fakultät Chemie der Universität Stuttgart
zur Erlangung der Würde eines Doktors der
Naturwissenschaften (Dr. rer. nat.) genehmigte Abhandlung

Vorgelegt von

Markus J. Buehler

aus Schorndorf/Württ.

Hauptberichter:	Prof. Dr. Huajian Gao
Mitberichter:	Prof. Dr. rer. nat. Hans-Rainer Trebin
Tag der Einreichung:	5. März 2004
Tag der mündlichen Prüfung:	12. Mai 2004

Max-Planck-Institut für Metallforschung, Stuttgart

Mai 2004

To my parents, Sigrid and Erich

Max-Planck-Institut für Metallforschung, Stuttgart, 2004
355 Seiten, 162 Abbildungen, 16 Tabellen.

Als Manuskript gedruckt. Printed in Germany.

Acknowledgements

First and foremost, my deepest appreciation goes to Prof. Dr. Huajian Gao, who accepted me as his doctoral student and gave me the unique opportunity to work on some of the most challenging problems in materials science. I am deeply indebted for the guidance, support and encouragement that he provided during my years at the Max Planck Institute. With his warm and positive spirit towards the endeavor of carrying out research, he taught me a deep understanding of the mechanics of materials, and most importantly, provided me with a vision of future materials research. Working with Huajian has been a tremendous experience. I am grateful for the guidance and support by Dr. Farid Abraham from IBM Almaden Research Center, San Jose (CA, USA), who taught me important lessons in computational physics. Farid also provided me with some of his parallelized molecular-dynamics simulation codes. I am also greatly indebted to Dr. Alexander Hartmaier (MPI for Metals Research), with whom I enjoyed working on numerous scientific projects in the area of deformation mechanisms of thin copper films as well as plasticity of small-scale materials. At the same time, I have benefited much from discussion and collaboration with Prof. Dr. Yonggang Huang from the University of Illinois, Urbana-Champaign (USA) on various problems related to fracture and dynamics of carbon nanotubes.

Of course, this endeavor would not have been possible without the help of my colleagues and friends who provided support and encouragement as well as scientific discussion. In particular, Dr. Jizeng Wang, Dr. Xiang Wang, Dr. Baohua Ji, Dr. Jicun Wang, Dr. Yong Kong, Dr. Shaohua Chen, Haimin Yao, Tian Furong, Joan Gao, Sean Coyer, Nils Brödling, as well as all other colleagues in our group helped me toward my goal of completing my PhD research. I enjoyed numerous conversations with Dr. Ernst-Helmut Brandt (MPI for Metals Research), and commend him for the guidance and advice he has given to me. I am also grateful for the extremely supportive and scientifically stimulating working atmosphere at MPI, and for the support of the technical staff. Important parts of my work depend on reliable computer systems, and I am therefore grateful to Dipl.-Ing. Igor Kanter and Mr. Giovani Estrada, as well as to the EDV department at MPI for Metals Research for the excellent IT support. For the introduction of the new Power4 IBM supercomputer system "Regatta", I would like to thank Dipl.-Math. Armin Schumacher and Dr. Armin Burkhard. Most of my large-scale computations were carried out at the Max Planck Society's supercomputer center in Munich, and I like to commend Dr. Ingeborg Weidl and Dr. Herrmann Lederer in particular for the excellent professional and unparalleled support. For some of my calculations I used the "ITAP-IMD" MD code developed by the group of Prof. Dr. Trebin at the University of Stuttgart (Institut für Theoretische und Angewandte Physik). I am further grateful for the use of advanced MD codes that were developed by Dr. Art Voter (Los Alamos

National Laboratories, NM, USA), as well as for using the Quasi-Continuum method among others developed by Dr. Ellad Tadmore (Technion, Israel).

Particular thanks go to Dr. Thomas Michelitsch (former member of Gao's group at MPI, now lecturer at the University of Sheffield, UK), who supported and helped me significantly to find my way when I started at MPI in the end of 2001. Thomas also read the complete manuscript of my dissertation and provided helpful comments. For numerous fruitful scientific discussions and collaborations I like to commend Dr. Patrick Wellner (alumni of Prof. Arzt's group), Christoph Eberl, Dr. Florian Kauffmann, Dr. Ralph Spolenak (all in Prof. Arzts group at MPI), Dr. Patrick Klein, Dr. Jonathan Zimmerman, Dr. Vicky Ngyuen (all at Sandia National Lab, CA, USA), as well as Erik Bitzek, Dr. Zhaohui Jin, and Prof. Dr. Peter Gumbsch (all at the University of Karlsruhe). I like to highlight the fruitful experimental-theory collaboration with Dr. John Balk and Dr. Gerhard Dehm (both members of Prof. Arzt's group at MPI) on deformation mechanisms of ultra thin copper films. I also benefitted from the interaction with my former advisors from Michigan Tech, Prof. Dr. Bernie Bettig and Prof. Dr. Gordon Parker.

I thank my thesis committee members, Prof. Dr. Hans-Rainer Trebin for agreeing on assuming the "Mitbericht" for my dissertation, and for Prof. Dr. Eduard Arzt for agreeing on assuming the "Prüfungsvorsitz". I am particularly grateful to Prof. Arzt also for helpful discussions on various topics in the field of materials science, both during joint meetings of the Arzt and Gao group on dislocation mechanics, and in separate meetings and discussions. I also acknowledge grants and fellowships from the Klein, Schanzlin and Becker foundation (Frankenthal, Germany), the Materials Research Society (Warrendale, PA, USA), the US Association for Computational Mechanics (Troy, NY, USA), the "Deutsche Forschungsgemeinschaft" (DFG), and Prof. Dr. Siegfried Hofmann (MPI for Metals Research) as well as the National Institute for Materials Science (NIMS, Tsukuba, Japan). I am grateful to the Max Planck Society for the Advancement of Science for providing the funding for my position. I also acknowledge our departmental secretary, Silvia Casanova for always being very helpful and providing much encouragement. The work reported in this thesis was performed at the Max Planck Institute for Metals Research between November 2001 and March 2004.

Finally, I acknowledge the help and support of my family and all my friends.

Abstract

We describe joint atomistic and continuum studies of deformation and failure in brittle solids and thin film systems. The work is organized in four parts. In the first part, we present a review on atomistic modeling and analysis tools, including a summary of recent research activities in the field.

The second part is dedicated to joint continuum-atomistic modeling of dynamic fracture of brittle materials, where we employ one-, two- and three-dimensional models. The main focus is a systematic comparison of continuum mechanics theory with atomistic viewpoints. An important point of interest is the role that material nonlinearities play in the dynamics of fracture. The elasticity of a solid clearly depends on its state of deformation. Metals will weaken or soften, and polymers may stiffen as the strain approaches the state of materials failure. It is only for infinitesimal deformation that the elastic moduli can be considered constant and the elasticity of the solid linear. However, many existing theories model fracture using linear elasticity. Certainly, this can be considered questionable since material fails at the tip of a dynamic crack because of extreme deformation. We show by large-scale atomistic simulations that hyperelasticity, the elasticity of large strains, can play a governing role in the dynamics of fracture and that linear theory is incapable of capturing all phenomena. We introduce the concept of a characteristic length scale for the energy flux near the crack tip and demonstrate that the local hyperelastic wave speed governs the crack speed when the hyperelastic zone approaches this energy length scale. This length scale implies that in order to sustain crack motion, there is no need for long-range energy transport. Instead, only energy stored within a region defined by the characteristic energy length scale needs to be transported toward the crack tip in order to sustain its motion. This new concept helps to form a more complete picture of the dynamics of fracture. For instance, the characteristic energy length scale explains the observation of crack motion faster than all wave speeds in the solid, including recent experimental reports of mode I cracks faster than the shear wave speed. The existence of this novel length scale is verified for mode I and mode III cracks. Further, we show that hyperelasticity also governs dynamic crack tip instabilities. Stiffening material behavior allows for straight crack motion up to super-Rayleigh speeds, and softening material behavior causes the crack tip instability to occur at speeds as low as one third of the theoretical limiting speed, in accordance with experimental results. Additional studies focus on the dynamics of suddenly stopping cracks as well as the dynamics of fracture along interfaces of dissimilar materials. An important result in this area is the discovery of a novel mother-daughter mechanism of mode I cracks moving along interfaces of stiff and soft materials, leading to supersonic mode I fracture.

The third part is devoted to the mechanical properties of ultra thin submicron copper films. We discuss a novel material defect referred to as a diffusion wedge, recently

proposed theoretically and observed indirectly in experiment. The theory predicts that tractions along the grain boundary are relaxed by diffusional creep and a diffusion wedge is built up. Due to traction relaxation, the diffusion wedge behaves as a crack along the grain boundary in the long-time limit. As a consequence, large resolved shear stresses on glide planes parallel to the film surface develop that cause nucleation of dislocations on glide planes parallel to the film surface and close to the film-substrate interface, referred to as parallel glide dislocations. This new dislocation mechanism in thin films, though standing in contrast to the well known Mathews-Freund-Nix mechanism of threading dislocation propagation, has been observed recently in experiments of ultra thin submicron copper films subject to thermal stress. We discuss joint atomistic-continuum modeling of such diffusion wedges, with a focus on the relation of diffusion and nucleation of dislocations. We propose a Rice-Thomson model for nucleation of parallel glide dislocations, and report a critical condition for initiation of grain boundary diffusion in thin films leading to a threshold stress for diffusion initiation independent of the film thickness. We extend the existing continuum model to account for the new concept of a threshold stress and model experimental thermal cycling curves. The new model improves the stress-temperature curves particularly at high temperatures. By large-scale atomistic modeling, we study the atomic details of buildup of the diffusion wedge and subsequent parallel glide dislocation nucleation. Based on our atomistic simulation results, we calculate a critical stress intensity factor as a condition for nucleation of parallel glide dislocations. We show that this criterion can serve as input parameter for mesoscopic discrete dislocation modeling of constrained diffusional creep. By atomistic studies of polycrystalline thin films, we study the transition from classical threading dislocations to parallel glide dislocations. In agreement with experimental findings and the classical understanding, threading dislocations are found to dominate when tractions are not relaxed by diffusion. If grain boundary tractions are relaxed by diffusional creep, parallel glide dislocations dominate due to the crack-like deformation field near the diffusion wedge. Another result is that the structure of grain boundaries has impact on dislocation nucleation and on the motion of dislocations along grain boundaries. Low-energy grain boundaries provide more fertile sources for dislocations than high-energy grain boundaries. We also discuss the role of the grain boundary structure on the diffusivities and show by large-scale atomistic studies of diffusional creep in polycrystalline thin films that high-energy grain boundaries provide faster diffusion paths than low-energy grain boundaries. Finally, a deformation map summarizes the range of dominance of different strain relaxation mechanisms in ultra-thin films. We show that besides the classical "threading dislocation" regime, there are numerous novel mechanisms once the film thickness approaches nanoscale.

In the fourth and last part of this thesis, we emphasize the potentials and limitations of molecular-dynamics simulations in studying small-scale materials phenomena, and include a critical assessment of the simulation methods employed in this work and the validity of the results. Finally, the most important results of this thesis are briefly summarized and an outlook to possible future research is provided.

Parts of this thesis have been published

- M.J. Buehler, F.F. Abraham, and H. Gao. Hyperelasticity governs dynamic fracture at a critical length scale. *Nature*, 426:141–146, 2003.
- M.J. Buehler, H. Gao, and Y. Huang. Continuum and atomistic studies of a suddenly stopping supersonic crack. *Computational Materials Science*, 28(3-4):385–408, 2003.
- M.J. Buehler, H. Gao, and Y. Huang. and continuum studies of stress and strain fields near a rapidly propagating crack in a harmonic lattice. *Theoretical and Applied Fracture Mechanics*, 41: 21–42, 2004.
- M.J. Buehler, F.F. Abraham, and H. Gao. Deformation fields near radidly propagating mode I cracks. *Springer Lecture Notes*, in the press.
- M.J. Buehler, A. Hartmaier, and H. Gao. Atomistic and continuum studies of crack-like diffusion wedges and dislocations in submicron thin films. *J. Mech. Phys. Solids*, 51:2105–2125, 2003.
- M.J. Buehler, A. Hartmaier, and H. Gao. Atomistic and continuum studies of crack-like diffusion wedges and dislocations in submicron thin films. *Mat. Res. Soc. Proceedings*, 779:W4.7, 2003.
- M.J. Buehler and H. Gao. Biegen und Brechen im Supercomputer. *Physik in unserer Zeit*, 35(1):30-37, 2004.
- M.J. Buehler, A. Hartmaier, and H. Gao. Hierarchical multi-scale modeling of plasticity of submicron thin metal films. *Modelling and Simulation in Materials Science and Engineering*, in the press.
- M.J. Buehler, T.J. Balk, E. Arzt, and H. Gao. *Handbook of Theoretical and Computational Nanotechnology*, Chapter "Constrained grain boundary diffusion in thin copper films". American Scientific Publishers (ASP), to appear 2005.
- M.J. Buehler and H. Gao. *Handbook of Theoretical and Computational Nanotechnology*, Chapter "Ultra-large scale simulations of dynamic materials failure". American Scientific Publishers (ASP), to appear 2005.

Contents

List of Figures

List of Tables

Nomenclature

Variable	Description
U	Total potential energy of the system
ϕ_i	Potential energy of atom i
ϕ_{ij}	Interatomic potential for atom i neighboring atom j
r_{ij}	Distance of atom i to atom j
k, k_i	Spring constant of the harmonic potential
ϵ_0	Well depth of the Lennard-Jones potential
σ	Length parameter of the Lennard-Jones potential
$\mathbf{f}$	Atomic force vector
$\mathbf{r}$	Atomic position vector
$\dot{\mathbf{r}}$	Atomic velocity
$\ddot{\mathbf{r}}$	Atomic acceleration
E	Young's modulus
μ	Shear modulus
ν	Poisson's ratio
ρ	Material density
c_{ijkl}	Elasticity tensor coefficients
S	Strain energy density
P_i	Dynamic Poynting vector
P	Magnitude dynamic Poynting vector
r_{on}	Critical atomic separation for hyperelastic effect
r_{rbreak}	Critical atomic separation for breaking of bonds
$\varepsilon_{\mathrm{on}}$	Critical onset strain for hyperelastic effect
χ	Characteristic energy length scale
t	Time (usually in reduced atomic units)
t^l	Loading time of cracks
t_{init}	Fracture initiation time
T	Temperature (in Kelvin)
$H(s)$	Heaviside unit step function
δ_{ij}	Kronecker delta function
a	Crack length
$\dot{a} = v$	Time derivative of crack length(=crack speed)
u_i	Displacement vector
$\dot{u}_i$	Particle velocity vector
c_0	Wave speed in a one-dimensional model string of atoms

c_r	Rayleigh-wave speed
c_s	Shear wave speed
c_l	Longitudinal wave speed
Θ	Angle in cylindrical coordinate system at crack tip
r	Radial direction in cylindrical coordinate system at crack tip
σ_{ij}	Stress tensor
ε_{ij}	Strain tensor
$\sigma_i,\ \varepsilon_i$	Principal stress/strain
$\sigma_\Theta,\ \varepsilon_\Theta$	Hoop stress/hoop strain
σ_Y	Yield stress
σ_0^cr	Initiation stress for grain boundary diffusion
γ_s	Fracture surface energy
G	Energy release rate
K	Stress intensity factor
F	Dynamic J-integral
m	Atomic mass
Ξ	Elastic mismatch across bimaterial interface
c_i	Centrosymmetry parameter atom i
s_i^α	Slip vector atom α
b_i, $\mathbf{b}$	Burgers vector
b	Magnitude of Burgers vector ($=\mid \mathbf{b} \mid$)
a_0	Lattice constant of cubic metals
h_f	Film thickness
d	Grain size
τ	Characteristic time for stress relaxation
δz	Diffusive displacement
T_h	Homologous temperature
$\delta_\mathrm{gb} D_\mathrm{gb}$	Grain boundary diffusivity
D_s	Surface diffusivity

1. Introduction

Understanding how materials fail has always been of great interest to human beings. Over many thousands of years, the knowledge about materials has furnished the way for our modern technologies. Stone age, bronze age... materials even served as eponyms for civilization eras.

At this moment we are at the crossroads to a new era where humans, for the first time, start creating technologies at the scale of single atoms. Such nanotechnology could revolutionize the way we live, learn and organize our lives in the next decades. Computer modeling is becoming increasingly important in the development of new technologies. Since on the nanoscale the effects of single atoms dominate material behavior, atomistic simulations are expected to be important not only for scientists but also for engineers.

This thesis focuses on atomistic modeling of small-scale dynamics phenomena with large-scale simulations. The main question we are concerned with is how materials fail under extreme conditions, and how the macroscopic failure process is related to atomistic details?

1.1. Different classes of materials behavior

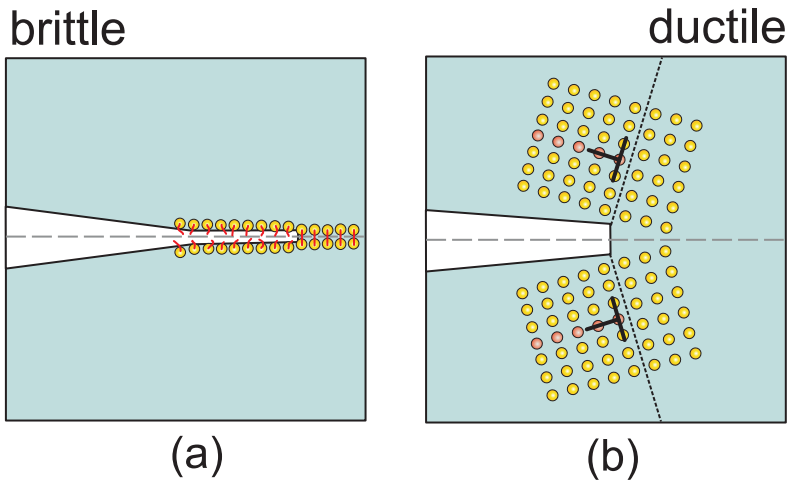

Figure 1.1.: Schematic of brittle (a) versus ductile (b) materials behavior.

When materials are deformed, they display a small regime where deformation is reversible, a behavior referred to as the *elastic regime*. Once the forces on the material are increased, deformation becomes irreversible, and the deformation of a body caused by an applied stress remains after the stress is removed. This behavior is referred to as the *plastic regime*, and may cause the material to fail [51].

Materials failure is classically divided into two generic types: brittle and ductile. In the brittle case, atomic bonds are broken as material separates along a crack front. The type of failure of such materials is often characterized by the simultaneous motion of thousands of small cracks, as it is for example observed when glass shatters. This type of failure usually happens rapidly, as cracks under large impact loading propagate at velocities close to the speed of sound in materials [78, 81, 82]. An enormous amount of research has been carried out over the last century, which has been summarized in recent books [78, 29]. The origin of fracture research dates back to the early 20$^{\text{th}}$ century in studies by Griffith [93] and Irwin [120]. The Griffith criterion provides a quantitative estimate of the condition under which material fails, and is based on simple energetic and thermodynamic arguments. The Griffith criterion states that materials fail when the mechanical elastic energy released by crack propagation equals the fracture surface energy $2\gamma_s$:

$$G = 2\gamma_s, \tag{1.1}$$

where G is the mechanical energy release rate [78]. This thermodynamic view of fracture was the foundation for the field of fracture mechanics. The continuum mechanics theory of fracture is a relatively well-established framework. In the continuum theory, the stress field in the vicinity of the crack tip is given by the asymptotic solution [246, 22, 78] and exhibits a universal character independent of the details of the applied loading. The loading of cracks can be separated into three different modes. Mode I is opening loading, mode II is shear loading and mode III is antiplane shear loading.

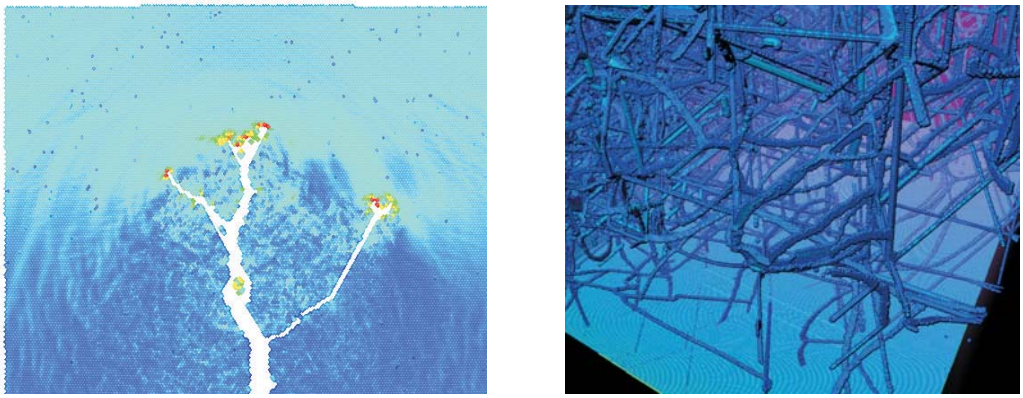

Figure 1.2.: Brittle (a) versus ductile (b) materials behavior, observed in atomistic computer simulations. In brittle materials failure, thousands of cracks break the material. In ductile failure, material is plastically deformed by motion of dislocations.

In ductile failure, a catastrophic event such as rapid propagation of thousands of cracks does not occur. Tough materials like metals do not shatter; they bend easily because plastic deformation occurs by the motion of dislocations in the material. Ductility is sometimes defined as the property of a metal which allows it to be drawn into wires or filaments. Since their discovery in the early 1930s, dislocations have helped explain

many of the perplexing physical and mechanical properties of metals, some of which remained mysterious even until this date [209]. One of the topics that were discussed controversially is that the resistance of materials to shear is significantly less than the theoretical strength [209, 92, 149]. This phenomenon can only be explained by the existence of dislocations and their motion. The behavior of dislocations in crystals is very complex and involves multiple mechanisms for generation and annihilation, as summarized in [109]. Collective events may occur through interaction among many dislocations or between dislocations and other defects such as grain boundaries.

The tendency of materials to be ductile or brittle depends on the atomic microstructure. The face-centered-cubic (fcc) packing is known to have a strong propensity toward ductility; body-centered-cubic (bcc) much less so. Glasses do not have extended crystallinity because atoms are randomly packed. They have no slip-planes and mostly exhibit brittle failure with little ductility. While atomic bonds are broken by stretching the solid in brittle fracture, the sliding between planes is achieved by shearing the solid in ductile failure. The ease of the atomic slip depends on the atomic arrangement of the slip planes. The more compact and consequently less bumpy planes slip better. Ductile versus brittle failure is schematically summarized in Figure 1.1. Figure 1.1 (a) shows brittle materials failure by propagation of cracks, and Figure 1.1 (b) depicts ductile failure by generation of dislocations at a crack tip. The atomic details of such different behavior is shown in Figure 1.2. Although brittle and ductile failure have both been studied extensively, for a long time it remained unclear what separates ductile from brittle failure.

What is the origin of such fundamentally different behaviors? It was established that the origin of brittle versus ductile behavior is at the atomic scale. Studies by Rice and Thomson [181] revealed that there exists a competition between ductile (dislocation emission) and brittle (cleavage) mechanisms at the tip of a micro-crack. Imperfections such as micro-cracks are considered the seeds for failure and exist in real materials. The model by Rice and Thomson has been extended recently to include a new material parameter, the unstable stacking fault energy γ_{us} [178, 179]. The unstable stacking fault energy describes the resistance of the material to motion of dislocations, while the fracture surface energy describes the resistance of materials to fracture. At a crack tip, the unstable stacking fault energy competes with the fracture surface energy γ_s [78] Once these material parameters are known, it is often possible to quantitatively predict material behavior.

Recent research results indicate that dislocation based processes and cleavage are not the only mechanism for deformation of materials. Materials under geometrical confinement, also referred to as materials in small dimensions, show a dramatically different behavior. This is believed to be caused by the fact that the behavior of these materials is characterized by the interplay of interfaces (e.g. grain boundaries), constraints (e.g. substrates) and free surfaces. Examples for such materials are nanocrystalline materials [240, 241] or ultra-thin sub-micron films [25]. It was also shown by computer simulation that in materials with ultra-small grain sizes of tens of nanometers and below, deformation can be completely dominated by grain boundary processes such as grain boundary diffusion [240, 241]. Due to the small sizes of the grains, dislocations can not be generated, because for instance Frank-Read sources are too large to fit within a

grain, or because dislocations are energetically very expensive under very small geometrical confinement [77, 167, 169]. Even though such material behavior is ductile (since materials can be bent without cleavage), no dislocation motion is required. Another recent observation in both computer simulation and experiment is that partial dislocations dominate in nanostructured materials, as opposed to complete dislocations in coarse-grained materials [235].

1.2. Motivation for the atomistic viewpoint: Nanoscale governs dynamics of materials failure

Historically, the classical physics of continuum has been the basis for most theoretical and computational tools of engineers. In early stages of computational plasticity, dislocations and cracks were often treated using linear continuum mechanics theory, relying on numerous phenomenological assumptions. Over the last decades, there has been a new realization that understanding nanoscale behavior is required for understanding how materials fail (e.g. [6, 149]). This is partly due to the increasing trend towards miniaturization as relevant length scales of materials approach several nanometers in modern technology. Once the dimensions of materials reach sub-micron length scales, the continuum description of materials is questionable and the full atomistic information is often necessary to study materials phenomena.

Atomistic simulations have proved to be a unique and powerful way to investigate the complex behavior of dislocations, cracks and grain boundary processes at a very fundamental level. Atomistic methods are increasingly important in modern materials modeling. One of the strengths and the reason for the great success of atomistic methods is its very fundamental viewpoint of materials phenomena. The only physical law that is put into the simulations is Newton's law and a definition of how atoms interact with each other. Despite this very simple basis, very complex phenomena can be simulated. Unlike many continuum mechanics approaches, atomistic techniques require no *a priori* assumption on the defect dynamics. A drawback of atomistic simulations is the difficulty of analyzing results and the large computational resources necessary to perform the simulations. This becomes more evident as the simulation sizes increase to systems with billions of atoms [12, 185]. Even with today's largest computers, system sizes with only a few billion atoms can be simulated, whereas a cubic centimeter of material already contains more than 10^{23} atoms.

Once the atomic interactions are chosen, the complete material behavior is determined. While in some cases it is difficult to find the correct potential for a specific material, atomic interactions can often be chosen such that *generic properties* common to a large class of materials are incorporated (e.g. ductile materials). This allows design of "model materials" to study specific materials phenomena. Despite the fact that model building has been in practice in fluid mechanics for many years, the concept of "model materials" in materials science is relatively new [12]. On the other hand, atomic interactions can be calculated very accurately for a specific atomic interaction using quantum mechanics methods such as the density functional theory [202].

Richard Feynman says in his famous *Feynman's Lectures in Physics* [67]:

"If in some cataclysm all scientific knowledge were to be destroyed and only one sentence passed on to the next generation of creatures, what statement would contain the most information in the fewest words?
I believe it is the atomic hypothesis that all things are made of atoms - little particles that move around in perpetual motion, attracting each other when they are a little distance apart, but repelling upon being squeezed into one another. In that one sentence, you will see there is an enormous amount of information about the world, if just a little imagination and thinking are applied."

This underlines atomistic simulations as a natural choice to study materials failure at a fundamental level. The atomistic level provides the most fundamental, sometimes referred to as the *ab initio*, description of the failure processes [6]. Many materials phenomena are multi-scale phenomena. For a fundamental understanding, simulations should ideally capture the elementary physics of single atoms and reach length scales of thousands of atomic layers at the same time. Recently, an increasing number of researchers consider the computer as a tool to do science, similar as experimentalists use their lab to perform experiments. Computer simulations have thus sometimes been referred to as "computer experiments".

1.3. Organization of this thesis

Atomistic modeling of several mechanisms of dynamic materials failure is the focus of this thesis. We will discuss brittle fracture as well as plasticity of ultra thin submicron films. In all areas covered by this thesis, we try to answer these general questions:

- How can a coupling between continuum theories and atomistic methods be achieved?
- Can continuum mechanics theory be applied to study materials phenomena at very small scales?
- In which fields can atomistic simulations be applied and where are the simulations predictive?

This thesis is divided into four parts. In the first part, we present a review on atomistic simulation tools. We cover classical molecular dynamics, *ab initio* techniques, computing techniques as well as analysis approaches.

The second part is dedicated to dynamic fracture. We discuss a one-dimensional model of dynamic fracture illustrating some fundamental concepts. We then concentrate on two- and three dimensional models of mode I, mode II and mode III fracture. In the main focus of the work is a systematic comparison of the continuum mechanics theory with atomistic viewpoints. An important point of interest is the role that material nonlinearities play in the dynamics of fracture. By using harmonic systems as reference systems, we systematically increase the strength of the nonlinearities and show that hyperelasticity, the elasticity of large strains, governs dynamic fracture under certain conditions.

The third part is devoted to the mechanical properties of ultra thin submicron copper films. We will discuss a novel material defect referred to as a diffusion wedge, recently

proposed theoretically [88] and observed indirectly in experiment [25]. This new defect causes an unexpected deformation mechanism in thin films, called "parallel glide". Further studies focus on modeling of experimental thermal cycling experiments with continuum mechanics theories. The work done in this field helps to clarify the deformation mechanisms of ultra thin films.

The second and third part each feature a separate discussion and conclusion section. In addition, the forth part contains a more general discussion of the results of the work described in this thesis, including a critical evaluation of the simulation tools used and the generality of the results. We conclude with an outlook to possible future work.

Part I.

Review of atomistic simulation tools

2. Modeling of dynamic materials failure using atomistic methods

In this chapter we review modeling of dynamic materials failure using large-scale computer simulations. In recent years numerous researchers proposed that in materials failure, atomic-scale mechanisms could play a key role [11, 12, 150, 148, 97, 220, 240, 242]. For a fundamental understanding of materials failure, the atomic length scale needs to be incorporated into the modeling. In the last decades, ultra large-scale atomistic computer simulations of dynamic materials failure spanning several length-scales from Angstroms to micrometers within one simulation have emerged and the field is under rapid development due to exponentially increasing computer capacity [12, 186, 221].

Here we describe computational techniques associated with large-scale computing, review the most popular atomistic simulation methods and discuss several analysis tools.

2.1. Classical molecular-dynamics versus "ab initio" methods: Potentials and applications

Adapting the atomistic viewpoint, a fundamental description of the materials can be obtained. However, characterization of the interatomic interactions remains an important issue, since these are the core of atomistic modeling and simulation methods. The major differences between various atomistic methods are how atomic interactions are calculated.

With the expression for the potential energy ϕ_i of a particle i given by the chosen potential, the total energy of the system E_{tot} can be obtained by summing over all particles:

$$E_{\text{tot}} = \sum_{i=1}^{N} \phi_i, \tag{2.1}$$

where N is the total number of particles. The force vector $\mathbf{f}_i$ for a particle i is obtained by the gradient of the potential energy with respect to the particle location in space:

$$\mathbf{f}_i = -\nabla \phi_i. \tag{2.2}$$

Numerous potentials with different levels of accuracy have been proposed, each having its problems and strengths. The approaches range from accurate quantum-mechanics based treatments (e.g. first-principle density functional theory methods [202], or tight-binding potentials [40]), to multi-body potentials (e.g. embedded atom approaches as

proposed in [71]) to the most simple and computationally least expensive pair potentials (e.g. Lennard-Jones) [15, 46]. One of the first molecular-dynamics studies was a Lennard-Jones model of argon in 1964 [175]. Previous studies used hard-sphere models to describe phase transformations [13, 14].

In density functional theory and related methods [202], the full quantum mechanical equations are solved to calculate the force on particles and are therefore numerically most expensive. Since the full quantum mechanical information is incorporated, the complete chemistry of atoms can be modeled (e.g. chemical reactions). Multi-body potentials are often constructed based on quantum mechanical understanding of the binding, which is then devised into an empirical equation (e.g. electrons are not treated explicitly in EAM potentials but appear as electron density instead). Pair potentials assume that the force between atoms only depends on the distance between neighboring atoms. Empirical potentials have the advantage that they are computationally more feasible to study large systems required for investigations of mechanical properties of materials.

One of the most recent developments is *ab initio* molecular-dynamics, as reported by the group around Parrinello (Car-Parrinello molecular-dynamics) [40, 152]. In this method, only valence electrons are treated explicitly, and the interaction with the core electrons is treated based on pseudopotentials. Most quantum-mechanics methods scale as $O(N^3)$ or worse (the Car-Parrinello method, depending on the algorithm chosen, can scale slightly better), while molecular-dynamics methods based on empirical potentials scale linearly with the number of particles, as $O(N)$. Any scaling other than linear is a severe computational burden and basically inhibits usage of the method for very large simulations.

An overview over the most prominent materials simulation techniques is shown in Figure 2.1. In the plot we indicate which length- and timescale quantum mechanics-based methods, classical molecular-dynamics methods as well as numerical continuum mechanics methods can reach. Quantum-mechanics based treatments are still limited to very short time- and length scales on the order of a few nanometers and picoseconds. Once empirical interactions are assumed in classical molecular-dynamics schemes, the length-and timescales achieved are dramatically increased, approaching micrometers and nanoseconds [1, 12]. Continuum mechanics based simulation tools can treat virtually any length scale, but they lack a proper description at small scales and are therefore often not suitable to describe materials failure processes in full detail (see discussion in Section 1.2). Mesoscopic simulation methods such as discrete dislocation dynamics can bridge the gap between molecular-dynamics and continuum theories [147, 223, 47, 48, 49, 136, 137, 101].

The success of classical molecular-dynamics approach is further demonstrated in Figure 2.2. Over the last decades, the computer power available for atomistic simulations has dramatically increased. The figure summarizes the increase in computer power over the past, and illustrates how big systems could be treated using classical molecular-dynamics. The need for military applications has strongly driven the development of supercomputers (e.g. ASCI computers, which are among the most powerful supercomputers of the world, are being used to maintain the US stockpile of nuclear weapons).

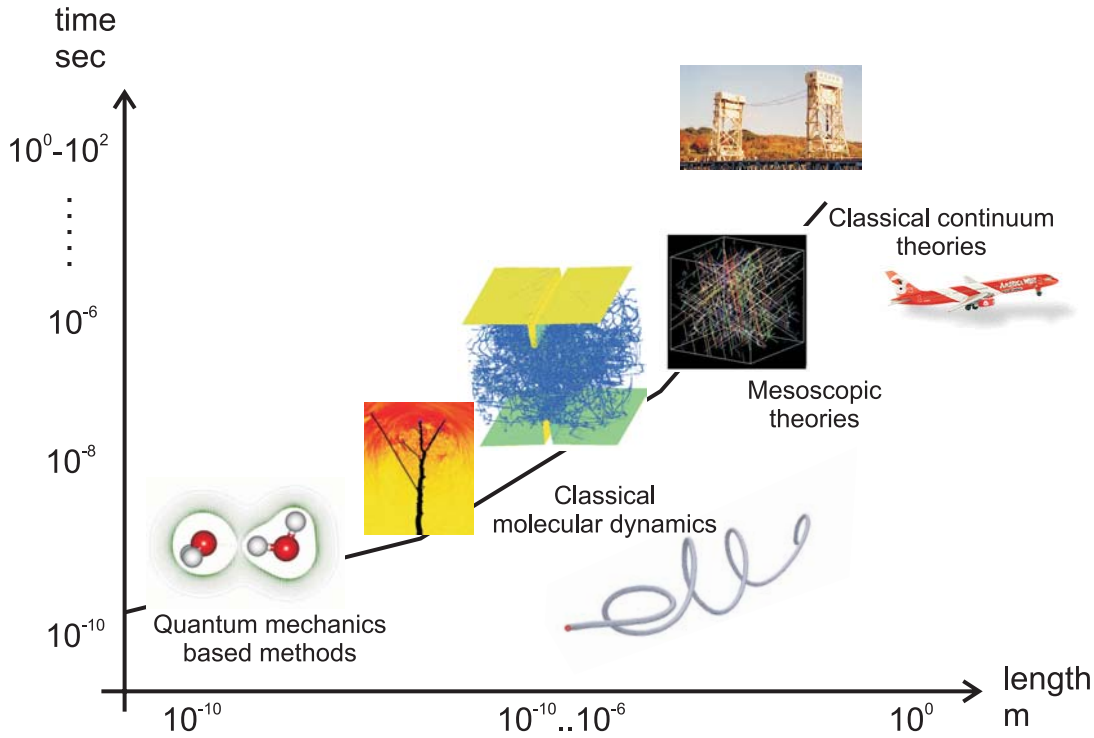

Figure 2.1.: Overview over different simulation tools and associated length-and time scales.

The most important conclusion from the discussion of the different methods is that the only feasible approach to study mechanical properties of materials at length scales up to micrometers is classical molecular-dynamics. The remainder of this chapter will be focused on the classical atomistic methods with empirical potentials.

2.2. Empirical interatomic potentials

Here we describe some of the most common empirical potentials.

2.2.1. Pair potentials

Pair potentials are the simplest choice for describing atomic interactions. For some materials interatomic interactions are best described by pair potentials. Prominent example are noble gases (e.g. argon) [175] and Coulomb interactions. Pair potentials have also proven to be a good model for more complex materials such as SiO_2 [214]. The potential energy of an atom is given by

$$\phi_i = \sum_{j=1}^{N_i} \phi_{ij}(r_{ij}) \tag{2.3}$$

where N_i is the number of neighbors of atom i. Usually, the number of neighbors is limited to the second or third nearest neighbors. Popular pair potentials for the simulation

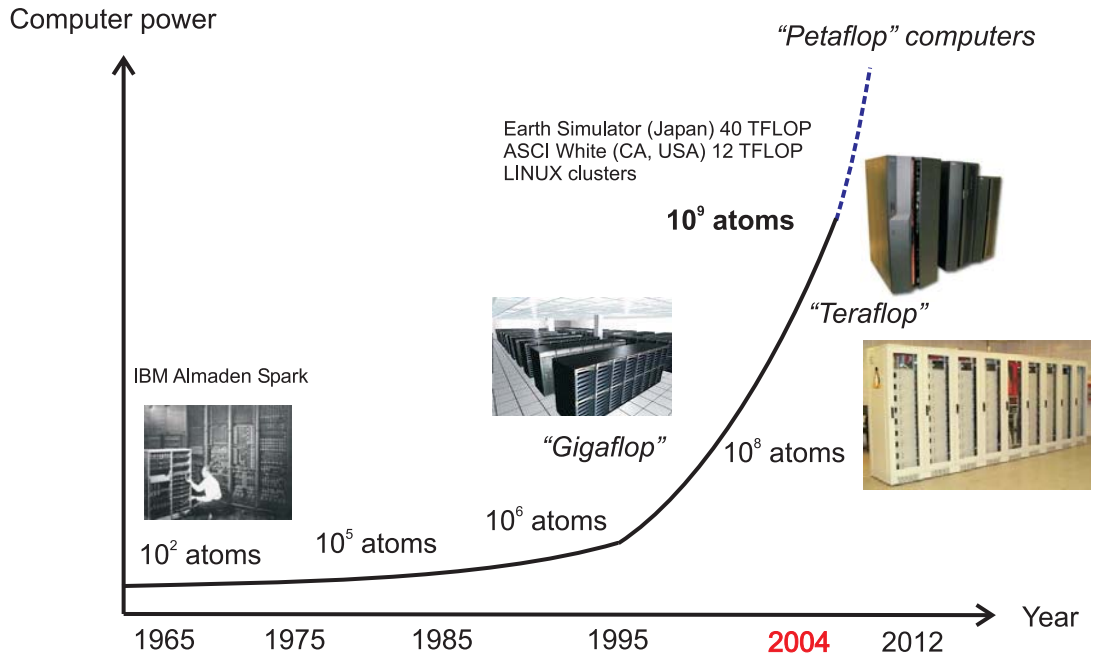

Figure 2.2.: Increase in computer power over the last decades and possible system sizes for classical molecular-dynamics modeling. Petaflop computers expected by the end of the current decade will allow simulations with hundreds of billions of atoms.

of metals include the Morse potential [160] and the Lennard-Jones (LJ) potential, which are described for instance in [15, 231, 46]. The LJ 12:6 potential is defined as

$$\phi_{ij}(r_{ij}) = 4\epsilon_0 \left[\left(\frac{\sigma}{r_{ij}} \right)^{12} - \left(\frac{\sigma}{r_{ij}} \right)^{6} \right]. \tag{2.4}$$

The LJ potential can be fitted to the elastic constants and lattice spacing of metals, but the result has significant shortcomings with respect to the stacking fault energy and the elasticity of metals. The term with power 12 represents atomic repulsion, and the term with power 6 represents attractive interactions. The parameter σ scales the length, and ϵ_0 the energy of atomic bonds. Often, pair potentials are cutoff smoothly with a spline cutoff function (see for instance [231] or [98]).

Another popular pair potential is the Morse potential, defined as

$$\phi_{ij}(r_{ij}) = D \left[1 - \exp\left(-\beta (r_{ij} - r_0) \right) \right]^2. \tag{2.5}$$

Fit of this potential to different metals (as well as different forms of the Morse potential) can be found for instance in [135]. The parameter r_0 stands for the nearest neighbor lattice spacing, and D and β are additional fitting parameters. The Morse potential is computationally more expensive than the LJ potential due to the exponential term (however, this is more realistic for many materials).

An indication to use pair potentials can also be the requirement to save computational resources. Another important advantage is that fewer parameters are involved (simplifying parameter studies and fit to different materials). For example the LJ potential has only two parameters, and the Morse potential has only three.

The potentials given by equations (2.4) and (2.5) are strongly nonlinear functions of the radius r. In some cases it is advantageous to linearize the potentials around the equilibrium position and define the so-called harmonic potential

$$\phi_{ij}(r_{ij}) = a_0 + \frac{1}{2}k(r_{ij} - r_0)^2 \tag{2.6}$$

where k is the spring constant, and r_0 the equilibrium spacing, and a_0 is a constant parameter. An important drawback of pair potentials is that elastic properties of metals can not be modeled correctly. An implication of the fact that the energy of an atom depends only on pair interactions is that the so-called Cauchy relation holds, and therefore $c_{1122} = c_{1212}$ [26]. This condition is violated in most real materials.

2.2.2. Multi-body potentials

The idea behind multi-body potentials is to incorporate more specific information on the bonds between atoms than simply the distance between two neighbors. In such potentials the energy of bonds therefore depends not only on the distance of atoms, but also on its local environment.

This allows to include quantum mechanical effects such as the influence of the electron gas in metals. In the case of metals, interactions of atoms can be quite accurately described using embedded atom potentials (EAM) or n-body potentials (e.g., [71, 155] or variations of the classical EAM potential [45, 26]). Other very similar multi-body potentials are based on the effective medium theory (EMT) [237, 238]. Good models for metals like copper and nickel have been published, while other metals (e.g. aluminum) are more difficult to model with such approaches [260, 257]. The elastic constants can be fitted much better to real materials when the Cauchy relation is violated.

The EAM potential for metals is typically given in the form

$$\phi_i = \sum_{j=1}^{N_i} \phi_{ij}(r_{ij}) + f_i(\rho_i), \tag{2.7}$$

where ρ_i is the local electron density and f_i is the embedding function. The electron density ρ_i depends on the local environment of the atom i. The potential features a contribution by a two-body term (repulsion and attraction of atoms), in conjunction with a multi-body term that accounts for the local electronic environment of the atom.

For other materials like silicon, bond-order multi-body potentials have been proposed (e.g. Tersoff potential [210], or Stillinger-Weber potential [204]; see also discussion in [112]). This accounts for the fact that in many materials, the order of the bonding has a significant effect on the strength of the material. Modified embedded atom potentials (MEAM) have recently been proposed that can be parameterized for silicon [206]. Multi-body potentials allow the elastic properties of metals to be better fitted (e.g. [26]).

In most empirical potentials, it is common that only the small-strain elastic properties are fitted. This could sometimes lead to problems in modeling strongly nonlinear phenomena such as brittle fracture.

2.3. Simulation methods

We review simulation methods that incorporate atomistic information.

2.3.1. Classical molecular-dynamics

The simplest tool for atomistic studies is classical molecular-dynamics [15]. Molecular-dynamics predicts the motion of a large number of atoms governed by their mutual interatomic interaction, and it requires numerical integration of the equations of motion. This method was first introduced by Alder and Wainwright in the late 1950's [13, 14] to study the interactions of hard spheres, and was advanced to modeling water by Rahman in 1964 [175]. The molecular-dynamics method is one of the simplest numerical techniques in modern materials modeling. The governing equation of motion for every atom is

$$\mathbf{f} = m\ddot{\mathbf{r}}, \tag{2.8}$$

where $\mathbf{f}$ is the force vector on a atom and $\ddot{\mathbf{r}}$ is the acceleration of an atom.

The equations of motion are integrated using a velocity verlet scheme [15, 207, 1], which has proven to be an effective and reliable method for since long-term energy conservation is very good. The velocity verlet algorithm is obtained by a Taylor expansion of the position of particle i at t_{n-1} and t_{n+1}, and is a second order integration scheme. In this scheme, the position vector $\mathbf{r}$ and velocity vector $\dot{\mathbf{r}}$ are obtained as

$$\mathbf{r}(t+\Delta t) = \mathbf{r}(t) + \dot{\mathbf{r}}(t)\Delta t + \ddot{\mathbf{r}}(t)(\Delta t)^2/2, \tag{2.9}$$

$$\dot{\mathbf{r}}(t+\Delta t) = \dot{\mathbf{r}}(t) + (\ddot{\mathbf{r}}(t) + \ddot{\mathbf{r}}(t+\Delta t))\,\Delta t/2. \tag{2.10}$$

The forces at each integration step are obtained by the formulas described in equation (2.2), and the acceleration $\ddot{\mathbf{r}}$ in equation (2.9) and equation (2.10) is obtained by $\ddot{\mathbf{r}} = \mathbf{f}/m$. The time step Δt must be chosen such that the atomic vibrations are accurately modeled, and is usually taken on the order of several 10^{-15} seconds. In order to simulate the dynamical evolution of atoms over the time span of one nanosecond, several 100,000 integration steps have to be performed.

Depending on which macroscopic observables are held constant, different ensembles can be defined for the calculation. In the basic molecular-dynamics setting, the number of particles N, the system volume V as well as the total energy E are held constant. After the initial velocities of the particles are drawn from the appropriate Maxwell-Boltzmann distribution, the system is simply evolved according to Newton's law of motion. This corresponds to the microcanonic NVE ensemble and is most frequently used because it is the most reliable simulation scheme. However, different ensembles may be advantageous for other purposes, such as the canonical NVT ensemble for studying non-equilibrium processes at constant temperature or the isothermal-isobaric NPT ensemble to investigate phase transitions. There are several subtleties associated with the NVT and NPT ensemble [15]. In this thesis we mostly use an NVE ensemble.

2.3.2. Advanced molecular-dynamics methods

In the classical molecular-dynamics schemes, it is in principle possible to simulate arbitrarily large systems, provided sufficiently large computers are available. However, the time scale remains confined to several nanoseconds. Surprisingly, this is also true for very small systems (independent of how large computers we use). The reason is that very small systems can not be effectively parallelized. Also, time can not easily be parallelized. Therefore, surprisingly there exists little tradeoff between desired simulation time and desired simulation size. This problem is referred to as the time-scale dilemma of molecular-dynamics [229, 90, 213].

Many systems of interest spend a lot of time in local free energy minima before a transition to another state occurs. In such cases, the free energy surface has several local minima separated by large barriers. This is computationally highly inefficient for simulations with classical molecular-dynamics methods.

An alternative to classical molecular-dynamics schemes is using Monte-Carlo techniques such as the Metropolis algorithm. In such schemes, all events and their associated energy must be known in advance. Note that in kinetic Monte-Carlo schemes all events and associated activation energy that take place during the simulation should be known in advance. For that purpose, the state space for the atoms has to be discretized on a lattice. Besides having to know all events, another drawback of such methods is that no real dynamics is obtained.

To overcome the time scale dilemma and still obtain real dynamics while not knowing the events prior to the simulation, a number of different advanced simulation techniques have been developed in recent years (for a more extensive list of references see [140]). They are based on a variety of ideas, such as flattening the free energy surface, parallel sampling for state transitions, finding the saddle points or trajectory based schemes. Such techniques could find useful applications in problems in nano-dimensions. Time spans of microseconds, seconds or even years may be possible with these methods. Examples of such techniques are the parallel-replica (PR) method [227, 159], the hyperdynamics method [226] and the temperature-accelerated dynamics (TAD) method [158]. These methods have been developed by the group around Voter [229] (further references could be found therein) and allow calculating the real time-trajectory of atomistic systems over long time spans. Other methods have been proposed by the group around Parrinello, who for instance developed a Non-Markovian coarse grain dynamics method [140]. The method finds fast ways out of local free energy minima by adding a bias potential wherever the system has been previously, thus quickly "filling up" local minima.

The methods discussed in these paragraphs could be useful for modeling deformation of nano-sized structures and materials over long time spans, such as biological structures (e.g. mechanical deformation of proteins and properties at surfaces). A drawback in many of these methods is that schemes to detect state transitions need to be known. Also, the methods are often only effective for a particular class of problems and conditions.

We give an example of using the temperature accelerated dynamics (TAD) method in calculating the surface diffusivity of copper (modeled by an EAM potential [225]). We briefly review the method. The simulation is speeded up by simulating the system

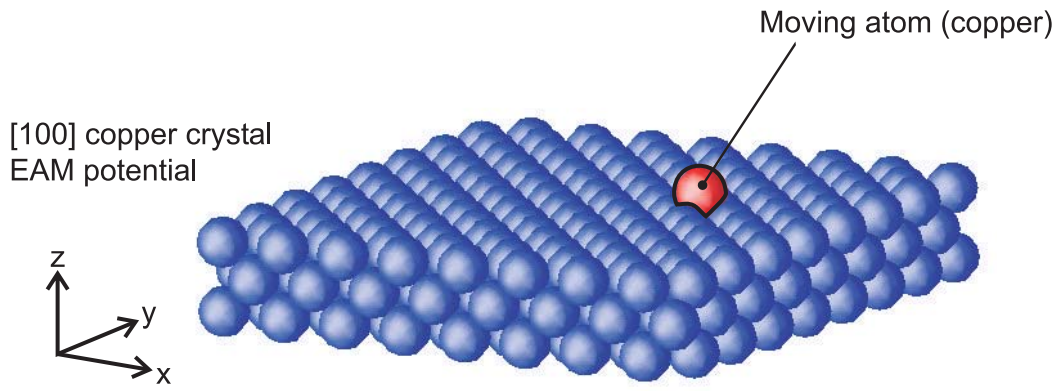

Figure 2.3.: Atomistic model to study surface diffusion on a flat [100] copper surface.

at a temperature higher than the actual temperature of interest. Therefore, in this method two temperatures are critical: The low temperature at which the dynamics of the system is studied, and a high temperature where the system is sampled for state transitions during a critical sampling time. This critical sampling time can be estimated based on theoretical considerations in transition state theory [229]. For every state transition, the time at low temperature is estimated based on the activation energy of the event. Among all state transitions detected during the critical sampling time, only the state transition that would have occurred at low temperature is selected to evolve the system and the process is repeated.

To calculate the surface diffusivity of copper, we consider a single atom on top of a flat [100] surface as shown in Figure 2.3. The atom is constrained to move at the surface. The total simulation time approaches $\Delta t = 3 \times 10^{-4}$ seconds. This is a very long time scale compared to classical molecular-dynamics time scales (see Figure 2.1)! The surface diffusivity is calculated according to

$$D_s = \lim_{t \to \infty} \frac{\langle \mid x_i(t) - x_i(t_0) \mid^2 \rangle}{6(t - t_0)} \tag{2.11}$$

The simulation is carried out at a temperature of $T \approx 400$ K with $N = 385$ atoms. The high temperature in the TAD method is chosen to be 950 K. The integration time step is $\delta t = 2 \times 10^{-15}$ seconds. We calculate the diffusivity to be

$$D_s^{\mathrm{MD}} = 7.53 \times 10^{-14} \ \mathrm{m}^3/\mathrm{s}. \tag{2.12}$$

This value is comparable to experimental data $D_s^{\mathrm{exp}} \approx 11 \times 10^{-14}$ m^3/s [122]. In Figure 2.4 we show the diffusive displacement over a time interval $0 < t < 2.5 \times 10^{-4}$ seconds from which the diffusivity is calculated. The activation energy of all state transitions is found to be 0.57 eV.

We show another example of how the temperature accelerated method could be used. Here we consider the atomic activities near a surface step in a [100] copper surface. We find that atoms at the surface step tend to hop away from the perfect step. This defines two states (A), the perfect step, and (B), when the atom is hopped away from the step. The simulation suggests that over time, the two states A and B interchange. Figure 2.5 shows the time-averaged stability of the two states as a function of temperature.

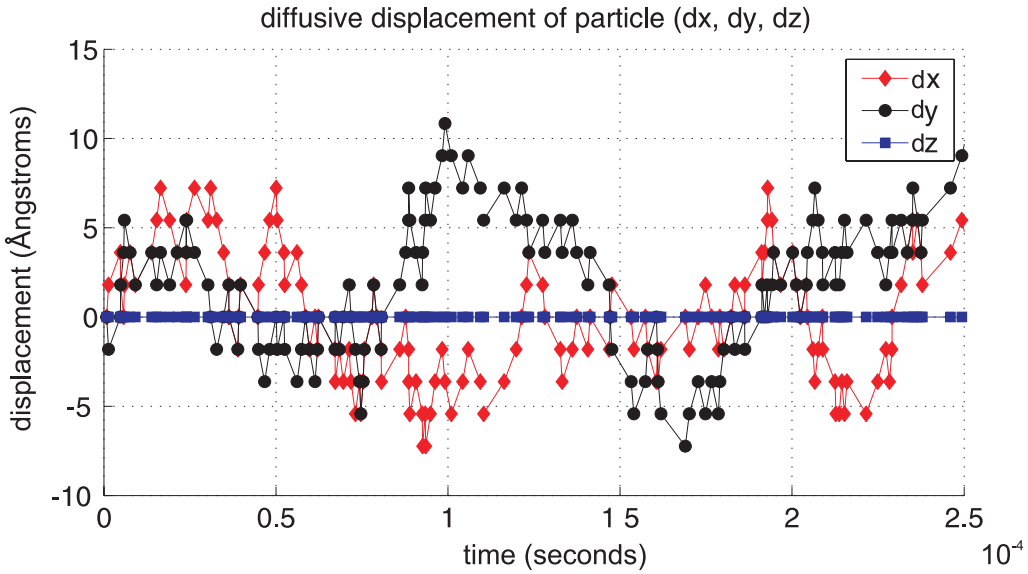

Figure 2.4.: Diffusive displacement of a single copper atom on a flat [100] copper surface. Since the atom is constrained to move on top of the surface, $dz = 0$.

State transition (from to)	activation energy (eV)
A → B	0.609
B → A	0.217

Table 2.1.: Activation energy for different state transitions.

It can be observed that for low temperatures, the living time of state (B) is much smaller compared to that of state (A). State (A) is observed to be stable up to several hundred seconds. Figure 2.6 shows the two states in a three-dimensional atomic plot. Table 2.1 summarizes the different activation energies. The activation energies to get from state (A) to state (B) are different. This immediately explains why state (B) is not as stable as state (A).

These examples illustrate the great appeal of these advanced simulation techniques. Experimental techniques are currently not able to provide the resolution in space and time to track the motion of single atoms. On the other hands, advanced molecular-dynamics simulation techniques can track the motion of atoms on a surface on a relatively long time scale, with a very high resolution of time.

2.3.3. Concurrent and hierarchical multi-scale methods

It is not always necessary to calculate the full atomistic information in the whole simulation domain. Some researchers have articulated the need for multi-scale methods [134, 95, 38, 8, 208, 196] by combining atomistic simulations with continuum mechanics methods (e.g. finite elements). A variety of different methods have to be developed to achieve this. The primary motivation is to save computational time and by doing that, to extend the scale accessible to the simulations. It is common to distinguish between

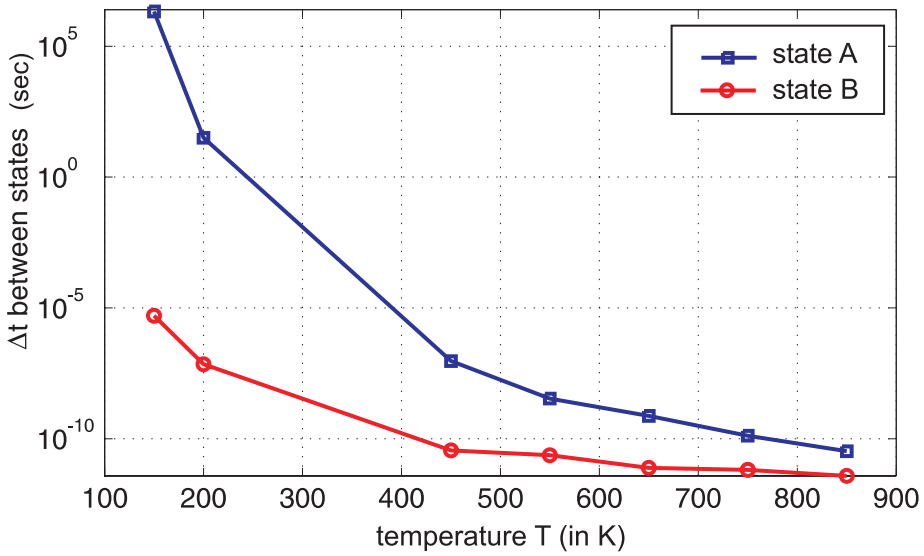

Figure 2.5.: Study of atomic mechanisms near a surface step at a [100] copper surface. Living time (stability) of states A (perfect step) and B (single atom hopped away from step) as a function of temperature. The higher the temperature, the closer the living times of states A and B get.

hierarchical multi-scale methods and on-the-fly concurrent multi-scale methods. In on-the-fly multi-scale methods, the computational domain is divided into different regions where different simulation methods are applied. A critical issue in all such methods is the correct mechanical and thermodynamical coupling among different regions in a concurrent approach and different methods in a hierarchical approach.

Progress in this field was reported by Gumbsch and Beltz [96] in 1995. They discuss simulations performed with a hybrid atomistic-finite element (FEAt) model, and compared the results with the continuum-based Peirls-Nabarro model for different crack orientations in a nickel crystal. The researchers demonstrated the basic assumptions of the continuum model for dislocation nucleation, that is, stable incipient slip configurations are formed prior to dislocation nucleation, and found relatively good agreement of the FEAt model with the Peierls model for critical loading associated with dislocation nucleation. In the FEAt model, the region with atomistic detail is determined prior to computation, and can not be updated during the simulation.

A quasi-continuum (QC) model for quasi-static simulations was developed by Tadmor and coworkers [208, 197, 196] starting in 1996. This method has the advantage of an adaptive formulation of the atomistic region during simulation. The dislocation core region is treated fully atomistically, while most of the bulk region is treated as a continuum. The method is mostly limited to quasi-static conditions at zero temperature. For higher dislocation densities, the computational effort approaches that of a fully atomistic treatment.

The QC method could find useful applications in studies of thin films constrained by substrates. A set of results for this case is shown in Figure 2.7. Here we investigate a thin copper film with a (111) surface on a rigid substrate (the film thickness is $h_f \approx 30$

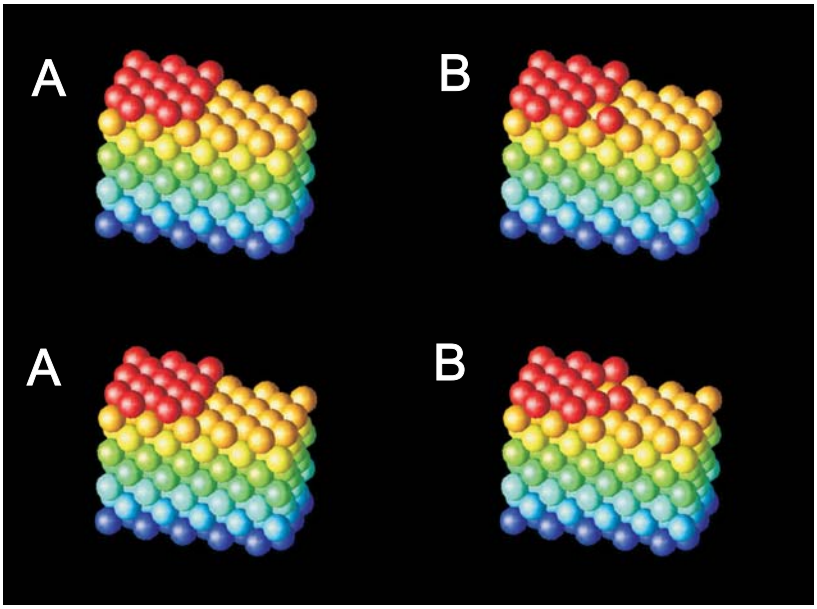

Figure 2.6.: Snapshots of states A (perfect step) and B (single atom hopped away from step).

nm). The interatomic interactions are modeled by Voter and Chen's EAM potential for copper [225, 228]. We consider a crack orthogonal to the surface. Such a crack could for instance be created by grain boundary cracking or constrained grain boundary diffusion [88]. Figure 2.7 (a) shows different snapshots as the lateral mode I opening loading of the film is increased (the black line indicates the interface of substrate and thin film). The atomic region adapts and expands, as dislocations gliding on glide planes parallel to the film surface are nucleated and flow into the film material. Figure 2.7 (b) shows a zoom into the crack tip region.

Abraham *et al.* [4, 8] (1998-2000) proposed a method to couple quantum mechanics (QM), molecular-dynamics and finite element (FE) methods in a concurrent, seamless way. The method is referred to as MAAD, which is short for "macro atomistic *ab initio* dynamics". As a sample problem, a finite-length penny-shaped crack in Silicon was treated. So far, the method is only suitable for covalently bonded systems. A similar approach is being developed for metals [123]. Further reports of multiscale simulations of nanosystems describe hybrid FE, molecular-dynamics and QM calculations [163] for a silicon crystal. The authors report several studies in this work, among them a simulation of oxidation of a silicon [100] surface.

Another active field of research in the multi-scale area is hierarchical methods. In such an approach, molecular-dynamics simulation results or results obtained from first principle calculations serve as input parameters for higher-order simulations. A prominent example in materials science is mesoscopic simulations. In mesoscopic methods, dislocations are treated as particles embedded in a linear elastic continuum. An important issue in these approaches is to identify proper coupling variables to transition between the different scales. Probably the most popular example of hierarchical simulation methods is discrete dislocation dynamics (see, for instance [192, 223, 165, 147]).

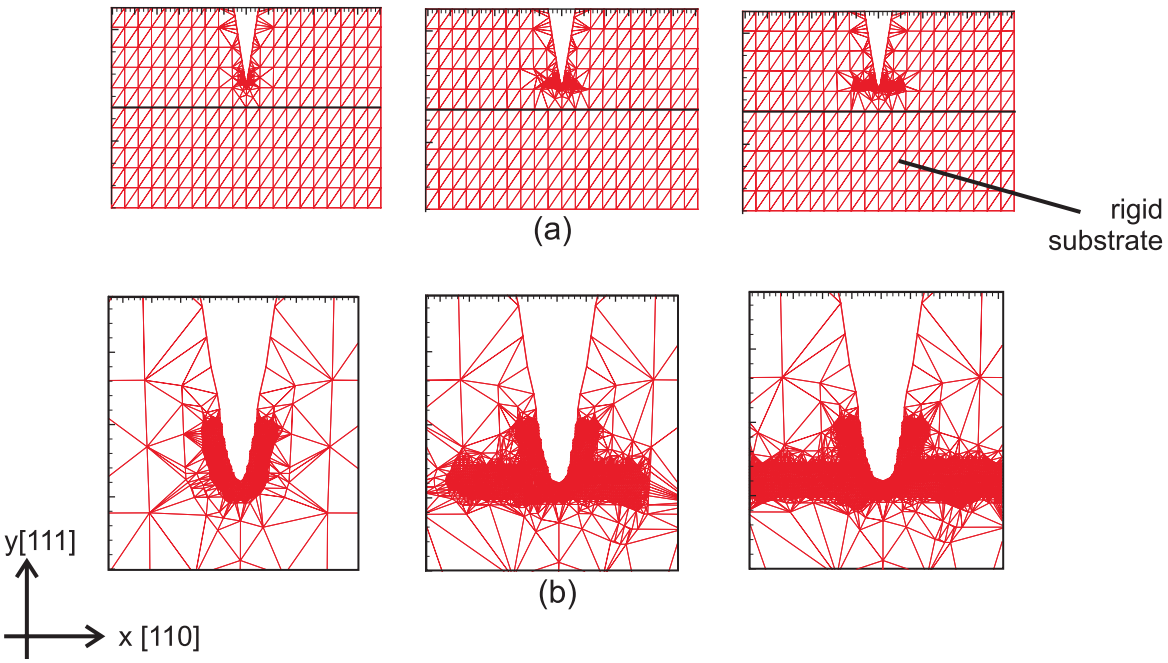

Figure 2.7.: Results of a simulation of a crack in a thin film constrained by a rigid substrate, exemplifying a study using a concurrent multi-scale simulation method, the quasi-continuum approach [208].

Here, dislocations interact according to their linear-elastic fields and move according to empirical laws for dislocation mobility. All non-elastic reactions between dislocations that potentially occur have to be put into the simulation setup as rules and laws. This information can for instance be obtained from atomistic simulations.

A recent example for hierarchical multi-scale modeling is a study by Horstemeyer *et al.*[114]. The authors investigated the shear strength of crystals based on a multi-scale analysis, incorporating molecular-dynamics, crystal plasticity and macroscopic internal state theory applied to the same system. The objective of the studies was to compare different levels of description and to determine coupling parameters. Further studies of climb dislocations in diffusional creep in thin films [101] and mesoscopic treatment of grain boundaries during grain growth processes [102, 157] have also used hierarchical simulation approaches.

We note that such coupling of length scales is just at its beginning and much research remains to be done in the future. The most difficult issue is finding correct quantities for correct coupling between the different simulation methods.

2.3.4. Continuum approaches incorporating atomistic information

Recently, a virtual internal bond (VIB) model has been proposed as a bridge of continuum models with cohesive surfaces and atomistic models with interatomic potentials [129]. The VIB method differs from an atomistic model in a sense that a phenomenological "cohesive force law" is adapted to act between material particles, which are not

necessarily atoms. A randomized network of cohesive bonds is statistically incorporated into the constitutive response of the material based on the Cauchy-Born rule. This is achieved by equating the strain energy function on the continuum level to the potential energy stored in the cohesive bonds due to an imposed deformation. Other features of the VIB model [129] could be found elsewhere.

The method has been used to study crack propagation in brittle materials, and is able to reproduce many experimental phenomena such as crack tip instabilities or branching of cracks at low velocities. An important implication of the VIB method is that it provides a direct link between the atomic microstructure and its elastic properties, for any given potential. The method was recently extended to model viscoelastic materials behavior [164]. The fact that this method is able to perform simulations on entirely different length scales makes it interesting for numerous applications particularly in engineering, where more complex situations have to be modeled.

2.3.5. Discussion

We have presented a selection of four different popular simulation tools which all incorporate atomic information. Classical molecular-dynamics is the simplest approach among all of them. It can reach length-scales up to micrometers, but is still severely limited with respect to the time scale. Techniques for fast time sampling can achieve "parallelization of time", but are difficult to apply in general problems. Multiscale methods are a promising field, but it remains challenging how to seamlessly couple the different length and time scales where different simulation approaches are applied in real-time within the domain. Hierarchical methods avoid some of the problems, but seem limited in terms of applicability. For example, a new phenomenon or mechanism might occur in the real system at a larger scale, but it is not resolved because a higher order technique is applied in the whole domain. Continuum mechanics methods such as VIB have difficulties describing atomistic and atomic-scale processes, because the size of the finite elements is often on the order of several hundred micrometers, far too large to capture many atomic scale processes and phenomena.

In the remainder of this thesis we will limit our attention to model dynamic materials failure based on classical molecular-dynamics.

2.4. Classical molecular-dynamics implemented on supercomputers

Large-scale molecular-dynamics simulations often require an enormous amount of computer power. Here we focus on the implementation of classical molecular-dynamics on modern supercomputers, made out of hundreds of single computers.

It was only a few decades ago that computer scientists were concerned that the speed of scientific computers could not go much beyond gigaflops (billion arithmetic operations per second). It was predicted that this plateau would be reached by the year 2000. Computer scientists now expect petaflop computers by the middle or end of the current

decade [221, 12]. Based on the concept of concurrent computing, modern parallel computers are made out of hundreds or thousands of small computers (for example personal computers) working simultaneously on different parts of the same problem. Information between these small computers is shared by communicating, which is achieved by message-passing procedures (MPI) [94].

Parallel molecular-dynamics is relatively straight-forward to implement with great efficiency in a message-passing environment. It is important to have an effective algorithm for handling the summations of N interacting particles. If summations had to be carried out for each particle over all particles, the problem would scale with N^2. This is a computational catastrophe for large systems! However, if the interactions between particles are short ranged, the problem can be reduced so that the execution time scales linearly with the number of particles (that is, execution time scales with N). The computational space is divided up into cells such that in searching for neighbors interacting with a given particle, only the cell in which it is located and the next-nearest neighbors have to considered. Since placing the particles in the correct cells scales linearly with N, the problem originally scaling with N^2 can therefore be reduced to N. With a parallel computer whose number of processors increases with the number of cells (the number of particles per cell does not change), the computational burden remains constant.

The speedup factor S is defined as the ratio of execution time on one processor (T_s) over the execution time on p processors (T_p):

$$S = \frac{T_s}{T_p}. \tag{2.13}$$

The perfectly efficient parallel computer would exhibit linear speedup. This would mean that the computation time for p processors is $1/p$ times the execution time on one processor. However, the speedup depends strongly on the fraction of the work done in parallel. We refer the reader to Plimpton's algorithms for molecular-dynamics with short-range forces [173].

One of the major concerns in atomistic modeling has always been the need for huge computational resources. Computational material scientists could only handle a few hundred atoms in the 1960s, and this number increased up to 100,000 in the mid-80s.

The state-of-the art size of molecular-dynamics simulations is well into billions. With the advent of teraflop (=one trillion floating point operations per second) computing using massively parallelized concurrent computers, systems with over 1,000,000,000 atoms can be simulated today [12, 185]. In a recent publication by the group around Trebin and coworkers [185], a molecular-dynamics simulation with over 5 Billion particles was conducted. This allows for three-dimensional simulations of systems reaching micrometer size, a length scale associated with the behavior of dislocations. Even a few years ago, it was not anticipated that molecular-dynamics simulations could be performed with systems of micrometer size.

We emphasize that the "size" of the simulations does not determine how "useful" a simulation is by itself. Instead, the most important issue and measure for a successful simulation is always the physics that can be extracted from the simulation. This objective should dictate the system size. In many cases, such as for dislocation-dislocation interaction, system sizes on the order of micrometers are needed (dislocation interaction

is associated with a characteristic length scale of micrometers). This example illustrates that there is still a need for the development of simulation techniques and more computer power.

Future development using cheap off-the-shelve technology based on LINUX clusters to build supercomputers (instead of using very expensive UNIX based supercomputers) is promising, as indicated by recent publications [240, 241] (see also the discussion in the Appendix, Section C.3).

2.5. Visualization and analysis techniques

Measures like strain, stress or potential energy of atoms are important quantities that can be used to analyze atomistic data, in particular with respect to continuum mechanics theories (for a definition of atomic stress and strain see the Appendix, Chapter A). However, it is often advantageous to post-process the data and derive new quantities providing more information of the defect structure. Here we discuss a few examples for the analysis of crystal defects in metals that will become particularly important in the third part of this thesis.

Richard Hamming's saying "*the purpose of scientific computing is insight, not numbers*" underlines the importance of processing the raw simulation data appearing as "useless" numbers in order to gain understanding. Visualization, defined as a method of computing transforming the symbolic into the geometric, enables to observe simulations and computations. Visualization is also considered an approach for seeing the unseen, which enriches the process of scientific discovery and fosters profound and unexpected insights. Visualization of computational results is undoubtedly becoming an increasingly important and challenging task in supercomputing.

2.5.1. Energy method

To visualize crystal defects, the easiest approach is to use the energy method. This method has frequently been used to "see" into the interior of the solid (e.g. [7, 12]). In this method, only those atoms with potential energy greater than or equal to a critical energy ϕ_{cr} above the bulk energy ϕ_{b} are shown. The energy method has been very effective for displaying dislocations, microcracks and other imperfections in crystal packing. This reduces the number of atoms being displayed by approximately two orders of magnitude in three dimensions [12].

An example of an analysis of a dislocation network using the energy method is shown in Figure 2.8. Figure 2.8 (a) shows the whole simulation cell with two cracks at the surfaces serving as sources for dislocations, and Figure 2.8 (b) shows a zoom into a small subvolume of the material revealing a complex dislocation microstructure. The data is taken from a simulation of work-hardening in nickel that comprises of about 150,000,000 atoms [34].

Assuming a crystal defect is identified as a dislocation, it can be studied in more detail based on a geometric analysis of the lattice close to the dislocation core allowing to determine the Burgers vector and the slip plane. For that purpose, one can rotate

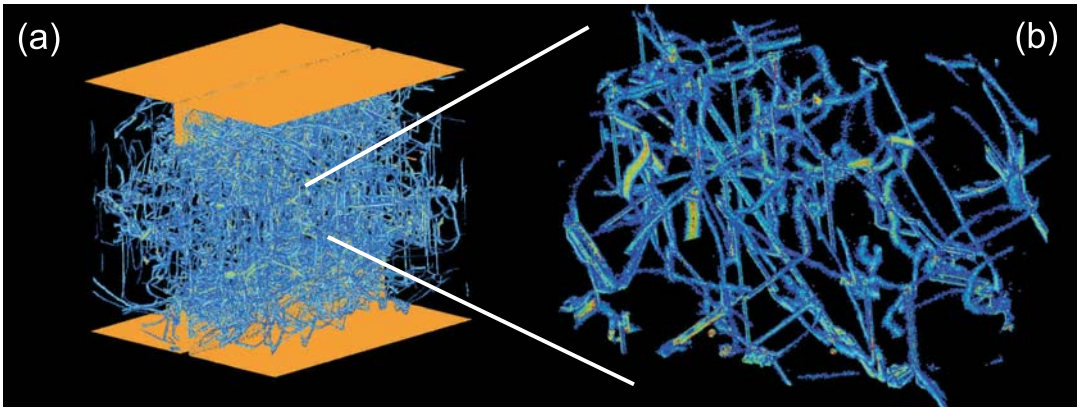

Figure 2.8.: Analysis of a dislocation network using the energy filtering method in nickel with 150,000,000 atoms [34, 35]. Subplot (a) shows the whole simulation cell with two cracks at the surfaces serving as sources for dislocations, and subplot (b) shows a zoom into a small subvolume. Partial dislocations appear as wiggly lines, and sessile defects appear as straight lines with slightly higher potential energy.

the atomic lattice such that one is looking onto a {111}-plane, with the horizontal (x) axis oriented into a $< 110 >$ direction, and the vertical (y) axis aligned with a $< 111 >$ direction. To help visualizing dislocations, stretching the atomic lattice by a factor of five to ten in the $< 110 >$ direction is helpful. A systematic rotation of the atomic lattice to investigate all possible Burgers vectors is then necessary. Instead of analyzing a part of the atomic lattice containing many dislocations, one can choose a domain of the atomic lattice which contains only one dislocation. This approach requires a very detailed understanding of the lattice and dislocations [109, 118]. This way of analysis is like analysis of TEM images from "real" laboratory experiments.

2.5.2. Centrosymmetry parameter

A more advanced analysis can be performed using the centrosymmetry technique proposed by Kelchner and coworkers [126]. This method makes use of the fact that centrosymmetric crystals remain centrosymmetric after homogeneous deformation. Each atom has pairs of equal and opposite bonds with its nearest neighbors. During deformation, bonds will change direction and/or length, but they remain equal and opposite within the same pair. This rule breaks down when a defect is close to an atom under consideration. The centrosymmetry method is particularly helpful to separate different types of defects from one another, and to display stacking faults (in contrast, using the energy method it is difficult to observe stacking faults). The centrosymmetry parameter for an atom is defined as [126]

$$c_i = \sum_{j=1}^{6} \left\{ \mid \sum_{k=1}^{3} r_{k,j} + r_{k,j+6} \mid^2 \right\}, \tag{2.14}$$

where $r_{k,j}$ is the $k-$th component of the bond vector($k = 1, 2, 3$ corresponding to the directions x, y and z) of atom i with its neighbor atom j, and $r_{k,j+6}$ is the same quantity

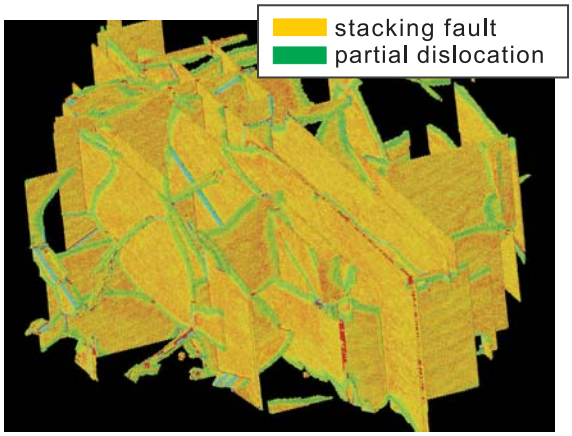

Figure 2.9.: The figure shows a close view on the defect structure in a simulation of work-hardening in nickel analyzed using the centrosymmetry technique [34, 35]. The plot shows the same subvolume as in Figure 2.8 (b).

Defect	c_i/a_0^2	range $\Delta c_i/a_0^2$
Perfect lattice	0.00	$c_i < 0.1$
Partial dislocation	0.1423	$0.01 \leq c_i < 2$
Stacking fault	0.4966	$0.2 \leq c_i < 1$
Surface atom	1.6881	$c_i > 1$

Table 2.2.: Centrosymmetry parameter c_i for various types of defects, normalized by the square of the lattice constant a_0^2. In the visualization scheme, we choose intervals of c_i to separate different defects from each other.

with respect to the opposite neighbor. We summarize the interpretation of c_i in Table 2.2 (assuming that the nearest neighbor distance does not change near a defect). For the analysis, it is reasonable to display ranges of these parameters. The method can also be applied at elevated temperature, which is not possible using the energy method due to the thermal fluctuation of atoms.

An example using this centrosymmetry technique is shown in Figure 2.9. This plot shows the same section as in Figure 2.8 (b). Unlike in the analysis with the energy method, stacking fault regions can be visualized with the centrosymmetry technique.

2.5.3. Slip vector

Although the centrosymmetry technique can distinguish well between different defects, it does not provide information about the Burgers vector of dislocations. The slip vector approach was first introduced by Zimmerman and coworkers in an application of molecular-dynamics studies of nano-indentation [258]. This parameter also contains information about the slip plane and Burgers vector. The slip vector of an atom α is defined as

$$s_i^\alpha = -\frac{1}{n_s} \sum_{\alpha \neq \beta}^{n_\alpha} \left\{ x_i^{\alpha\beta} - X_i^{\alpha\beta} \right\}, \tag{2.15}$$

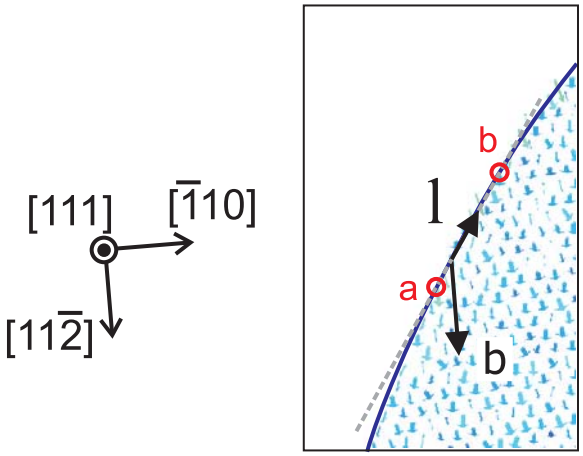

Figure 2.10.: Analysis of a dislocation using the slip vector approach. From the result of the numerical analysis, direct information about the Burgers vector can be obtained. The slip vector **s** is drawn at each atom as a small arrow. The Burgers vector **b** is drawn at the dislocation (its actual length is exaggerated to make it better visible). The dislocation line is approximated by discrete, straight dislocation segments. A line element between "a" and "b" is considered.

where n_s is the number of slipped atoms, $x_i^{\alpha\beta}$ is the vector difference of atoms α and β at the current configuration, and $X_i^{\alpha\beta}$ is the vector difference of atoms α and β at the reference configuration at zero stress and no mechanical deformation. The slip vector approach can be used for any material microstructure, unlike the centrosymmetry parameter which can only be used for centrosymmetric microstructures.

Figure 2.10 shows the result of a slip vector analysis of a single dislocation in copper [36]. The slip vector **s** is drawn at each atom as a small arrow. The Burgers vector **b** is drawn at the dislocation, where its actual length is exaggerated to make it better visible. The dislocation line can be determined from an energy analysis, and the line direction of a segment between point "a" and "b" of the dislocation line is indicated by the vector **l**. The Burgers vector **b** is given by the slip vector **s** directly. The analysis reveals that the dislocation has Burgers vector $\mathbf{b} = \frac{1}{6}[11\bar{2}]$. The unit vector of line direction of the segment is $\mathbf{l} \approx [-0.3618 \;\; 0.8148 \;\; -0.4530]$. The length of the line segment is approximately 9 nearest neighbor distances in the $[\bar{1}10]$ direction. The slip plane normal is given by the cross product $\mathbf{n}_s = \mathbf{l} \times \mathbf{b} \sim [\bar{1}\bar{1}\bar{1}]$, and the dislocation thus glides in the (111) plane.

2.5.4. Other methods

Other researchers have used a common neighbor analysis to analyze their results [189, 64, 113]. In this method, the number of nearest neighbors is calculated, and that allows to distinguish between different defects. Additional analysis to analyze more complex structures such as grain boundaries is possible based on the medium-range-order (MRO) analysis. This method is capable of determining the local crystallinity class. The MRO analysis has been applied in the analysis of simulations of nanocrystalline materials, where an exact characterization of the grain boundary structure is important (e.g. [56,

66, 217]).

Part II.

Brittle fracture

3. Modeling of brittle materials failure

As schematically visualized in Figure 3.1, brittle fracture is a complex multiscale process. At the scale of several Ångstroms, interatomic bonding and the atomic microstructure determine important material properties for fracture, as for instance the fracture surface energy. At this scale, the chemistry of atomic interaction and therefore quantum mechanics can play an important role. Breaking of atomic bonds occurs in the fracture process zone at length scales of several nanometers [78]. In a region around the crack tip extending a few tens of nanometers, the material experiences large deformation and nonlinearities between stress and strain become apparent. The macroscopic fracture process on a scale of several micrometers can only be understood if the mechanisms on smaller length scales are properly taken into account.

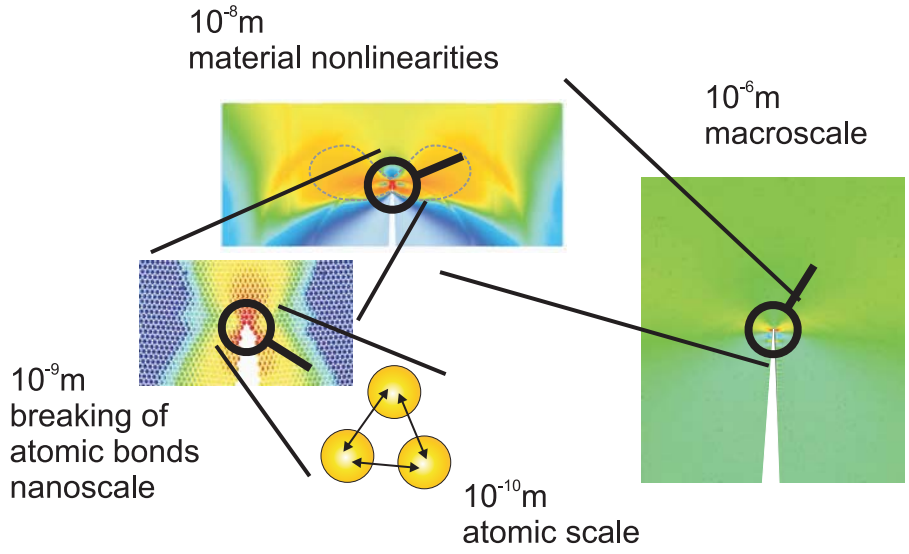

Figure 3.1.: Different length scales associated with dynamic fracture. Relevant length scales reach from the atomic scale of several Ångstrom to the macroscopic scale of micrometers and more.

Despite the fact that there exists a nonlinear zone near the crack tip due to strong material deformation, most existing theories [78, 29] assume linear elastic material behavior also in the vicinity of the crack. However, existing theories of fracture fail to explain several phenomena observed in computer simulation and in experiment. Examples for discrepancies include significantly reduced maximum crack speeds in experiment compared to theory prediction, and the observation of dynamic crack tip instabilities at reduced speeds [69, 70]. We hypothesize that the discrepancies between experiment, computer simulation and theory can be explained based on the erroneous assumption of linear elastic material behavior in regions very close to the crack tip. Fracture is a highly

nonlinear process and thus nonlinear theories are required to capture all phenomena!

The main focus of this part will be on understanding the role of material nonlinearities in dynamic fracture. We will show that hyperelasticity, the elasticity of large strains, governs dynamic fracture under certain conditions. Several existing theories fail to describe the observations and must be replaced by nonlinear theories of fracture.

Modeling of dynamic fracture can be quite challenging. A variety of numerical tools have been developed over the last decades. Modeling attempts focused on cohesive surface models [65] and continuum models incorporating atomistic information like VIB [129, 130] (see also discussion in Section 2.3.4), for instance. Since these methods are based on continuum mechanics theories, *a priori* knowledge about the failure path must be known. In contrast, atomistic methods require no *a priori* knowledge about the failure. Studying rapidly propagating cracks using atomistic methods is particularly attractive, because cracks propagate at speeds of km/sec, which corresponds to nm/ps. This scale is readily accessible with classical molecular-dynamics methods. Much of the research of dynamic fracture focused on understanding the atomic details of crack propagation and its relation to macroscopic theories [78] as well as experiments of fracture [69]. The first part of this review describes simulation work that mostly treats generic "brittle model materials" rather than specific materials. Later we focus on simulations that discuss fracture in specific materials.

3.1. Atomistic simulations of fracture

The earliest molecular-dynamics simulations of fracture were carried out almost 30 years ago by Ashurst and Hoover [20]. Many features of dynamic fracture were described in the paper, although their simulation size was extremely small (only 64×16 atoms with crack lengths around ten atoms).

A classical paper by Abraham and coworkers published in 1994 stimulated much further research [5]. In this work, the authors reported molecular-dynamics simulations of fracture in systems up to 500,000 atoms, which was a significant number at that time. In these atomistic calculations, a Lennard-Jones potential as described in equation (2.4) was used. The results in [5, 7] were striking because the molecular-dynamics simulations reproduced phenomena that were discovered in experiments a few years earlier [69]. The most important observation was the so-called "mirror-mist-hackle" transition. It was observed that the crack face morphology changes as the crack speed increases. The phenomenon is also referred to as dynamic instability of cracks. Up to a speed of about one third of the Rayleigh wave speed, the crack surface is atomically flat (mirror regime). For higher crack speeds the crack starts to roughen (mist regime) and eventually becomes very rough (hackle regime), accompanied by dislocation emission. Such phenomena were observed at similar velocities in experiments [69]. Since the molecular-dynamics simulations are performed in a perfect lattice, it was concluded that these dynamic instabilities are a universal property of cracks. The instabilities were subject to numerous other studies (e.g. [150]) in following years.

A question that has attracted numerous researchers is that of the limiting speed of cracks [78]. The crack speed is limited by an impenetrable barrier that is related to the

speed of sound in the material. The limiting speed for mode I cracks is the Rayleigh wave speed. For mode II cracks, velocities below the Rayleigh speed and those between the shear wave speed and the longitudinal wave speeds are admissible. Between these two regimes, there is an impenetrable velocity gap, which led to the uncertainty that mode II cracks may also be limited by the Rayleigh wave speed.

In contrast, experiments have recently shown that shear-loaded (mode II) cracks can move at intersonic velocities through a mother-daughter mechanism [184, 183]. Molecular-dynamics simulations by Abraham and Gao (2001) reproduced this observation, and provided a quantitative continuum mechanics analysis of this mechanism [83]. A short distance ahead of the crack, a shear stress peak develops that causes nucleation of a daughter crack at a velocity beyond the shear wave speed. This topic is an example where atomistic simulations could immediately be coupled to experiments. This also led to the development of the fundamental solution of intersonic mode II cracks by Huang and Gao [116]. The fundamental solution was then used to construct the solution describing the dynamics of a suddenly stopping intersonic crack [117].

Other research by Gao *et al.*[83] reported simultaneous continuum mechanics and atomistic studies of rapidly propagating cracks. The main objective of the studies was to investigate if the linear continuum theory can be applied to describe nanoscale dynamic phenomena. The studies included the limiting speed of cracks and Griffith analysis [83]. The results suggest that continuum mechanics concepts could be applied to describe crack dynamics even at nanoscale, underlining the power of the continuum approach.

Materials in small dimensions have also attracted interest in the area of dynamic fracture. Studies of such kind involve crack dynamics at interfaces of different materials (e.g. in composite materials). Since interfaces play an important role in the dynamics of earthquakes, cracks at interfaces have been significantly studied in recent years [89]. Some investigations revealed that shear-dominated cracks at interfaces between dissimilar materials can move at intersonic and even supersonic velocities [11, 3]. If shear dominated cracks propagate along interfaces between two dissimilar materials, multiple mother-daughter mechanisms have been observed, and they were referred to as mother-daughter-granddaughter mechanisms [11].

Other studies of brittle fracture were based on lattice models of dynamic fracture [150, 148]. These models have the advantage that crack dynamics can be solved in closed form for some simplified cases [148]. In contrast to the large-scale molecular-dynamics models described above, lattice models are usually small and do not rely on big computers.

In [112], the authors report an overview over atomistic and continuum mechanics theories of dynamic fracture, emphasizing the importance of the atomic scale in understanding materials phenomena. They discuss scaling arguments allowing to study crack dynamics in small atomic systems and scaling it up to larger length scales comparable to experiment. A study of fracture in tetravalent silicon based on the Stillinger-Weber (SW) potential is discussed. The authors state that the SW potential has problems describing brittle fracture in silicon well, since the experimentally preferred fracture planes (111) and (110) could not be reproduced. The authors further discuss other possible potentials for silicon in terms of their applicability to model fracture of silicon. A velocity gap is discussed implying that at zero temperature there is a minimum speed at

which cracks can propagate. Various simulations of fracture of silicon are summarized [111]. In [148], further issues of atomic brittle fracture are discussed, such as lattice trapping. Also, the author showed a relation of crack velocity and loading indicating that there are regimes of forbidden velocities, so that the crack speed increases discretely with increase of loading. In another publication they compared the crack velocity as a function of energy release rate calculated by molecular-dynamics to experimental results [104]. Further discussion on the role of the potential in dynamic fracture can be found in a recent review article [3].

The group around Vashishta [220] reported large-scale atomistic studies of dynamic fracture involving 10 to 100 million atoms. They studied fracture of silicon nitride, fracture of graphite and fracture in gallium arsenide. They also report studies of fiber-reinforced ceramic composites (silicon nitride reinforced with silica-coated carbide fibers). More recently, the research group reported molecular-dynamics simulations with up to one billion atoms [193, 221]. In a recent review, further approaches of modeling dynamic fracture are summarized [186].

Gumbsch and coworkers [98] reported a series of molecular-dynamics simulations to evaluate the influence of several aspects on the dynamic crack tip instability based on various potentials. The authors also report a velocity gap for crack speeds. They use a particular type of boundary conditions leaving the crack in an elliptical shaped boundary with viscous damping at the outside to avoid reflection of waves from the boundary. Due to its shape similar to a stadium, it was referred to as "stadium damping" by Gumbsch and coworkers [98]. The crack propagates within an NVE ensemble in an elliptical "stadium" that is characterized by center and stadium. Outside this inner ellipse viscous damping or NVT temperature control is applied. This setup is chosen because stress waves reflecting from the boundaries can severely influence the dynamics of cracks, leading to crack arrest. The authors find that the limiting speed of cracks is between 30-40 percent depending on the potential. It was reported that cracks release the excess energy by emitting strong acoustic waves during breaking of every single atomic bond. Further, the authors did not observe crack branching since the velocity was too low for this phenomenon to be observed.

Other research in recent years focused on mechanical behavior of quasicrystals [154, 211]. Quasicrystals, for the first time observed 1984, show a symmetry "between crystal and liquids" and can not be described as a Bravais lattice [128]. They are metallic alloys whose positions of atoms are long range translationary ordered. Research in this field focused on dislocation motion and crack propagation. Unlike in crystals where dislocations leave the lattice undisturbed after they have passed, in quasicrystals they leave a phason-wall that weakens the binding energy and may serve as paths for crack propagation [153, 154, 211]. Atomic studies helped to clarify the fracture mechanism in such materials.

3.2. Outline of the studies presented in this part

The studies in the area of dynamic fracture will be focused on the following points.

- How do atomistic simulations results compare with continuum mechanics theory

predictions?

- What is the role of material nonlinearities (hyperelasticity) in dynamic fracture?
- What is the effect of geometric confinement and crack propagation along interfaces?

We start with a discussion of a one-dimensional model of fracture in Chapter 4. We discuss a linear elastic continuum theory serving as a basis for the extension of the analytical model to the nonlinear case. We report an atomistic model of one-dimensional fracture and show that the continuum theories agree reasonably well with the atomistic simulation results. It is shown that hyperelasticity can significantly alter the dynamics of fracture, in agreement with the analytical model. The one-dimensional model allows to study some of the phenomena that also appear in higher dimensional models in a mathematical and numerical simple framework.

Chapter 5 is devoted to a discussion on mechanical and physical properties of two-dimensional solids. Good understanding of these is critical in order to compare the atomistic simulation results with continuum mechanics theories. We present methods to calculate elastic properties and wave speeds from the interatomic potential. Various choices of interatomic potentials are discussed. We also address the issue of calculating the fracture surface energy.

In Chapter 6, we report joint continuum-atomistic studies of the deformation fields near a moving mode I crack in a harmonic lattice. We show that in harmonic lattices corresponding to linear elastic material, continuum mechanics theory is a reasonable model. We compare the stress and strain fields, particle velocity distribution, potential energy field and energy flow. We show that the predicted limiting speed of cracks agrees with the simulation result and the harmonic atomistic model can be used as a reference system.

Chapter 7 focuses on the role that material nonlinearities play on the limiting speed of cracks propagating along a prescribed straight fracture path. We show that hyperelasticity can govern dynamic fracture when the size of the nonlinear region around the crack tip approaches a newly discovered length scale associated with energy flux to the crack tip. The characteristic energy length scale helps to explain many experimental and computational results. The analysis illustrates that under certain conditions, cracks can break through the sound barrier and move supersonically through materials. An important aspect of the analysis is the prediction of intersonic mode I cracks.

Whereas the preceding chapter focused on the dynamics of constrained cracks, Chapter 8 focuses on the dynamics of unconstrained cracks and the effect of hyperelasticity. The main focus is an investigation of the critical crack speed when straight crack motion becomes unstable. By a systematic study with different model materials representing weak and strong hyperelastic effects we show that hyperelasticity governs the critical speed of crack tip instabilities.

Chapter 9 discusses several aspects of dynamic fracture along interfaces of dissimilar materials. We will show that mother-daughter mechanisms, formerly believed to exist only under mode II loading, also exist in the dynamics of mode I cracks along interfaces of elastically dissimilar materials. Further, we illustrate that mode II cracks moving along interfaces of dissimilar materials feature a mother-daughter-granddaughter mechanism.

In Chapter 10 we discuss inertia properties of cracks by investigating the dynamics of suddenly stopping cracks. We will show good agreement of suddenly stopping mode I cracks with theory and experiment [230, 78], and discuss the dynamics of suddenly stopping mode II cracks with respect to recently developed continuum mechanics theories [117]. We also address the role of material nonlinearities, and report a Griffith analysis for crack initiation for different interatomic potentials.

The final two chapters are devoted to the dynamics of mode III cracks. Since mode III cracks can only be modeled with three-dimensional models, we discuss mechanical and physical properties of three-dimensional solids in Chapter 11. The results include calculation of wave speeds for different potentials used.

Chapter 12 contains a discussion of the dynamics of mode III cracks. We will study a crack in a stiff material layer embedded in a soft matrix, and confirm existence of the characteristic length scale for energy flux also for mode III cracks. The results of atomistic simulations are quantitatively compared with recently developed continuum mechanics theory.

4. A one-dimensional model of dynamic fracture

Here we show by simultaneous continuum-atomistic studies of a one-dimensional model of fracture that hyperelasticity, the elasticity of large strains, plays the governing role in the dynamics of fracture in brittle materials and that linear theory is incapable of capturing all phenomena, such as the speed of crack propagation in real materials.

The first part of the chapter is dedicated to a systematic comparison of the linear elastic continuum model with molecular-dynamics simulations featuring harmonic interatomic potentials. The results for wave propagation velocities, the critical condition for fracture, inertia properties of the crack as well as stress and deformation fields around the crack tip suggest good agreement of our atomistic model with the continuum theory.

In the second part of the chapter, the one-dimensional model is used to study crack dynamics in nonlinear materials. Based on the concept of local elastic properties [81], an analytical model is proposed for the dynamics of the crack and for the prediction of the deformation field. An important prediction of this model is the possibility of supersonic crack propagation if there is a local elastically stiff region close to the crack tip. By atomistic simulations, we show that this hypothesis is true and that an elastically stiff zone at the crack tip allows for supersonic crack propagation. This suggests that local elasticity at the crack tip is crucial for the dynamics of fracture. In most classical theories of fracture it is believed that there is a unique definition of how fast waves propagate in solids. Our results prove that this concept can not capture all phenomena in dynamic fracture, and instead should be replaced by the concept of local wave speeds.

4.1. Introduction

Most of the theoretical modeling and most computer simulations have been carried out in two or more dimensions (e.g. [78, 29, 5, 11]). One of the important objectives in understanding hyperelasticity in dynamic fracture is to obtain analytical models. However, finding analytical solutions for dynamic fracture in nonlinear materials seems extremely difficult, if not impossible in many cases [99]. In order to investigate the nonlinear dynamics of fracture at a simple level, we propose a one-dimensional (1D) model of dynamic fracture, as originally reported by Hellan [108] for linear elastic material behavior.

The model can be described as a straight, homogeneous bar under lateral loading σ_0. Part of the bar is attached to a rigid substrate, and this attachment can be broken, so that a crack-like front of debonding moves along the bar (in the following, we refer to the front of debonding as crack tip). The model is depicted in Figure 4.1. A complete analytical solution of this problem is available based on linear elastic continuum

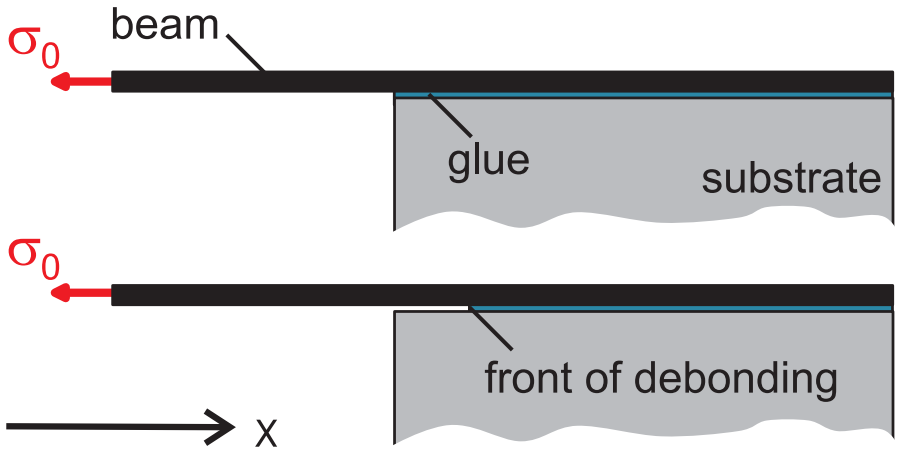

Figure 4.1.: Geometry of the one-dimensional model of fracture.

mechanics theory [108]. Theory predicts that the 1D model has many of the features of higher-dimensional models of dynamic fracture. For instance, there exists a limiting speed for the one-dimensional crack associated with the wave velocity, and a critical condition for fracture initiation similar to the Griffith criterion can be formulated.

Due to its simplicity, the one-dimensional model of fracture seems an ideal starting point for analyses of the complex dynamics of fracture in nonlinear materials, rather than immediately relying on two-dimensional models. We show that it is possible to extend the linear continuum model to describe the nonlinear dynamics of cracks for a bilinear stress-strain law. This elastic behavior is characterized by two distinct Young's moduli, one for small strains and one for large strains, and provides the most simple constitutive law of hyperelasticity. The new continuum model predicts that the crack propagates supersonically, if there exists a local zone around the crack tip with stiffer elastic properties than in the rest of the material (which is elastically softer).

Based on the continuum model, we construct an atomistic model as illustrated in Figure 4.2. The model features a one-dimensional string of atoms. Part of the atoms are bonded to a rigid substrate by a "weak potential", whose bonds snap early leading to a finite fracture energy. Bonds between the atoms never break. Using harmonic interatomic potentials, the elasticity of a string of atoms corresponds to a straight linear elastic bar of homogeneous material. Using nonlinear interatomic potentials, the atomistic model is readily able to model a nonlinear material response. A bilinear stress-strain law as assumed in the continuum model can be mimicked at the atomic scale by using a biharmonic potential. The new continuum model of one-dimensional fracture in nonlinear materials in conjunction with the nonlinear atomistic simulations allow to carry out simultaneous atomistic-continuum studies of the nonlinear dynamics of fracture.

The plan of this chapter is as follows. After a review of the linear continuum theory of one-dimensional dynamic fracture, we present the continuum model for one-dimensional fracture in the nonlinear case. In joint continuum-atomistic studies, we investigate the predictions of both linear and nonlinear continuum theory with atomistic simulation results. We find reasonable agreement at the two scales. Our results provide evidence that the predictions of the new continuum model for a bilinear stress-strain law are

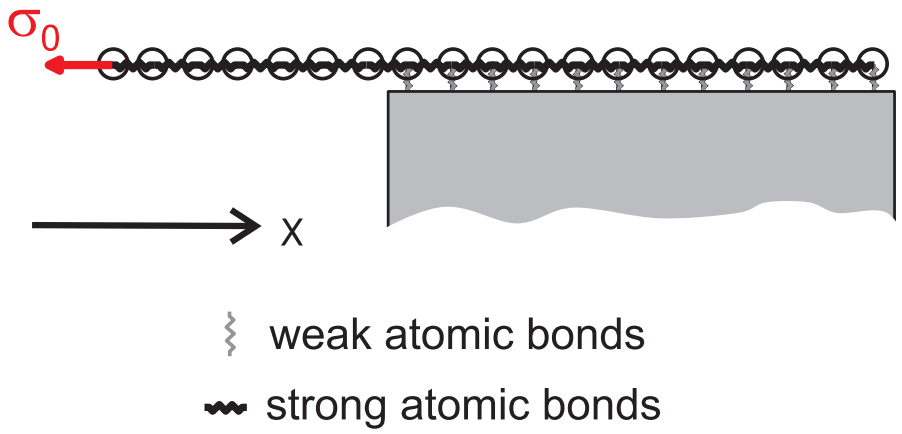

Figure 4.2.: One-dimensional atomistic model of dynamic fracture.

reasonable. We will show that the crack limiting velocity is indeed associated with the elastic properties localized to the crack tip.

4.2. Linear-elastic continuum model

The analytical continuum solution is discussed in detail elsewhere [107, 76, 108]. We only summarize the main results here. With particle displacement u, particle velocity $\dot{u} = \partial u/\partial t$, density ρ, coordinate system x and stress σ, the equation of motion in the absence of body forces is

$$\frac{\partial \sigma}{\partial x} = \rho \frac{\partial^2 u}{\partial t^2}, \tag{4.1}$$

where c_0 is the wave velocity. This equation can be combined with Hooke's law, given by

$$\sigma = E\varepsilon = E\frac{\partial u}{\partial x}, \tag{4.2}$$

with E as Young's modulus and ε as strain. This leads to a partial differential equation to be solved for $u(x,t)$

$$c_0^2 \frac{\partial u^2}{\partial x^2} = \frac{\partial^2 u}{\partial t^2} \tag{4.3}$$

where c_0 is the wave velocity. It can be shown that equation (4.3) has solutions of the form $u = f(x \mp c_0 t) = f(\xi)$, because

$$\frac{\partial^2 u}{\partial x^2} = \frac{\partial^2 f}{\partial \xi^2}, \quad \frac{\partial^2 u}{\partial t^2} = c_0^2 \frac{\partial^2 f}{\partial \xi^2}. \tag{4.4}$$

This solution represents a signal travelling in the positive or negative x direction. Also, it follows that a stress wave

$$\sigma = E\frac{\partial f}{\partial \xi} = E\,H(\xi) = E\,H(x \mp c_0 t) \tag{4.5}$$

is moving with the sound velocity c_0, and the particle velocity

$$\dot{u} = \mp c_0 \frac{\partial f}{\partial \xi} = \mp c_0 H(x \mp c_0 t) = \mp \frac{c_0}{E}\sigma. \tag{4.6}$$

In equations (4.5) and (4.6), the function $H(s)$ is the unit step function ($H(s) = 0$ for $s < 0$, and $H(s) = 1$ for $s \geq 0$). In the model of one-dimensional fracture (as shown in Figure 4.1), we assume that the left part of the string of atoms (which is free and not attached to the substrate) is loaded with stress σ_0. We assume that the crack front moves at propagation velocity $\dot{a}$ in the positive x direction. When the crack front has moved by the length $\mathrm{d}a = \mathrm{d}t\dot{a}$, a point which has formerly been situated at the crack tip is displaced backward by $\mathrm{d}u = -\varepsilon \mathrm{d}a$, because the detached part of the string has attained the axial strain ε. A crack represents a signal constrained to be travelling at a lower velocity than $\dot{a} \leq c_0$. According to equation (4.6), this corresponds to the particle velocity

$$\dot{u} = -\varepsilon \dot{a} = -\frac{\dot{a}}{E}\sigma_t, \tag{4.7}$$

where σ_t is the local stress to the left to the crack tip. Furthermore, we assume that the stress behind the crack tip can be expressed as the sum of the initial stress σ_0, and an emitted stress wave to the separation, σ_e, so that

$$\sigma_t = \sigma_0 + \sigma_e. \tag{4.8}$$

The emitted stress wave is related to the particle velocity

$$\dot{u} = \frac{c_0}{E}\sigma_e. \tag{4.9}$$

Equations (4.7) through (4.9) can be solved for the three unknowns σ_t, σ_e and $\dot{u}$. We define $\alpha = \dot{a}/c_0$ as the ratio of crack propagation velocity to the sound velocity. The particle velocity behind the crack tip is given by

$$\dot{u} = -\frac{\dot{a}}{1+\alpha}\frac{\sigma_0}{E}, \tag{4.10}$$

and the local stress wave behind the crack tip carries

$$\sigma_t = \frac{1}{1+\alpha}\sigma_0. \tag{4.11}$$

The emitted stress wave is

$$\sigma_e = -\frac{\alpha}{1+\alpha}\sigma_0. \tag{4.12}$$

The ratio of local to initial strain is

$$\varepsilon_t/\varepsilon_0 = \frac{1}{1+\alpha}, \tag{4.13}$$

where ε_0 is the initial strain prior to crack propagation. Also,

$$\varepsilon_t = \frac{1}{1+\alpha}\frac{\sigma_0}{E}. \tag{4.14}$$

In these equations, the crack speed $\dot{a}$ remains an unknown. However, we can make use of the energy balance

$$G = W - \frac{\mathrm{d}T}{\mathrm{d}a} - \frac{\mathrm{d}\phi}{\mathrm{d}a} = R(\alpha), \tag{4.15}$$

where W is the external work, $\mathrm{d}T$ is the increment of kinetic energy and $\mathrm{d}\phi$ is the increment of potential energy, and $R(\alpha)$ is the dynamic fracture resistance. Balancing kinetic and potential energy using equations (4.9), (4.10) and (4.12) we arrive at $G = G_0 g(\alpha) = R(\alpha)$ with $G_0 = \sigma_0^2/(2E)$, and

$$g(\alpha) = \frac{1-\alpha}{1+\alpha}. \tag{4.16}$$

We emphasize that the crack driving force vanishes for $\alpha \to 1$, independent of how large we may choose G_0, because $g(\dot{a}) \to 0$ in this case, and therefore the sound velocity provides an upper bound for the crack propagation velocity. An energy balance for fracture initiation ($\dot{a} = 0$) in the spirit of Griffith's analysis leads to an expression for crack initiation

$$\frac{\sigma_0^2}{2E} = R_0 \tag{4.17}$$

where R_0 is fracture surface energy defined as the energy required to break atomic bonds per unit crack advance. Since $R(\dot{a})$ is generally not known, it has to be determined from experiments or numerical calculations. In order to determine the curve $R(\alpha)$, one may apply a stress σ_0, measure the crack limiting speed α and calculate the value of $R(\alpha)$ as

$$R(\alpha) = \frac{\sigma_0^2}{2E}\frac{1-\alpha}{1+\alpha}. \tag{4.18}$$

If this curve is known, the crack equation of motion can be solved completely. A simplification in order to make the one-dimensional problem solvable in closed form is to assume a constant dynamic fracture toughness, thus $R(\alpha) = R_0\, g(\alpha)$. This assumption is usually a good approximation for low propagation velocities. For higher velocities close to the crack limiting speed $\dot{a} \to c_0$, however, it is expected that even though the stress is increased significantly, the crack speed will not change much [78, 108].

Equation (4.18) states that the dynamics of the crack responds immediately to a change in loading or fracture energy, implying that the crack carries no inertia. However, the information about the change in loading or fracture resistance is transmitted with the sound velocity, as indicated by equation (4.5). When the crack suddenly stops from a high propagation velocity, the local strain immediately changes from the magnitude at high propagation velocity to $\varepsilon_t = \varepsilon_0$ (static field solution). This can be verified using equation (4.12). The crack carries no inertia since the crack immediately responds to a

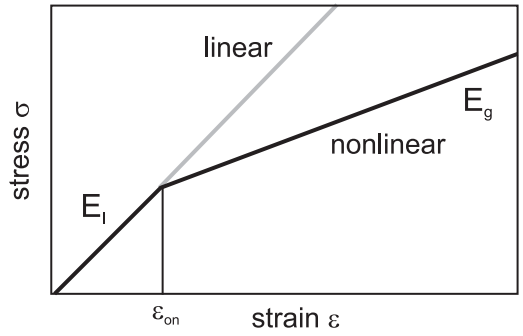

Figure 4.3.: Bilinear stress-strain law as a simplistic model of hyperelasticity. The parameter $\varepsilon_{\mathrm{on}}$ determines the critical strain where the elastic properties change from local (E_{l}) to global (E_{g}).

change in the boundary conditions. The crack tip velocity responds instantaneously to a change in fracture energy.

We summarize the predictions of the continuum model. A critical loading is necessary to initiate fracture (that is, to break the first bond), similar to the Griffith condition. While the crack propagates, it sends out a stress wave with a magnitude depending on the crack propagation velocity. For $\alpha = 0$, no stress wave is emitted and the local stress $\sigma_t = \sigma_0$. For $\alpha \to 1$, the local stress wave has magnitude $\sigma_t = \sigma_0/2$. For intermediate values of α, the stress wave magnitude decreases monotonically from σ_0 to $\sigma_0/2$, as α increases from zero to one. The theory predicts that the largest velocity the crack may achieve is the sound velocity c_0, hence $\alpha^{\max} = 1$. As higher-dimensional cracks, it is predicted that the 1D crack carries no inertia.

4.3. Hyperelastic continuum mechanics model for bilinear stress-strain law

If the stress-strain dependence is not linear as assumed in equation (4.2), the theory discussed in the last paragraph does not hold. However, the linear theory can be extended employing the concept of local elastic properties and local wave velocities, in the spirit of the work discussed in [81]. It was hypothesized that hyperelastic effects become important in the dynamics of cracks because of the strong deformation gradients in the vicinity of the crack [81, 11]. Within a relatively small region, elastic properties may change drastically due to hyperelastic effects. The term "local" is hereby referred to as the region very close to the crack tip, and "global" refers to regions far away from the crack tip.

A bilinear stress-strain law serves as a unique tool to study the nonlinear dynamics of cracks: This model features two Young's moduli, E_{l} associated with small perturbations from the equilibrium position (strain smaller than $\varepsilon_{\mathrm{on}}$), and E_{g} associated with large deformations (strain larger or equal than $\varepsilon_{\mathrm{on}}$). The parameter $\varepsilon_{\mathrm{on}}$ allows tuning the strength of the hyperelastic effect. The bilinear stress-strain law is shown schematically in Figure 4.3.

There is a conceptual difference between the higher-dimensional models of fracture and the one-dimensional model of fracture. In the higher-dimensional models of fracture, the zone of large deformation is local to the crack tip, with large deformation gradients. In the one-dimensional model of fracture, the zone of large-deformation is found in regions far away from the crack tip, but the zone of small deformation close to the crack tip is associated with large deformation gradients. Considering the stress field in the vicinity of a moving crack based on the continuum model, this can be verified straightforwardly, since $1/2\sigma_0 \leq \sigma_t \leq \sigma_0$, and the stress ahead of the crack is zero, while it is σ_0 far behind the crack tip. Therefore, if the stress-strain law shows softening with increasing strain, the elastic properties at the crack tip tend to be stiffer than in the far-field. Even though there exists this qualitative difference of the elastic fields near a 1D and a higher-dimensional crack, the dynamics of these systems can be compared immediately if proper interpretation of the features of the deformation fields is done. A stiffening potential in higher-dimensional models tends to yield an elastically stiff zone at the crack tip. In the 1D model, a potential softening with strain is required to provide an elastically stiff zone at the crack tip.

Here we focus on the case when $E_\mathrm{l} > E_\mathrm{g}$, which implies that there exists a region close to the crack tip where the material is elastically stiffer than in regions far away. In a string of atoms, the stress σ due to strain ε is given by

$$\sigma = \begin{cases} E_\mathrm{l}\varepsilon & \text{if } \varepsilon < \varepsilon_\mathrm{on}, \\ E_\mathrm{g}\left(\varepsilon - \varepsilon_\mathrm{on}\right) + E_\mathrm{l}\varepsilon_\mathrm{on} & \text{if } \varepsilon \geq \varepsilon_\mathrm{on}, \end{cases} \tag{4.19}$$

where ε_on is the critical onset strain for hyperelasticity. Therefore, the initial equilibrium strain due to an applied stress σ_0 is given by

$$\varepsilon_0 = \begin{cases} \sigma_0/E_\mathrm{l} & \text{if } \varepsilon_0 < \varepsilon_\mathrm{on}, \\ \sigma_0/E_\mathrm{g} - \varepsilon_\mathrm{on}E_\mathrm{l}/E_\mathrm{g} + \varepsilon_\mathrm{on} & \text{if } \varepsilon_0 \geq \varepsilon_\mathrm{on}. \end{cases} \tag{4.20}$$

In the remainder, we confine our investigations to the choice of $E_\mathrm{l}/E_\mathrm{g} = 4$. Equation (4.20) is then simplified to

$$\varepsilon_0 = \begin{cases} \sigma_0/E_\mathrm{l} & \text{if } \varepsilon_0 < \varepsilon_\mathrm{on}, \\ 4\sigma_0/E_\mathrm{l} - 3\varepsilon_\mathrm{on} & \text{if } \varepsilon_0 \geq \varepsilon_\mathrm{on}. \end{cases} \tag{4.21}$$

The concept of local and global elastic properties leads to two reduced crack speeds $\alpha_\mathrm{g} = v/c_\mathrm{g}$ and $\alpha_\mathrm{l} = v/c_\mathrm{l}$. We note that

$$\alpha_\mathrm{g} = \sqrt{\frac{E_\mathrm{l}}{E_\mathrm{g}}} \cdot \alpha_\mathrm{l}, \tag{4.22}$$

which yields $\alpha_\mathrm{g} = 2\alpha_\mathrm{l}$ in the case considered here.

In the following, we derive expressions for the local strain field near the crack tip for a crack moving in a hyperelastic material. We distinguish two cases:

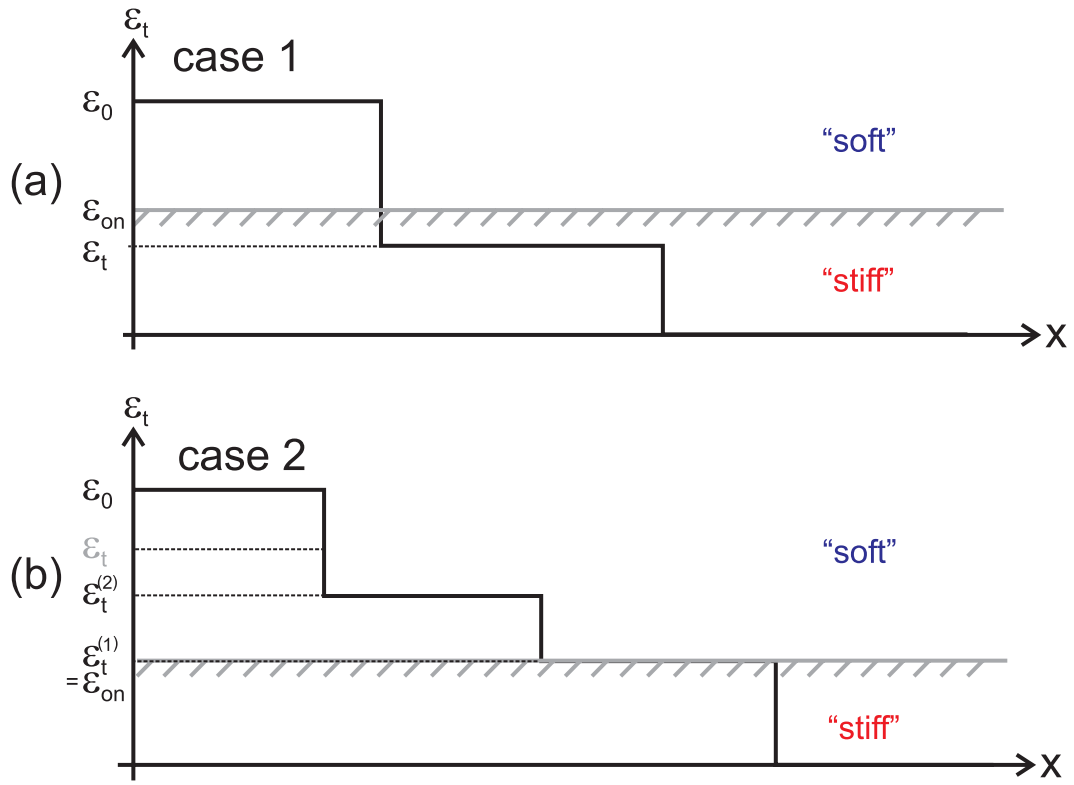

Figure 4.4.: Continuum model for local strain near a supersonic crack. The plot shows a schematic of the two cases 1 (subplot (a)) and case 2 (subplot (b)).

- Case 1: The local strain near the crack tip ε_t, is smaller than the onset strain of the hyperelastic effect, $\varepsilon_{\mathrm{on}}$. The crack dynamics is governed by the local elastic properties in this case, and due to the signal travelling to the left with lower strain, the hyperelastic stiff region expands to the left of the crack (see Figure 4.4 (a)).
- Case 2: The local strain near the crack tip ε_t is larger than the onset strain of the hyperelastic effect $\varepsilon_{\mathrm{on}}$. Therefore, the region of hyperelastic material response remains confined to the vicinity of the moving crack tip (see Figure 4.4 (b)).

4.3.1. Case 1: Expanding region of local elastic properties

We assume that the crack advance and material detachment occurs in a region with local elastic properties (associated with E_{l}), as shown schematically in Figure 4.4 (a). The local strain wave in the hyperelastic case is therefore predicted to be

$$\varepsilon_t = \frac{1}{1+\alpha_{\mathrm{l}}} \frac{\sigma_0}{E_{\mathrm{l}}}. \tag{4.23}$$

This equation is only valid if $\varepsilon_t < \varepsilon_{\mathrm{on}}$, that is, the local strain wave lays completely within the zone of local (stiff) elastic properties. An important implication of the assumption is that the limiting speed of the crack is determined by the local elastic wave speed. Since $\alpha_{\mathrm{l}}^{\max} = 1$, and $\alpha_{\mathrm{g}} = 2\alpha_{\mathrm{l}}$, the crack can propagate supersonically with respect to the

global elastic properties. The ratio of local strain to initial strain is given by combining equation (4.23) and (4.20)

$$\varepsilon_t/\varepsilon_0 = \begin{cases} \dfrac{1}{1+\alpha_\mathrm{l}} & \text{if } \varepsilon_0 < \varepsilon_\mathrm{on}, \\ \dfrac{1/(1+\alpha_\mathrm{l})\sigma_0/E_\mathrm{l}}{\sigma_0/E_\mathrm{g} - \varepsilon_\mathrm{on}E_\mathrm{l}/E_\mathrm{g} + \varepsilon_\mathrm{on}} & \text{if } \varepsilon_0 \geq \varepsilon_\mathrm{on}. \end{cases} \tag{4.24}$$

4.3.2. Case 2: Local hyperelastic region

Here we consider the case when ε_t as given by equation (4.23) is larger than the onset strain of the hyperelastic effect, that is $\varepsilon_t \geq \varepsilon_\mathrm{on}$. The emitted strain wave can not lay within the soft material since crack motion is supersonic with respect to the global soft elastic properties and no signal faster than the sound speed can be transported through the material. Therefore, a shock wave will be induced when the elastic properties change from stiff to soft. The signal of stress relief is transported through the soft material as a secondary wave and represents a wave travelling at c_g, the wave speed of the soft material, independent of how fast the crack propagates.

In summary, there are two waves propagating behind the crack tip. The first wave features a magnitude

$$\varepsilon_t^{(1)} = \varepsilon_\mathrm{on}, \tag{4.25}$$

independent of the crack speed. The second wave has magnitude

$$\varepsilon_t^{(2)} = \left(\frac{\sigma_0/2}{E_\mathrm{g}} - \varepsilon_\mathrm{on}\frac{E_\mathrm{l}}{E_\mathrm{g}} + \varepsilon_\mathrm{on}\right) + \varepsilon_\mathrm{on} \tag{4.26}$$

representing a signal travelling in the soft material at the wave speed of the soft material, also independent on the crack speed. The model is schematically summarized in Figure 4.4 (b).

4.3.3. Summary of the predictions of the hyperelastic continuum model

We summarize the major predictions of the hyperelastic continuum model for a bilinear stress-strain law. We distinguish two cases, case 1 when the local strain near the moving crack is smaller than the onset strain of the hyperelastic effect and case 2 when it is larger.

In case 1, the local elastic properties completely govern the dynamics of the crack. As a consequence, the model predicts that the crack can propagate supersonically. The upper limit of the propagation speed is given by the wave speed associated with the local elastic properties.

In case 2, detachment of the material occurs completely in the hyperelastic region and remains confined during crack growth. In this case, two waves with magnitude $\varepsilon_t^{(1)}$ and $\varepsilon_t^{(2)}$ are moving behind the crack tip, one is a shock front associated with the change in elastic properties and the other represents a signal travelling in the elastically soft

material carrying the stress relief due to crack propagation at the wave speed of the soft material. As the size of the hyperelastic zone shrinks with decreasing ε_{on}, the limiting crack speed is also expected to decrease and approach the limiting value of $\alpha_{\text{g}} \to 1$ for $\varepsilon_{\text{on}} \to a_0$. This is because the material detachment eventually occurs completely within the zone of soft elastic properties. On the other hand, if ε_{on} is chosen larger, the stiff zone expands and eventually the situation corresponding to case 1 is attained when $\varepsilon_t < \varepsilon_{\text{on}}$ and the dynamics is completely governed by the local elastic properties.

In any case, when the crack propagates supersonically, a dramatic reduction in the ratio $\varepsilon_t/\varepsilon_0$ is possible due to the local stiffening effect.

4.4. Molecular-dynamics simulations of the one-dimensional crack model: The harmonic case

According to Figure 4.2, the atoms are numbered from left to right with increasing index, with a total number of atoms N_t. We assume that atoms with index $i > N_f$ are attached to the substrate, and atoms with $i \leq N_f$ are free and only interact with other nearest neighbor atoms. The state of an atom i is uniquely defined by a position x_i and its velocity $\dot{x}_i$. The mass of each particle is $m = 1$. Only nearest neighbor interaction is considered. The systems contain up to $20,000$ atoms, which equals a string of atoms of length of about twenty micrometers in physical dimensions. In order to study one-dimensional fracture, we have developed a specific molecular-dynamics code optimized for one-dimensional analyses.

The basis for our atomic interactions is the Lennard-Jones interatomic potential defined in equation (2.4). We express all quantities in reduced units, so lengths are scaled by the LJ-parameter σ which is assumed to be unity in this study, and energies are scaled by the parameter $\epsilon_0 = 1/2$, the depth of the minimum of the LJ potential. The reduced temperature is $\mathrm{k}T/\epsilon_0$ with k being the Boltzmann constant. To study a harmonic system, we expand the LJ potential around its equilibrium position $a_0 = 2^{1/6} \approx 1.12246$, and consider only first order terms yielding harmonic atomic interactions.

In our simulation procedure, we distinguish an equilibration phase and a fracture simulation phase. In the equilibration phase, we initialize the free part of the bar with a prescribed homogeneous strain, given by $\varepsilon_0 = \sigma_0/E$ and let the system equilibrate for a longer time. During that time, we introduce a viscous damping force $f_{d,i} = -\dot{u}_i\,\eta$ into the system with $\eta = 0.3$ in order to damp out waves generated during equilibration, so that the particle velocities (and strain gradients) are damped out relatively fast. During equilibration, atomic bonds glued to the substrate can never break, and the total energy of the system is given by

$$U = \sum_{i,j} \left(\frac{1}{2} k (r_{ij} - a_0)^2 \right) + \sum_i \left(\frac{1}{2} H(i - N_f) k_p \hat{r}_i^2 \right) \tag{4.27}$$

where k is the spring constant for interatomic interaction, k_p is the spring constant of the pinning potential. The variable

$$\hat{r}_i = \mid x_{0,i} - x_i \mid, \tag{4.28}$$

and the variable x_i is the current position of the atom i. The variable $x_{0,i}$ stands for the initial position of atom i. We integrate the equations of motion using a velocity verlet algorithm, and choose a time step $\Delta t = 0.000,036$ in reduced atomic units of $\sigma\sqrt{m/\epsilon}$.

When all strain is equilibrated in the free standing part of the string, we begin the fracture simulation phase where the bonds to substrate have finite energy. The total energy of the system is then given by

$$U = \sum_{i,j} \left(\frac{1}{2} k (r_{ij} - a_0)^2 \right) + \sum_i \left(\frac{1}{2} H(i - N_f) H(r_{\text{break}} - \hat{r}_i) k_p \hat{r}_i^2 \right) \tag{4.29}$$

where r_{break} is the snapping bond distance for the pinning potential. The fracture energy R_0 in equation (4.17) is given by

$$R_0 = \frac{1}{2} \frac{k_p \hat{r}^2}{a_0}, \tag{4.30}$$

Assuming a stress-strain law as given by equation (4.2), we define a Young's modulus for a one-dimensional string of atoms [206]

$$E = k\, a_0, \tag{4.31}$$

The wave velocity in a string of atoms is given by

$$c_0 = \sqrt{\frac{E}{\rho}} \tag{4.32}$$

with density $\rho = m/a_0$ for the present one-dimensional lattice. For $k = 28.5732$, Young's modulus $E = 32.07$, and $c_0 \approx 6$. The elastic properties are determined numerically as a check if the assumptions are valid.

We define an atomic strain of atom i which is directly related to the continuum mechanics concept of strain [260], considering only nearest neighbors in a one-dimensional system

$$\varepsilon_i = \frac{x_{i-1} - x_{i+1}}{2\, a_0}. \tag{4.33}$$

In the remainder of this chapter, we preferably use the atomic strain to analyze our simulation results, since it provides a useful way to study the state of deformation in the atomic lattice.

We start with a comparison of the theoretical prediction of the elastic properties of the one-dimensional string of atoms with atomistic simulations. The numerically estimated elastic properties agree well with the theory. The measurements of applied stress σ_0 versus strain, and the numerically estimated local modulus in the string of atoms match the theoretical predictions given by equation (5.13) well. Additional studies of wave propagation velocity show good agreement of the predicted wave velocity with the measured wave velocity. Simulations with other spring constants and consequently other wave velocities provide evidence that the agreement of theory and simulation is generally good.

k_p/k	R_0^{pred}	R_0
10.0	0.0039	0.00014×10^{-4}
1.0	0.0039	0.0015
0.1	0.0039	0.0030
0.01	0.0039	0.0040
0.003	0.0039	0.0040

Table 4.1.: Critical load R_0 for fracture initiation, for different values of the spring constant k_p of the pinning potential. The results are in good agreement with the theory prediction when k_p becomes much smaller than k.

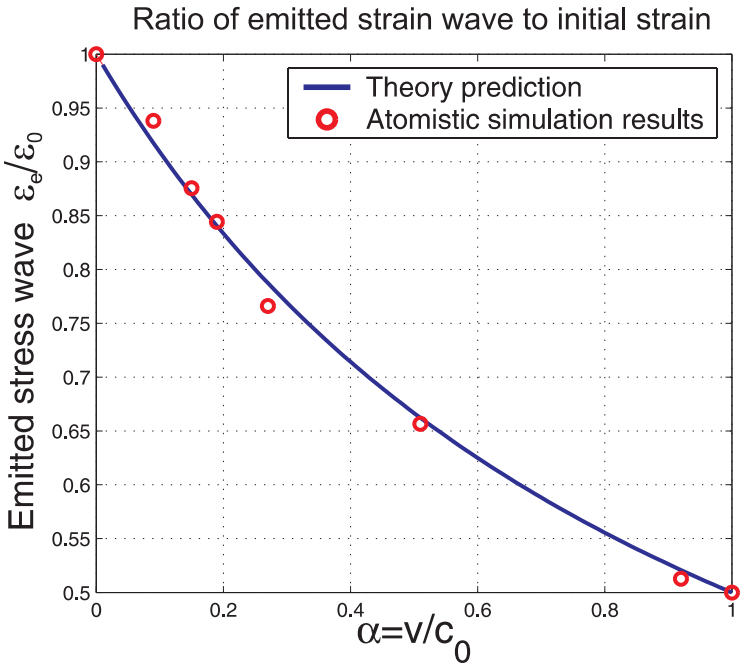

Figure 4.5.: Magnitude of the local stress wave for different crack propagation velocities from atomistic simulations, in comparison with the theory prediction.

Griffith criterion predicts that fracture initiates when the elastic energy released per unit crack advance equals the energy to create free surface per unit crack advance. The fracture energy is given by equation (4.30). Setting this quantity equal to the energy release rate allows to determine the critical load to initiate fracture. The computational results are compared to the theory prediction in Table 4.1. A result of the simulations is that the results converge to the theory prediction as k_p becomes much smaller than k, but we find larger disagreement with the theory prediction if k_p is large. This could be due to the fact that the fracture process zone becomes very small when k_p is large, leading to very large strain gradient at the crack.

Equation (4.12) predicts that the local stress wave depends on the crack propagation velocity. Figure 4.5 plots the magnitude of the local stress wave for different propagation velocities from atomistic simulations, in comparison with the theory prediction.

The dynamic fracture toughness is a function of α and σ_0, and is given by equation

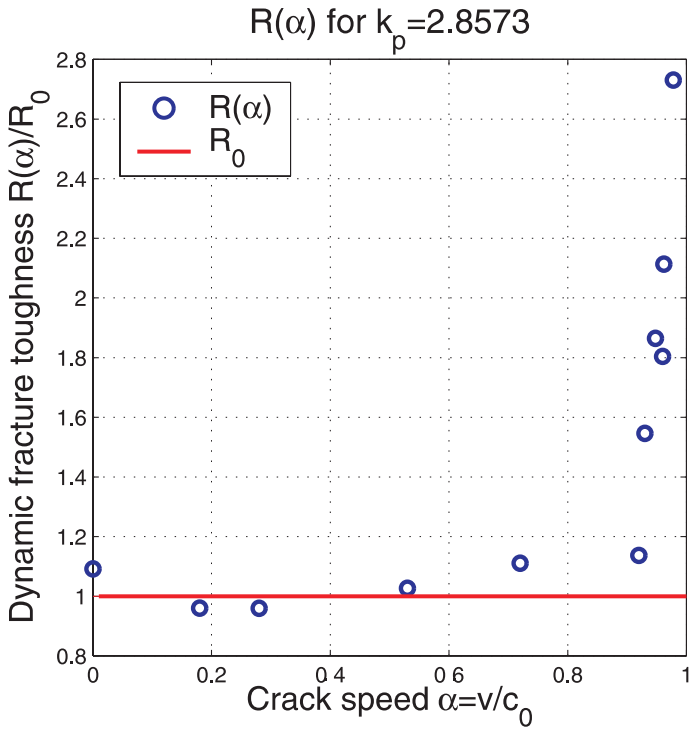

Figure 4.6.: Dynamic fracture toughness for different crack propagation velocities.

(4.18). Atomistic simulations provide an ideal tool in order to provide information on this curve. Figure 4.6 plots the dynamic fracture toughness for different crack propagation velocities. As can be verified, the assumption that $R_0 = \text{const.}$ is reasonable as long as the crack velocity is below 80 percent of the wave velocity. For larger velocities, the curve deviates significantly from a constant and increases dramatically. This behavior is expected from theory [107] (and also for higher dimensions, as discussed for instance in [78]).

If $\alpha < 1$, the crack front propagates slower than the local wave front behind the crack. If the material left to the crack is of finite length, the reflected wave from the left end will eventually hit the crack tip at a time

$$\delta t = \frac{2L + \Delta a}{c_0}, \tag{4.34}$$

where L denotes the initial free length of the bar, and Δa is the distance the crack has travelled until it is hit. Once the reflected wave front impinges the crack, the stress will suddenly increase causing a jump in crack propagation speed [107]. In the atomistic simulations, we observe this effect, but note that the crack does not reach a steady-state as predicted by the theory. Instead, the crack speed seemed to decrease continuously, much below the value predicted by the theory. During this process, the temperature in the system increased continuously and energy seems to be dissipated into heat ("thermalization" process).

To investigate the dynamics of a suddenly stopping crack, we let the crack propagate at a high velocity $\alpha \approx 0.9$, and then force the crack to stop. This is achieved by setting $\hat{r}$ to a large number $\hat{r}_\infty \gg \hat{r}$ for all atoms with identification number greater than

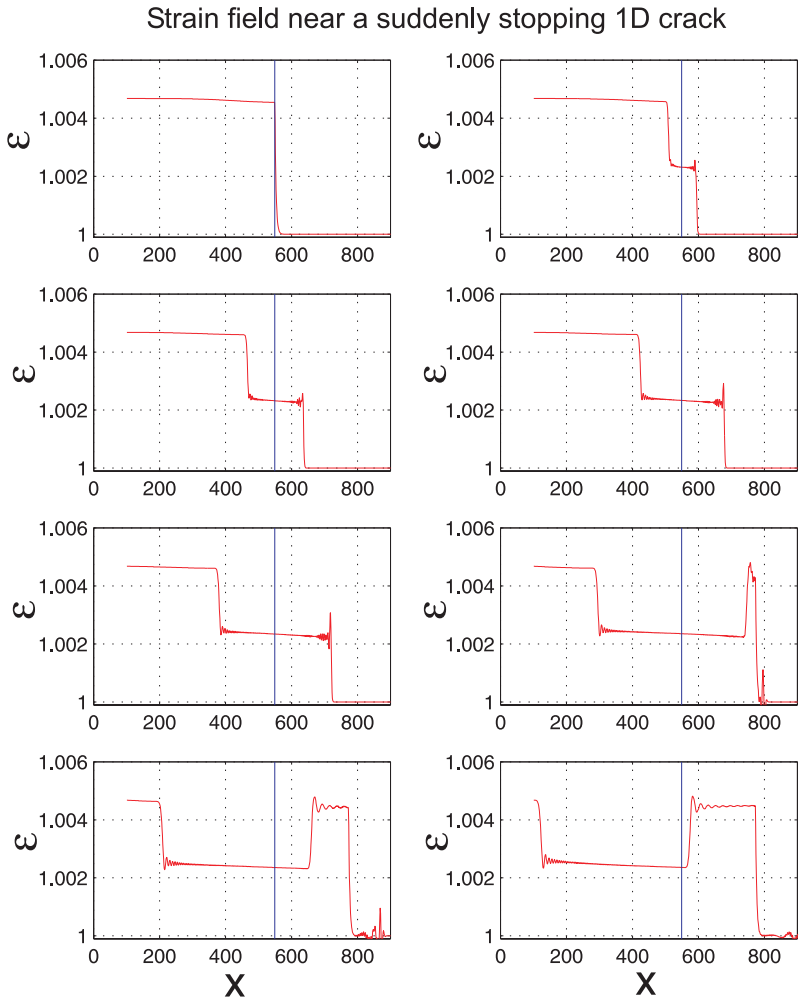

Figure 4.7.: Strain field near a suddenly stopping one-dimensional crack. The crack is forced to stop at $x \approx 790$. As soon as the crack stops, the strain field of the static solution is spread out with the wave speed.

$i_{\text{stop}} > N_f$. This forces the crack to suddenly stop once the crack tip reaches the atom with index equal i_{stop}:

$$\hat{r}(i) = \begin{cases} \hat{r}_0 & \text{if } i < i_{\text{stop}}, \\ \hat{r}_\infty & \text{if } i > i_{\text{stop}}. \end{cases} \tag{4.35}$$

The simulation results illustrate that the theory prediction is satisfied, and the local strain immediately attains the magnitude ε_0 as soon as the crack is stopped. The static field spreads out with the wave velocity. The results are plotted in Figure 4.7.

The discussion of the suddenly stopping one-dimensional crack proves that a one-dimensional crack carries no inertia. According to this observation, the crack tip velocity should immediately respond to a change in the fracture energy. For example, if the crack senses a higher fracture surface energy, the velocity should instantaneously decrease, and if the crack senses a lower fracture surface energy, vice versa. We test this statement by introducing a periodically varying fracture surface energy as the crack propagates along

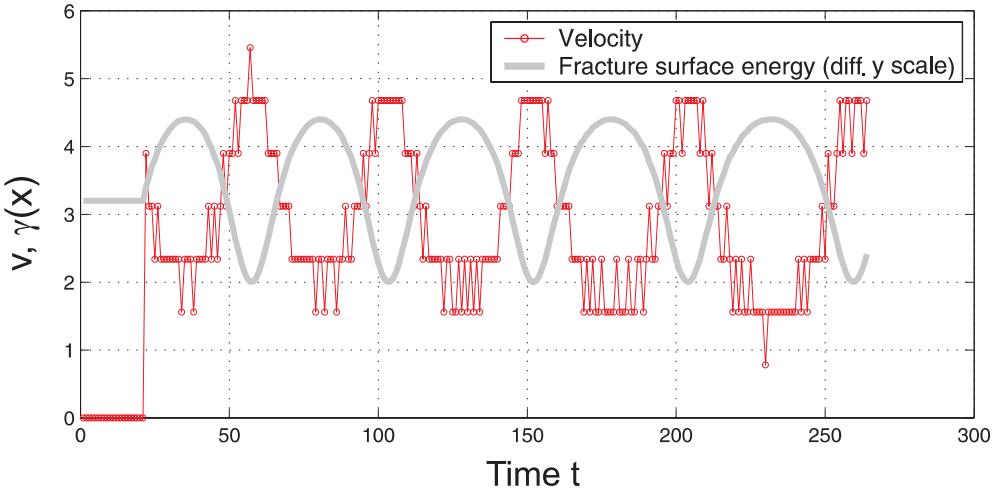

Figure 4.8.: Prescribed fracture toughness and measured crack velocity as the crack proceeds along x.

x. The velocity should change in anti-phase with the change of fracture surface energy. A variation in fracture energy is achieved by varying the bond snapping distance $\hat{r}$ of the pinning potential (see equation (4.30)) according to

$$\hat{r} = \hat{r}_0 + \Delta\hat{r}\,\sin(x/p), \tag{4.36}$$

where $\hat{r}_0$ is the value around the snapping distance. The bond snapping distance oscillates with amplitude $\Delta\hat{r}$ and period factor p.

In Figures 4.8 and 4.9, results are plotted for $\hat{r}_0 = 0.008$, $\Delta\hat{r} = 0.003$ and $p = 30$. The velocity oscillates around $\alpha \approx 0.6$, which is in agreement with the velocity of a crack under loading $\sigma_0 = 0.02$ and a fracture toughness of $\hat{r} = 0.008$. The same observation applies to the upper and lower limit of the propagation velocity, which correspond to the limiting velocity of the crack if it would be propagating along a path with constant fracture energy of the corresponding magnitude. Therefore,

$$v = \hat{v}_0 + \Delta v\,\sin(x/p), \tag{4.37}$$

where v_0 is the velocity associated with $\hat{r}_0$, and $\Delta v \approx 1.3$ can be approximated by the difference of the propagation velocity associated with $\hat{r}_0 + \Delta\hat{r}$.

4.5. Molecular-dynamics simulations of the one-dimensional crack model: The supersonic case

This section is dedicated to molecular-dynamics simulations of supersonic cracks. In order to achieve a bilinear stress-strain law according to equation (4.19), the total potential

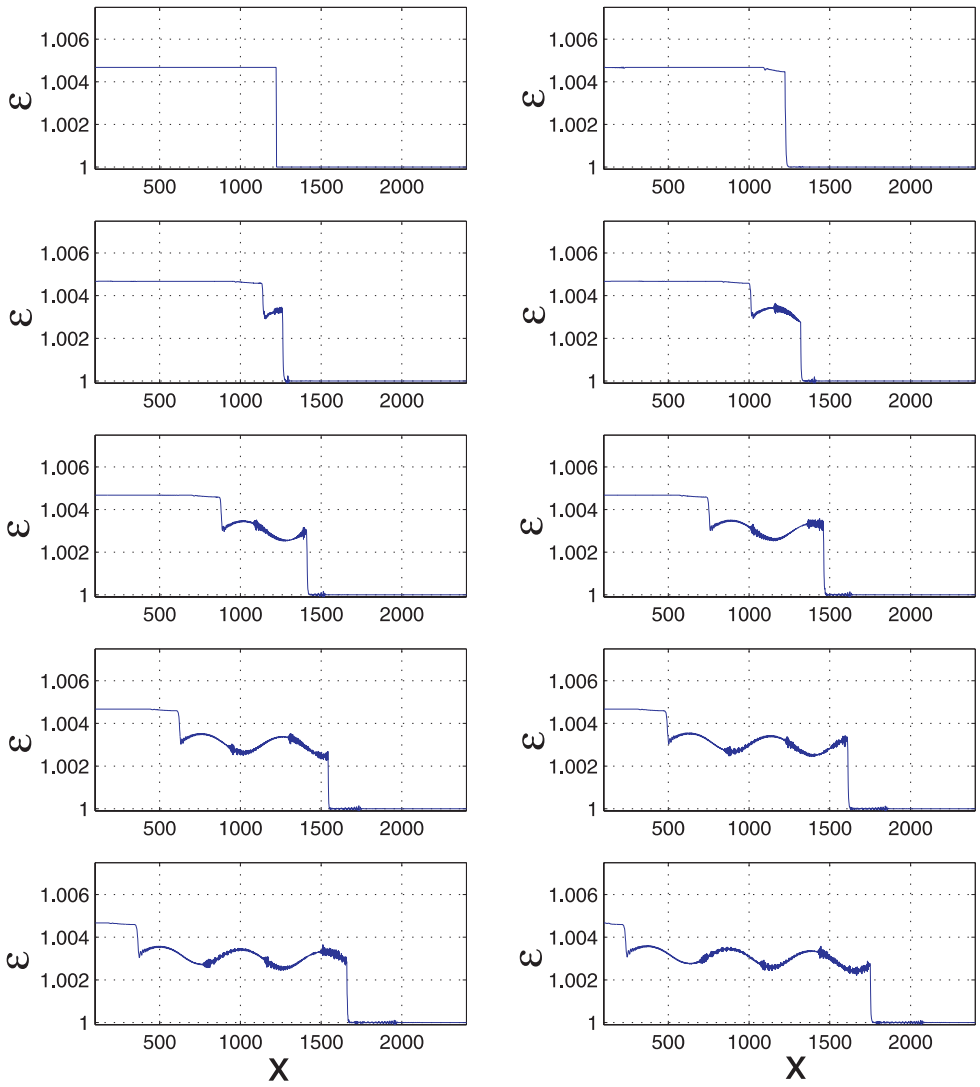

Figure 4.9.: Strain field of a crack travelling in a material with periodically varying fracture toughness.

energy of the nonlinear system is given by

$$\begin{aligned} U = &\sum_{i,j} \left(\frac{1}{2} k (r_{ij} - a_0)^2 + \frac{1}{2} \beta k \, H(r - r_{\text{on}})(r_{ij} - r_{\text{on}})^2 \right) \\ &+ \sum_{i} \left(\frac{1}{2} H(i - N_f) H(r_{\text{break}} - \hat{r}_i) k_p \hat{r}_i^2 \right), \end{aligned} \tag{4.38}$$

where r_{on} is a potential parameter allowing for different onset points of the hyperelastic effect (thus controlling the strength of the hyperelastic effect), and

$$\varepsilon_{\text{on}} = \frac{r_{\text{on}} - a_0}{a_0}. \tag{4.39}$$

The choice of β allows for different types of nonlinearities. If $-1 < \beta \leq 0$, the potential softens with strain, and if $\beta = 0$, the model reduces to harmonic interactions. The small-

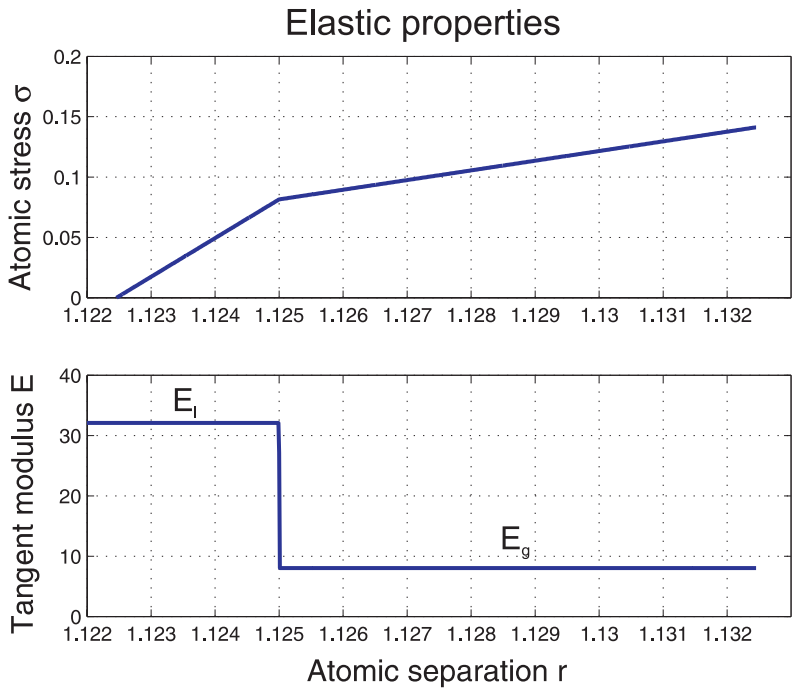

Figure 4.10.: Elastic properties associated with the biharmonic interatomic potential, for $r_{\mathrm{on}} = 1.125$ and $E_{\mathrm{g}} = 8 = 1/4E_{\mathrm{l}}$.

perturbation spring constant is always given by $k_0 = k$, and the large-strain spring constant is given by $k_1 = (1 + \beta)k$. Elastic properties for $\beta = -3/4$ are shown in Figure 4.10, which plots the atomic stress σ versus atomic separation and the tangent modulus E. The local sound velocity $c_{0,l}$ is readily obtained from E. The Figure shows that the tangent modulus softens with strain. We reiterate that if the stress-strain law softens with strain, the elastic properties at the crack tip are stiffer than in the far-field.

The simulation procedure when using the bilinear stress-strain law is identical to the previously described procedure. However, the dynamics of the crack with the bilinear stress-strain law is significantly different from the harmonic case. We observe that the crack can propagate supersonically with respect to the global elastic properties. Figure 4.11 (a) plots the limiting velocity of the crack for different values of the potential parameter r_{on}. For large values of r_{on}, the local hyperelastic zone becomes larger and the limiting velocity approaches Mach 2, or $\alpha_{\mathrm{g}} \approx 2$. For $r_{\mathrm{on}} \to a_0$, the hyperelastic zone shrinks and the velocity of the crack approaches $\alpha_{\mathrm{g}} \approx 1$. This plot proves that the limiting velocity of the crack is very sensitive with respect to the potential parameter r_{on}. A small change in r_{on} affects the extension of the hyperelastic area and has impact on the limiting velocity. The simulation results prove that supersonic crack propagation is possible even if the hyperelastic zone is very small.

When the crack is propagating at $\alpha_{\mathrm{g}} > 1$, the local strain wave has a magnitude of less than 50 percent of the equilibrium strain. This is in disagreement with the classical theory stating that the local strain wave is always equal or larger than 50 percent of the equilibrium strain for a crack propagating at the limiting speed (sound velocity). However, these observations can be explained well by the new continuum model proposed

based on the concept of local elastic properties. Figure 4.11 (b) plots a comparison of the continuum model with molecular-dynamics simulation results of supersonic crack propagation. The agreement is reasonable. The regimes where case 1 and case 2 are valid is also indicated. Figure 4.12 depicts the strain field in the vicinity of a supersonic crack for $r_{\text{on}} = 1.124$.

4.6. Discussion and conclusions

We have used a simple one-dimensional model of dynamic fracture to investigate fundamentals of the nonlinear dynamics of fracture. Based on the continuum model of one-dimensional dynamic fracture, we have proposed an atomistic model of a string of atoms. We have verified that the continuum model of one-dimensional dynamic fracture can be successfully applied at the atomistic level, if harmonic interactions are assumed between atoms. We have shown that the one-dimensional crack carries no inertia, a phenomenon that is also found in higher dimensions [75, 230, 117]. The fact that we find good agreement of the one-dimensional atomistic model featuring harmonic interactions with the continuum theory corresponds to recent work on comparison of the atomistic level with continuum theory [83] for mode II cracks.

Finding analytical solutions for dynamic fracture in hyperelastic materials in higher dimensions is very difficult, if not impossible in many cases. However, analytical understanding of the nonlinear dynamics becomes possible based on the simple one-dimensional model. We have proposed a continuum model based on the local elastic properties to predict the elastic fields around the crack tip, when a bilinear stress-strain law is assumed. The major prediction of the continuum model is supersonic crack propagation, if there exists a local elastically stiff region confined to the crack tip. By molecular-dynamics simulations, we have shown that the local elastic properties at the crack tip indeed govern the dynamics of fracture, in agreement with the predictions of the model. If there is an elastically stiff zone close to the crack tip, the crack can propagate supersonically through the material. We emphasize that this is true even if the hyperelastic region is highly confined to the crack tip. The observation of supersonic crack motion has been found by other researchers as well in 2D and 3D studies [11]. Our finding that the dynamics of the crack is governed by the local elastic properties (the local wave speed) has been predicted theoretically [81] and observed previously [11, 5]. The case of stiffening material response corresponds to materials such as polymers, showing a hyperelastic stiffening effect. Due to the large deformation in the vicinity of the crack, the elastic properties in such materials are stiffer close to the crack than in regions far away from the crack. Laboratory experiments of dynamic fracture in such materials could provide further insight into the nature of hyperelastic stiffening dynamic fracture and associated supersonic crack propagation.

In this chapter, we have concentrated on the case when local elastic properties are stiffer than in the far-field elastic properties, crack propagation is supersonic. In the same sense, if the local elastic properties are softer, crack propagation must be subsonic on a local scale. We have also performed similar one-dimensional molecular-dynamics simulations as reported in this work, and find similar results.

Prior to this study, it has been widely believed that there is a unique definition of how fast waves propagate in solids. Our results prove that this concept can not capture all phenomena in dynamic fracture, and instead should be replaced by the concept of local wave speeds. In materials where the large-strain elasticity differs significantly from the small-strain elasticity, the concept of *global wave velocities* can not be used any more to describe the dynamics of the crack. Instead, the concept of local elastic properties, and associated *local wave velocities* govern the dynamics of the crack. Since "real" materials all show strong nonlinear effects, this suggests that hyperelasticity is crucial for dynamic fracture.

The one-dimensional model could find useful applications in addressing other fundamental questions of mechanics of materials. A potential application is strain gradient effects in elasticity, and its possible implications on dynamic fracture. The mechanics of one-dimensional structures could also be important in the newly emerging bio-nano-technology, often involving functionalization of single molecules. An objective of future studies could be the development of experimental techniques based on the one-dimensional model of fracture.

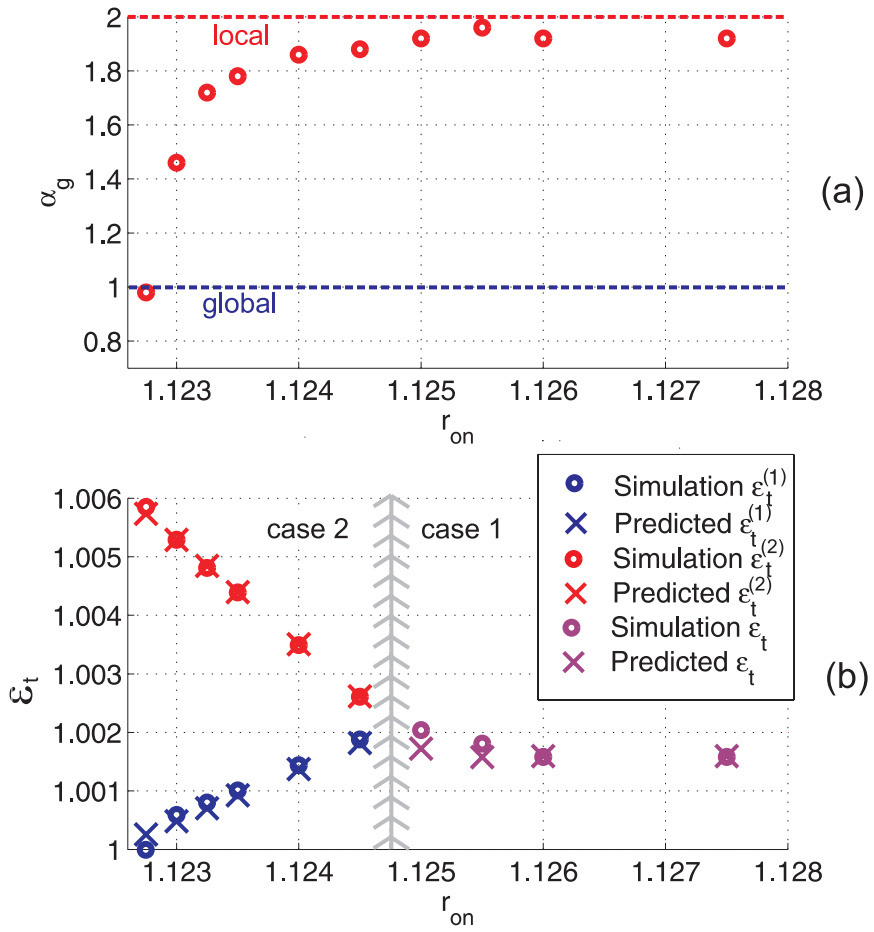

Figure 4.11.: Subplot (a): Velocity of the crack for different values of the potential parameter r_{on}. The larger r_{on}, the larger the stiff area around the crack tip. As the hyperelastic area becomes sufficiently large, the crack speed approaches the local wave speed $\alpha_{\text{l}} = 1$ corresponding to $\alpha_{\text{g}} = 2$. Subplot (b) shows a quantitative comparison between theory and computation of the strain field near a supersonic crack as a function of the potential parameter r_{on}. The different regimes corresponding to case 1 and case 2 are indicated. The loading is chosen $\sigma_0 = 0.1$, with $k_p/k = 0.1$ and $\hat{r} = 0.001$.

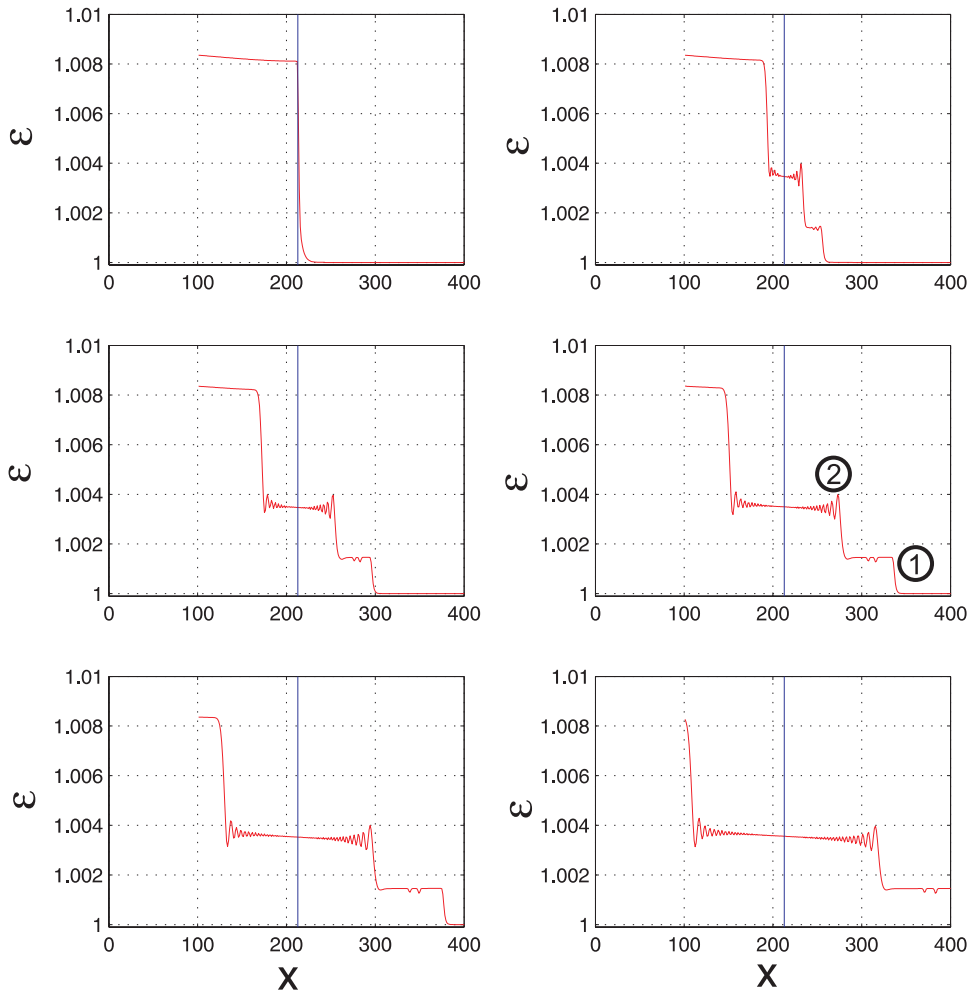

Figure 4.12.: Sequence of strain field near a rapidly propagating supersonic 1D crack moving with Mach 1.85 for $r_{\text{on}} = 1.124$. The primary (1) and secondary wave (2) are indicated in the plot. The wave front (1) propagates supersonically through the material.

5. Mechanical and physical properties of two-dimensional solids

The one-dimensional model of dynamic fracture provided insight into the nonlinear dynamics of cracks. For studies of cracks under mode I and mode II loading as shown schematically in Figure 5.1, two-dimensional atomistic models of dynamic fracture are required. Since the mechanical and physical properties of two-dimensional models are more complex than in the one-dimensional case, we dedicate this chapter to the discussion of mechanical and physical properties of two-dimensional solids associated with a triangular lattice. The aim is to develop several "model materials" for computer experiments that will be used to study specific features of dynamic fracture later. In the development of interatomic potentials for model materials, the major objective is to model the generic properties of a class of materials rather than being specific to a certain material.

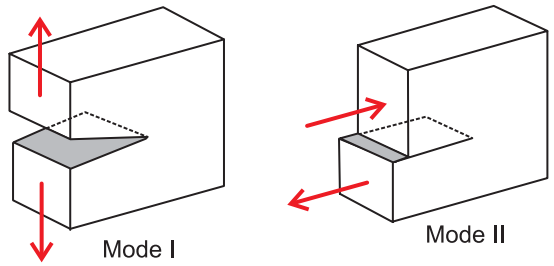

Figure 5.1.: Schematic of cracks under mode I and mode II crack loading.

The outline of this chapter is as follows. After a theoretical consideration of calculation of elastic properties, the wave speeds and the fracture surface energy in triangular lattices, we discuss numerical results for different potentials. We discuss a Lennard-Jones, a tethered Lennard-Jones potential, a harmonic potential with and without snapping bonds and new a biharmonic potential similarly to that used in the previous chapter (see Section (4.5)). For all potentials, we give expressions for the fracture surface energy.

5.1. Elastic properties and wave speeds

The need to advance methods that combine atomistic and continuum analysis is becoming increasingly compelling with rapid advance in computational resources. Many supercomputer centers offer significant peak performances of several TFLOPs per second, and system sizes with billions of particles can readily be simulated [12, 221]. In order to compare atomistic simulations with continuum analysis level, it is necessary to

use methods that allow transition between the two levels of descriptions [129, 252, 86]. Of particular interest is the relationship between interatomic potentials and associated elastic properties. Many methods have been proposed in recent years, but still lack proper interpretation and description of quantities like stresses and strains [130, 252]. A possible method of linking atomistic and continuum concepts is to use is the Cauchy-Born rule [28, 115] which provides a relation between the energy created from a macroscopic strain field and the atomistic potential energy found in a stretched crystal lattice [233, 129, 252, 86].

Classical hyperelastic continuum theory is based on the existence of a strain energy function [170]. Using the Cauchy-Born rule, applied to the triangular lattice considered in this chapter, the strain energy density per unit undeformed area is given by [28, 115, 81]

$$\Phi = \frac{2}{\sqrt{3}} \left(\phi(l_1) + \phi(l_2) + \phi(l_3) \right), \tag{5.1}$$

where the values of l_i are determined from geometric relations of the triangular lattice as shown in Figure 5.2. The function $\phi(r)$ refers to the interatomic potential. The unknowns E_{ij} are the Green-Lagrangian strain components [170, 151], and these can be determined to be

$$E_{xx} = \left(\Lambda_1^2 - 1 \right)/2, \;\; E_{yy} = \left(\Lambda_2^2 - 1 \right)/2, \;\; E_{xy} = E_{yx} = \Lambda_1 \Lambda_2 \cos\left(\Theta/2 \right). \tag{5.2}$$

Here, Θ is the shear angle, while Λ_i describe the elongation of the sides of a lattice unit cell as indicated in Figure 5.2. From geometric relations, it is found that

$$l_1 = \sqrt{1 + 2E_{xx}}, \tag{5.3}$$

$$l_2 = \sqrt{1 + 1/2E_{xx} + 3/2E_{yy} - \sqrt{3}/2(E_{xy} + E_{yx})}, \tag{5.4}$$

and

$$l_3 = \sqrt{1 + 1/2E_{xx} + 3/2E_{yy} + \sqrt{3}/2(E_{xy} + E_{yx})}. \tag{5.5}$$

The symmetric second Piola-Kirchhoff stress tensor is given by

$$S_{ij} = \frac{\partial \Phi}{\partial E_{ij}}. \tag{5.6}$$

The "slope" of the $S - E$ relationship is often called the material tangent modulus

$$C_{ijkl} = \frac{\partial^2 \Phi}{\partial E_{ij} \partial E_{kl}}. \tag{5.7}$$

For infinitesimal strains, the Green-Lagrangian strain reduces to the stress tensor of linear elasticity $E_{ij} \rightarrow \varepsilon_{ij}$. The same argument can be used for the stresses, and the second symmetric Piola-Kirchoff stress tensor reduces to the linear elasticity stress tensor $S_{ij} \rightarrow \sigma_{ij}$, as well as $C_{ijkl} \rightarrow c_{ijkl}$. This scheme is universally applicable, as long as the interatomic potential and thus the strain energy function Φ is known (it can for instance be applied to pair potentials or the embedded atom method for metals).

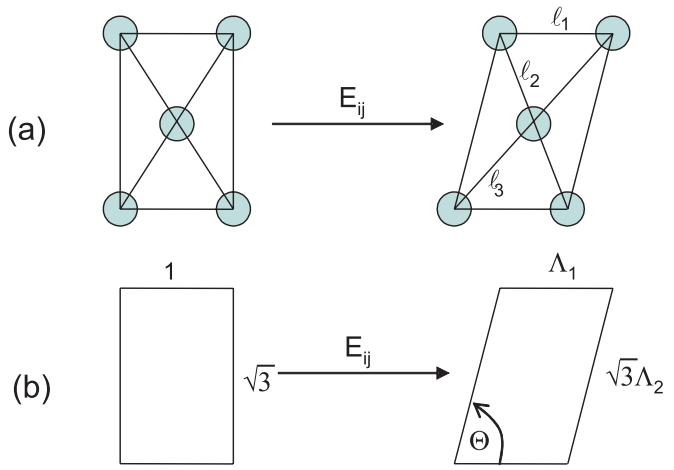

Figure 5.2.: Subplot (a) Rectangular cell in a uniformly deformed triangular lattice; subplot (b) the geometrical parameters used to calculate the continuum properties of the lattice.

Poisson's ratio ν is defined as the ratio of transverse strain to longitudinal strain in the direction of stretching force. Poisson's ratio can be found by choosing a Green-Lagrangian strain E_{xx} and finding a value for E_{yy} such that S_{yy} assumes zero (and vice versa). We can define

$$\nu = -\frac{E_{yy}}{E_{xx}} \tag{5.8}$$

as Poisson's ratio valid also for large strain.

To obtain a linear elasticity formulation with first order stress-strain law, the strain energy given in equation (5.1) is expanded up to second order terms. After some lengthy calculations it can be shown that

$$\Phi = \frac{\sqrt{3}}{8}\phi''(r_0)\left(3\varepsilon_{xx}^2 + 2\varepsilon_{xx}\varepsilon_{yy} + \varepsilon_{yy}^2 + (\varepsilon_{xy} + \varepsilon_{yx})^2\right) \tag{5.9}$$

where r_0 is the nearest neighbor distance. Using

$$\sigma_{ij} = \frac{\partial \Phi}{\partial \varepsilon_{ij}}, \tag{5.10}$$

one can derive expressions for stress-strain relations, like for instance

$$\sigma_{yy} = \frac{\partial \Phi}{\partial \varepsilon_{yy}} = \frac{\sqrt{3}}{4}\phi''(r_0)\left(\varepsilon_{xx} + 3\varepsilon_{yy}\right). \tag{5.11}$$

5.1.1. Lennard-Jones potential

We begin with the elastic properties of a solid in which atoms interact according to a LJ potential as defined in equation (2.4) (we choose $\sigma = \epsilon_0 = 1$). LJ type potentials have frequently been used in simulating fracture using molecular-dynamics [7]. Solids defined by this potential behave as a very brittle material in a two-dimensional triangular lattice.

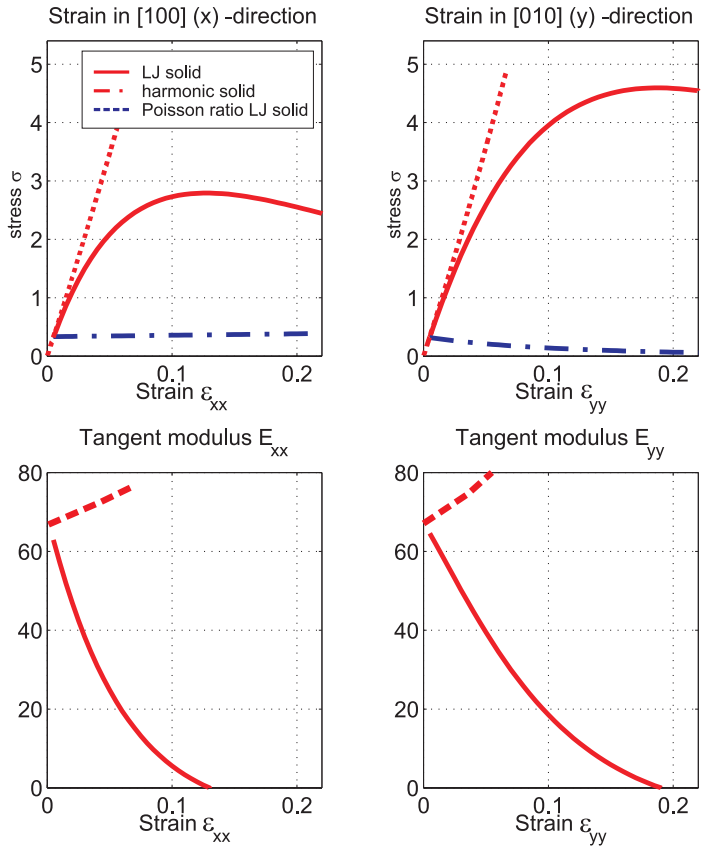

Figure 5.3.: Elastic properties of the Lennard-Jones solid (continuous line) and elastic properties associated with the harmonic potential (dashed line). The dash-dotted lines in the upper plots show Poisson's ratio.

Figure 5.3 shows numerical estimates of the elastic properties of a LJ solid. The systems are loaded uniaxially in the two symmetry directions of the triangular lattice.

The plot of the LJ system shows that the y-direction requires a higher breaking strain than in the x-direction (about 18 percent versus 12 percent). The tangent Young's modulus drops significantly from around 66 for small strain until it reaches zero when the solid fails [170]. Poisson ratio remains around 1/3, but increases slightly when loaded in the x-direction and decreases slightly when loaded in the orthogonal direction.

5.1.2. Nonlinear tethered LJ potential

The objective is to obtain a solid with the property that its tangent moduli stiffen with strain, in contrast to the LJ potential described above [170]. In addition, the small-strain elastic properties should be the same as in the LJ potential. The nonlinear tethered LJ potential is obtained by modifying the well-known LJ 12:6 potential: The potential is mirrored at $r = r_0 = 2^{1/6} \approx 1.12246$, leading to a strong stiffening effect instead of the

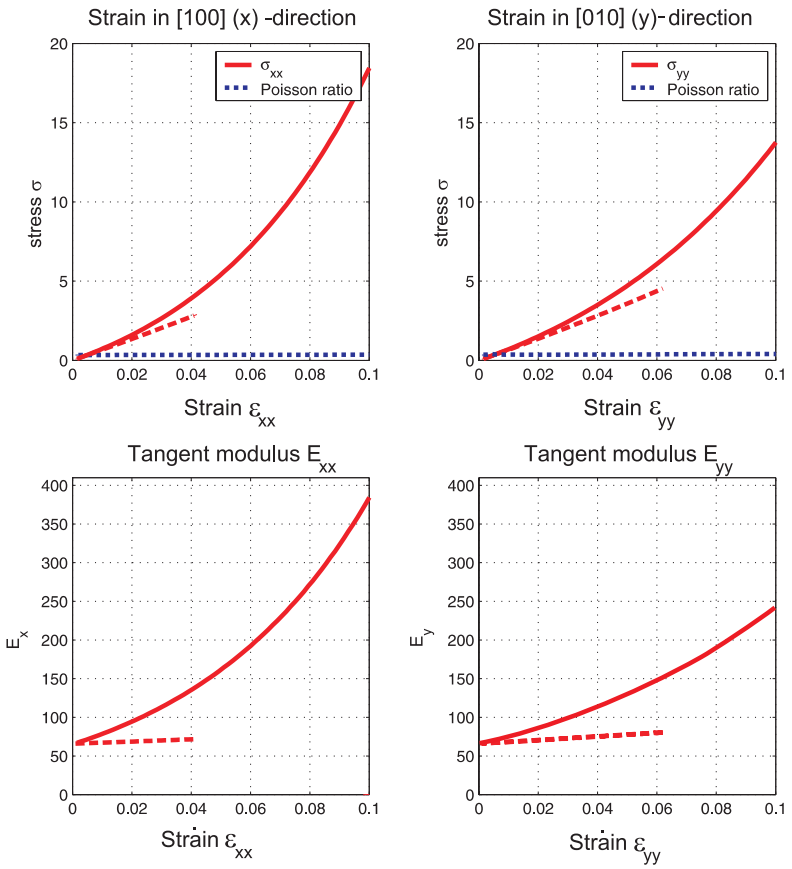

Figure 5.4.: Elastic properties associated with the tethered LJ potential, and in comparison, elastic properties associated with the harmonic potential (dashed line). Unlike in the softening case, where Young's modulus softens with strain (Figure 5.3), here Young's modulus stiffens with strain.

normal softening associated with atomic separation.

$$\phi_{ij}(r_{ij}) = \begin{cases} 4\epsilon_0 \left(\frac{1}{r_{ij}^{12}} - \frac{1}{r_{ij}^{6}} \right) & \text{if } r_{ij} < r_0, \\ 4\epsilon_0 \left(\frac{1}{(2r_0 - r_{ij})^{12}} - \frac{1}{(2r_0 - r_{ij})^{6}} \right) & \text{if } r_{ij} \geq r_0, \end{cases} \tag{5.12}$$

where the parameter ϵ_0 can be chosen to change the small-strain elastic properties (here we assume $\sigma = \epsilon_0 = 1$) [6, 83].

Figure 5.4 plots the elastic properties associated with this potential for a two-dimensional triangular lattice. The upper two subplots show the stress versus strain behavior under uniaxial stress loading. The left refers to uniaxial stress loading in the x direction, and the right plot shows the stresses for uniaxial y loading. The Poisson ratio is calculated to be around $\nu \approx 0.33$. The nonlinear nature of this potential can clearly be identified in these plots. The tangent moduli stiffen strongly with strain, and agree with the small-strain elastic properties of the LJ potential. Therefore, the wave velocities assuming small perturbation from the equilibrium position are the same in both the LJ and the tethered LJ potential.

5.1.3. Harmonic potential

We introduce a harmonic potential with the objective to mimic linear elastic material behavior, as assumed in most theories of fracture. The linear spring potential given by equation (2.6) corresponds to the "ball-spring" model of solids and yields a plane-stress elastic sheet for a triangular lattice.

Using expressions similar to equation (5.11), Young's modulus E and shear modulus μ can be shown to be

$$E = \frac{2}{\sqrt{3}}k, \quad \mu = \frac{\sqrt{3}}{4}k. \tag{5.13}$$

When we assume $k = 72\sqrt[3]{2} \approx 57.14$ so as to match the small-strain elastic properties of the LJ potential, $E \approx 66$ and $\mu \approx 24.8$. Equation (5.11) (expression for infinitesimal strains) can be used to show that Poisson's ratio $\nu = 1/3$. Using the above given values for elastic properties, the wave speeds can be obtained straightforwardly. The longitudinal wave speed can be calculated from the elastic properties to be

$$c_l = \sqrt{\frac{3\mu}{\rho}} \tag{5.14}$$

with $\rho = 2/2^{1/3}/\sqrt{3} \approx 0.9165$ (assuming mass $m = 1$). The shear wave speed is given by the square root of the ratio of the shear modulus μ to the density ρ thus

$$c_s = \sqrt{\frac{\mu}{\rho}}. \tag{5.15}$$

Finally, the speed of elastic surface waves, the Rayleigh speed, is given by

$$c_r \approx \beta c_s. \tag{5.16}$$

The value of β can be found by the following approach [21]. Considering a surface wave in an isotropic half space, one can derive a formula to determine the surface wave velocity as a function of the ratio of longitudinal to shear wave $\Gamma = c_s/c_l$:

$$\beta^6 - 8\beta^4 + 8\left(3 - 2\Gamma^2\right)\beta^2 - 16\left(1 - \Gamma^2\right) = 0. \tag{5.17}$$

Only one real and positive solution exists of the Rayleigh equation (5.17) [78, 21]. This solution is found to be $\beta \approx 0.9225$, which is a more accurate value than in used previous papers (since an accurate value for the Rayleigh wave velocity is required).

The wave speeds are given by

$$c_l = 9, \;\; c_s = 5.2, \;\; \text{and} \;\; c_r \approx 4.8. \tag{5.18}$$

Results for elastic properties and wave speeds are summarized in Table 5.1 for two different choices of the spring constant.

To check if the predictions by equation (5.13) hold even for large strains, we investigate the elastic properties numerically. The numerically estimated elastic properties for

k	E	μ	ν	c_l	c_s	c_r
$36\sqrt[3]{2} \approx 28.57$	33	12.4	0.33	6.36	3.67	3.39
$72\sqrt[3]{2} \approx 57.14$	66	24.8	0.33	9	5.2	4.8

Table 5.1.: Elastic properties and wave speeds associated with the harmonic potential (see equation (2.6)) in a 2D solid for different choices of the spring constant k.

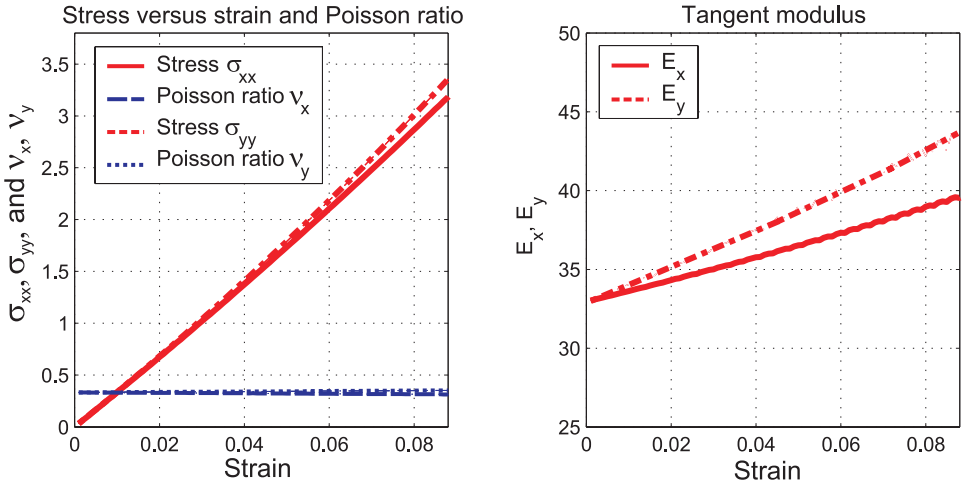

Figure 5.5.: Elastic properties of the triangular lattice with harmonic interactions, stress versus strain (left) and tangent moduli E_x and E_y (right). The stress state is uniaxial tension, that is the stress in the direction orthogonal to the loading is relaxed and zero.

uniaxial tension are shown in Figure 5.5 for the two different crystal orientations in a triangular lattice and $k \approx 28.57$. We find reasonable agreement, which could be verified by comparing the values reported in Table 5.1 with the results shown in Figure 5.5.

Young's moduli agree well with the continuum mechanics prediction for small strains. However, we observe a slight stiffening effect for large strains, that is, E is increasing with strain. As predicted, the lattice is found to be isotropic for small deformations, but the results show there exists an anisotropy effect for large deformations. The values of Poisson's ratio match the linear approximation for small strains, but deviate slightly for large strains. This suggests that even if harmonic potentials are introduced between atoms, the triangular lattice structure yields a slightly nonlinear stress-strain law.

We note that the values for Young's modulus associated with the LJ potential at small strains are in consistency with the results using the harmonic potential with $k \approx 57.14$ (see Figure 5.3). The small-strain elastic properties also agree in the case of the tethered LJ potential (see Figure 5.4). The comparison with the harmonic potential nicely illustrates the softening and stiffening effect of the LJ and tethered LJ potential. Since the small-strain elastic properties agree with the harmonic potential in both cases, the small-strain wave speed is also identical and thus given by equations (5.14)-(5.16). Note that there is no unique definition of the wave speed for large strains in the nonlinear potentials.

loading direction	Poisson relaxation	$\varepsilon_{\text{break}}$
x	yes	0.08
y	yes	0.1
x	no	0.26
y	no	0.09

Table 5.2.: Failure strain of the two-dimensional solid associated with the harmonic potential with snapping bonds under different modes of uniaxial loading, for $r_{\text{break}} = 1.17$.

5.1.4. Harmonic bond snapping potential

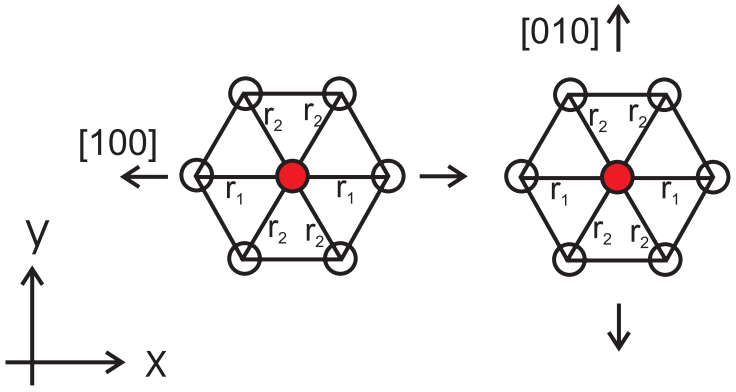

Figure 5.6.: The figure shows the stretching of the triangular lattice in two different directions.

In contrast to the elastic properties of a solid that never breaks as reported in Section 5.1.3, here we discuss the elastic properties of a triangular lattice with harmonic interactions where the bonds break upon a critical separation $r > r_{\text{break}}$. The interatomic potential is defined as

$$\phi_{ij}(r_{ij}) = \begin{cases} a_0 + \frac{1}{2}k(r_{ij} - r_0)^2 & \text{if } r_{ij} < r_{\text{break}}, \\ a_0 + \frac{1}{2}k(r_{\text{break}} - r_0)^2 & \text{if } r_{ij} \geq r_{\text{break}}. \end{cases} \tag{5.19}$$

The elastic properties for $r_{ij} < r_{\text{break}}$ are identical to those discussed in Section 5.1.3 and shown in Figure 5.5, but for large strains close to the failure of the solid there are strong differences. We focus on the differences in elastic properties due to stretching in the x-direction versus the y-direction. Figure 5.6 shows the crystal orientation for stretching of the triangular lattice in the two different directions. We define two different bond types r_1 and r_2: The bonds denoted by r_1 have a component only in the x-direction, whereas bonds r_2 have a component in the x as well as in the y-direction.

We start with a discussion of stretching in the x-direction (Figure 5.6 (a)), and consider stretching with and without Poisson relaxation. For uniaxial tension without Poisson contraction, the length of both bonds r_1 and r_2 increases. In contrast, for uniaxial tension with Poisson contraction, the length of bonds r_1 increases, whereas the condition that

$\sigma_{yy} = 0$ requires that $\mid r_2 \mid = r_0$. Therefore, with the assumption of Poisson relaxation, for arbitrarily large strains in the x-direction, only two bonds r_1 break while the other four bonds r_2 never break. However, these bonds do not contribute to the stress. In contrast, if no Poisson relaxation is assumed, these bonds do indeed contribute to the stress and fail at much higher strain than the first two bonds, this increasing the critical strain for bond breaking. Such behavior is indeed observed in our numerical calculation of the elastic properties. Figure 5.7 (left) shows uniaxial tension with Poisson relaxation. Under stretch in the x direction, the solid fails at about 8 % strain. As could be verified in Figure 5.8 (left), the solid fails at about 26 % strain when no Poisson relaxation is assumed. A reduced modulus $E \approx 10$ is found between the failure of the first two bonds and the failure of the remaining four bonds. Note that in the figures, the number of bonds is also indicated by the blue dotted line. The reason for the huge difference in the two cases is, as outlined above by theoretical considerations, the contribution of the four bonds r_2 which only break at very high strains. Note that for any stress state not equal to uniaxial tension, there will be a contribution to the stress from the two remaining bonds.

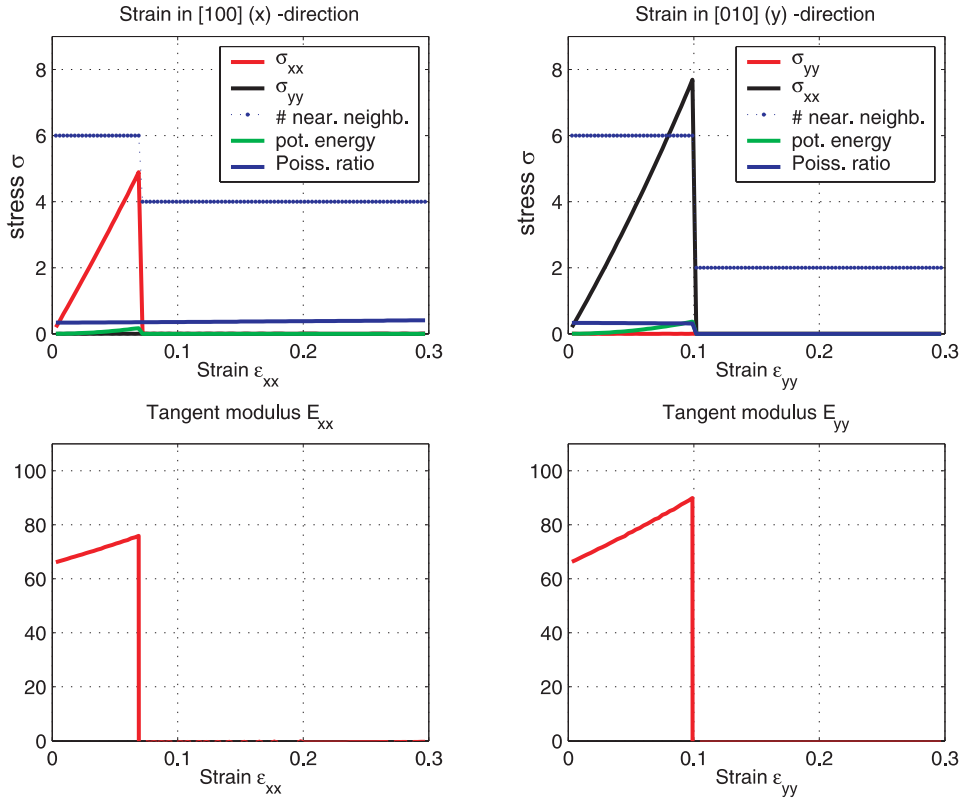

Figure 5.7.: The figure plots the elastic properties under uniaxial loading with Poisson relaxation for the harmonic potential. In the plot, stress versus strain, Poisson's ratio as well as the number of nearest neighbors are shown. The lower two subplots show Young's modulus

We continue with a discussion of stretching in the y-direction (Figure 5.6 (b)), and also consider stretching with and without Poisson relaxation. For uniaxial tension without

Poisson contraction, the length of both bonds r_2 increases while the bond length of bonds r_2 remains r_0 and does not contribute to the stress. Under unixial tension with Poisson relaxation, the length of all bonds is adjusted to satisfy the condition that $\sigma_{xx} = 0$. In both cases, upon a critical strain the number of bonds drops to two (since the four bonds r_2 break) and the remaining bonds r_1 do not contribute to the stress in both cases with and without Poisson relaxation. This is a significant difference to the behavior in the other loading direction. As a consequence, the critical strain for failure is comparable under both loading conditions in the y-direction. Such behavior is indeed observed in our numerical calculation of the elastic properties. Figure 5.7 (right) shows uniaxial tension with Poisson relaxation. Under stretch in the y direction, the solid fails at about 10 % strain. As could be verified in Figure 5.8 (right), the solid fails also at about 10 % strain when no Poisson relaxation is assumed.

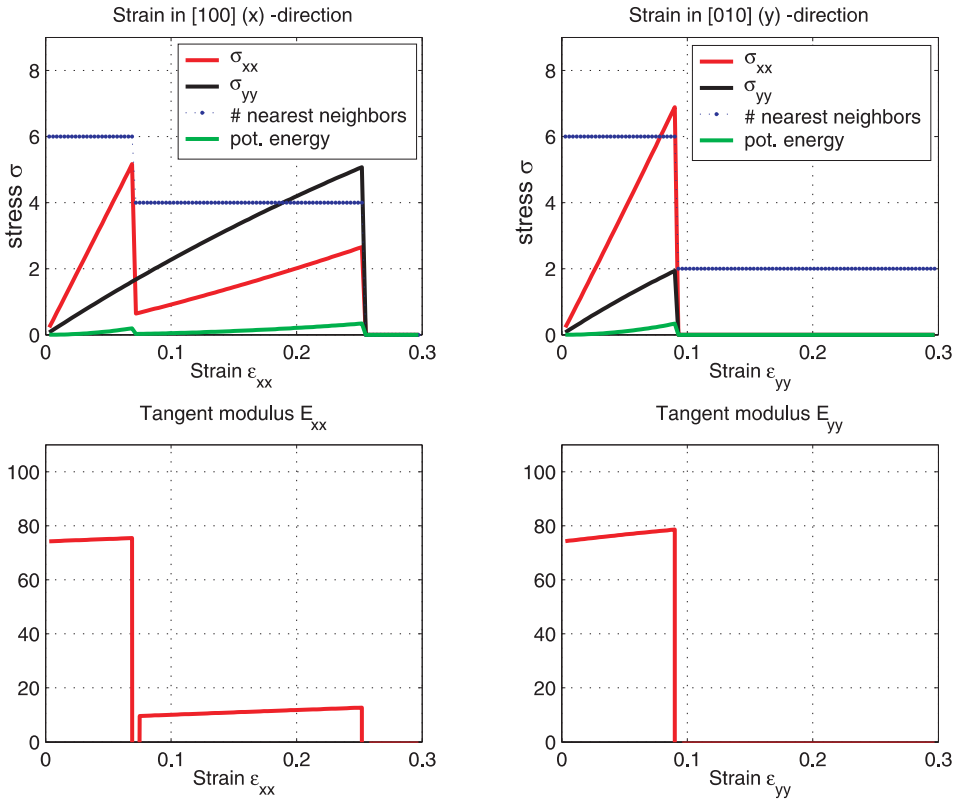

Figure 5.8.: The figure plots the elastic properties under uniaxial loading without Poisson relaxation for the harmonic potential. In the plot, stress versus strain, as well as the number of nearest neighbors are shown. The lower two subplots show Young's modulus.

In summary, there is a strong dependence of the failure strain on the loading condition. Table 5.2 summarizes the failure strains for different modes of loading in the x and y direction.

Under large stretching, harmonic lattices behave differently than solids defined by the LJ potential since bonds contribute little to the stress as they weaken strongly with strain. Therefore, the direction with lowest breaking strain is associated with loading in the x-direction, which is the direction with highest fracture surface energy.

The consequence of this is that crack propagation is stable along the direction of high fracture energy [2, 7]. Solids associated with harmonic bond snapping potentials show a different behavior: In the harmonic bond snapping systems, the failure strain is larger in the x-direction and smaller in the y-direction (see Figure 5.8). Cracks are therefore expected to propagate stable along the direction of lower fracture surface energy (crack extension along x-direction). We will verify this prediction with molecular-dynamics results in a forthcoming chapter.

5.1.5. Biharmonic potential

Thus far, we have studied a LJ potential that yields elastic properties that soften strongly with strain, a tethered LJ potential that yields a solid strongly stiffening with strain and a harmonic potential. To be able to smoothly interpolate between harmonic potentials and strongly nonlinear potentials, we adopt a biharmonic, interatomic potential composed of two spring constants k_0 and k_1 similar to that discussed in Section 4.5 for the 1D case (all quantities given are in dimensionless units).

We consider two "model materials", one with elastic stiffening and the other with elastic softening behavior. In the elastic stiffening system, the spring constant k_0 is associated with small perturbations from the equilibrium distance r_0, and the second spring constant k_1 is associated with large bond stretching for $r > r_{\text{on}}$. The role of k_0 and k_1 is reversed in the elastic softening system ($k_0 = 2k_1$, and $k_1 = 36/\sqrt[3]{2}$).

Purely harmonic systems are obtained if r_{on} is chosen to be larger than r_{break}. Poisson's ratio ν is found to be approximately independent of strain and around $\nu \approx 0.33$ for all potentials. In the stiffening system, the small deformation (up to about 0.5 percent of strain) Young's modulus is $E \approx 33$ with shear modulus $\mu \approx 12.4$, and the large deformations tangent Young's modulus is $E \approx 66$ with shear modulus $\mu \approx 28.8$. The values are reversed for the softening system where the small deformation Young's modulus is $E \approx 66$, and the large deformation tangent Young's modulus is $E \approx 33$.

The biharmonic potential is defined as

$$\phi_{ij}(r_{ij}) = \begin{cases} a_0 + \frac{1}{2}k_0(r_{ij} - r_0)^2 & \text{if } r_{ij} < r_{\text{on}}, \\ a_1 + \frac{1}{2}k_1(r_{ij} - r_1)^2 & \text{if } r_{ij} \geq r_{\text{on}} \end{cases} \tag{5.20}$$

where r_{on} is the critical atomic separation for onset of the hyperelastic effect, and

$$a_1 = a_0 + \frac{1}{2}k_0(r_{\text{on}} - r_0)^2 - \frac{1}{2}k_1(r_{\text{on}} - r_1)^2 \tag{5.21}$$

as well as

$$r_1 = \frac{1}{2}(r_{\text{on}} + r_0) \tag{5.22}$$

are found by continuity conditions of the potential at $r = r_{\text{on}}$. The values of k_0 and k_1 refer to the small-strain and large-strain spring constants.

The elastic properties associated with the biharmonic potential are shown in Figure 5.9. The wave speeds for small and large strains are given by the values of the

corresponding harmonic potentials. Therefore, the wave speeds associated with large strains are given by $c_{l,1} = \kappa c_{l,0}$, $c_{s,1} = \kappa c_{s,0}$ and $c_{r,1} = \kappa c_{r,0}$ where $\kappa = \sqrt{k_1/k_0}$.

Similarly as described in the previous section, a critical bond breaking distance r_{break} can be introduced allowing for snapping bonds.

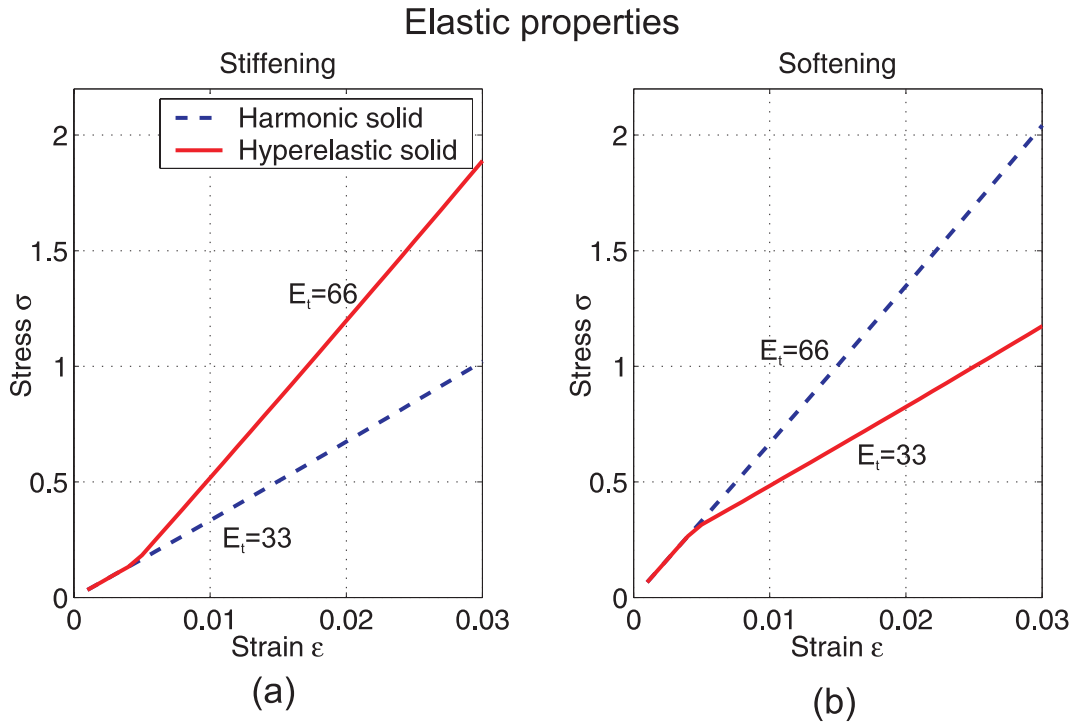

Figure 5.9.: Elastic properties of the triangular lattice with biharmonic interactions, stress versus strain in the x-direction (a) and in the y direction (b). The stress state is uniaxial tension, that is the stress in the direction orthogonal to the loading is relaxed and zero.

5.2. Fracture surface energy

The fracture surface energy γ_s is an important quantity for the nucleation and propagation of cracks. It is defined as the energy required to generate a unit distance of a pair of new surfaces (cracks can be regarded as sinks for energy, where elastic energy is converted into surface fracture energy). The Griffith criterion predicts that the crack tip begins to propagate when the crack tip energy release rate G reaches the fracture surface energy $2\gamma_s$, $G = 2\gamma_s$ [93]. The fracture surface energy can be expressed as

$$\gamma_s = -\frac{\Delta\phi}{d}, \tag{5.23}$$

where d is the crack advance and $\Delta\phi$ the energy necessary to break atomic bonds as the crack advances a distance d. The bond breaking process is depicted in Figure 5.10 (a) for cracks propagating along the direction with highest fracture surface energy. In this case, four bonds break while the crack proceeds $d = \sqrt{3}r_0$. Figure 5.10 (b) shows the

bond breaking process for crack orientation along the direction of lowest fracture surface energy. In this direction, two bonds break while the crack advances $d = r_0$.

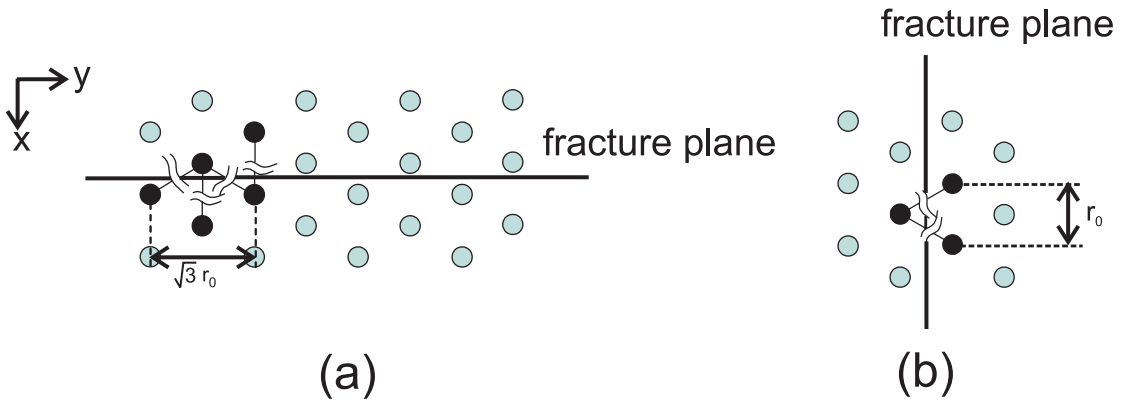

Figure 5.10.: Bond breaking process along the fracture plane and calculation of fracture surface energy for (a) direction of high fracture surface energy, and (b) direction of low fracture surface energy.

For the case considered in the simulations, the fracture surface energy is determined assuming that bonds between nearest neighbors snap during crack propagation. Unlike the wave velocity, the fracture surface energy is well-defined for both linear and nonlinear cases.

We summarize the results for different potentials described in this chapter.

5.2.1. Harmonic bond snapping potential

The fracture surface energy for the harmonic bond snapping model for crack propagation along the direction of high fracture surface energy (as shown in Figure 5.10) is given by

$$\gamma_s^{\mathrm{bs,h}} = \frac{k(r_{\mathrm{break}} - r_0)^2}{\sqrt{3} r_0} = \frac{E(r_{\mathrm{break}} - r_0)^2}{2 r_0}, \tag{5.24}$$

which yields $\gamma_{bs} = 0.0332$ for $r_{\mathrm{break}} = 1.17$. For the direction of low fracture surface energy,

$$\gamma_s^{\mathrm{bs,l}} = \frac{k(r_{\mathrm{break}} - r_0)^2}{2 r_0}, \tag{5.25}$$

which yields $\gamma_{bs} = 0.0288$ for $r_{\mathrm{break}} = 1.17$ and is about 15 % smaller than in the other direction.

5.2.2. Biharmonic bond snapping model

The surface energy for the biharmonic bond snapping model along the direction of high fracture surface energy is given by

$$\gamma_s^{\mathrm{bi,h}} = \frac{2a_1 + k_1(r_1 - r_{\mathrm{break}})^2}{\sqrt{3} r_0} = \frac{E_0(r_{\mathrm{on}} - r_0)^2 - E_1\left[(r_{\mathrm{on}} - r_1)^2 - (r_1 - r_{\mathrm{break}} - r_0)^2\right]}{2 r_0}. \tag{5.26}$$

Potential	γ_s^{h}	γ_s^{l}
harmonic (with $r_{\mathrm{break}} = 1.17$, $k \approx 28.57$)	0.033	0.029
harmonic (with $r_{\mathrm{break}} = 1.17$, $k \approx 57.14$)	0.066	0.057
Lennard-Jones	1.029	0.891
tethered LJ (with $r_{\mathrm{break}} = 1.17$)	0.119	0.103

Table 5.3.: Summary of fracture surface energies for a selection of different potentials.

For the purely harmonic case, the fracture surface energy reduces to the expression given by equation (5.24). In the direction of lower fracture surface energy,

$$\gamma_s^{\mathrm{bi,l}} = \frac{2a_1 + k_1(r_1 - r_{\mathrm{break}})^2}{2r_0} = \frac{E_0(r_{\mathrm{on}} - r_0)^2 - E_1\left[(r_{\mathrm{on}} - r_1)^2 - (r_1 - r_{\mathrm{break}} - r_0)^2\right]}{4/\sqrt{3}r_0}. \tag{5.27}$$

5.2.3. Other potentials

For other potentials, we do not give the analytical expression but summarize the results in Table 5.3. The results for harmonic and biharmonic potentials are also included.

5.3. Discussion

The studies shown in this chapter suggest that by designing the interatomic potential, different elastic properties can be obtained.

The LJ system shows a strong softening of Young's moduli with strains (see Figure 5.3). In contrast, the tethered LJ system yields a solid whose elastic properties stiffen with strain (see Figure 5.4). The harmonic potential serves as a reference that yields approximately linear elastic properties (see Figure 5.5). The LJ and tethered LJ potential yield continuously changing Young's moduli, which may complicate the analysis of crack dynamics. Therefore, we proposed a simplistic potential to describe hyperelastic effects, the biharmonic potential. The biharmonic potential is composed of two harmonic potentials and yields bilinear elastic properties (see Figure 5.9). An important feature of the biharmonic potential is that it allows to define unique wave speeds for small and large strains.

The work described in this chapter exemplifies the development of model materials for computer simulations. The potentials defined in this chapter will be used to study specific aspects of dynamic fracture.

6. Stress and deformation field near rapidly propagating cracks in a harmonic lattice

In this chapter, we report large-scale atomistic simulations to study the near-crack elastic fields in mode I dynamic fracture from both atomistic and continuum mechanics viewpoints. In the continuum theory, the stress field in the vicinity of the crack tip is given by an asymptotic solution [246, 22, 78]. With $K_I(t, v)$ as the dynamic stress intensity factor,

$$\sigma_{ij}(\Theta, v) = \frac{K_I(t, v)}{\sqrt{2\pi r}} \Sigma_{ij}(\Theta, v) + \sigma_{ij}^{(1)} + O(1). \tag{6.1}$$

The functions $\Sigma_{ij}(\Theta, v)$ represent the variation of stress components with angle Θ for any value of crack speed v [78]. These functions only depend on the ratio of crack speed to wave speeds (see discussion in the Appendix, Chapter B). The asymptotic field strongly depends on the crack velocity, and has universal character because it is independent of the details of applied loading. The values of $\sigma_{ij}^{(1)}$ and the first order contribution $O(1)$ are determined from the boundary conditions, and neglected in the remainder of this work since the first term dominates very close to the crack tip.

In the literature, there is no systematic comparison of atomistic simulations and linear elastic continuum theory of the stress and deformation field near rapidly propagating cracks. In this chapter, the continuum prediction is compared quantitatively to atomistic simulation results. Harmonic interatomic potentials are used to model a linear elastic plane-stress sheet. To compare the results for different crack velocities, we report atomistic simulations with different loading rates driving the crack to different terminal velocities.

Figure 6.1 shows the slab geometry used in the simulations. The slab size is given by l_x and l_y. The crack propagates in the y direction, and its extension is denoted by a. The crack propagates in a triangular hexagonal lattice with nearest neighbor distance along the crystal orientation shown in Figure 6.1. A weak fracture layer is introduced to avoid crack branching by assuming harmonic bonding in the bulk but a LJ potential across the weak layer (see also [83]).

All simulations presented here are two-dimensional. Previous studies have provided evidence that 2D molecular-dynamics is a good framework to investigate the dynamics of fracture [11, 83]. This is because the atomistic simulations of a two-dimensional solid and a three-dimensional solid show no difference in the details of the dynamics of the crack. The 2D model captures important features of dynamic fracture such as surface roughening and crack tip instabilities [5, 7]. Although the word "atomistic" is to some

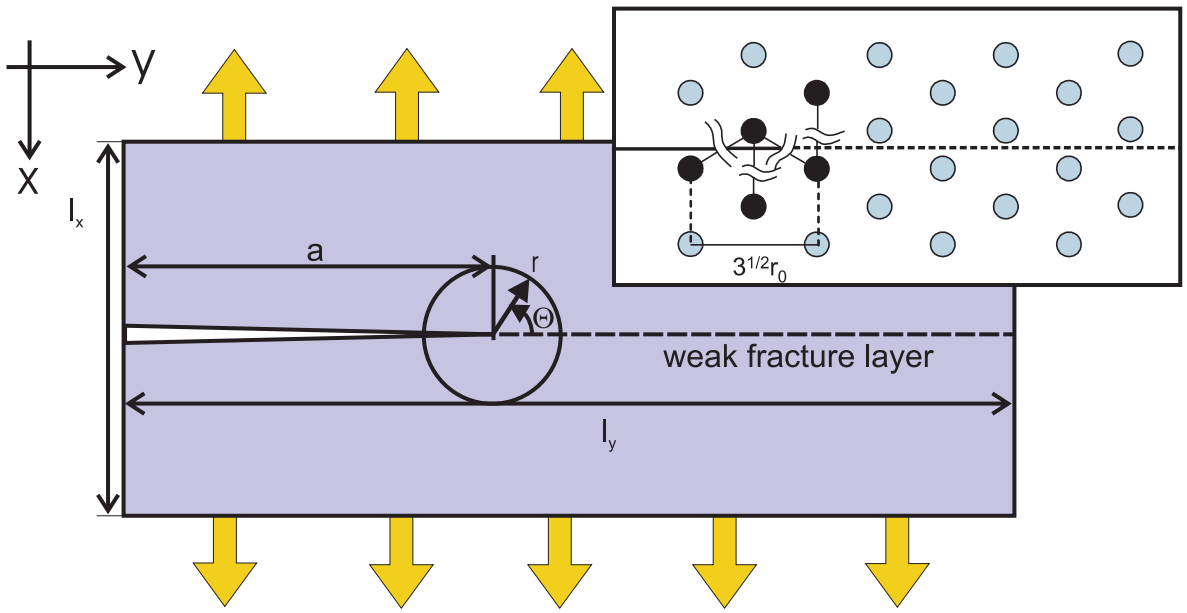

Figure 6.1.: Simulation geometry and coordinate system for studies of rapidly propagating mode I cracks in harmonic lattices.

extent not accurate, it still seems to be the best approximation in describing 2D lattice models which are now widely used to simulate dynamic fracture [256, 98, 150, 74].

The plan of this chapter is as follows. We show that in molecular-dynamics simulations of cracks travelling in perfect harmonic lattices the prediction of stress and strain fields by continuum mechanics is reproduced quantitatively. An important observation is that the hoop stress becomes bimodal at about 73 percent of Rayleigh speed, in agreement with the continuum theory. In addition, we report comparison of continuum theory with molecular-dynamics simulation of the strain energy field near the crack tip as well as the energy transport field near rapidly moving cracks.

6.1. Stress and deformation fields

In this section we compare stress and deformation field near a rapidly moving crack tip with continuum mechanics theories.

6.1.1. Angular variation of stress

We analyze the angular variation of the principal stress and hoop stress close to the crack tip and compare the results of the simulation to the continuum mechanics solution given by equation (6.1). Atomic quantities are evaluated in a small region around a constant radius of $r \approx 11$ centered at the crack tip. The continuum theory solution and the simulation results are both normalized with respect to the dynamic stress intensity factor.

We find that if the stress field measurements are taken while the crack accelerates too rapidly, the agreement of measured field and continuum theory prediction can be poor. Acceleration effects can severely change the resulting stress fields. Although the crack tip is regarded as inertia-less since it responds immediately to a change in loading or fracture surface energy, it takes time until the elastic fields corresponding to a specific crack speed spread out! In fact, the fields spread out with the Rayleigh velocity behind, and with the shear wave velocity ahead of the crack. In other regions around the crack tip, the fields are reached in the long-time limit ($t \to \infty$) [230, 78]. Therefore, we choose a moderate strain rate $\dot{\varepsilon}_{xx} = 0.000\,01$.

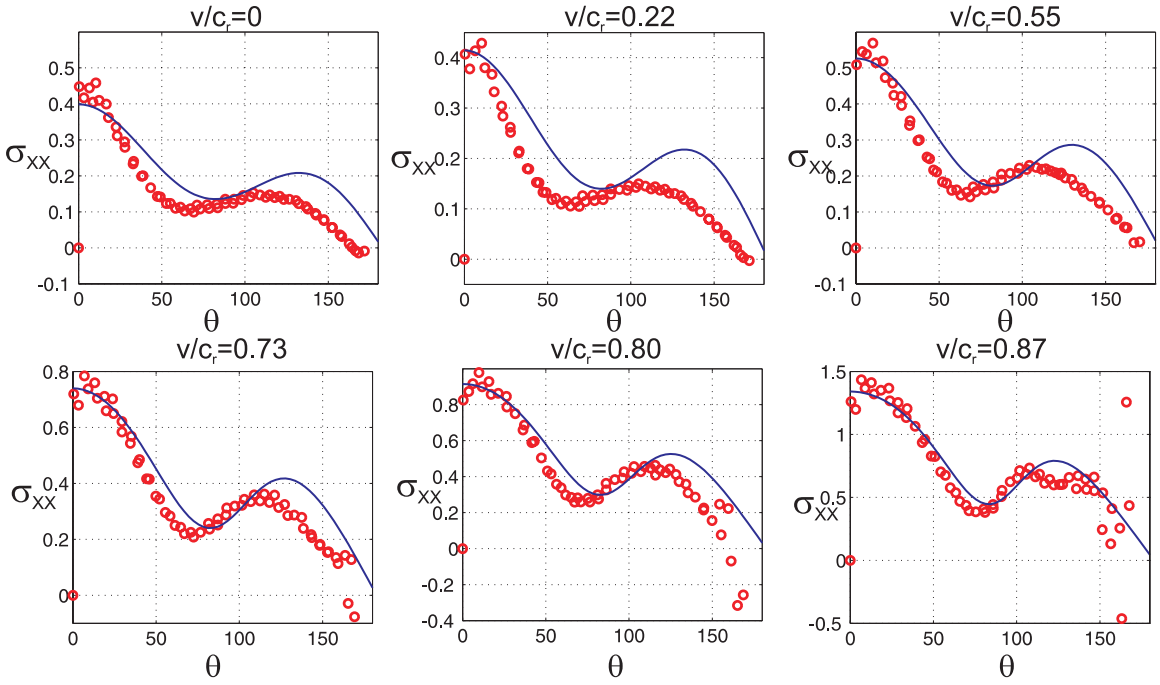

Figure 6.2.: Comparison between σ_{xx} from molecular-dynamics simulation with harmonic potential and the prediction of the continuum mechanics theory for different reduced crack speeds v/c_r.

As a consequence of the relatively low strain rate and the finite slab size, the crack only achieves about 87 % of Rayleigh-wave speed. We calculate the stress for different crack speeds ranging from 0 to 87 % of the Rayleigh speed. Figures 6.2 to 6.4 show the angular variation of σ_{xx}, σ_{yy} as well as σ_{xy}.

Figure 6.5 shows the angular variation of the hoop stress σ_Θ. Figure 6.6 shows the angular variation of the maximum principal stress σ_1 near the crack tip. In all figures, the continuous line is the corresponding analytical continuum mechanics solution [78]. It can be observed from the plots that the hoop stress becomes bimodal at a velocity of about 73 percent of the Rayleigh-wave velocity. This is in agreement with the predictions by continuum mechanics theories [78].

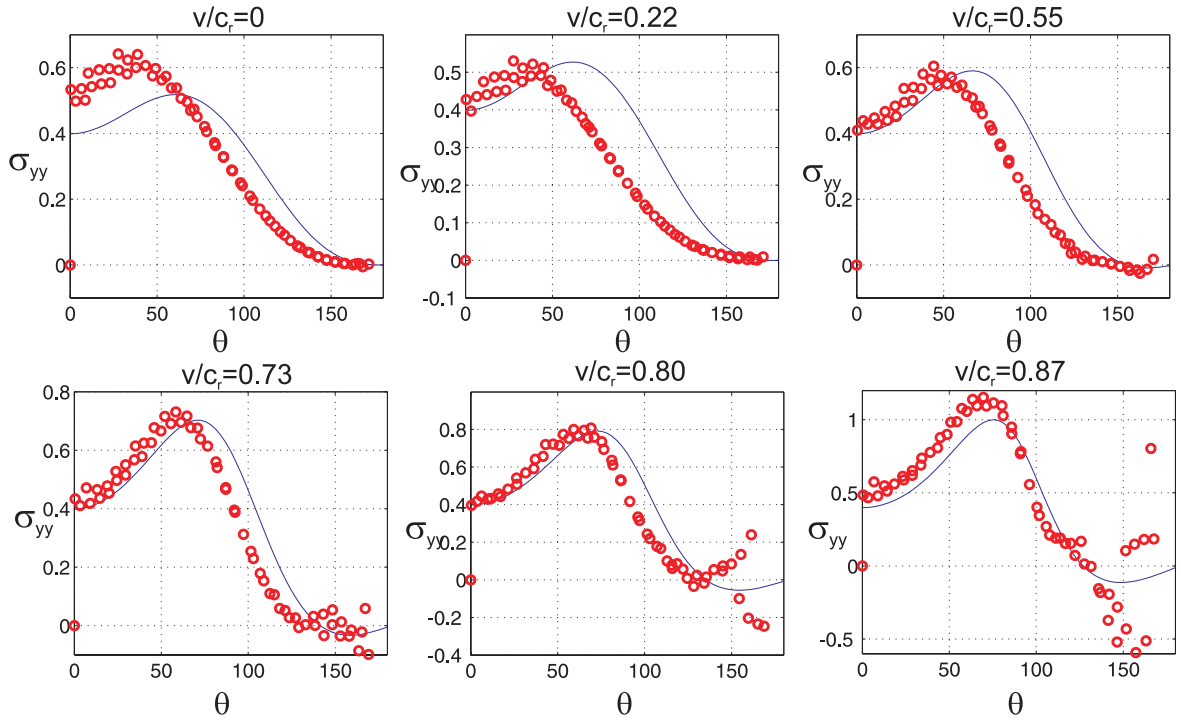

Figure 6.3.: Comparison between σ_{yy} from molecular-dynamics simulation with harmonic potential and the prediction of the continuum mechanics theory for different reduced crack speeds v/c_r.

6.1.2. Elastic fields near the crack tip

Here we use a higher strain rate of $\dot{\varepsilon}_{xx} = 0.000\,5$ in order to drive the crack close to the Rayleigh-wave speed.

The principal strain field is shown in Figure 6.7 for different velocities of $v/c_r \approx 0$, $v/c_r \approx 0.5$ and $v/c_r \approx 1$. The upper plot is the simulation result, while the lower part is the prediction by continuum mechanics. We note that the principal stress field is in good agreement with the continuum theory. The typical trimodal structure of the asymptotic principal strain and principal stress field develops close to the Rayleigh velocity, in contrast to the bimodal structure at low crack speeds.

The stress fields σ_{xx}, σ_{yy} and σ_{xy} for a crack propagating close to the Rayleigh-wave velocity are shown in Figure 6.8 (a)-(c). As before, the upper plot is the simulation result, while the lower part plots the prediction by continuum mechanics.

Finally, Figure 6.7 plots the particle velocity near the crack tip for a crack propagating close to the Rayleigh velocity. Figure 6.9 (a) shows $\dot{u}_x$, and Figure 6.9 (b) shows $\dot{u}_y$. The continuum theory prediction and the atomistic simulation result match well. The particle velocity field behind the crack tip is found to be smeared out more in the simulation results due to thermalization effects not accounted for in the continuum theory.

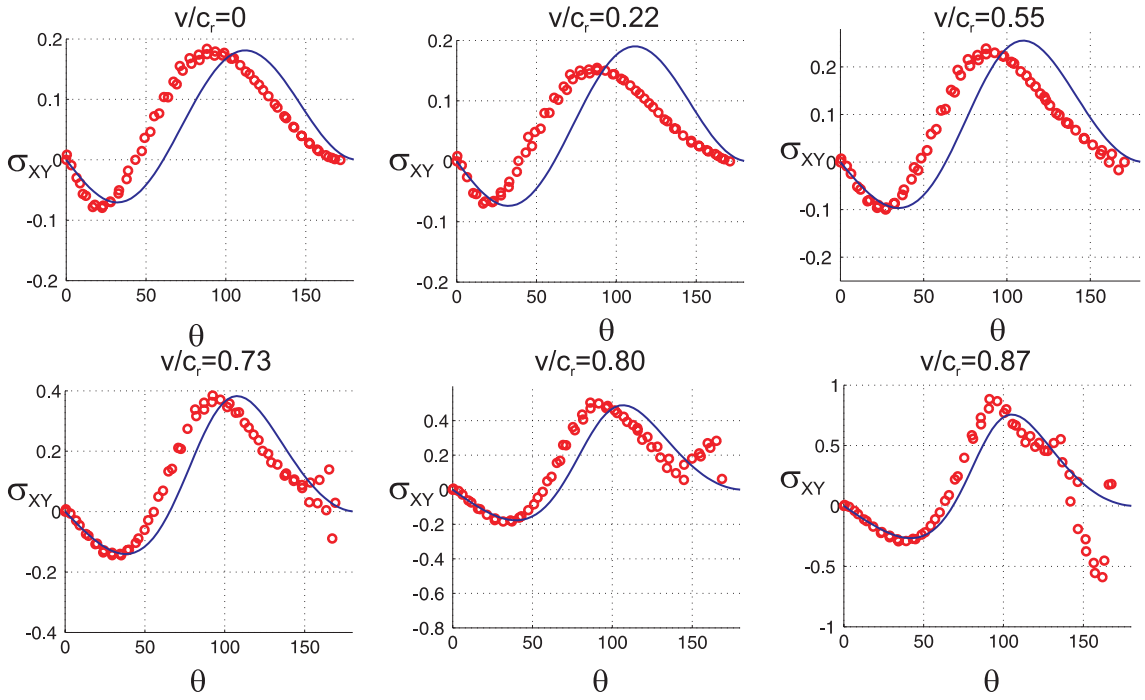

Figure 6.4.: Comparison between σ_{xy} from molecular-dynamics simulation with harmonic potential and the prediction of the continuum mechanics theory for different reduced crack speeds v/c_r.

6.2. Energy flow near the crack tip

Here we discuss the energy flow near a crack tip in molecular-dynamics simulations compared with the continuum theory [78]. A similar study has been reported recently [74]. In contrast to our treatment of the dynamic Poynting vector for steady-state cracks at high velocities (in analogy to the discussion in [78]), the authors in [74] only consider the static Poynting vector to study energy radiation of rapidly moving cracks.

The dynamic Poynting vector for a crack moving at velocity v in the y-direction can be expressed as

$$P_j = \sigma_{ij}\dot{u}_i + (U+T)v\,\delta_{2j}, \tag{6.2}$$

where δ_{ij} is the Kronecker delta function. The kinetic energy is given by $T = \frac{1}{2}\rho\dot{u}_i\dot{u}_i$, and the strain energy density for an isotropic medium is given by [27]

$$U = \frac{1}{2E}\left[\sigma_{11}^2 + \sigma_{22}^2 - 2\nu\sigma_{11}\sigma_{22} + 2(1+\nu)\sigma_{12}^2\right]. \tag{6.3}$$

The magnitude of the dynamic Poynting vector is calculated as $P = \sqrt{P_1^2 + P_2^2}$, and can be identified as a measure for the local energy flow.

Figure 6.10 (a) shows the strain energy field near the crack tip predicted by both the continuum theory prediction and the molecular-dynamics simulation result. Figure 6.10 (b) shows the magnitude of the dynamic Poynting vector field. Figure 6.11 shows in panel (a) the continuum mechanics prediction, and in panel (b) the molecular-

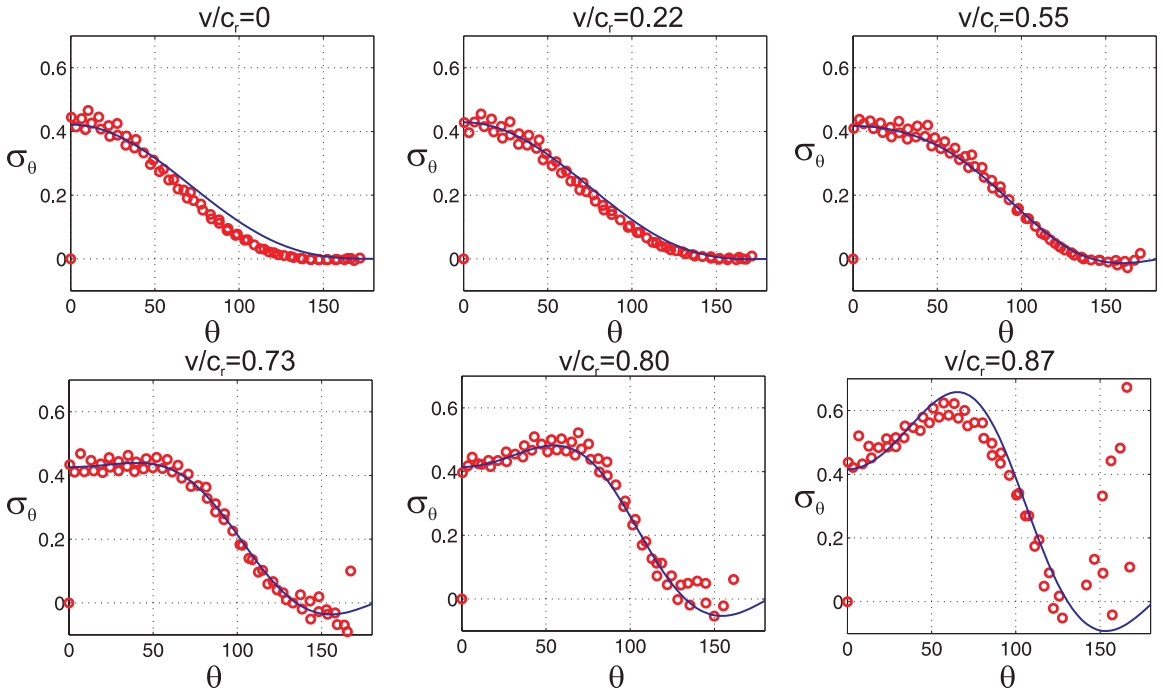

Figure 6.5.: Comparison between hoop stress from molecular-dynamics simulation with harmonic potential and the prediction of the continuum mechanics theory for different reduced crack speeds v/c_r.

dynamics simulation result of the dynamic Poynting vector field in the vicinity of the crack tip, for a crack propagating close to the Rayleigh speed.

6.3. Limiting velocities of cracks in harmonic lattices

We also study the dependence of crack dynamics in harmonic materials with different spring constants. The discussion in Chapter 5 suggests that the limiting crack speed for mode I cracks should only depend on the elastic properties, and therefore, in case of harmonic potentials, on the spring constant k. For mode I cracks considered in this chapter, the limiting speed is given by the Rayleigh-wave speed [78].

Figure 6.12 shows the crack tip history $a(t)$ as well as the crack speed history $\dot{a}(t)$ for a soft as well as a stiff harmonic material. The results are in consistency with the predicted limiting speed (see data in Table 5.1).

6.4. Discussion

Simulations of cracks propagating along a confined fracture path in a harmonic lattice show that continuum mechanics theory of fracture can be successfully applied even at the atomistic level. We compared the virial stress and strain from atomistic simulation results with the continuum mechanics solution of the asymptotic field for different propagation velocities.

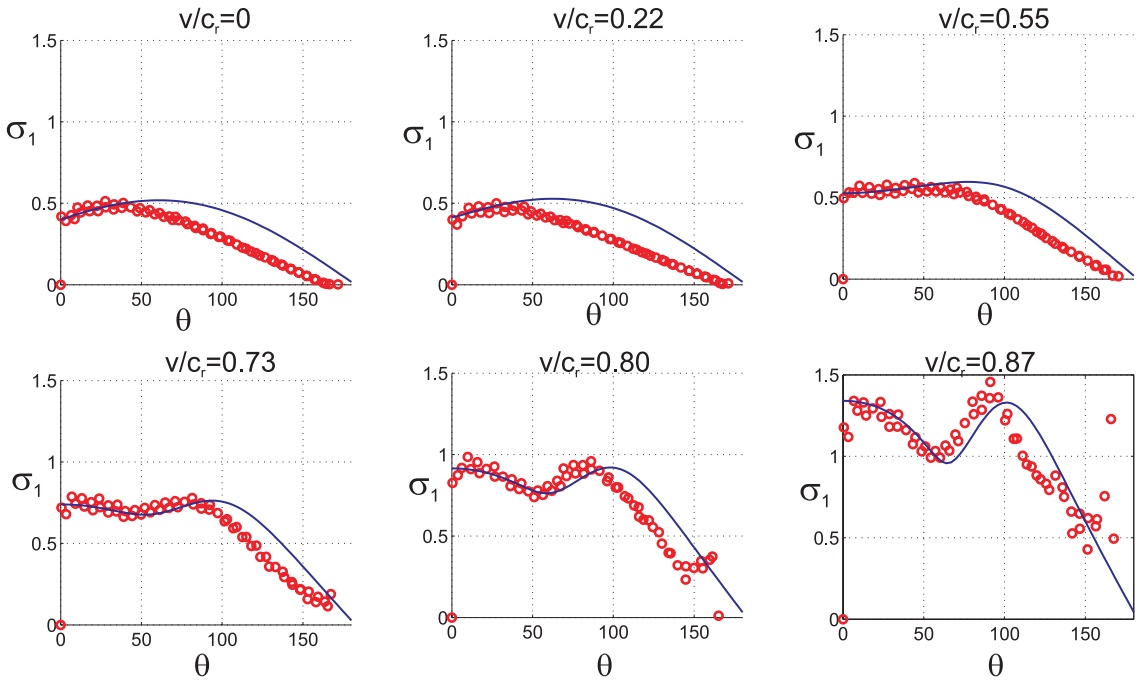

Figure 6.6.: Comparison between the maximum principal stress σ_1 from molecular-dynamics simulation with harmonic potential and the prediction of the continuum mechanics theory for different reduced crack speeds v/c_r.

The results suggest that the agreement of molecular-dynamics simulations and continuum mechanics is generally good, as it is shown for the stress tensor components σ_{xx}, σ_{yy} and σ_{xy}. We observe disagreement at large angles $\Theta > 150$ degrees, probably due to surface effects in the atomistic simulations. In Figure 6.2 we observe that for σ_{xx}, the shape of $\sigma_{xx}(\Theta)$ is qualitatively reproduced well over the entire velocity regime between 0 and 87 percent of Rayleigh speed. However, the angles of the local maxima and minima are shifted to slightly smaller values compared to the theory prediction.

Figure 6.3 illustrates that the shift of the maximum in the $\sigma_{yy}(\Theta)$ curve from about 60 degrees to about 80 degrees is reproduced only qualitatively. For low velocities the maximum is found at lower angles around 40 degrees, but it approaches the value of the continuum theory at higher velocities. At 87 percent of Rayleigh speed, the difference is only a few degrees. The shear stress σ_{xy} shown in Figure 6.4 also agrees qualitatively with the continuum theory. As in the previous cases, the angles of local minima and maxima are shifted to lower values in the simulation, but the agreement gets better when the crack velocity is faster. Even though we see small deviations in σ_{xx}, σ_{yy} and σ_{xy}, the hoop stress σ_Θ agrees quantitatively with the continuum theory as shown in Figure 6.5.

The angles of the maxima and minima during crack acceleration compare well with theory. However, the angles of the maxima and minima of the maximum principle stress shown in Figures 6.6 are also shifted to slightly lower values. However, we observe that two local maxima and one local minima develops at a velocity of about 73 percent in quantitative agreement with continuum theory ("trimodal structure"). The magnitude of the local maxima and minima also agree quantitatively.

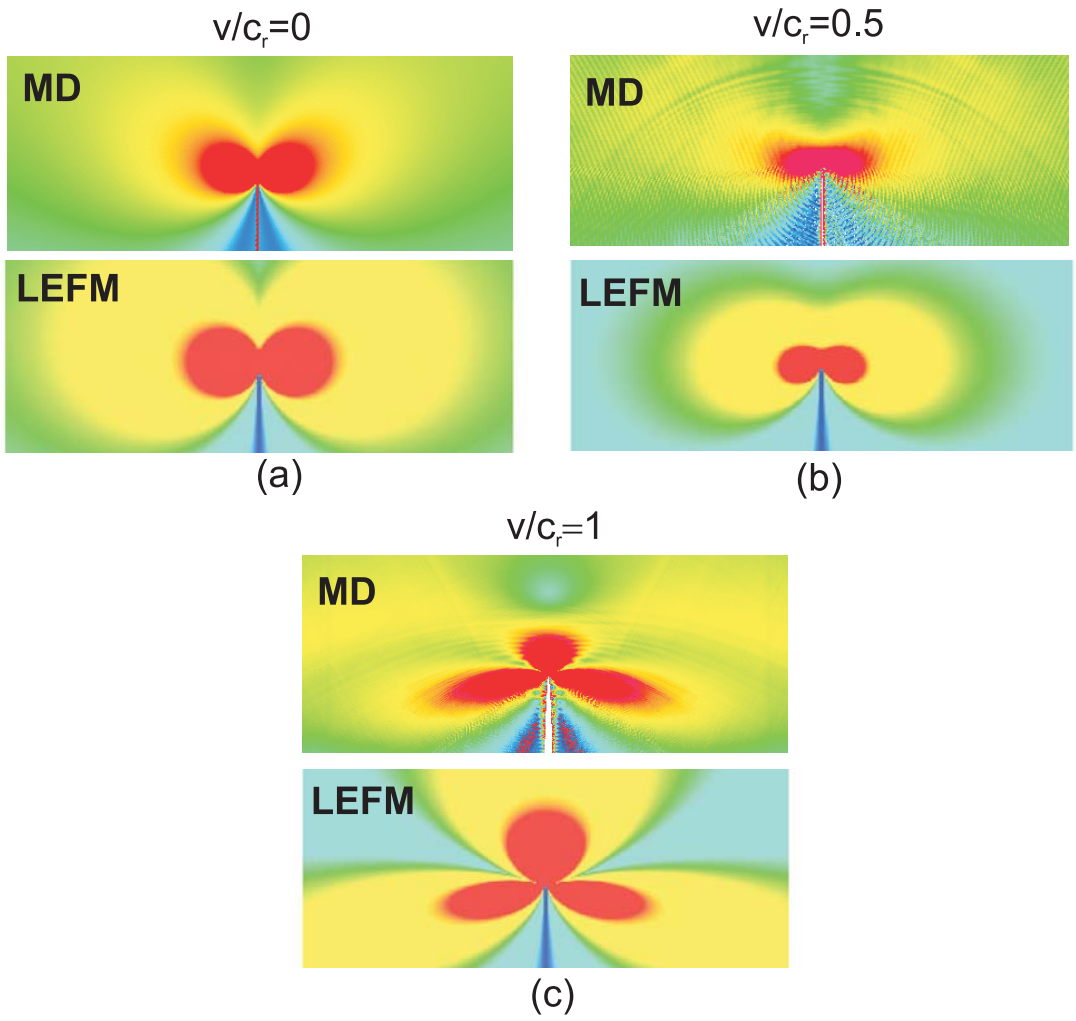

Figure 6.7.: Principal strain field at various crack velocities (a) $v/c_r \approx 0$, (b) $v/c_r \approx 0.5$, (c) $v/c_r \approx 1$. In each of the plots (a)-(c), the upper plot is the simulation result and the lower part is the prediction by continuum mechanics.

The analysis of the potential energy field near a crack close to the Rayleigh speed agrees qualitatively with the prediction by the continuum mechanics theory. As Figure 6.10 (a) shows, in both theory and computation the field clearly shows two three local maxima with respect to the angular variation ("trimodal structure"), similar to the principal stress field. At larger distances away from the crack tip we observe that other stress terms begin to dominate in the simulation, so the distribution of the potential energy deviates from the prediction by theory. As is expected since only the first term of equation (6.1) is considered, these contributions are missing in the continuum solution.

Similar observations also hold for the magnitude of the dynamic Poynting vector, as it can be verified in Figure 6.10 (b). The dynamic Poynting vector field calculated by molecular-dynamics is also in reasonable agreement with the continuum mechanics prediction. This could be verified in Figure 6.11. In both theory (Figure 6.11 (a)) and molecular-dynamics calculation (Figure 6.11 (b)), the orientation of the dynamic

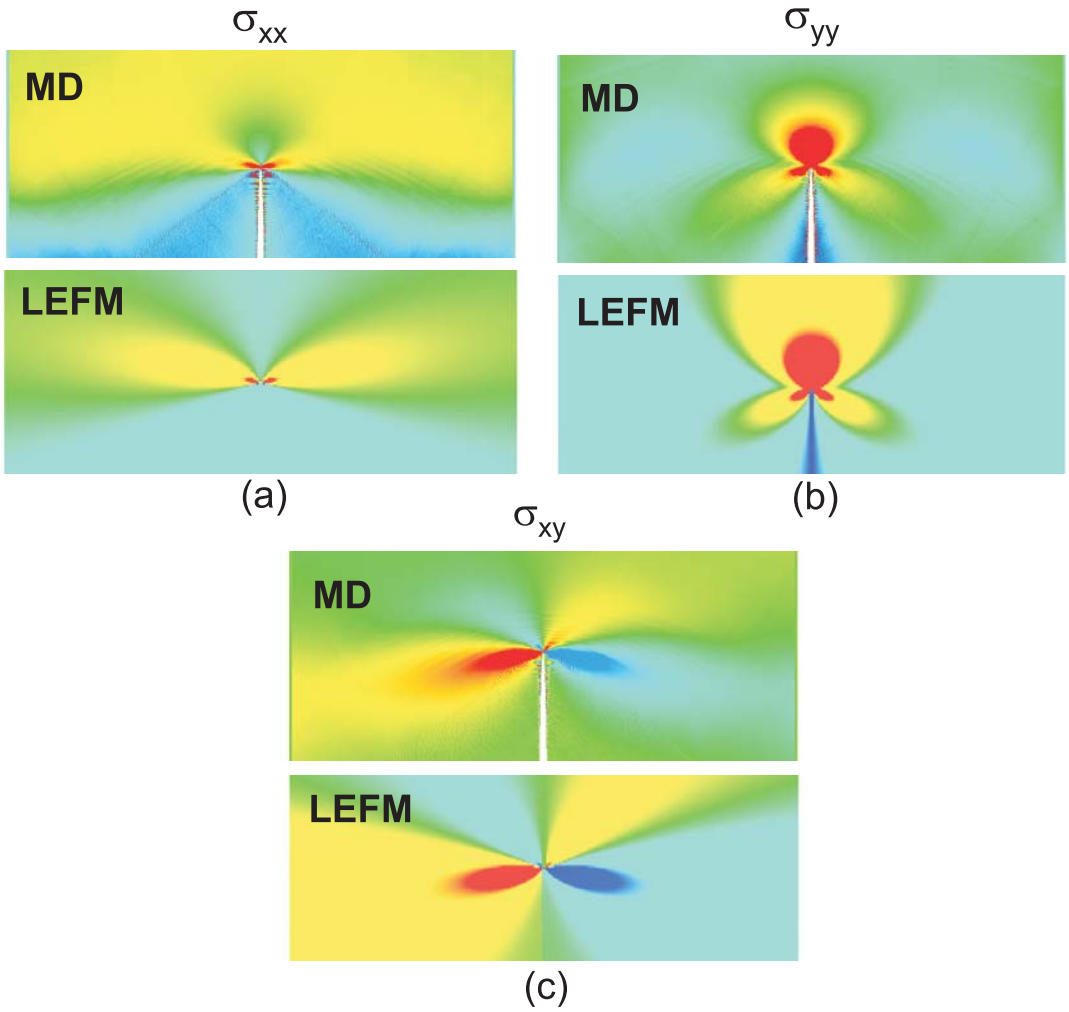

Figure 6.8.: Stress fields close to the crack tip for a crack propagating close to the Rayleigh velocity $v/c_r \approx 1$. Plots (a), (b) and (c) show σ_{xx}, σ_{yy} and σ_{xy}. In each of the plots (a)-(c), the upper plot is the simulation result and the lower part is the prediction by continuum mechanics.

Poynting vector is dominated by the direction opposite to crack motion. The vector field seems to bow out around the crack tip, an effect that is more pronounced in the simulation than predicted by theory. Also, the flow ahead of the crack is larger in simulation than predicted by theory. At the free surface of the crack, the measurement from the simulation and the prediction by theory show differences. This could be based on the fact that the continuum theory does not treat surface effects properly, in particular short-wave length Rayleigh waves (see also discussion in [74]).

Our calculation of the virial stress does not include the particle velocity contribution (see Appendix, Chapter A). This is in consistency with the recent investigations of Zhou and coworkers [253] on the linkage between virial stress and Cauchy stress of continuum mechanics. Finally, we note that the virial expression of the stress tensor is classically thought to be only valid under equilibrium conditions [212]. Our results reported in

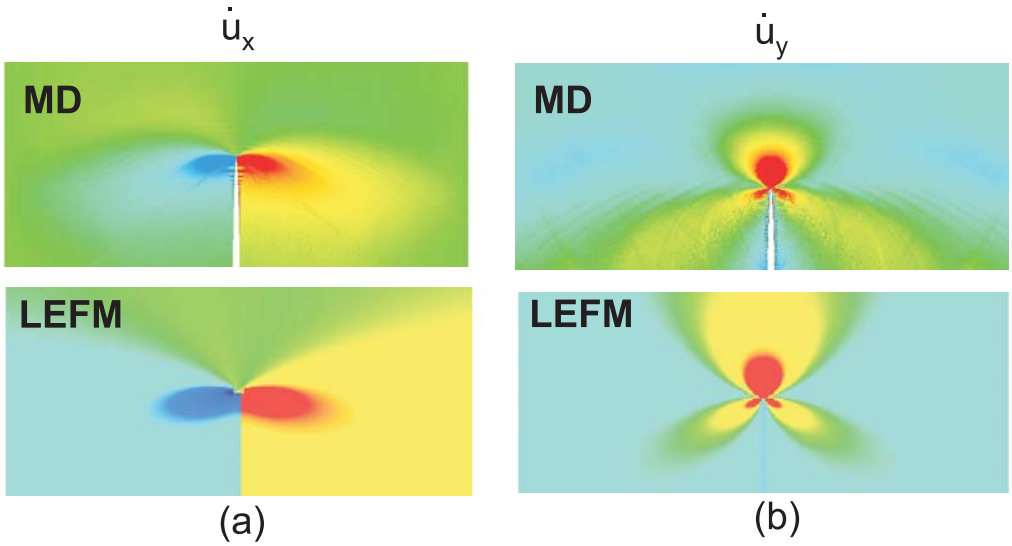

Figure 6.9.: Particle velocity field close to the crack tip for a crack propagating close to the Rayleigh velocity, $v/c_r \approx 1$. Plots (a) shows $\dot{u}_x$ and plot (b) shows $\dot{u}_y$. In each of the plots (a) and (b), the upper plot is the simulation result and the lower part is the prediction by continuum mechanics.

this chapter show that it is approximately valid even under dynamic fracture conditions which are far from equilibrium.

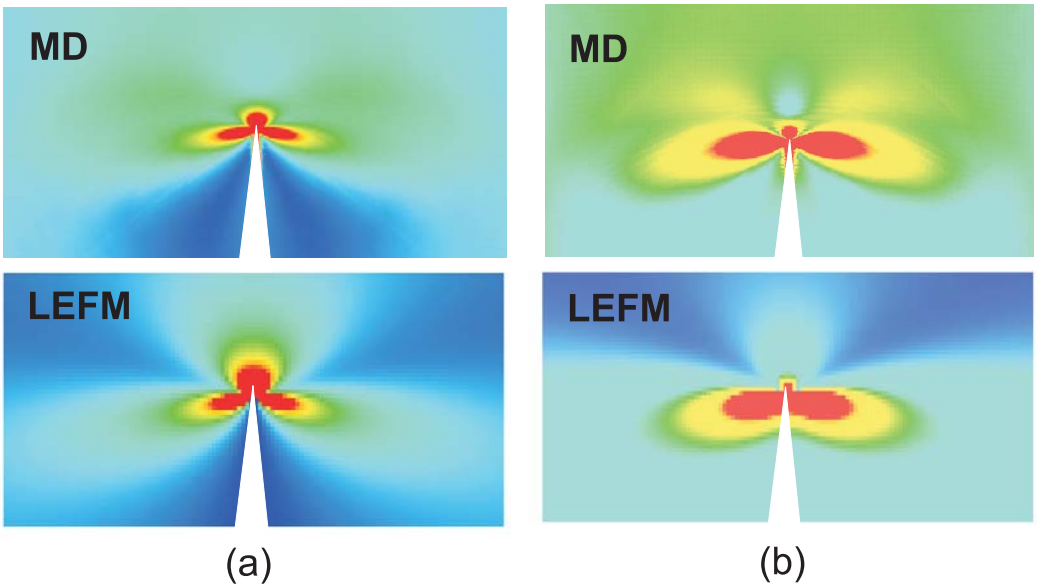

Figure 6.10.: Potential energy field and magnitude of the dynamic Poynting vector. (a) Potential energy field near a crack close to the Rayleigh speed. (b) Energy flow near a rapidly propagating crack. This plot shows the magnitude of the dynamic Poynting vector in the vicinity of a crack propagating at a velocity close to the Rayleigh speed.

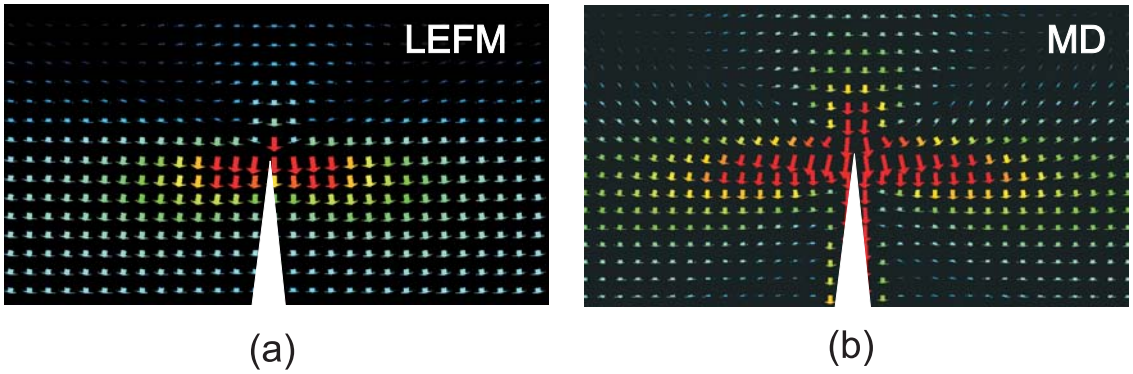

Figure 6.11.: Energy flow near a rapidly propagating crack. This plot shows (a) the continuum mechanics prediction, and (b) the molecular-dynamics simulation result of the dynamic Poynting vector field in the vicinity of the crack tip, for a crack propagating close to the Rayleigh-wave speed.

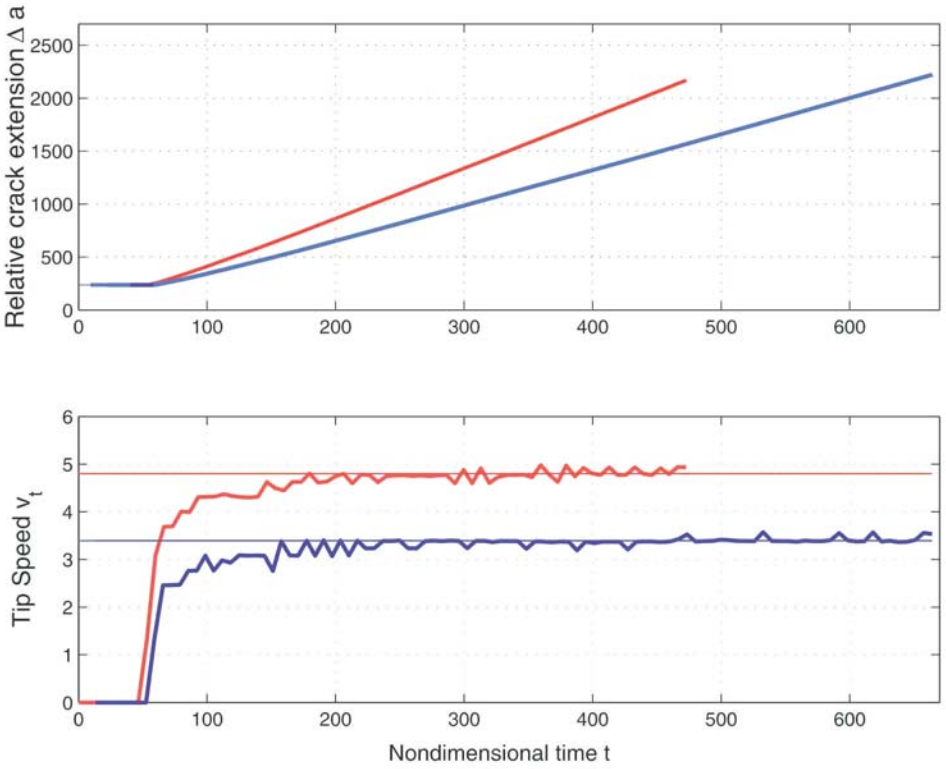

Figure 6.12.: Crack tip history as well as the crack speed history for a soft as well as a stiff harmonic material (two different choices of spring constants as given in Table 5.1).

7. Hyperelasticity governs dynamic fracture at a critical length scale

The elasticity of a solid clearly depends on its state of deformation. Metals will weaken, or soften, and polymers may stiffen as the strain approaches the state of materials failure. It is only for infinitesimal deformation that the elastic moduli can be considered constant and the elasticity of the solid linear. However, many existing theories model fracture using linear elasticity. Certainly, this can be considered questionable since material is failing at the tip of a dynamic crack because of the extreme deformation. We show by large-scale atomistic simulations that hyperelasticity, the elasticity of large strains, can play a governing role in the dynamics of fracture and that linear theory is incapable of capturing all phenomena. We introduce the concept of a characteristic length scale for the energy flux near the crack tip and demonstrate that the local hyperelastic wave speed governs the crack speed when the hyperelastic zone approaches this energy length scale.

7.1. Introduction

Why and how cracks spread in brittle materials is of essential interest to numerous scientific disciplines and technological applications, and a theoretical understanding is essential for numerous engineering applications. We show by large-scale atomistic simulation that hyperelasticity, the elasticity of large strains, can play a governing role in the dynamics of brittle fracture. This is in contrast to many existing theories of dynamic fracture where the linear elastic behavior of solids is assumed sufficient to predict materials failure [78, 29, 199].

Real solids have elastic properties that are significantly different for small and for large deformations. Many phenomena associated with rapidly propagating cracks are not thoroughly understood. Some experimental work [70, 176] as well as many computer simulations [7, 5, 65] have shown a significantly reduced crack propagation speed in comparison with the predictions by the theory. In contrast, other experiments indicated that over 90 percent of the Rayleigh wave speed can be achieved [232, 194, 68, 52, 105, 104, 119]. Such discrepancies between theories, experiment and simulations can not always be attributed to the fact that real solids have all sorts of imperfections such as grain boundaries and microcracks (either pre-existing or created during the crack propagation), as similar discrepancies also appear in molecular-dynamics simulations of cracks travelling in perfect atomic lattices. Gao [81, 82] and Abraham [5, 7] have independently proposed that hyperelastic effects at the crack tip may play an important role in the dynamics of fracture. Their suggestions have been used to help explaining

phenomena related to crack branching and dynamic crack tip instability, as well as explaining the significantly lower maximum crack propagation speed observed in some experiments and many computer simulations. However, it is not generally accepted that hyperelasticity should play a significant role in dynamic fracture.

One reason for this belief stems from the fact that the zone of large deformation in a loaded body with a crack is highly confined to the crack tip, so that the region where linear elastic theory does not hold is extremely small compared to the extensions of the specimen [78, 29]. In this study, we use large-scale molecular-dynamics simulations [11] in conjunction with continuum mechanics concepts [78, 29] to prove that hyperelasticity can be crucial for understanding dynamic fracture.

Our study shows that local hyperelasticity around the crack tip can significantly influence the limiting speed of cracks by enhancing or reducing local energy flow. This is true even if the zone of hyperelasticity is small compared to the specimen dimensions. The hyperelastic theory completely changes the concept of the maximum crack velocity in the classical theories. For example, the classical theories clearly predict that mode I cracks are limited by Rayleigh wave speed and mode II cracks are limited by longitudinal wave speed. In contrast, both super-Rayleigh mode I and supersonic mode II cracks are allowed by hyperelasticity and have been seen in computer simulations [6, 11].

In our simulations, we find that there exists a characteristic length scale associated with energy flow near the crack tip such that hyperelasticity completely dominates crack dynamics if the size of hyperelastic region approaches this characteristic length. In earlier simulations [6, 11], a nonlinear interatomic stiffening was assumed, and there was no sharp distinction between the linear and nonlinear elastic regimes for the stretched solid. In contrast, our model is based on a biharmonic potential composed of two spring constants, one associated with small deformations and the other associated with large deformations (see discussion in Section 5.1.5). This serves as a simplistic model material for hyperelasticity, allowing us to investigate the generic features of hyperelasticity common to a large class of real materials.

7.2. Modeling

We consider propagation of a crack in a two-dimensional simulation geometry shown in Figure 6.1. The slab size is given by l_x and l_y. The crack propagates in the y direction, and its extension is denoted by a. The crack propagates in a triangular hexagonal lattice with nearest neighbor distance along the crystal orientation shown in Figure 6.1. To avoid crack branching, a weak fracture layer is introduced by assuming that atomic bonds across the prospective crack path snap at a critical atomic snapping distance r_{break} while those in the rest of the slab never break. As outlined in Section 5.2, the snapping distance can be used to adjust the fracture surface energy 2γ.

For a systematic study of hyperelastic effects in dynamic fracture, we adopt the biharmonic potential defined in equation (4.19). This potential is composed of two spring constants k_0 and k_1. Here we consider two "model materials", one with elastic stiffening and the other with elastic softening behavior. In the elastic stiffening system, the spring constant k_0 is associated with small perturbations from the equilibrium distance r_0, and

the second spring constant k_1 is associated with large bond stretching for $r > r_{\text{on}}$. The role of k_0 and k_1 is reversed in the elastic softening system ($k_0 = 2k_1$, and $k_1 = 36/\sqrt[3]{2}$). The elastic properties associated with this potential are shown in Figure 5.9.

To strain the system, we use two approaches. The first is using a constant strain rate applied over a loading time by displacing the outermost rows of atoms. After the loading time, the boundaries are kept fixed. In the second method, we strain the system prior to simulation in the loading direction, and keep the boundary fixed during simulation. In either way, the crack starts to move once a critical strain is applied. It can be shown that the stress intensity factor remains constant in a strip geometry inside a region of [206]

$$3/4l_x < a < (l_y - 3/4l_x). \tag{7.1}$$

This ensures that the crack achieves a steady-state during propagation through the slab. The slab is initialized at zero temperature prior to simulation.

The length l_y is several times larger than l_x, with the ratio ranging from two to five. The slab width l_x considered ranges from 1,150 (smallest) up to 4,597 (largest, corresponding to micrometer length scale in physical dimensions). The largest model contains over 70 million atoms. All quantities in this chapter are given in reduced units. The condition for small-scale yielding is satisfied in all cases (with harmonic, stiffening and softening potentials), since breaking of atomic bonds occurs over a region involving only a few atoms along the weak layer (that is, very small fracture process zone). There is no dislocation processes and the system is perfectly brittle. The slab is loaded with a maximum of a few percent strain, according to the crack loading mode. The loading is significantly lower than other studies [206]. A slit of length a is cut midway through the slab as an initial, atomically sharp crack.

Accurate determination of crack tip velocity is important because we need to be able to measure even smallest changes in the propagation speed. The crack tip position is determined by finding the surface atom with maximum y position in the interior of a search region inside the slab. This quantity is averaged over a small time interval to eliminate very high frequency fluctuations. To obtain the steady state velocity of the crack, the measurements are taken within a region of constant stress intensity factor [206]. In addition to checking the velocity history, steady state is verified by path-independency of the energy flux integral [78].

7.3. Crack speed and energy flow

We show by molecular-dynamics simulations that a localized, small hyperelastic region around the crack tip can have significant effects on the dynamics of crack propagation. In all simulations, the slab is statically loaded with 0.32 percent strain in mode I. The strain energy density far ahead of the crack tip is given by

$$S = \frac{\varepsilon_{xx}^2 l_x E}{2(1-\nu)^2}, \tag{7.2}$$

where E is the Young's modulus at small strain. The linear elastic expression of strain energy density is valid because material far ahead of the crack is strained always below

the onset threshold of the bilinear law, that is it remains in the linear elastic regime of material response. The strain and strain energy density both vanish far behind of the crack. For a unit distance of crack propagation, a strip of material with energy density S ahead of the crack is replaced by an identical strip with zero strain energy behind the crack.

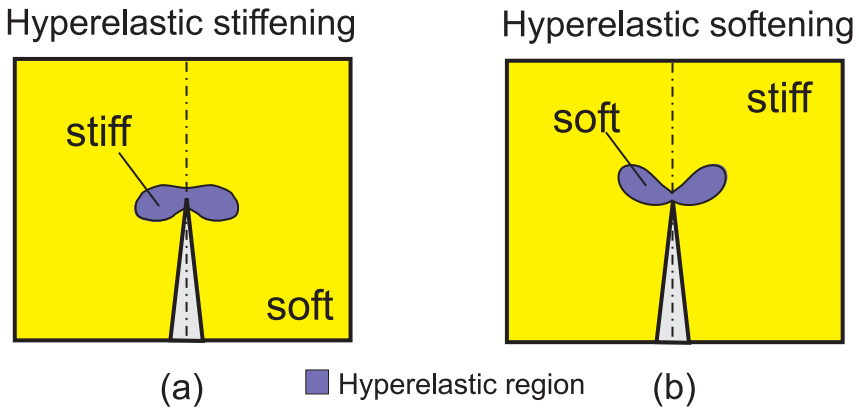

Figure 7.1.: Hyperelastic region in a (a) softening and (b) stiffening system.

According to the linear elastodynamic theory of fracture [78], the crack speed should satisfy the dynamic energy release rate equation

$$A(v/c_r) = \frac{2\gamma}{S} \tag{7.3}$$

where the function $A(v/c_r)$ is a universal function of crack velocity v for a given material. Assuming that the small-strain elasticity completely governs the dynamics of fracture, the linear theory predicts that crack velocity should depend only on the ratio S/γ.

During crack propagation, the energy stored ahead of the crack tip is partly converted by the bond breaking process into fracture surface energy, and partly dissipated into atomic motion. In the purely harmonic case, the fracture surface energy γ depends on r_{break} and E. In the biharmonic case, the fracture surface energy depends on r_{break}, r_{on}, E_0 and E_1. Our strategy is to focus on the prediction from linear theory that crack velocity depends only on the ratio S/γ. To achieve this objective, we keep the ratio S/γ constant in all of the simulations. In the harmonic systems, as $S \sim E$ and $\gamma \sim E$, we choose the parameter r_{break} to be identical in all cases. In the biharmonic systems, we adjust the parameter r_{break}, at given values of r_{on}, E_0 and E_1, to always keep S/γ constant.

We choose $r_{\text{break}} = 1.17$ for the harmonic systems. The failure strain at the crack tip can reach a magnitude of several per cent, which is comparable to many "real materials". In the harmonic systems (with Young's modulus equal to E_0 or E_1), the crack achieves the same propagation velocity around 80 percent of the Rayleigh wave speed. This is consistent with the linear theory.

For the biharmonic systems, we choose $r_{\text{on}} = 1.1275$ and $r_{\text{break}} = 1.1558$ in the stiffening system and $r_{\text{break}} = 1.1919$ in the softening system to keep S/γ constant. In contrast to the linear theory prediction, we find that the crack propagation velocity is about 20

per cent larger in the stiffening system and 30 per cent smaller in the softening system. These deviations can not be explained by the linear theory. The fact that we change the large-strain elasticity while keeping the small-strain elasticity constant indicates that hyperelasticity is affecting crack dynamics.

7.3.1. Hyperelastic area

A geometric criterion based on the principal strain is used to characterize the area with hyperelastic material response close to the crack tip. The region occupied by atoms having a local maximum principal strain

$$\varepsilon_1 \geq \varepsilon_{\text{on}} = \frac{r_{\text{on}} - r_0}{r_0} \tag{7.4}$$

defines the hyperelastic area A_H by an integral over the whole simulation domain Ω

$$A_H = \int_{\Omega} H(\varepsilon_1 - \varepsilon_{\text{on}})\, \mathrm{d}\Omega. \tag{7.5}$$

Figure 7.1 (a) shows the hyperelastic area in the case of a stiffening material, and Figure 7.1 (b) shows the hyperelastic area in the case of an elastically softening material, indicating that the hyperelastic effect is highly localized to the crack tip (these pictures show a portion of the simulation slab near the crack tip). However, the effect of hyperelasticity on crack velocity is significant, independent of the slab size.

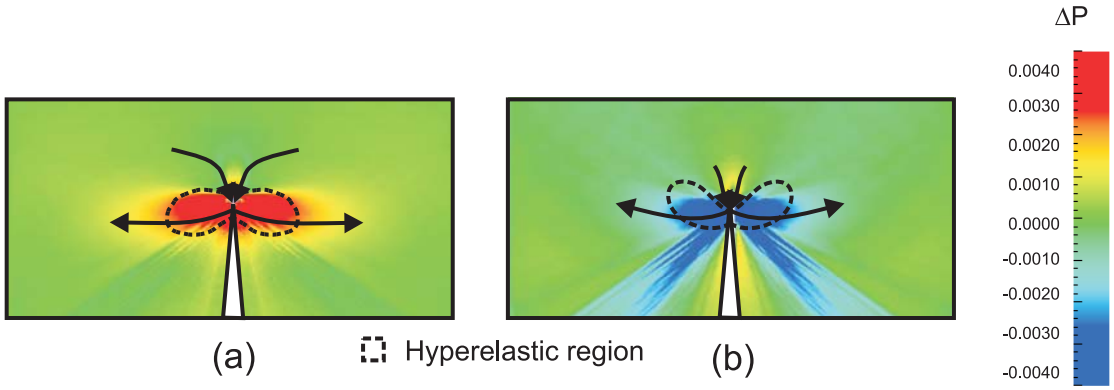

Figure 7.2.: Hyperelastic region and enhancement of energy flow in the (a) softening and (b) stiffening system.

7.3.2. Enhancement or reduction of energy flow

A measure for the direction and magnitude of energy flow in the vicinity of the crack tip is the dynamic Poynting vector [78, 74]. The magnitude of the dynamic Poynting vector

$$P = \sqrt{P_1^2 + P_2^2} \tag{7.6}$$

	Change of net energy flow to crack tip	Change of energy flow to crack tip	Change of energy flow away from crack tip	Change of limiting speed
Stiffening	+19 %	+20 %	+25 %	+20 %
Softening	-32 %	-32 %	-35 %	-30 %

Table 7.1.: Change of energy flow to the crack tip, due to a bilinear softening or stiffening interatomic potential.

may be identified as a measure for the local energy flow.

A measure for the enhancement or reduction of energy flow is obtained by subtracting the magnitude of the dynamic Poynting vector in the harmonic case from that in the biharmonic case at every point in the slab

$$\Delta P = P_{\text{biharm}} - P_{\text{harm}}. \tag{7.7}$$

If the difference is negative, energy flow is reduced, and if the difference is positive, energy flow is enhanced. The steady-state fields are averaged over space as well as time to obtain good statistics.

Figure 7.2 shows the energy flow enhancement and reduction in the vicinity of the crack tip for the elastically stiffening bilinear system (a) and for the elastically softening system (b). In each plot, the local hyperelastic zone is indicated by a dotted line. The energy flow in the vicinity of the crack tip is enhanced in the bilinear stiffening case and reduced in the softening case. In these plots, we also indicate the direction of energy flow with arrows and note that in the softening case, the energy flow ahead of the crack almost vanishes.

The plots show that the local hyperelastic effect leads to an enhancement (stiffening system) or reduction (softening system) in energy flow. The small hyperelastic regions enhance the energy flow around the crack tip. The higher crack velocity in the stiffening system and the lower velocity in the softening system are due to enhancement or reduction of the energy flow in the vicinity of the crack tip. Table 7.1 summarizes change of net energy flow, as well as change of energy flow toward and away from the crack tip, in comparison to the harmonic system. The results quantify those depicted in Figure 7.2 (a) and (b) and show that the net energy flow as well as the flow of energy toward and away from the crack tip are all enhanced in the stiffening case, and reduced in the softening case.

7.3.3. J-Integral analysis

The integral of energy flux, or path-independent dynamic J-integral is defined as

$$F(\Gamma) = \int_{\Gamma} (\sigma_{ij}\, n_j\, \dot{u}_i + (U+T) v\, n_2)\, \mathrm{d}\Gamma. \tag{7.8}$$

It can be shown that its value is path-independent for steady-state crack motion [78].

We find that $F(\Gamma)$ around the crack tip increases by 19 percent in comparison with the harmonic case for the stiffening system, while decreasing by 32 percent for the softening system. The results are shown in Figure 7.3. To calculate the integral, we choose a circular shape of Γ centered around the crack tip. Atomic quantities like stress and particle velocity are averaged spatially and over time and then the line integral is computed. The plot shows the value of the dynamic J-integral is independent of the shape of Γ which proves that crack motion is in steady-state.

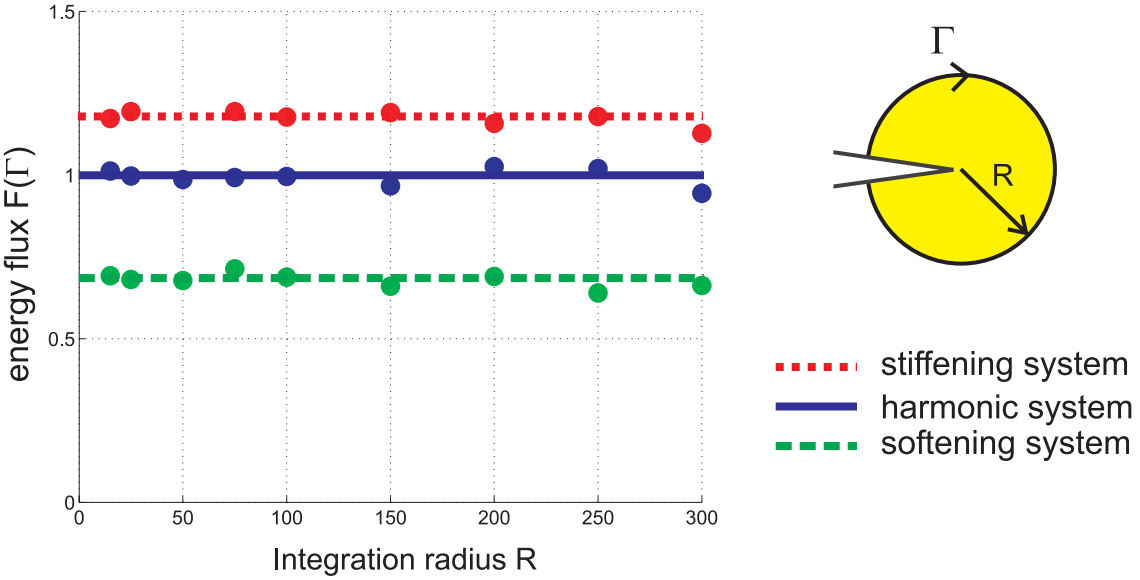

Figure 7.3.: J-integral analysis of a crack in a harmonic, softening and stiffening material, for different choices of the integration path Γ. The straight lines are a linear fit to the results based on the calculation of the MD simulation.

7.4. How fast can cracks propagate?

We have learned that a local hyperelastic zone around the crack tip can have significant effect on the velocity of the crack. For a mode I tensile crack, linear theory predicts that the energy release rate vanishes for all velocities in excess of the Rayleigh wave speed [76], implying that a mode I crack cannot move faster than the Rayleigh wave speed.

This prediction is indeed confirmed in systems with the harmonic potential where crack velocity approaches the Rayleigh wave speed independent of the slab size, provided that the applied strain is larger than 1.08 per cent and the slab width is sufficiently large ($l_x > 1,000$). The systems are loaded dynamically in this case. Our strain levels are about 10 times lower than in many other studies [206].

We consider hyperelastic effects of different strengths by using a biharmonic potential with different onset strains governed by the parameter r_{on}. The parameter governs the onset strain of the hyperelastic effect

$$\varepsilon_{\text{on}} = \frac{r_{\text{on}} - r_0}{r_0}. \tag{7.9}$$

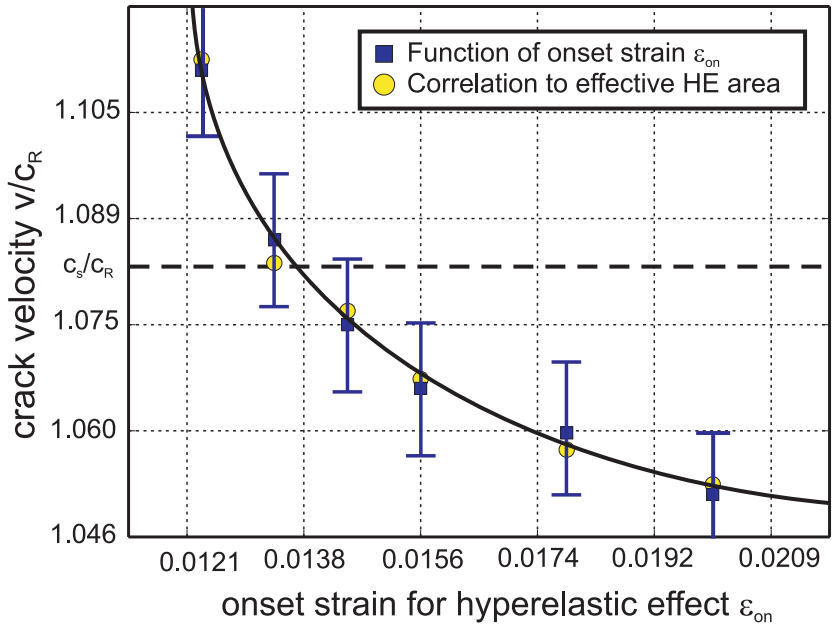

Figure 7.4.: Change of the crack speed as a function of ε_{on}. The smaller ε_{on}, the larger is the hyperelastic region and the larger is the crack speed.

The simulations reveal crack propagation at super-Rayleigh velocities in steady-state with a local stiffening zone around the crack tip.

7.4.1. Intersonic mode I cracks

Figure 7.4 plots the crack velocity as a function of the hyperelasticity onset strain ε_{on}. The crack speeds shown in Figure 7.4 are determined during steady-state propagation. We observe that the earlier the hyperelastic effect is turned on, the larger the limiting velocity. Measuring the hyperelastic area A_H using the principal strain criterion, we find that A_H grows as ε_{on} becomes smaller. A correlation of the square root of the hyperelastic area with the achieved limiting speed of the crack is shown in Figure 7.4. In Figure 7.5, we depict the shape of the hyperelastic area near the crack tip for different choices of ε_{on}. The shape and size of the hyperelastic region is found to be independent of the slab width l_x. In all cases, the hyperelastic area remains confined to the crack tip and does not extend to the boundary of the simulation.

Figure 7.4 shows that the hyperelastic effect is very sensitive to the potential parameter and the extension of the local hyperelastic zone. Mode I cracks can travel at steady-state intersonic velocities if there exists a locally stiffening hyperelastic zone.

For example, when the large-strain spring constant is chosen to be $k_1 = 4k_0$, with $r_{\text{on}} = 1.1375$ and $r_{\text{break}} = 1.1483$ (that is, "stronger" stiffening and thus larger local wave velocity than before), the mode I crack propagates 21 per cent faster than the Rayleigh speed of the soft material, and becomes intersonic, as shown by the Mach cone of shear wave front depicted in Figure 7.6.

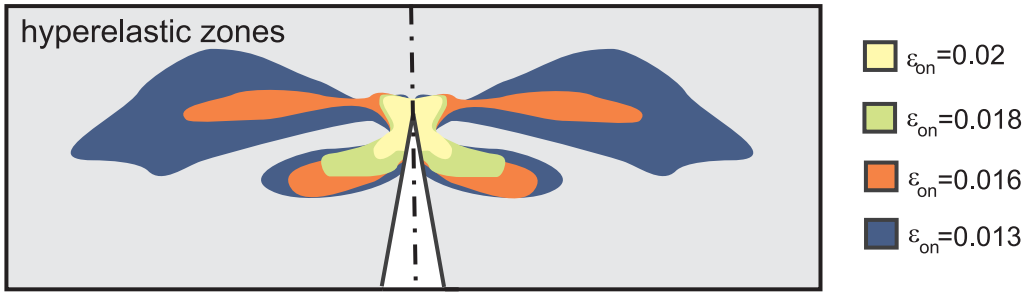

Figure 7.5.: Shape of the hyperelastic regions for different choices of ε_{on}. The smaller ε_{on}, the larger is the hyperelastic region. The hyperelastic region takes a complex shape.

7.4.2. Supersonic mode II cracks

We have also simulated a shear-dominated mode II crack using the biharmonic stiffening potential. We define $r_{\text{break}} = 1.17$, and r_{on} is chosen slightly below to keep the hyperelastic region small. The dynamic loading is stopped soon after the daughter crack is nucleated [11, 6, 83]. The result is shown in Figure 7.7. The daughter crack nucleated from the mother crack propagates supersonically through the material, although the hyperelastic zone remains localized to the crack tip region.

Supersonic mode II crack propagation has been observed previously by Abraham and co-workers [11] using an anharmonic stiffening potential. However, a clearly defined hyperelastic zone could not be specified in their simulations. Our result proves that a local hyperelastic stiffening effect at the crack tip causes supersonic crack propagation, in clear contrast to the linear continuum theory. The observation of super-Rayleigh and intersonic mode I cracks, as well as supersonic mode II cracks, clearly contradicts the prediction by the classical theories of fracture.

7.5. Characteristic energy length scale in dynamic fracture

The problem of a super-Rayleigh mode I crack in an elastically stiffening material is somewhat analogous to Broberg's [30] problem of a mode I crack propagating in a stiff elastic strip embedded in a soft matrix.

The geometry of this problem is shown in Figure 7.9. Broberg [30] has shown that, when such a crack propagates supersonically with respect to the wave speeds of the surrounding matrix, the energy release rate can be expressed in the form

$$G = \frac{\sigma^2 h}{E} f(v, c_0, c_1) \tag{7.10}$$

where σ is the applied stress, E the local Young's modulus of the strip material, h is the half width of the stiff layer and f is a non-dimensional function of crack velocity v and wave speeds in the strip (c_0) and the surrounding matrix (c_1). The dynamic Griffith energy balance requires $G = 2\gamma$, indicating that crack propagation velocity is a function

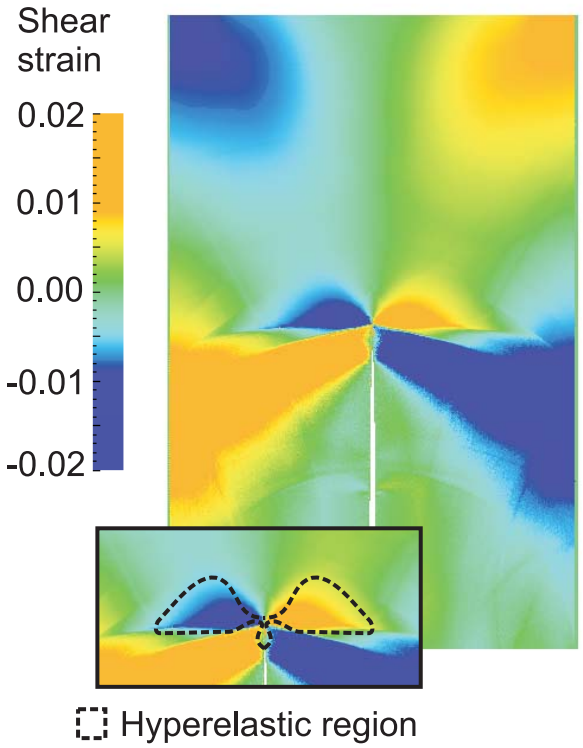

Figure 7.6.: Intersonic mode I crack. The plot shows a mode I crack in a strongly stiffening material ($k_1 = 4k_0$) propagating faster than the shear wave speed.

of the ratio h/χ where

$$\chi \sim \frac{\gamma E}{\sigma^2} \tag{7.11}$$

can be defined as a characteristic length scale for local energy flux. By dimensional analysis, the energy release rate of our hyperelastic stiffening material is expected to have similar features except that Broberg's strip width h should be replaced by a characteristic size of the hyperelastic region r_{H} (note that r_{H} could for instance be defined as the square root of the hyperelastic area, $r_{\mathrm{H}} = \sqrt{A_H}$). Therefore, we introduce the concept of a characteristic length

$$\chi = \beta \frac{\gamma E}{\sigma^2} \tag{7.12}$$

for local energy flux near a crack tip. The coefficient β may depend on the ratio between hyperelastic and linear elastic properties as well as on the dynamic energy balance. The characteristic energy length scale is defined such that h/χ equals one when the increase in crack speed is 50 % of the difference between the shear wave speed of soft and stiff material.

We have simulated the Broberg problem and found that the mode I crack speed approaches the local Rayleigh wave speed as soon as h/χ reaches values around 20. Numerous simulations verify that the scaling law in equation (7.12) holds when γ, E and σ are changed independently. The results are shown in Figure 7.10. From the simulations, we estimate numerically $\beta \approx 4.4$ and therefore $\chi \approx 38$. The potential energy field near a crack propagating at an intersonic speed is shown in Figure 7.11.

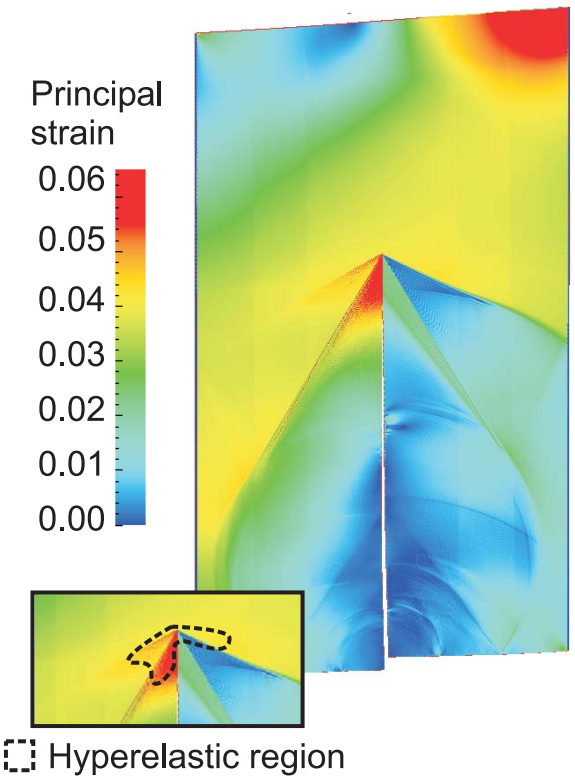

Figure 7.7.: Supersonic mode II crack. Cracks under mode II loading can propagate faster than all wave speeds in the material if there exists a local stiffening zone near the crack tip.

The transition from the limiting speed of the soft material to the limiting speed of the stiff material depicted in Figure 7.10 is reminiscent of the observations in the one-dimensional model of dynamic fracture (see Figure 4.11 (a) showing the dependence of the crack speed as a function of the potential parameter r_{on}).

The existence of a characteristic length χ for local energy flux near the crack tip has not been discussed in the literature and plays the central role in understanding the effect of hyperelasticity. Under a particular experimental or simulation condition, the relative importance of hyperelasticity is determined by the ratio r_{H}/χ. For small r_{H}/χ, the crack dynamics is dominated by the global linear elastic properties since much of the energy transport necessary to sustain crack motion occurs in the linear elastic region. However, when r_{H}/χ approaches unity, as is the case in some of our molecular-dynamics simulations, the dynamics of the crack is dominated by local elastic properties because the energy transport required for crack motion occurs within the hyperelastic region. The concept of energy characteristic length χ immediately provides an explanation how the classical barrier for transport of energy over large distances can be undone by rapid transport near the tip.

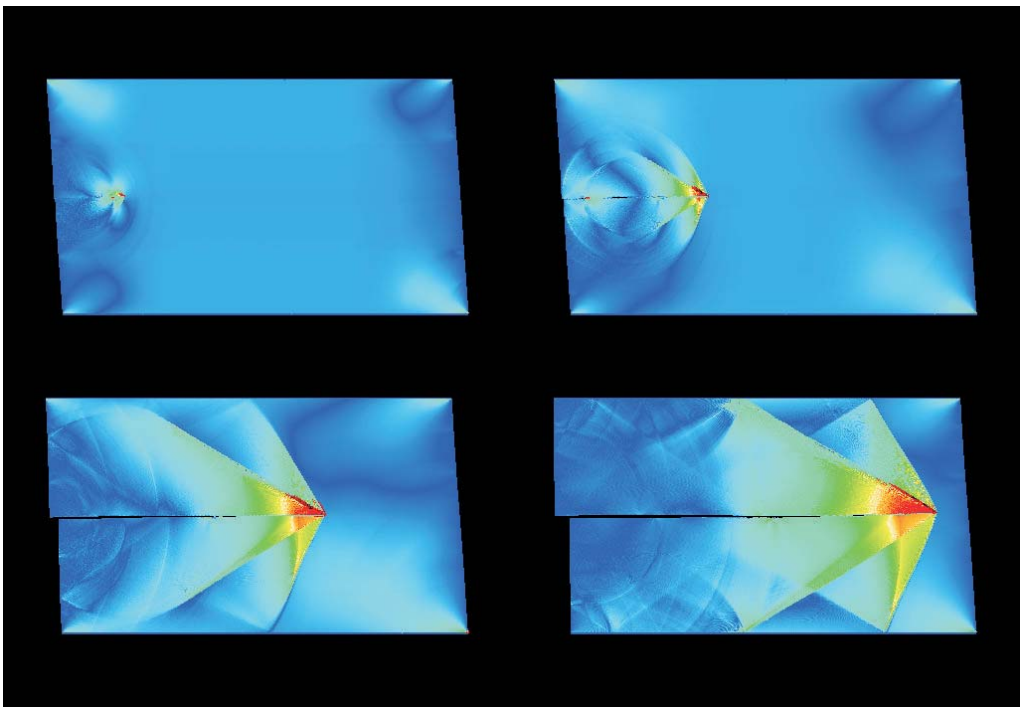

Figure 7.8.: The plot shows a temporal sequence of supersonic mode II crack propagation. The field is colored according to the σ_{xx} stress component.

7.6. Discussion

We have shown that local hyperelasticity has a significant effect on the dynamics of brittle crack speeds and have discovered a characteristic length associated with energy transport near a crack tip. The assumption of linear elasticity fails if there is a hyperelastic zone in the vicinity of the crack tip comparable to the energy characteristic length. Therefore, we conclude that hyperelasticity is crucial for understanding and predicting the dynamics of brittle fracture. Our simulations prove that even if the hyperelastic zone extends only a small area around the crack tip, there may be crucial effects on the limiting speed and the energy flow toward the crack tip, as illustrated in Figure 7.4. If there is a local softening effect, we find that the limiting crack speed is lower than in the case of harmonic solid.

Our study has shown that hyperelasticity dominates the energy transport process when the size of hyperelastic zone becomes comparable to the characteristic length

$$\chi \sim \gamma E/\sigma^2. \tag{7.13}$$

Under normal experimental conditions, the magnitude of stress may be one or two orders smaller than that under molecular-dynamics simulations. In such cases, the characteristic length χ is relatively large and the effect of hyperelasticity on effective velocity of energy transport is relatively small. However, χ decreases with the square of the applied stress. At about one percent of elastic strain as in our simulations, this zone is already on the order of a few hundred atomic spacing and significant hyperelastic effects are observed.

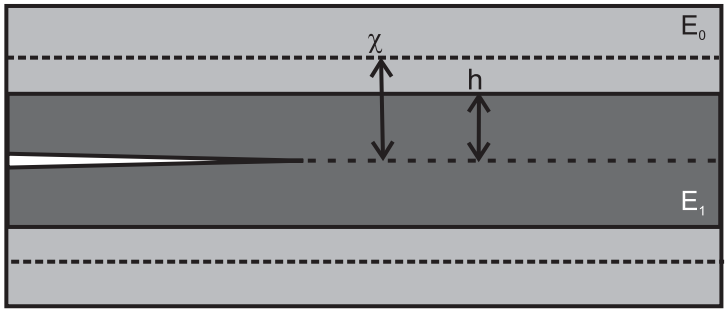

Figure 7.9.: Geometry of the Broberg problem of a crack propagating in a thin stiff layer embedded in soft matrix.

Our simulations indicate that the universal function $A(v/c_r)$ in the classical theory of dynamic fracture is no longer valid once the hyperelastic zone size r_{H} becomes comparable to the energy characteristic length χ. Linear elastic fracture mechanics predicts that the energy release rate of a mode I crack vanishes for all velocities in excess of the Rayleigh wave speed. However, this is only true if $r_{\mathrm{H}}/\chi \ll 1$. A hyperelastic theory of dynamic fracture should incorporate this ratio into the universal function so that the function should be generalized as

$$A(v/c_r, r_{\mathrm{H}}/\chi). \tag{7.14}$$

The local hyperelastic zone changes not only the near-tip stress field within the hyperelastic region, but also induces a finite change in the integral of energy flux around the crack tip.

We find that the dynamic J-integral around a super-Rayleigh mode I crack is still path-independent but no longer vanishes in the presence of hyperelasticity. Similarly, the supersonic mode II crack motion as shown in Figure 7.8 can only be understood from the point of view of hyperelasticity. A single set of global wave speeds is not capable of capturing all phenomena observed in dynamic fracture.

We believe that the length scale χ, heretofore missing in the existing theories of dynamic fracture, will prove to be helpful in forming a comprehensive picture of crack dynamics. In most engineering and geological applications, typical values of stress are much smaller than those in molecular-dynamics simulations. In such cases, the ratio r_{H}/χ is small and effective speed of energy transport is close to predictions by linear elastic theory. However, the effect of hyperelasticity will be important for nanoscale materials, such as highly strained thin films or nanostructured materials, as well as high speed impact phenomena.

Finally, we note that stimulated by the results discussed in this chapter [32], the prediction of intersonic mode I cracks (see Figure 7.6) has recently been verified in experiment [172].

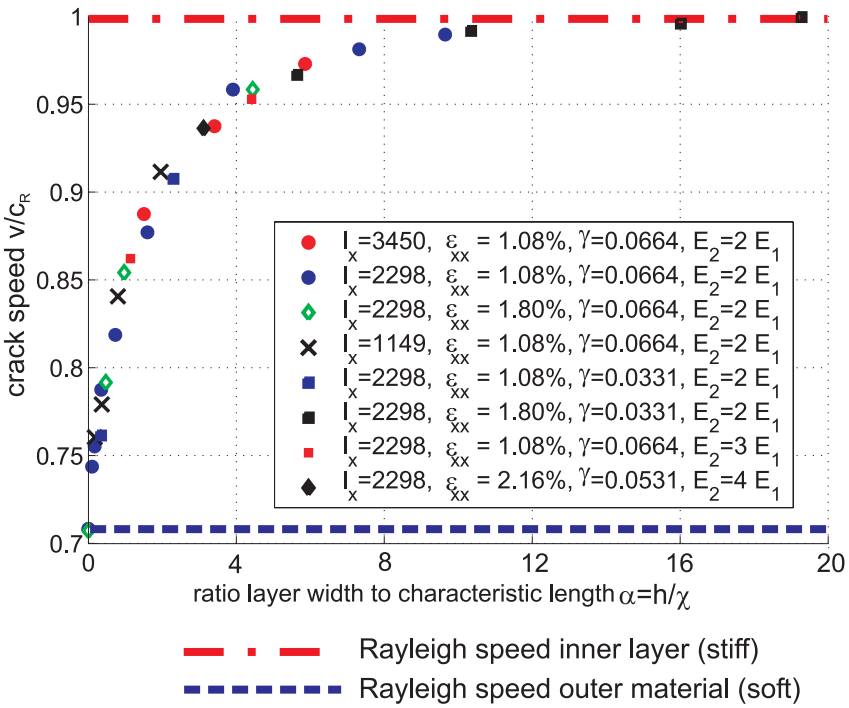

Figure 7.10.: Calculation results of the Broberg problem. The plot shows results of different calculations where the applied stress, elastic properties and fracture surface energy are independently varied. In accordance with the concept of the characteristic energy length scale, all points fall onto the same curve and the velocity depends only on the ratio h/χ.

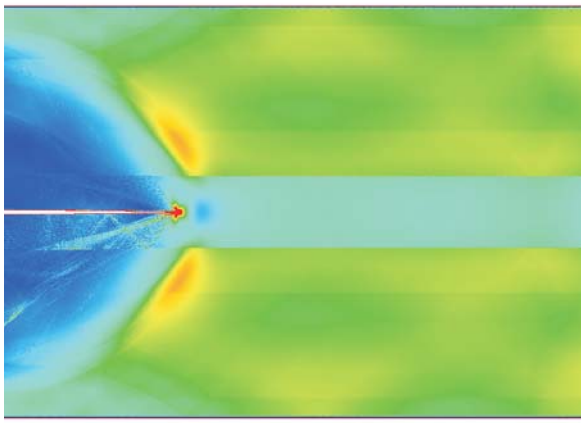

Figure 7.11.: The plot shows the potential energy field during intersonic mode I crack propagation in the Broberg problem. Since crack motion is intersonic, there is one Mach cone associated with the shear wave speed of the solid.

8. Hyperelasticity governs dynamic crack tip instabilities

In the previous chapters we limited attention to crack propagation along a weak layer serving as prescribed fracture path. Here we relieve this constraint and study crack dynamics in homogeneous materials.

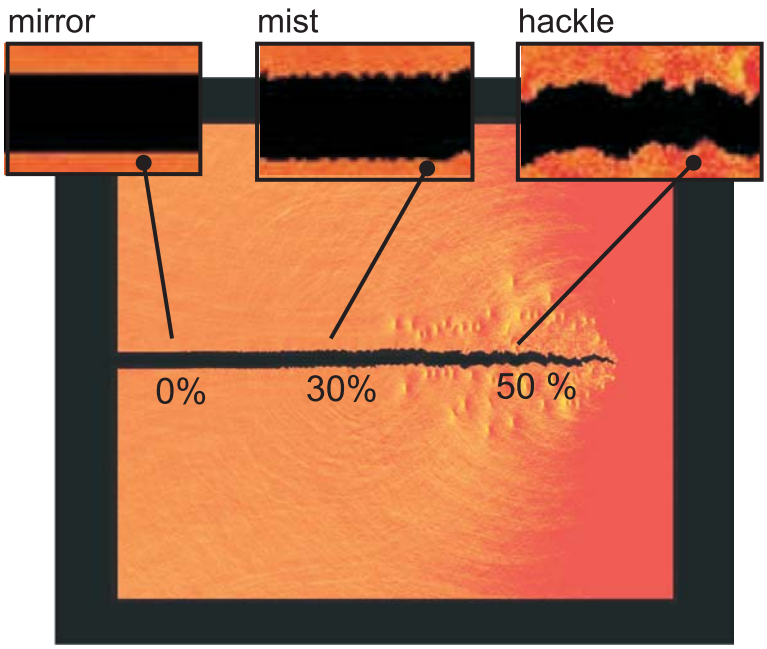

Figure 8.1.: Crack propagation in a LJ system as reported earlier in [5]. The plot shows the σ_{xx}-field and indicates the mirror-mist-hackle transition.

Cracks propagating in homogeneous materials show a very interesting dynamics: From experiment [69] and computer simulation [5, 7, 130, 129] it is known that cracks propagate straight for low speeds with perfect cleavage ("mirror"), and become unstable at higher speeds. The onset of instability results in an increasingly rough crack surface ('mist"), which becomes more intense when the crack speed increases further ("hackle"). This phenomenon was referred to as the "mirror-mist-hackle" transition. Computer simulation played an important role in this area [5], since it showed that the crack tip instability also occurs in perfect atomic lattices and is therefore not due to material imperfections. It was proposed [81, 5, 69] that the mirror-mist-hackle transition is due to an intrinsic dynamic crack tip instability.

The dynamic crack tip instability can nicely be observed in LJ systems [5, 7]. A simulation result of such a study is shown in Figure 8.1. After an initial phase where

cleavage is mirror-like, the crack surface starts to roughen at about 30 percent of the Rayleigh-wave speed. Eventually, the crack surface turns into a hackle region accompanied by emission of dislocations. The final speed of the crack is around 50 percent of the Rayleigh speed. These observations are in agreement with the results discussed in [5, 7].

8.1. Introduction

There are several models for the instability problem proposed in the literature. Some theories assume that the stress distribution ahead of the crack determines the onset of instability [246, 78, 5], while others are based on energy flow in the vicinity of the crack tip [81, 82].

In the classical literature based on linear elastic fracture mechanics, the instability was explained by the fact that the circumferential or hoop stress σ_θ [246, 78] has a maximum straight ahead of the crack at low speeds, but features two maxima in directions inclined to the crack at high crack speeds (see Figure 6.5). According to this criterion, the instability should occur at speeds around 73 % of Rayleigh-wave speed. Other suggestions were based on a perturbation analysis of the asymptotic stress field [80] that predicted unstable crack motion at 65 % of Rayleigh-wave speed, thus at a comparable speed as given by the Yoffe criterion. Both criteria predict that the crack changes to a another cleavage plane inclined about 60° to the initial crack plane.

There are two experimental and computational observations that disagree with the Yoffe criterion. Firstly, in most experimental and computational investigations, the instability establishes as wiggly crack path with crack branches inclined 30° to the initial crack plane. This is in contrast to Yoffe's prediction of an angle of 60° relative to the initial crack plane. In addition, in many experiments [69] as well as in computer simulations [5, 7] the crack tip instability was observed at speeds as low as 30 % of the theoretical limiting speed thus much lower than the theoretical prediction of 73 %.

In the literature it has been suggested that this lower critical speed for the instability may be due to hyperelastic softening around the crack tip [5, 7, 5, 81, 82]. One attempt of explanation was a nonlinear continuum analysis carried out by Gao [81, 82] focusing on the energy transport near the moving crack. The model, for the first time, allowed quantitative estimates for the instability speed. The main idea of the hyperelastic continuum mechanics analysis was that once the crack speed exceeds the speed of *local* energy transport near the crack tip (the local wave speed), the crack becomes unstable. Due to the strong softening of many materials, the speed of energy transport is significantly reduced in the vicinity of the crack tip. The theoretical analysis of the critical instability speed [81] was in consistency with the value observed in molecular-dynamics simulation for cracks propagating in LJ solids.

In contrast to Gao's analysis, Abraham and coworkers [5, 7] proposed that due to the local softening around the crack tip, the hoop stress becomes flattened at much lower speed than predicted by the linear elastic continuum theories. It was also suggested that the instability could be a consequence of lower lattice vibration frequencies in the soft region near the crack tip. It was argued that once the crack starts to see local

fluctuations of the atoms ahead of the crack tip, the crack becomes unstable. This was assumed to occur when the time for the crack to traverse one lattice distance becomes comparable to the lattice vibration period.

Despite important progress in the past, the existing literature does not provide a satisfactory explanation of the role of hyperelastic effects in the instability dynamics of fracture. We emphasize a few points:

- To our knowledge, up to date there is no systematic study showing the effect of hyperelasticity on the instability speed. In most publications, the analysis was performed only for a single potential (e.g. in [81, 5]). Also, most studies were carried out in nonlinear materials, and no comparison of the instability dynamics in linear elastic lattices with the linear continuum theory has been achieved.

- So far, only elastically softening effects were considered in the analysis. Dynamic crack tip instabilities in elastically stiffening materials have not been investigated up to date.

- An important aspect that remains unexplained as of today is the governing mechanisms for the instability. Whether the onset of instability is stress controlled as in the Yoffe picture [246] or energy controlled as in Gao's analysis [81] remains an open question.

By systematically changing the large-strain elastic properties while keeping the small-strain elastic properties constant and thus tuning the strength of the hyperelastic effect, we will show that the elasticity of large strains governs the instability dynamics of cracks. Linear elastic materials serve as reference systems for our studies, where we find that the instability speed agrees well with the predicted value from Yoffe's linear analysis [246]. Changing the strength and type of hyperelastic effect (stiffening versus softening) allows tuning the instability speed.

We will show that Gao's model of a local limiting speed can be successfully applied to predict the instability speed in softening materials. In the stiffening case, we illustrate that a generalized Yoffe model [246] helps to explain the computational results. We propose that the onset of instability is *stress controlled* in harmonic and stiffening systems and is *energy flux controlled* in softening systems.

The outline of this chapter is as follows. We start with a discussion on the direction of stable crack propagation in harmonic lattices. In agreement with the analysis described in Section 5.1.4, crack propagation is favored along the direction of lowest fracture surface energy. In accordance with Yoffe's analysis [246], cracks become unstable at a speed of about 73 % of Rayleigh-wave speed in harmonic solids. We continue with models using stiffening and softening potentials and show that the instability speed can be correlated with the strength of the hyperelastic effect: Hyperelasticity, the elasticity of large strains, plays the governing role in the stability of cracks. In softening systems, cracks become unstable at speeds significantly below the Rayleigh-wave speed, and in stiffening systems, the critical speeds for instability is shifted to higher speeds. In clear contradiction to linear elastic theory [246, 78], cracks can propagate straight up to the Rayleigh-wave speed in strongly softening solids! The simulation results are finally compared with the

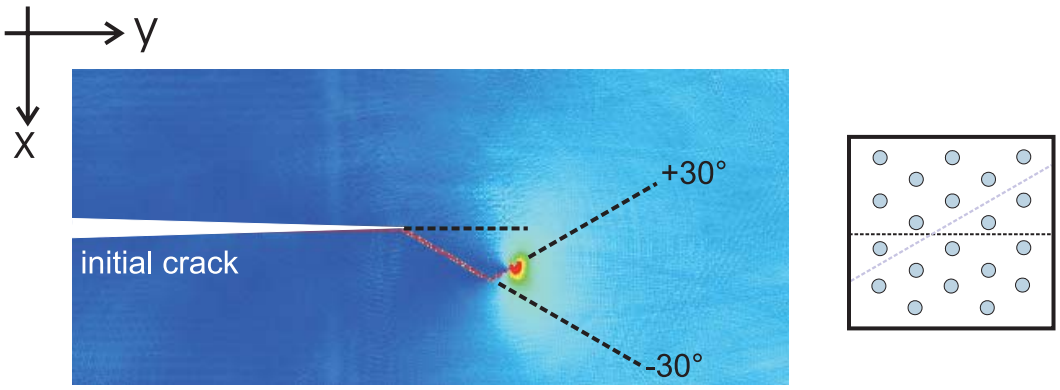

Figure 8.2.: Crack propagation in a harmonic homogeneous solid where the initial crack is oriented along the direction of high fracture surface energy, which is the y direction. As soon as the crack is nucleated, it starts to branch off at an angle of 30 degree toward the direction of low fracture surface energy.

predictions by the continuum models. In the last section of the chapter, we discuss a newly observed phenomenon of nucleation of intersonic cracks from mode I cracks moving in homogeneous materials.

8.2. Crack tip instabilities in harmonic lattices

In this section we show agreement of the linear elastic theories of continuum mechanics with atomistic simulations of cracks in harmonic lattices.

For the studies reported in this section we assume a harmonic bond snapping potential, since we want to mimic a perfect linear elastic material. The loading rate is chosen very low to ensure careful crack loading, slow acceleration and low crack speeds. The loading rate is on the order of $\varepsilon_{xx} \approx 0.000,005$. We pre-strain the slab prior to simulation in order to reduce the simulation time.

The triangular lattice features two symmetry directions. According to the discussion in Section 5.1.4, if the crack is oriented in the direction of high fracture surface energy crack propagation should not be stable and the crack should immediately branch toward the direction of lower fracture surface energy. Indeed, the results in Figure 8.2 show that in agreement with the predictions by the elastic analysis, the crack starts to branch off at an angle of 30° as soon as the crack is nucleated. Due to the symmetry in the triangular-lattice, this is the direction of lowest failure strain and low fracture surface energy. We therefore choose crack propagation along the x-direction as the reference system for the instability studies.

Figure 8.3 shows a crack moving in a harmonic lattice with snapping bonds along the direction of lowest fracture surface energy, the stable crack propagation direction. The most important result is that the crack initially propagates straight with perfect cleavage where the crack faces are atomically flat. At a velocity of about 73 % of Rayleigh-wave speed, the crack starts to oscillate and the crack surface roughens. This leads to significantly reduced propagating speeds. Comparing this result to the predictions by the continuum mechanics theories [246, 78], we find good agreement. The analysis of

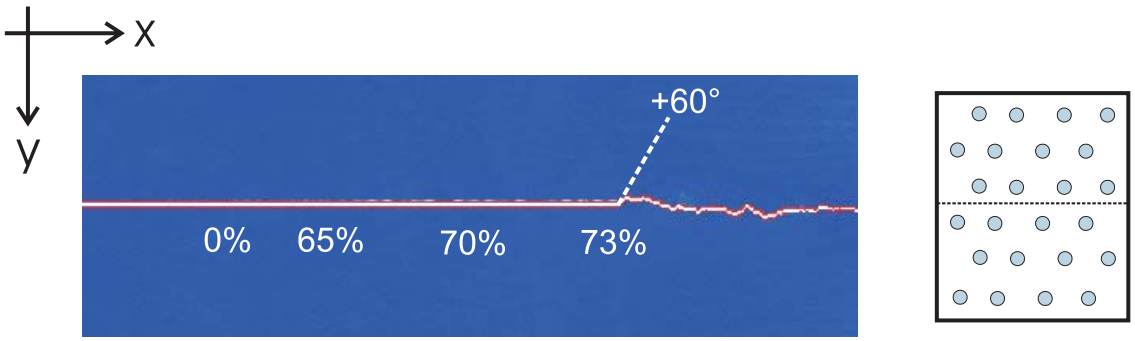

Figure 8.3.: Crack propagation in a harmonic homogeneous solid. The crack propagates along the direction with high fracture surface energy. When the crack reaches a velocity of about 73 percent of Rayleigh wave speed, the crack becomes unstable in the forward direction and starts to branch at an angle of 60° (the dotted line indicates the 60° fracture plane).

the hoop stress shown in Figure 6.5 revealed that the hoop stress becomes bimodal upon a critical speed of about 73 % of Rayleigh-wave speed.

An important observation is that at onset of instability, the crack branches at an angle of 60°. Since the hoop stress maximum is at about ±60°, this observation corroborates the notion that the hoop stress governs the instability in harmonic systems! In summary, we have shown:

- The stable crack propagation direction is the crystal orientation with the smallest fracture surface energy. This result is in agreement with the classical understanding [78].
- The instability speed in harmonic lattices agrees reasonably well with the prediction by linear elastic fracture theory. The observation of branching at an angle of 60° supports the notion that the hoop stress governs this mechanism [78].

8.3. Crack tip instabilities in biharmonic softening and stiffening lattices

To check if the assertion is correct that the large-strain elastic properties govern the critical speed for the instability, we propose to use a biharmonic potential similar, but not identical to that employed in the previous chapter: We observed that the bond snapping potential is problematic because crack acceleration is not smooth and the loading rate needs to be extremely small in order to observe the instability (otherwise see multiple cracking). Another issue is lattice trapping that results in finite minimum crack speeds [150, 104]. In particular in softening systems where the instability speed can be quite low, the crack becomes unstable very early after crack nucleation and thus the instability speed is very difficult to determine exactly.

We believe that some of these problems may be due to the "artificial" bond snapping processes. A slight modification of the potential by adding a smooth cutoff function

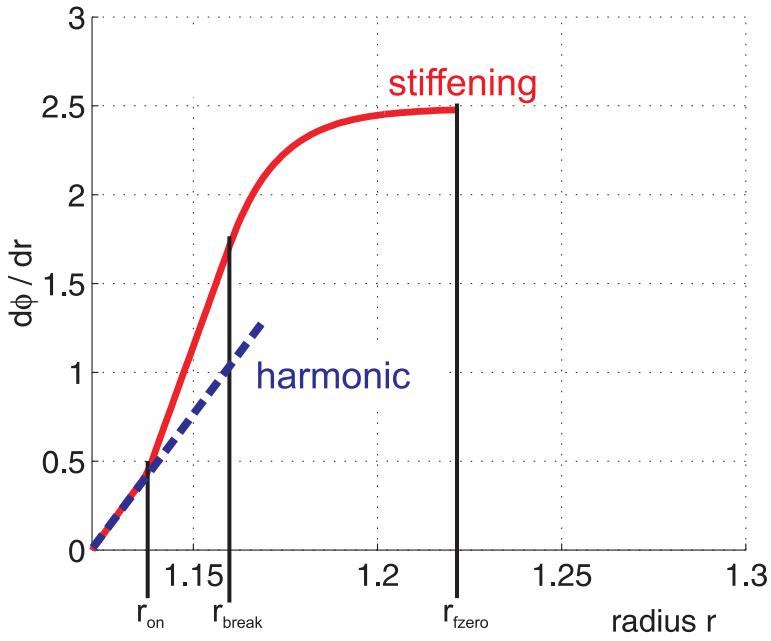

Figure 8.4.: Modified biharmonic bond snapping potential to study the dynamic crack tip instability. It is composed of a biharmonic potential discussed earlier and a smooth tail to account for smooth bond breaking and vanishing of the tangent Young's modulus at the breaking of atomic bonds. In the stiffening system, $r_{\mathrm{fzero}} = 1.22$.

helps to improve and allows for smooth crack acceleration also at higher strain rates. The atomic force versus separation is shown in Figure 8.4 for the stiffening system and the harmonic system in comparison. Another issue is the fact that all "real" materials show a softening close to bond breaking, and thus the new potential provides a refinement with respect to the original bond snapping potential.

The modified potential is given by equation (5.20) for $r < r_{\mathrm{break}}$. For $r \geq r_{\mathrm{break}}$,

$$\phi_{ij}(r_{ij}) = -\frac{A}{\exp\left(r_{ij}\xi\right)} + Br_{ij} + C \tag{8.1}$$

to model smoothly breaking bonds. The constant ξ can be chosen arbitrarily and determines how fast the bonds weaken close to separation (usually, $50 < \xi < 100$). The parameters

$$A = -\frac{k_1}{\xi^2}\exp\left(r_{\mathrm{break}}\xi\right), \tag{8.2}$$

$$B = k_1(r_{\mathrm{break}} - r_1) - \frac{A\xi}{\exp\left(r_{\mathrm{break}}\xi\right)}, \tag{8.3}$$

and

$$C = a_1 + \frac{1}{2}k_1(r_{\mathrm{break}} - r_1)^2 - r_{\mathrm{break}}B + \frac{A}{\exp\left(r_{\mathrm{break}}\xi\right)} \tag{8.4}$$

are determined from continuity of potential and force. The potential is cut off at r_{fzero} where the force drops to zero.

Besides allowing for smooth crack acceleration, another advantage of this potential is that it can be used to define a strongly softening and stiffening solid while the crack

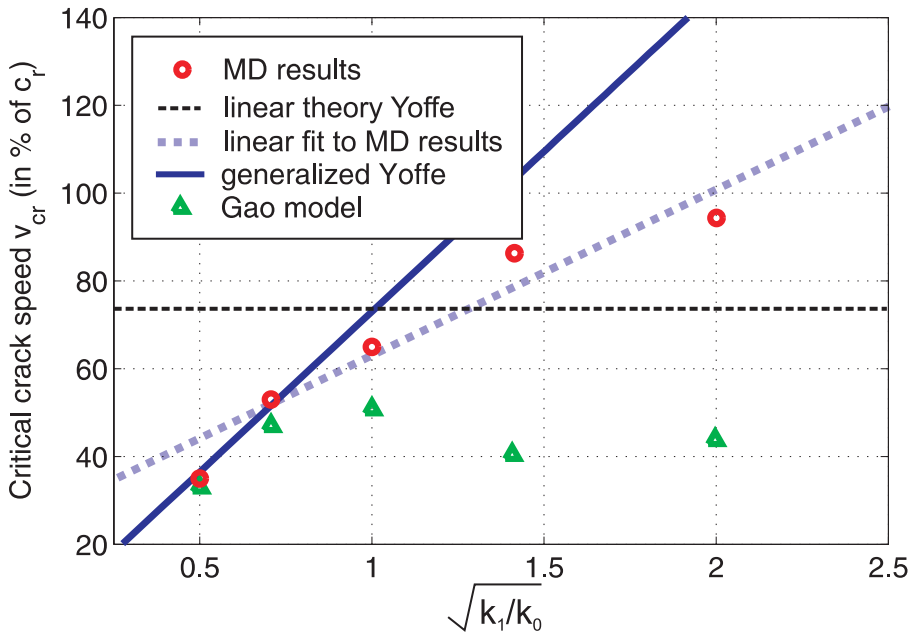

Figure 8.5.: Critical instability speed as a function of the square root of the ratios of large-strain versus small-strain spring constants. For softening materials, the prediction of instability speed by Gao's model [81] agrees well with simulation results, and for stiffening materials, the instability speed deviates from the prediction by the Gao model.

k_1/k_0	ξ	r_{break}	r_{fzero}
1/4	50	1.17	1.26
1/2	50	1.17	1.25
1	50	1.17	1.26
2	75	1.16	1.22
4	100	1.15	1.22

Table 8.1.: Choice of ξ, r_{break} and r_{rfzero} for the different simulations of the instability dynamics of cracks.

is constrained to propagate along a weak layer. For this purpose, r_{fzero} is chosen finite across a weak fracture layer and chosen much larger in the bulk. This approach allows to search for signatures of the instability by driving the crack speed far beyond the critical instability speed and then measuring the close-crack tip stress field.

We perform simulations with systematic variation of $1/4 < k_1/k_0 < 4$. In all simulations, the loading rate is chosen $\dot{\varepsilon}_{xx} = 0.000\,01$ and the loading is never stopped. We choose $r_{\text{on}} = 1.1375$ to keep the hyperelastic zone highly confined at the crack tip. The choice of ξ, r_{break} and r_{rfzero} is summarized in Table 8.1.

8.3.1. Simulation results

The main result is that depending on the ratio of k_1/k_0, the instability occurs at different speeds: In the harmonic case corresponding to $k_1/k_0 = 1$, the instability occurs at about

63 % of Rayleigh-wave speed. This is slightly lower than in the pure harmonic case (see previous section) but is explained by the softening in the potential at large strains. If $k_1/k_0 > 1$, the instability speed is shifted to velocities beyond 63 % of Rayleigh-wave speed, and if $k_1/k_0 < 1$, the instability is shifted to speeds below 63 % of Rayleigh-wave speed. Figure 8.5 shows the critical instability speed over the square root of the ratio of the large-strain versus small-strain spring constants. The plot also contains a linear fit through the MD simulation results to illustrate the dependence of the instability on the ratio $\sqrt{k_1/k_0}$.

For softening materials, the prediction of the instability speed based on Gao's model is consistent with the simulation results. For stiffening materials, the instability speed deviates from the prediction by the Gao model and lies in between the prediction by the generalized Yoffe criterion and the Gao model. The deviation of the results from the generalized Yoffe criterion is explained by the fact that even in the stiffening systems, there exists a small zone that is elastically soft (due to softening close to bond breaking). The plot also indicates the predicted instability speed according to the linear elastic Yoffe criterion. Since this model only considers the small-strain linear elastic properties, the instability speed is predicted to be independent of $\sqrt{k_1/k_0}$ and therefore constant.

The finding that cracks become unstable at speeds significantly below the Rayleigh-wave speed in softening systems is in agreement with experimental results [69] and numerical modeling in softening materials [5].

In stiffening systems, the critical speed for instability is shifted to higher speeds. In clear contradiction to linear elastic theory [246, 78], cracks can propagate straight up to the Rayleigh-wave speed in strongly softening solids!

An important observation is that the critical speed for the instability is governed by the *local* elastic properties at the crack tip (large-strain spring constant). The critical speed for the instability is independent of the crack acceleration rate. In some simulations the loading is stopped immediately after onset of crack motion. In this case no difference in the dynamics is observed and the instability occurs at the same velocity. This provides evidence that the instability is predominantly crack-speed controlled. What are the underlying mechanisms of the dynamic crack tip instability? We address this question in the forthcoming section.

8.3.2. Governing mechanism for instability

We have shown that hyperelasticity governs the critical speed of the instability. However, it remains an open question what is the governing mechanism for the onset of instability.

We hypothesize that the instability is governed by a generalized Yoffe criterion in the stiffening case, and governed by limited energy transport in the softening case.

Energy flux controlled mechanism or local limiting speed

Gao's model [81] predicts an instability speed

$$c_{\mathrm{crit}}/c_r = \sqrt{\frac{\sigma_{\mathrm{coh}}}{\rho c_r^2}} \tag{8.5}$$

Figure 8.6.: The effect of a soft and stiff zone near the crack tip on the energy flux. In softening materials, energy flux at the crack tip is reduced due to reduced local wave speeds. In contrast, energy flux is enhanced in the vicinity of the crack tip in stiffening materials.

where σ_{coh} is the maximum stress under biaxial loading. This model is based on the limitation of energy flux due to softening near the crack tip rather than considering the deformation fields.

If the crack speed exceeds the speed of energy transport near the crack tip crack motion becomes unstable. Crack motion must be subsonic on a local and a global scale! Energy flow toward the crack tip is the dominating process in softening materials and responsible for the instability.

In stiffening materials, energy transport is faster in the vicinity of the crack tip and is therefore not expected to dominate the crack stability. Once energy is transported into regions close to the crack tip, it can rapidly flow toward the crack tip and feed its forward motion. If energy flow is not responsible for the instability, the change in deformation fields is likely responsible for the instability.

Wether the instability is energy flux or deformation field controlled should have important consequences on the crack surface after the instability has occurred. If the instability is energy flux controlled, the crack should start to oscillate around its forward motion. The crack should not propagate off at inclined angles to the forward motion.

The effect of a soft and stiff zone near the crack tip on the energy flux is summarized schematically in Figure 8.6. We note that it was shown in Chapter 7 that hyperelasticity can change the local energy flux at the crack tip (see also Figure 7.2).

Generalized Yoffe criterion

Linear elastic theory assumes that the deformation field near the crack tip only depends on the ratio v/c_r. It was proposed that if $v/c_r < 0.73$, the field is of “low-inertia” character, and that for $v/c_r \geq 0.73$ the field is of “high-inertia” character [81].

In the case of a bilinear hyperelastic material, we propose to extend this view according to a suggestion in [81]. Therefore, the deformation field within the zone where large-strain elastic properties dominate depends on $v/c_{r,1}$ where $c_{r,1}$ is the local Rayleigh-wave speed associated with k_1. If the crack moves in a stiffening material, for instance, the local wave speeds are higher so that the deformation field are low-inertia on a local scale. It is obvious that the critical speed for branching would be shifted to higher speeds. The

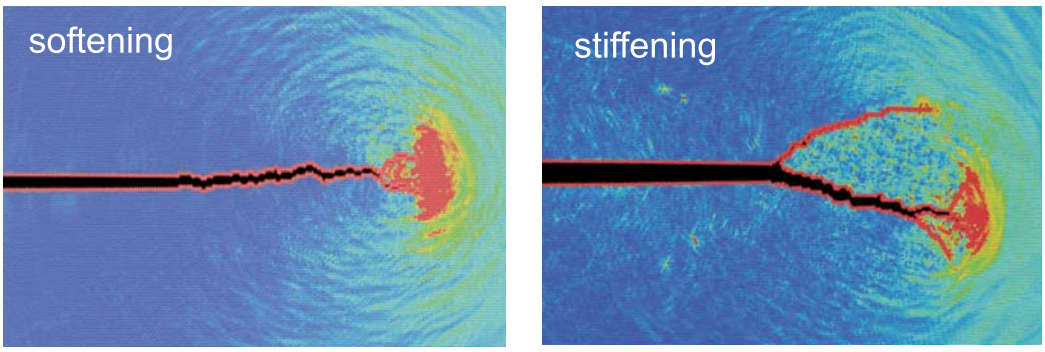

Figure 8.7.: Dynamic crack tip instability in softening and stiffening system. In the softening case, the instability establishes as roughening of the crack surface, while in the stiffening case, the instability corresponds to the nucleation of two crack branches.

critical speed according to the generalized Yoffe criterion is then given by

$$c_{\mathrm{crit}}/c_r = \beta\sqrt{\frac{k_1}{k_0}}, \tag{8.6}$$

where $\beta = 0.73$ according to the simulation results in the purely harmonic lattice.

If the crack tip instability is governed by the generalized Yoffe criterion and therefore the maximum hoop stress, the crack should branch off at the onset of instability at inclined angles with respect to the initial straight forward motion.

8.3.3. Comparison of simulation results with the proposed governing mechanisms for instability

A snapshot of the crack surface reveals some insight on the governing mechanism for the crack tip instability. Figure 8.7 shows how the crack surface changes once the critical instability speed is exceeded. In the softening case, the crack exerts slight fluctuations around its forward motion, and in the stiffening case the crack branches into two cracks in agreement with the fact that the hoop stress shows two maxima at inclined angles.

The hypothesis that the deformation field does not govern the instability in softening materials is supported by the following analysis. We investigate the hoop stress field near a strongly softening system with $k_1/k_0 = 1/4$, when the crack is constrained to propagate along a weak layer about 30 % beyond the instability speed (bonds never break in the bulk but only in the weak layer). Despite the nonlinear character of the elastic response close to the crack tip, the hoop stress agrees remarkably well with the continuum mechanics prediction corresponding to the reduced crack speed $v/c_{r,0}$ (relative to the small-strain wave speed). The hoop stress field is shown in Figure 8.8 (a), and the angular variation in combination with a comparison to continuum mechanics theory is shown in Figure 8.8 (b). This result strongly suggests that the hoop stress does not govern the onset of instability in softening materials!

In contrast to this observation in the softening case, in the stiffening case the hoop stress does show two maxima at inclined angles at the onset of the instability. The hoop stress field lags behind the continuum mechanics prediction and does not develop

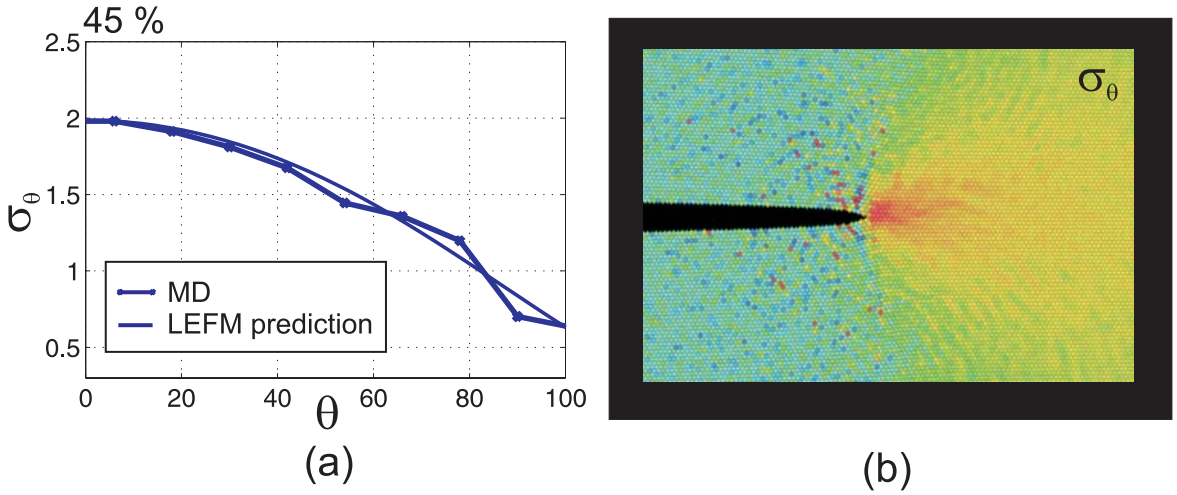

Figure 8.8.: Hoop stress near a rapidly propagating crack in a strongly softening solid ($k_1/k_0 = 1/4$) at a speed 35 % beyond the critical speed of the instability. Subplot (a) angular variation (at $r \approx 11$), (b) hoop stress field.

a bimodal structure until the crack approaches speeds close to the instability. This observation is not contradicting the notion of a local "low-inertia" zone due to material stiffening close to the crack tip in the framework of the generalized Yoffe criterion! The hoop stress analysis for different velocities is shown in Figure 8.9. The figure depicts the angular variation of the hoop stress near a rapidly propagating crack in a strongly stiffening solid ($k_1/k_0 = 4$). Acceleration effects only can not explain this observation since the loading rate and crack acceleration is rather small. The loading rate is identical as in Section 6.1.1 where excellent agreement of the hoop stress in simulation and theory is observed.

Another important point is the change in the hoop strain field. Figure 8.10 shows the angular variation of hoop strain for different crack speeds. At low speeds, there is a clear maximum of the hoop strain ahead of the crack. However, the situation changes drastically as the crack accelerates: The local maximum of the hoop strain ahead of the crack remains also at higher speeds leading to a trimodal structure. This strain distribution contradicts the single- or bimodal structure predicted by linear theory [78]. Most importantly, the crack does not get unstable until the local maximum of the hoop stress ahead of the crack starts to vanish and the maximum at 60° dominates! This analysis strongly indicates that the instability in stiffening systems is deformation field controlled.

A comparison of the molecular-dynamics results of instability speed with predictions from the generalized Yoffe criterion [246] as well as Gao's model [81, 82] of local limiting speed is shown in Figure 8.5. Equation (8.6) is used to predict the instability speed for the generalized Yoffe criterion, and equation (8.5) is used to predict the instability speed based on Gao's model. Additional simulations with different softening potentials agree well with the prediction of Gao's model. In particular, by changing the cohesive stress the shift in limiting speed is predicted correctly (results not shown here).

As predicted by our considerations, the MD results agree well with Gao's model in

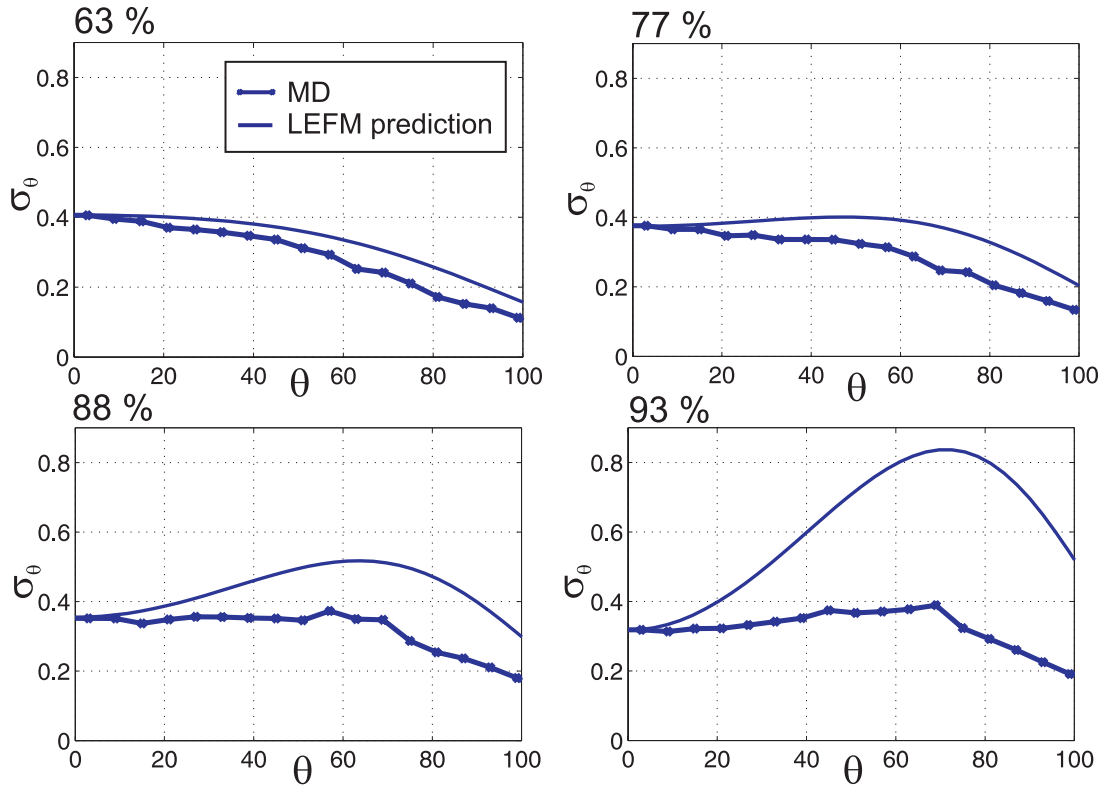

Figure 8.9.: Hoop stress field (at $r \approx 11$) near a rapidly propagating crack in a strongly stiffening solid ($k_1/k_0 = 4$). The development of the bimodal hoop stress lags behind the continuum mechanics prediction, suggesting a local "low-inertia" zone due to material stiffening close to the crack tip.

the softening cases, but deviates strongly in the stiffening case. Although the instability speed is higher than predicted by Gao's model, we observe that in the harmonic and stiffening case the agreement with the generalized Yoffe criterion is not as good. As discussed earlier, a possible reason could be that there is still a small softening zone very close to the crack tip, so that the energy flux plays at least some role.

8.4. Nucleation of intersonic shear cracks under mode I loading in harmonic lattices

In this section we address crack dynamics in unconstrained harmonic lattices with snapping bonds under high strain rates with cracks oriented in the direction of highest fracture surface energy. As we have shown in Section 8.2, crack motion along this direction is not stable. As a consequence, cracks on inclined cleavage planes will be nucleated. These cracks experience no longer pure mode I loading but also mode II loading. It is known that cracks under mode II loading can propagate at intersonic velocities. The question we address here is: can secondary intersonic daughter cracks be nucleated from cracks in unconstrained lattices under mode I loading?

The loading is applied more rapidly than in the previous sections (we choose $\dot{\varepsilon}_{xx} =$

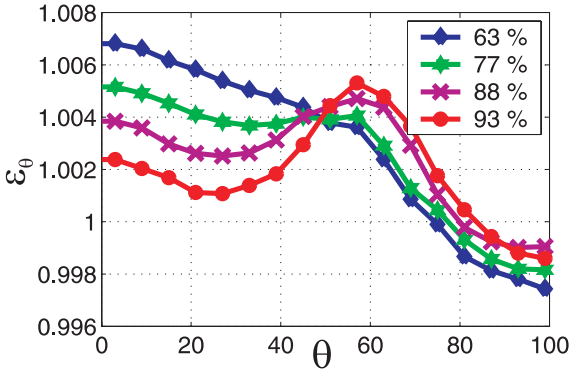

Figure 8.10.: Angular variation of hoop strain (at $r \approx 11$) near a rapidly propagating crack in a strongly stiffening solid ($k_1/k_0 = 4$). At the onset of the crack tip instability, the hoop strain features a strong maximum close to 60° (study shown corresponds to $\sqrt{k_1/k_0} = 2$, case (2) in Figure 8.5).

0.000 05), so that the final strain in the systems is a few times larger. We use the harmonic bond snapping potential.

We observe that shortly after nucleation of the crack the speed increases and approaches the critical speed of the instability. This causes the crack starting to wiggle, and due to the large energy release rate multiple cracks are nucleated. The most important observation is that from some of the numerous small cracks, daughter cracks travelling at intersonic velocities are generated! Such cracks are perfectly straight and no crack tip instability is observed. Such intersonic cracks nucleated from mode I cracks in harmonic lattices are shown in Figure 8.11. To our knowledge, this phenomenon has not been reported in the literature.

This observation is in agreement with the concept that inclined cracks are not under pure mode I loading but also feature mode II loading. The assertion of nucleation of daughter cracks moving at intersonic velocities from mother cracks is supported by the simulation results [83]. Figure 8.11 reveals that the intersonic daughter cracks all propagate along 30° inclined planes, thus moving along the plane of low fracture surface energy. In summary, there is a strong tendency to nucleate secondary daughter cracks at intersonic velocities along cleavage planes with low fracture surface energy.

8.5. Discussion and summary

In this chapter we investigated the dynamics of crack tip instabilities. We find that the onset of the instability is governed by a critical crack speed, the instability speed. This agrees with earlier reports that cracks feature an intrinsic dynamic instability [78, 5, 150, 81]. The most important result of this chapter is that hyperelasticity, the elasticity of large strains governs the instability speed. By keeping the small-strain elastic properties constant and systematically changing the large-strain elasticity, we demonstrated that the instability speed can be tuned to higher and lower values.

An important consequence of the results is that linear elastic theory can not be applied to describe the instability dynamics in nonlinear materials. Since most real materials

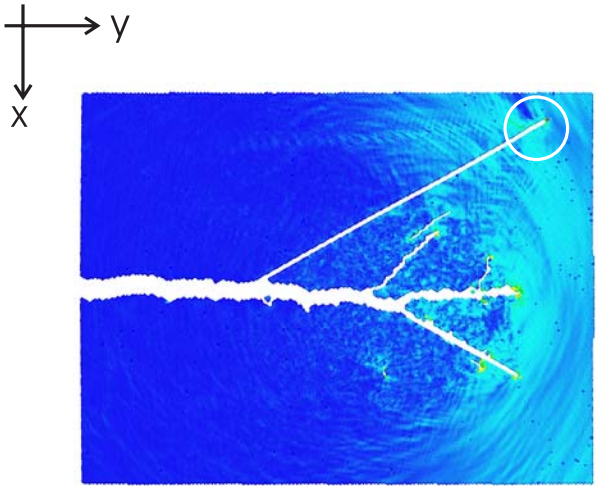

Figure 8.11.: Unconstrained fracture in a harmonic solid. The plot illustrates propagation of intersonic cracks nucleated from mode I cracks at off-angle direction. An intersonic crack is highlighted by a white circle.

show nonlinearities at large strains, linear elastic theory can not be applied to describe crack dynamics in real materials!

Our results are in agreement with the hypothesis that the *local* wave speed near the crack tip governs the dynamics [81]. This also explains experimental [69] and other computational results [5, 7]. We summarize the main findings.

- Cracks in purely harmonic lattices with the harmonic bond snapping potential move straight as long as the propagation speed is below about 73 % of the Rayleigh-wave speed. This finding is in agreement with the classical theory proposed by Yoffe [246]. This matches the results shown in Figure 6.5 where it was demonstrated that this is the crack speed where the hoop stress develops a bimodal structure.

- Large-strain elastic properties and therefore the *local* wave speeds dominate the instability dynamics. This result could be verified in Figure 8.5 where a correlation of the instability speed to the local wave speed is shown.

- With respect to the governing mechanism of the dynamic crack tip instability, the stiffening and softening case need to be distinguished. In softening systems, the reduction in local energy flow governs the instability, and in stiffening systems, the change in deformation field near the crack tip is responsible.

  - In softening materials, limitation of energy flow toward the crack tip is the dominating process and therefore responsible for the instability (see Figure 8.6). This hypothesis was supported by an analysis of the hoop stress field showing that the hoop stress is *not* bimodal close to the crack tip at the onset of instability.
  - In stiffening materials, energy transport is faster in the vicinity of the crack tip and is therefore not mainly influencing the crack stability (see Figure 8.6).

	governing mechanism	
	deformation field	reduced energy transport
harmonic	×	
stiffening	×	
softening		×

Table 8.2.: Governing mechanism for the crack tip instability in the harmonic, stiffening and the softening case.

In this case, the change in deformation field is responsible for the onset of the instability. As shown in Figure 8.9, the hoop stress does not get bimodal up to speeds beyond 93 % of Rayleigh-wave speed. The change in hoop stress and development of a maximum at inclined angles with respect to the straight crack direction could be correlated with the onset of instability.

The different failure mechanisms in the harmonic, stiffening and softening case are summarized in Table 8.2.

- As shown in Figure 8.11 and highlighted by a white circle, intersonic daughter cracks can be nucleated from sub-Rayleigh mode I mother cracks on the planes with lowest fracture surface energy. This failure mode has, to our knowledge, not been described before.

Hyperelasticity, the elasticity of large strains, governs dynamic crack tip instabilities. This explains the discrepancy of measured instability speeds in "real materials" [69] and predicted instability speeds by linear elastodynamic theory [78]. The reason is that virtually all real materials show a strong softening close to materials failure. There has been a discussion whether hyperelasticity [5, 81] or the existence of microcracks or other material imperfections [70] are responsible for crack tip instabilities. Our simulation results suggest that (1) the crack tip instability is an intrinsic dynamic phenomena, and (2) the crack tip instability is not due to microcracking but instead governed by the large-strain elastic properties.

Our simulation results are in qualitative agreement with experimental results of crack tip instabilities at speeds as low as one third of the Rayleigh-wave speed [69, 70]. We note that experiments for instabilities in stiffening materials are yet to be performed. However, recent observation of intersonic mode I cracks in *homogeneous* materials [172] are not contradicting the notion that stiffening material response tends to stabilize straight crack motion.

The main result of this chapter was to show that the instability speed is shifted to lower crack velocities in softening systems, and shifted to higher velocities in stiffening systems. However, there are several questions that remain yet to be answered. For instance, preliminary results suggest that the choice of the potential parameters also influences the instability speed. For instance, when the parameter r_{break} is changed from 1.15 to 1.16 in the case when $k_1/k_0 = 4$ while all other parameters remain constant, the crack propagates straight up to super-Rayleigh speed (105 % of c_r) until the instability

sets in! Future research in this field could therefore focus on the impact of the potential shape at large strains (e.g. variation of the parameter ξ or r_{break}). Such research could elucidate some of the fundamental atomic mechanisms of crack advancement and bond breaking, and help to develop better potentials to model fracture.

9. Cracks at interfaces

In this chapter we study cracks propagating along interfaces between two dissimilar materials, as schematically shown in Figure 9.1. Cracks at interfaces are technologically important, since the bonding between two dissimilar materials as for instance between epoxy and aluminum is usually weak and serves as a potential failure initiation point of a structure. Our atomistic model featuring the weak layer could be regarded as an idealization of such cases. Another important field where interfaces between dissimilar materials play an important role is the dynamics of earthquakes.

Figure 9.1.: Geometry of the simulations of cracks at bimaterial interfaces.

Several theoretical studies were carried out on cracks in dissimilar media [180, 177, 58]. Most of the early investigations focused on static cracks. One of the interesting features of the elastic interfacial crack problem is the characteristic oscillating stress singularity that was determined by Williams [156]. This theoretical finding is incompatible with real materials since the crack faces would penetrate each other at the crack tip. The stress intensity factor is complex-valued for interfacial cracks and it is generally difficult to define a crack nucleation criterion based on the Griffith condition [180].

In recent years, the dynamics of cracks along dissimilar interfaces was increasingly researched. For instance, the asymptotic stress field near dynamic cracks at bimaterial interfaces was studied [244, 145]. The analysis discussed in [244] assumed steady-state crack propagation and provided the spatial structure of square-root singular stress field very close to the dynamic crack tip. The analysis led to definition of a complex dynamic stress intensity factor. Later, this analysis was refined relaxing the steady-state assumption and including higher order terms [145].

There are also experimental results available on interfacial cracks, as for instance studies reported in [141, 182, 183] of cracks propagating along interfaces of PMMA and metals. In [141], the researchers focused on the development of a crack growth criterion along interfaces. They also compared the experimental results with theoretical predictions of the stress field near the crack tip. Crack speeds that exceeded that of the shear wave speed of the soft PMMA material were observed.

However, very few molecular-dynamics simulations of dynamic fracture along bimaterial interfaces have been reported. One example is recent molecular-dynamics simulations of mode II cracks along a weakly bonded interface of harmonic-anharmonic materials (material defined by a harmonic potential neighboring a material defined by a tethered LJ potential) [11].

In summary, for cracks at interfaces, existing theory and experiment predicts that

- The limiting speed of mode I cracks at bimaterial interfaces can exceed the Rayleigh-wave speed of the soft material [145, 144]. However, intersonic or supersonic crack propagation with respect to the soft material layer is not predicted by theory and has not been observed in experiment.

- The limiting speed of mode II cracks is given by the longitudinal wave speed of the stiff material and the crack speed can thus be truly supersonic with respect to the soft material [182].

The most important research objective of our studies is the limiting speed of cracks: The fact that the wave speed changes discontinuously across the interface makes it difficult to define a unique wave speed near the interface, and thus difficult to predict the limiting speed of the crack. Using molecular-dynamics, can we determine what is the limiting speed of a crack along dissimilar materials?

In mode II cracks, in an earlier study a mother-daughter-granddaughter mechanism was observed through which the crack finally approached a velocity faster than the longitudinal wave speed of one of the layers [11]. In this setup, however, one of the half spaces was modeled by harmonic interactions, and the other was modeled by a tethered LJ potential. Although this setup constitutes an interface of different materials, the wave speeds associated with each half space could not be clearly defined since one of the material was hyperelastic. To obtain a more clean model of cracks at interfaces, we propose to study two half spaces with harmonic interatomic potentials, but with different spring constants $k_0 < k_1$. The ratio

$$\Xi = \frac{k_1}{k_0} \tag{9.1}$$

measures the elastic mismatch of the two materials, and the wave speeds are thus different by a factor $\sqrt{\Xi}$.

The plan of this chapter is as follows. We start with simulations of mode I cracks along interfaces and show that under sufficiently large loading, the crack approaches the Rayleigh wave speed of the stiffer of the two materials via a mother-daughter mechanism. We continue with a study of mode II cracks along interfaces. We show that a mother-daughter-granddaughter mechanism, in agreement with previous analyses [11], exists and allows the crack to approach the longitudinal wave speed of the stiffer of the two materials. We finally discuss the simulation results and compare the elastic fields of the mode I crack with the solution of continuum mechanics results and the results of atomistic modeling as reported earlier in this thesis.

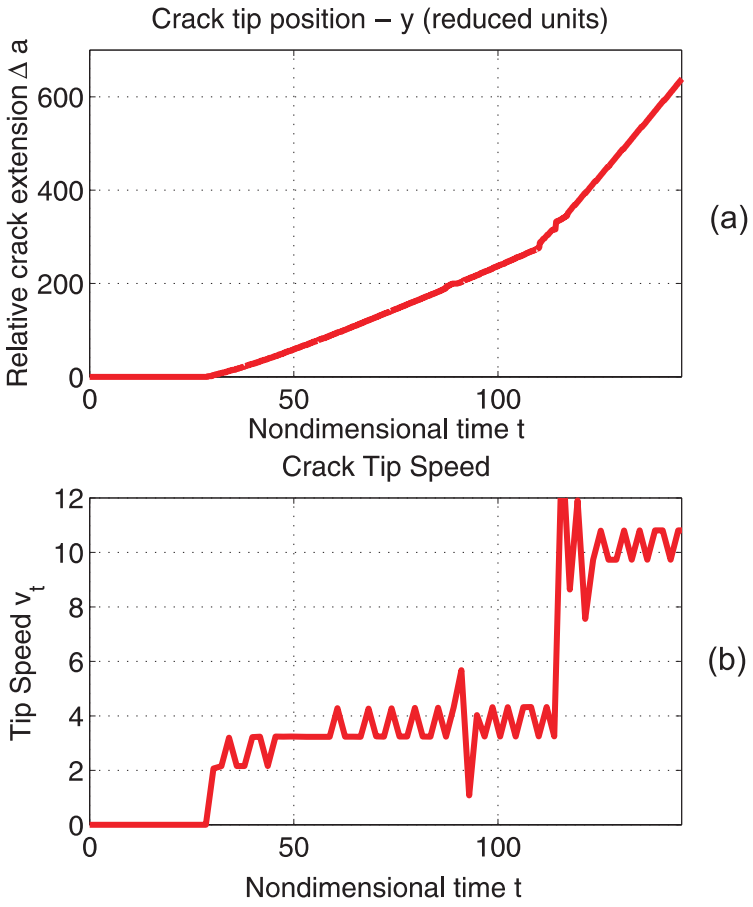

Figure 9.2.: Crack tip history and crack velocity history for a mode I crack propagating at an interface with $\Xi = 10$. Subplot (a) shows the crack tip history, and subplot (b) shows the crack tip velocity over time. A secondary daughter crack is born propagating at a supersonic speed with respect to the soft material layer.

9.1. Mode I cracks at bimaterial interfaces

In the simulations, the left part of the slab is the stiff solid, while the right part has lower Young's modulus and is soft. We consider the case when the elastic mismatch is $\Xi = 10$. For comparison, the elastic mismatch as between PMMA and aluminum is about 15. Figure 9.2 (a) shows the crack tip history, and Figure 9.2 (b) shows the crack tip velocity over time. The crack nucleates at time $t \approx 35$, and quickly approaches the Rayleigh speed of the soft material $v \to c_{r,0} \approx 3.4$. As loading is increased, the crack speed increases slightly and becomes super-Rayleigh. We observe a large jump in the crack velocity at $t \approx 110$, when a secondary crack is nucleated which quickly approaches the Rayleigh speed of the stiff material $v \to \sqrt{\Xi} c_{r,0} \approx 10.7517 > c_{l,0} \approx 6.36$. The secondary crack is nucleated approximately at a distance $\Delta a = 11$ ahead of the mother crack and propagates with Mach 1.7 through the material! Nucleation of secondary cracks under mode I loading is only found under high-strain rate loading ($\dot{\varepsilon}_{xx} = 0.000\,05$). If the strain rate is too low, the crack moves at a super-Rayleigh speed until the solid has separated.

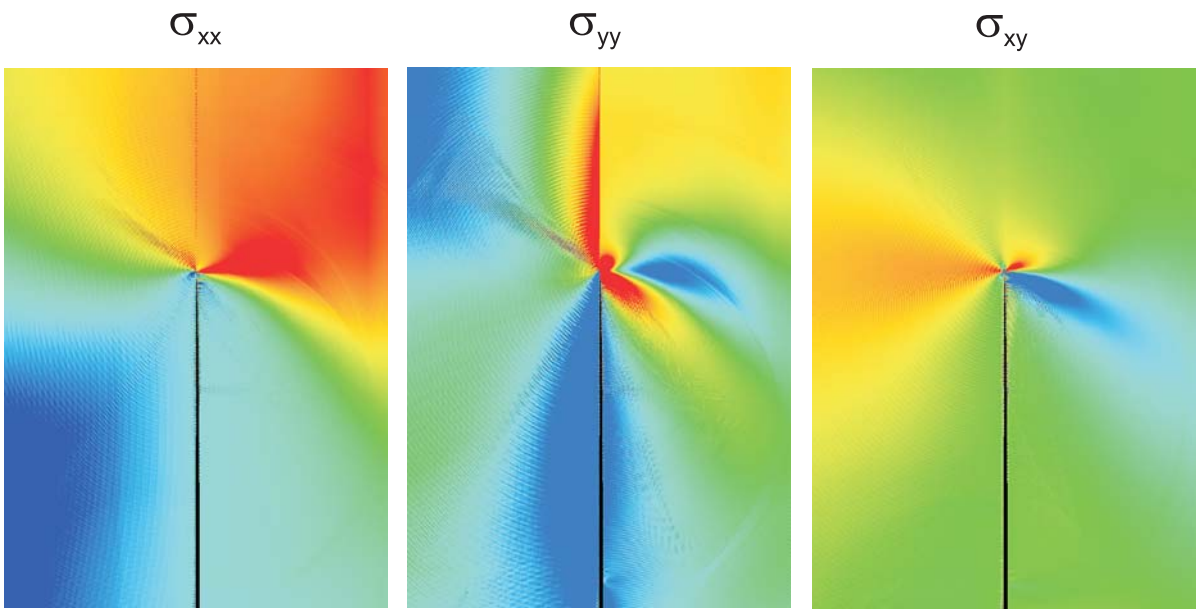

Figure 9.3.: The plot shows the stress fields σ_{xx}, σ_{yy} and σ_{xy} for a crack at an interface with elastic mismatch $\Xi = 10$, before a secondary crack is nucleated. In contrast to the homogeneous case, the deformation field is asymmetric. The red color corresponds to large stresses, and the blue color to small stresses.

The mechanism of nucleation of a secondary crack is reminiscent of the mother-daughter mechanism, a phenomenon so far only observed in cracks under mode II loading.

The result suggests that at a bimaterial interface, mode I cracks under very large loading can propagate with the Rayleigh speed of the stiffer materials, and cracks can reach speeds beyond the fastest wave speeds in the soft material. This observation is surprising and has not been reported in experiment so far [183]. In experimental studies of mode I cracks along interfaces, the crack slightly exceeds the Rayleigh speed of the soft material but is never observed to become intersonic or supersonic.

Figure 9.3 shows the stress field, and Figure 9.4 the particle velocity field before the secondary crack is nucleated. At the time the snapshots are taken, the crack propagates at a super-Rayleigh speed through the material. Since crack motion is subsonic, no shock front is established.

Figure 9.5 shows the potential energy field for a crack after the secondary crack is nucleated and crack motion of the daughter crack is supersonic. Figures 9.6 and 9.7 show the stress field and the particle velocity field. The secondary crack propagates supersonically through the material and the Mach cones in the right half space (soft material) is clearly visible.

The mother-daughter mechanism in mode I cracks at interfaces is also observed for elastic mismatch $\Xi = 2$, $\Xi = 5$, $\Xi = 7$ and $\Xi = 10$ (note that not in all cases crack motion is supersonic with respect to the soft material since the Rayleigh-wave speed of the stiff material is smaller than the longitudinal wave speed of the soft material).

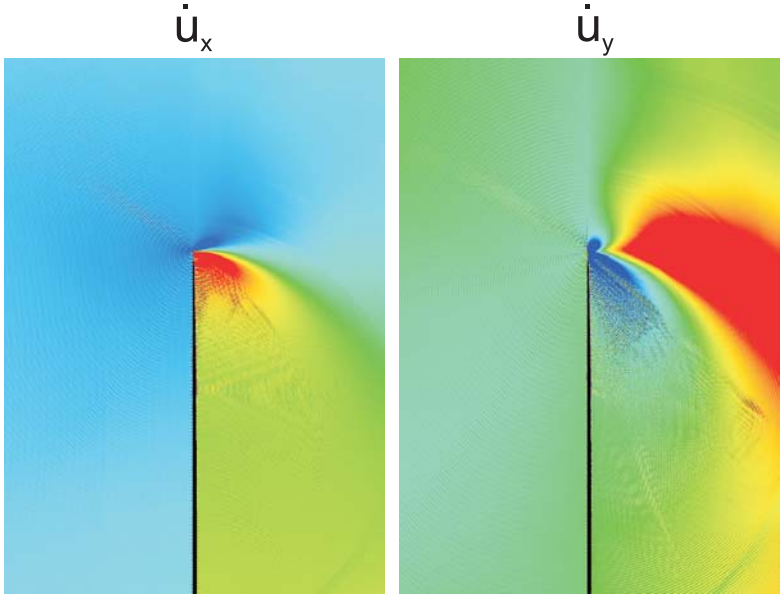

Figure 9.4.: The plot shows the particle velocity field (a) $\dot{u}_x$ and (b) $\dot{u}_y$ for a crack at an interface with elastic mismatch $\Xi = 10$, before a secondary crack is nucleated. The asymmetry of the particle velocity field is apparent.

9.2. Mode II cracks at bimaterial interfaces

For the studies of mode II cracks along interfaces we choose $\Xi = 3$. The crack tip history is depicted in Figure 9.8. The loading rates are $\dot{\varepsilon}_{xx} = 0.000\,03$ for slight mode I opening loading and for the shear loading $\dot{\varepsilon}_{xy} = 0.000\,125$.

Initially, the (mother) crack propagates close to the Rayleigh velocity of the soft slab part ($v \approx 4.8$). After a secondary daughter crack is born travelling at the longitudinal wave speed of the soft material, a granddaughter crack is born at the longitudinal wave speed of the stiff material. The granddaughter crack propagates at a supersonic speed with respect to the soft material layer. If the loading is stopped after the granddaughter crack has nucleated, this velocity is maintained until the whole slab is cracked. For a choice of $\Xi = 2$, the qualitative behavior is the same. In Figure 9.9 (a) we depict the potential energy field near a supersonic mode II crack along a bimaterial interface. We mark the different cracks: (A) is the mother crack, (B) is the daughter crack and (C) refers to the granddaughter crack. Figure 9.9 (b) shows a schematic of the allowed limiting speeds and the observed jumps in crack speed.

The stress fields for two different instants in time are shown in Figure 9.10. Figure 9.10 (a) shows the stress field before nucleation of the daughter crack, and Figure 9.10 (b) shows the stress field after nucleation of the granddaughter crack. Figure 9.10 (c) shows a magnified view into the crack tip region.

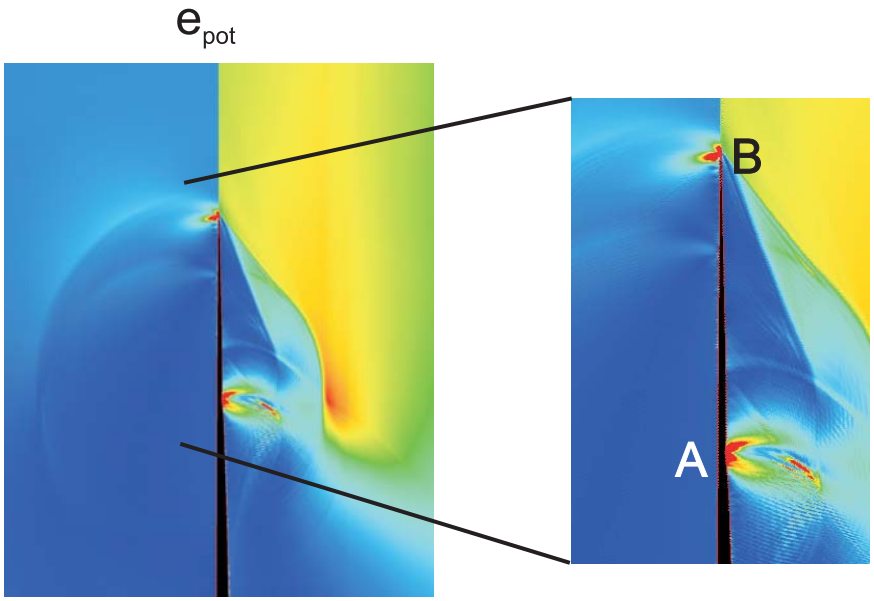

Figure 9.5.: The plot shows the potential energy field for a crack at an interface with elastic mismatch $\Xi = 10$. Two Mach cones in the soft solid can clearly be observed. Also, the mother and daughter crack can be seen. In the blow-up on the right, the mother (A) and daughter crack (B) are marked.

9.3. Discussion

The studies reported in this section show that cracks at interfaces show a very different dynamics than cracks in homogeneous materials. At the interface, the limiting crack speed is not well-defined any more since the wave velocities change discontinuously across the interface. Both mode I and mode II cracks can propagate supersonically with respect to the wave speeds in the soft material. We summarize the main findings.

- In Mode I, we observe that the limiting speed of cracks at bimaterial interfaces is the Rayleigh-wave speed of the stiff material. We observe nucleation of a secondary daughter crack from the primary mother crack. Supersonic crack motion with respect to the soft layer is possible, and the mother-daughter crack mechanism is reminiscent of the observations in mode II cracks in the homogeneous case. This is a new phenomenon in dynamic fracture not reported in the literature. It is also in contrast to published experimental results [183]. Preliminary continuum mechanics analysis stimulated by our atomistic simulation results provides theoretical evidence that this dynamical phenomena is possible. The analysis revealed that the energy release rate is positive for crack motion close to the Rayleigh-speed of the stiff material [42].

- In mode II, we observe that the limiting speed is the longitudinal wave speed of the stiff material. Supersonic crack motion with respect to the soft layer is possible, and the we observe a mother-daughter-granddaughter mechanism [11]. This is reminiscent of computer simulations reported previously. Our results also confirm theoretical [145] as well as experimental results [182].

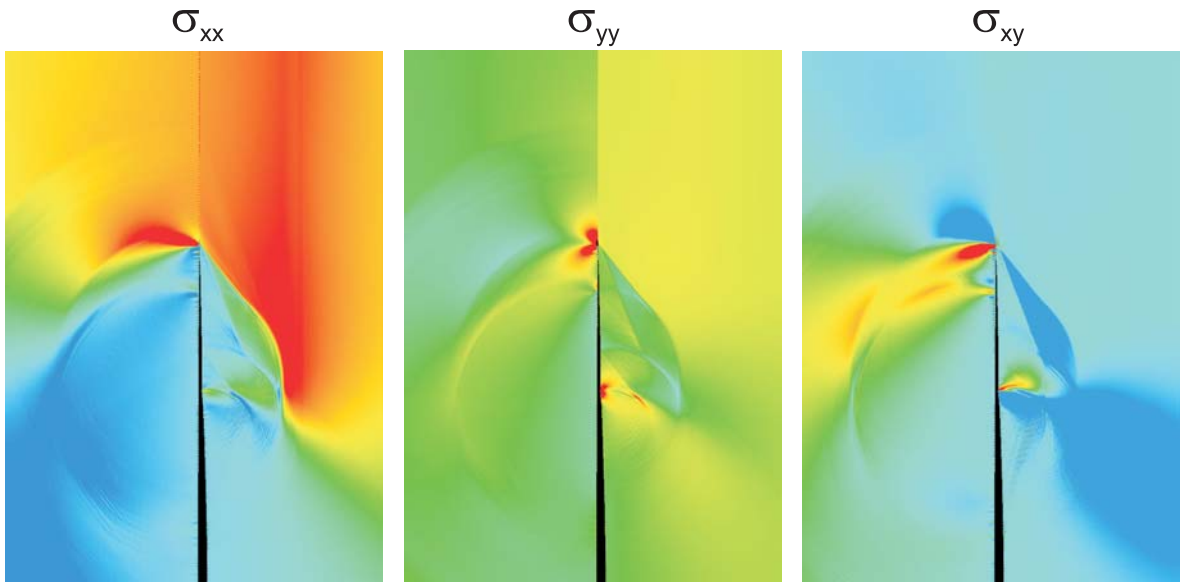

Figure 9.6.: The plot shows the stress fields σ_{xx}, σ_{yy} and σ_{xy} for a crack at an interface with elastic mismatch $\Xi = 10$. In all stress fields, the two Mach cones in the soft material are seen. The mother crack appears as surface wave behind the daughter crack.

- The elastic fields in mode I and mode II cracks establish very differently from homogeneous materials. If crack propagation is supersonic with respect one of the half spaces, multiple shock fronts are observed as shown in Figure 9.10. If the elastic mismatch is small or nucleation of daughter cracks is suppressed in mode I cracks, the elastic fields in the left and right half are asymmetric. The asymmetric shape of the asymptotic deformation fields matches the predictions by continuum mechanics theories [145].

Atomistic simulations are a feasible approach to study the dynamics of cracks at interfaces. Future investigations could focus on the comparison of the asymptotic stress field in simulation and theory, as well as on a more detailed and theoretical analysis of the observed mother-daughter and mother-daughter-granddaughter mechanisms, particularly focusing on the nucleation process of secondary cracks.

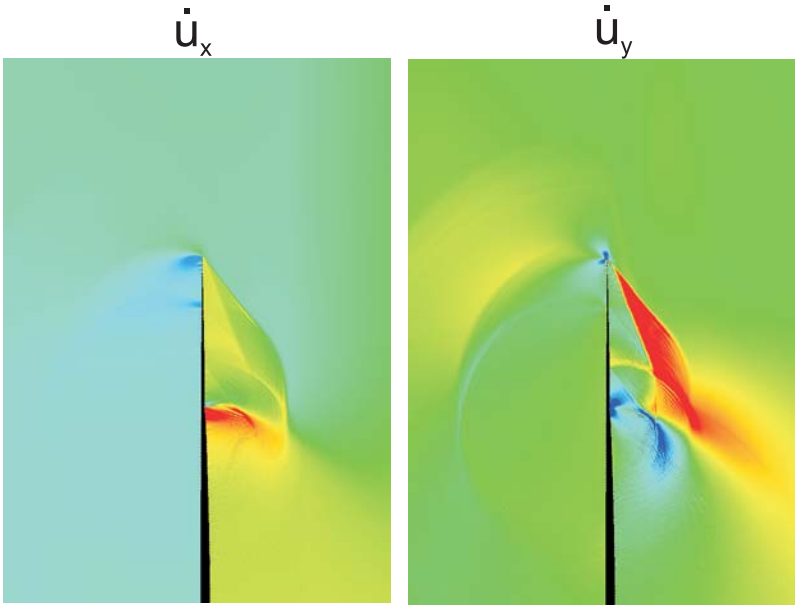

Figure 9.7.: The plot shows the particle velocity field (a) $\dot{u}_x$ and (b) $\dot{u}_y$ for a crack at an interface with elastic mismatch $\Xi = 10$. The shock fronts in the soft solid are obvious.

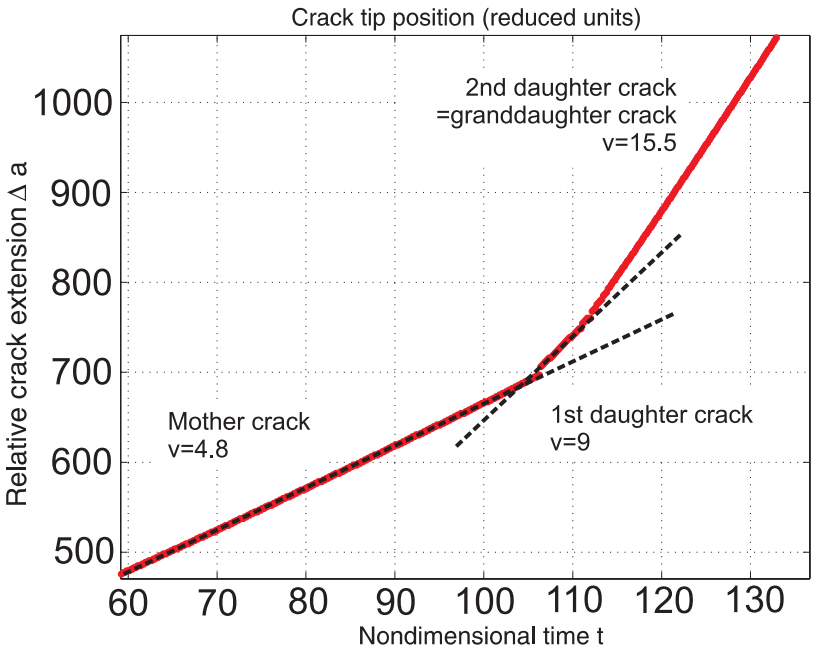

Figure 9.8.: Crack tip history for a mode II crack propagating at an interface with $\Xi = 3$. The plot illustrates the mother-daughter-granddaughter mechanism. After a secondary daughter crack is born travelling at the longitudinal wave speed of the soft material, a granddaughter crack is born at the longitudinal wave speed of the stiff material. The granddaughter crack propagates at a supersonic speed with respect to the soft material layer.

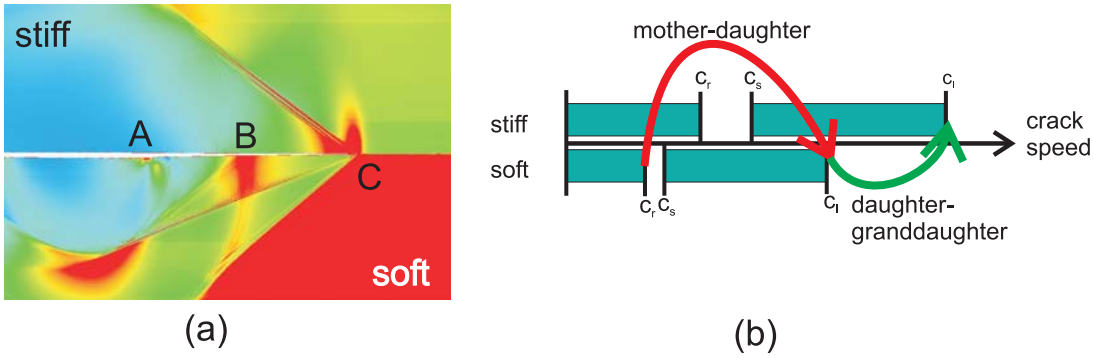

Figure 9.9.: Supersonic mode II crack motion at a bimaterial interface. Subplot (a): Potential energy field of a mode II crack at a bimaterial interface with $\Xi = 3$, supersonic crack motion. (A) mother crack, (B) daughter crack and (C) granddaughter crack. Subplot (b): Allowed limiting speeds and the observed jumps in crack speed.

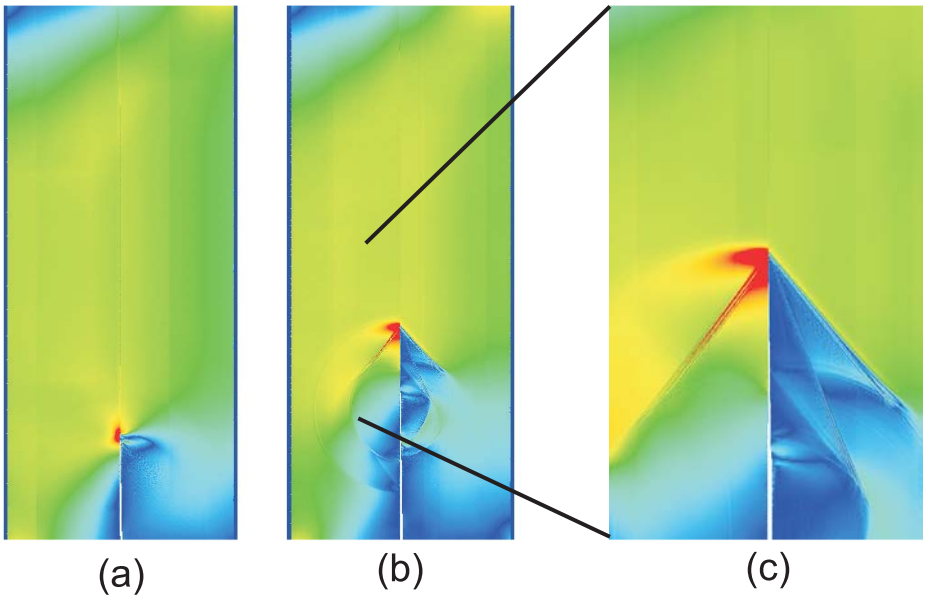

Figure 9.10.: The plot shows the σ_{xx} field of a mode II crack at a bimaterial interface with $\Xi = 3$. Subplot (a) and (b) are consecutive time steps, and subplot (c) is a blowup.

10. Suddenly stopping cracks

This chapter addresses the following question: "What happens if a crack propagating at very high velocities suddenly comes to rest?" We all know that if we try to stop a heavy object like a car, we feel considerable resistance due to its inertia. How does a crack stop? Does the crack carry properties like "inertia" or mass? The research in the last decades has shed light on these fundamental questions about the nature of fracture. It was found that the stress field at the crack immediately responds to changes in loading condition or fracture surface energy for velocities lower than or equal to the Rayleigh wave speed. This result led to the terminology of the crack being "mass less", because it responds *instantaneously* to a change in crack driving force. If we turn back to the analogy of stopping a heavy object, this implies that we could stop it instantly from any velocity without feeling any resistance, and the object would react to any applied force immediately without delay. In this chapter, we carry out large-scale atomistic simulations to focus on the atomic details of the dynamics of suddenly stopping cracks.

10.1. Introduction

Large-scale atomistic simulations are used to study suddenly stopping cracks under mode I (tensile) as well as mode II (shear) loading conditions. The crack velocity, denoted as v, is related to the crack tip position a by $v = \dot{a} = \mathrm{d}a/\mathrm{d}t$. The time history of the crack tip velocity is arranged to be

$$v = v^* - v^* H\left(t - t_{\mathrm{stop}}\right). \tag{10.1}$$

where t denotes the time, and $H(s)$ is the unit step function. The variable v^* stands for the constant propagation velocity which corresponds to the limiting velocity of cracks in our simulations. As shown by equation (10.1), we study a crack that propagates at its limiting speed up to time t_{stop} and then suddenly stops. The reason for crack stopping could, for example, be that the resistance of the material to fracture increases dramatically. This problem is important for constructing solutions for nonuniform crack growth [78, 75, 62], and for understanding crack propagation in materials with changing resistance to fracture.

The limiting speed of a mode I crack is the Rayleigh-wave velocity, therefore

$$v \leq c_{\mathrm{r}}. \tag{10.2}$$

In mode II, the allowed velocities are sub-Rayleigh (equation (10.2)) as well as intersonic [11, 83, 183, 247]

$$c_s < v \leq c_l \tag{10.3}$$

crack propagation speeds. There is a forbidden velocity regime

$$c_r < v \leq c_s \tag{10.4}$$

which can be overcome by a mother-daughter mechanism involving nucleation of a secondary crack (daughter crack) at some distance away from the primary crack (mother crack) [83, 10, 16]. Intersonic crack propagation has also been reported in earthquakes since 1982 [17] and has led to active research in this field. The discovery of intersonic crack propagation has almost doubled the limiting crack velocity from Rayleigh to longitudinal wave speed. In the case of nonlinear materials, the limiting velocities can be lifted to even higher speeds! This allows for supersonic crack propagation as reported in Chapter 7. The allowed velocity regimes are depicted in Figure 10.1.

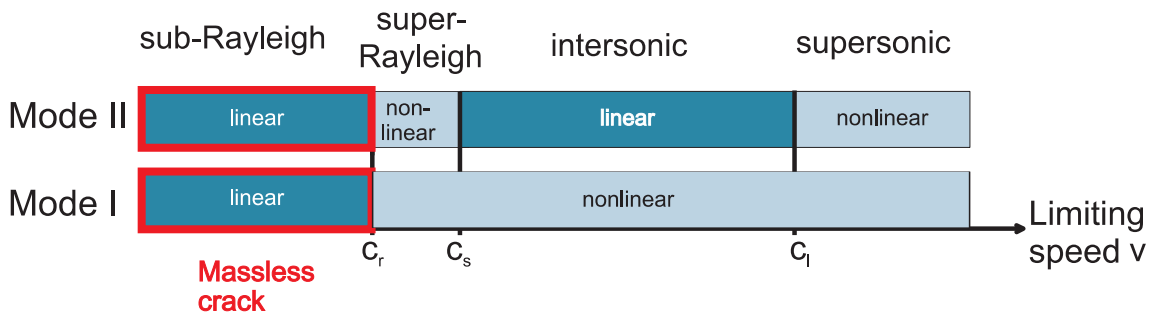

Figure 10.1.: Allowed velocities for mode I and mode II crack propagation, linear and nonlinear stiffening case.

The stress field around a crack propagating rapidly (also referred to as the dynamic field) is very different from the field around a static crack, as discussed in Chapter 6. In mode I, the static field is expected to arise as soon as the crack stops and is emitted with the shear wave speed. For sub-Rayleigh mode II cracks, the situation is the same. For intersonic crack propagation in mode II, it has been shown [117] that the static field spreads out with the shear wave speed as soon as the mother crack has "reached" the daughter crack tip. In any loading case, the corresponding static field is established instantaneously on a line ahead and behind the crack propagation direction ("prospective crack plane") [75], while in other areas around the crack tip this is achieved only in the long-time limit (after a number of elastic eaves have been emitted) [78, 230]. Although we do not study a mode III crack in this chapter, we would like to note that the static field is radiated out behind a circular wave front and the region of instantaneous "switch" to the static field is not confined to the prospective crack line [62]. First experimental observations on nonuniform crack growth in the sub-Rayleigh regime were published in [138].

We extend recently developed molecular-dynamics methods [6, 83, 148] to modeling a suddenly stopping crack. Explaining this phenomenon at the atomistic scale will help forming a more complete picture of dynamic fracture. We propose to study crack dynamics using a combination of continuum theory, laboratory experiments and computer simulations. Important references for our study will be [78] and [230], where analytical and experimental results for the mode I case are described. For the mode II case, we will

compare our findings to the analytical work in [116, 117], where the fundamental solution for an intersonic mode II crack and the solution for a suddenly stopping crack was derived. No laboratory experiments are available up to date for the suddenly stopping intersonic mode II crack.

The outline of this chapter is as follows: For both mode I and mode II loading conditions, linear system solutions are established by assuming the interaction between atoms to be a central pair potential similar to a harmonic ball-spring model. It will be shown that these simulations reproduce the continuum mechanics solution for the plane stress case. Subsequently, we use the linear study as a reference to probe crack dynamics in nonlinear materials characterized by an "anharmonic" tethered LJ potential [10, 83, 11]. The harmonic potential is the first-order approximation of the anharmonic potential. It will be shown, for the first time at the atomistic scale, that the sub-Rayleigh crack indeed behaves like a massless particle and that this feature does not hold for the intersonic case. It will also be demonstrated that the massless feature of cracks does not hold for nonlinear materials: The crack does not behave like a massless particle in the nonlinear case. Cracks being strictly massless is therefore confined to sub-Rayleigh cracks.

10.2. Theoretical background of suddenly stopping cracks

The suddenly stopping crack is important for studies related to non-uniform crack growth. Solutions to this problem are often denoted as fundamental solutions for crack growth. The core idea is to construct the solution of non-uniform crack growth from the solution for uniform crack growth at constant velocity [75, 78]. This becomes possible because the dynamic stress intensity factor can be written as a product of the static stress intensity factor for given geometry and a universal function which depends only on the propagation velocity. The dynamic stress intensity factor can be expressed by [78]

$$K_{I,II}(a, \dot{a}) = k_{I,II}(\dot{a}) K_{I,II}(a, \dot{a} = 0). \tag{10.5}$$

The universal functions k_I and k_{II} may be approximated by [78]

$$k(\dot{a})_I \approx \frac{1 - \dot{a}/c_r}{\sqrt{1 - \dot{a}/c_l}} \tag{10.6}$$

and

$$k(\dot{a})_{II} \approx \frac{1 - \dot{a}/c_r}{\sqrt{1 - \dot{a}/c_s}} \tag{10.7}$$

for most practical purposes. The stress intensity factor responds instantaneously to a change in propagation velocity. In fracture mechanics, one often writes the so-called equation of motion of a crack as [78]

$$G(a, \dot{a}, \text{loading}, \dots) = \Gamma(\dot{a}). \tag{10.8}$$

where G denotes the dynamic energy release rate and $\Gamma(\dot{a})$ represents the dynamic fracture toughness, a material property measuring the fracture resistance. For mode I,

one can write more precisely,

$$\frac{E\Gamma(\dot{a})}{(1-\nu^2)K_I(a,0)^2} \approx g(\dot{a}). \tag{10.9}$$

The right hand side can be shown to be [78, 206, 148]

$$g(\dot{a}) = 1 - \dot{a}/c_r. \tag{10.10}$$

In linear elastic fracture mechanics, the bulk elastic properties consist of elastic constants, while the effects of loading and geometry are included in the expression for $K_I(a,0)$. Equations of this type can be integrated to obtain a solution for $a(t)$, if $\Gamma(\dot{a})$ and $K_I(a,0)$ are both known. We would like to remark that the crack propagation history $a(t)$ could in principle be solved using molecular-dynamics simulations. In contrast, the dynamic fracture resistance $\Gamma(\dot{a})$ can not be determined from continuum mechanics theory and is also difficult to be measured by experiments. The massless behavior of the crack is also reflected by the fact that only the first derivative of the crack tip position appears in the equation of motion (10.8). This is different from a moving dislocation: It takes an infinite time for the static field to establish itself around a suddenly stopping dislocation [109]. Equations (10.5)-(10.10) are only valid for sub-Rayleigh crack growth [116, 117, 78, 230]. In the intersonic case, it will take some time after the crack has completely stopped before the shear and Rayleigh waves reach the tip, as will be discussed shortly.

The analytical solution for the suddenly stopping crack can be derived using the superposition principle: First, the solution for a crack propagating at a constant velocity v is determined. Subsequently, the solution for a moving dislocation is superposed to negate the crack opening displacement ahead of the crack tip where the crack has stopped. The solution for mode I loading was derived in [75], and that for mode II sub-Rayleigh cracks was first considered in [73]. The fundamental solution for the *intersonic* crack was recently determined in [116, 117]. In this paper, the Wiener-Hopf technique [78] was used to address this problem, by transforming the problem into the complex space and then applying the theory of complex functions. A scalar Wiener-Hopf problem is derived which can be solved by transforming the complex functions back to real space employing the deHoop method of integral inversion.

10.3. Atomistic simulation setup

Figure 10.2 shows our simulation geometry which consists of a 2D atomic lattice with dimensions l_x and l_y. The suddenly stopping crack is modeled by a *finite length weak layer*. Once the crack tip reaches the end of the weak layer, it can not propagate any further and is forced to stop. The crack tip does not sense the existence of the barrier before it actually reaches it because the material is elastically homogeneous.

The simulations are performed using a microcanonical NVE ensemble (constant number of particles N, constant volume V, and constant energy E), an appropriate choice for non-equilibrium phenomena such as dynamic fracture. The slab is initialized with very low temperature, $T \approx 0$, which increases during the simulation to slightly higher

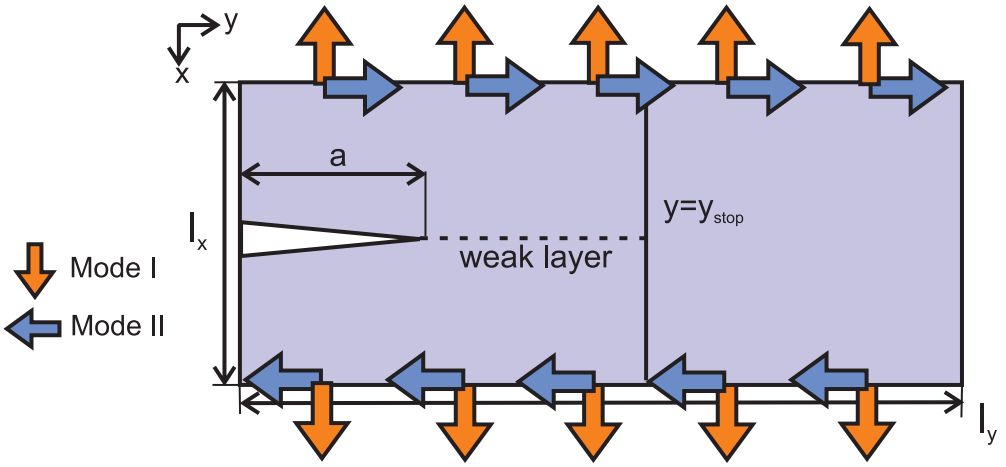

Figure 10.2.: Simulation geometry for the stopping crack simulation.

temperatures. The loading starts when the outermost rows are displaced according to a given strain rate. To avoid wave emission from the boundaries, an initial velocity field according to the prescribed strain rate is established prior to simulation. This procedure is the same as that used in many other studies [5, 6, 7]. The simulations are done with a slab size of 1512×3024 atom rows, and the system contains about $4,500,000$ particles.

10.3.1. Suddenly stopping mode I crack: Simulation setup

The crack is stopped after it reaches its limiting speed (the Rayleigh wave speed, or higher for nonlinear simulations) and has travelled at this velocity for some time. The value of y_{stop} denotes the position at which the crack stops, corresponding to the coordinate of the end of the weak layer (Figure 10.2). The system is loaded until time t^l, after which the boundaries are no longer displaced but held fixed. Somewhat different loading histories are chosen for different simulations and will be indicated in the corresponding sections.

10.3.2. Suddenly stopping mode II crack: Simulation setup

Similar to the mode I case, we also perform mode II simulations. For the mode II simulations, the loading has to be significantly larger in order to achieve nucleation of the daughter crack and the limiting speed. The large deformation around the crack tip leads to large local dilatations soon after the crack has been stopped. In the simulation, this could cause bonds to break as they are driven out of the cutoff radius. Nearest neighbors are searched only within a cutoff radius ($r_{\text{cut}} = 2$ in reduced atomic units). This leads to finite values of r_{break} instead of the theoretical, continuum mechanics assumption $r_{\text{break}} \to \infty$. The variable r_{break} stands for the atomic separation when atomic bonds snap. Breaking of atomic bonds in the bulk is avoided by increasing the potential energy barrier for higher strains by introducing a fourth order term in the potential. Modifying the potential gives additional barrier for bond breaking without affecting the rest of the

slab, where the strains are much lower. Only very localized to the crack tip, and only for a very short time after the crack is stopped, this modification of the potential marginally affects the dynamics. This procedure is not applied with the tethered LJ potential (see Section 5.1.2), because the barrier for bond breaking has proven to be high enough due to its natural stiffening. In addition to a slight opening displacement loading, we impose a strong shear loading on the outermost rows, displacing the upper border atoms to the left and the lower border atoms to the right during loading.

We quickly note here that without the additional potential barrier, dislocations would be observed to emit when the crack is stopped. This phenomenon shows the competing mechanisms of atom separation and atom sliding in nature [181]; the former yielding brittle fracture and the latter giving ductile response. We deliberately avoid such effects because we wish to focus on the crack dynamics.

10.3.3. Interatomic potentials

We briefly present an analysis of the interatomic pair potentials used for the simulations. It is not yet feasible from a computational standpoint to apply a quantum mechanics based treatment of the atomic interactions. We rely on empirical potentials and tailor these to yield generic material properties. Our choice of simple interatomic force laws is consistent with our objective to study *generic properties* of a many-body problem common to a large class of real physical systems. We deliberately avoid the specific complexities of a particular atomic force law. The simple interatomic force laws can be regarded as providing *model materials* for computer experiments. In this study, we use two model materials to study brittle fracture:

1. Linear elastic material with bond snapping across the weak layer,

2. Hyperelastic stiffening material, also with bond snapping across the weak layer.

We use pair potentials (for instance harmonic potentials or modified Lennard-Jones potentials), rather than multi-body EAM potentials [71], to model a generic *brittle material*. Results that have been obtained with such model materials have proven to be useful in the past [5].

A horizontal slit of 400 atoms distance is cut midway along the left-hand vertical slab boundary. The crack is oriented orthogonal to the close-packed direction of the the triangular lattice. For positions $y < y_{\text{stop}}$, atomic bonds are assumed to snap at $r_{\text{break}} = 1.1625$ across the weak layer. The quantity r_{break} can be used to control the fracture surface energy distribution. This confines the crack to propagate along prescribed weak layer without branching. With this approach, we deliberately try to suppress branching and dislocation emission in the current work by introducing a weak interface.

For the linear spring potential, the value for k is assumed to be $k = 140/r_0^2$. Wave velocities are $c_s \approx 7.10$, $c_l \approx 12.29$, and $c_r \approx 6.55$ [21]. The nonlinear tethered LJ potential is described in detail in Section 5.1.2, and we choose $\epsilon = 1.9444$ to match the small-strain elastic properties with the elastic properties of the harmonic potential associated with the spring constant $k = 140/r_0^2$.

10.3.4. Griffith analysis

The question why, how and under which conditions cracks initiate can be investigated by comparing atomistic and continuum predictions. We assume that the onset of crack motion is governed by the Griffith criterion. The Griffith criterion predicts that the crack tip begins to propagate when the crack tip energy release rate G reaches the fracture surface energy 2γ:

$$G = 2\gamma. \tag{10.11}$$

The energy release rate G can be universally expressed as

$$G = \frac{K_I^2 + K_{II}^2}{E}, \tag{10.12}$$

where $K_{I,II}$ are the mode I and mode II stress intensity factors. In both cases, bonds across the weak layer breaks at $r_{\text{break}} = 1.1625$. For the triangular lattice and the given crack orientation, the fracture surface energy is $\gamma^{\text{harm}} = 0.0914$ for the harmonic system. For the tethered LJ potential, the fracture surface energy is determined to be $\gamma^{\text{LJ}} = 0.1186$ following the same approach described in Section 5.2.

Crack initiation time in an infinite solid with a semi-infinite crack

This analysis follows the considerations in [83] who studied a mode II crack using atomistic and continuum methods. To estimate the crack initiation time, an infinite plane stress solid containing a semi-infinite crack is subject to far field tensile (mode I) and shear (mode II) loading. Initially assuming a perfect solid without a crack, the background stress rate $\dot{\sigma}_{11}$ is given by

$$\dot{\sigma}_{11} = \left(\frac{2\lambda G}{\lambda + 2G} + 2G \right) \dot{\varepsilon}_{11} \tag{10.13}$$

with

$$\lambda = \frac{\nu E}{(1+\nu)(1-2\nu)}, \tag{10.14}$$

and

$$G = \frac{E}{2(1+\nu)}. \tag{10.15}$$

The background shear rate is given by

$$\dot{\sigma}_{12} = G\dot{\varepsilon}_{12}. \tag{10.16}$$

The stress intensity factor K_I can be determined as [78]

$$K_I(t) = \frac{4}{3}\dot{\sigma}_{11}\sqrt{\frac{\sqrt{2-2\nu}(1+\nu)c_s t^3}{\pi}}, \tag{10.17}$$

and K_{II} is found to be [78]

$$K_{II}(t) = \frac{4}{3}\dot{\sigma}_{12}\sqrt{\frac{2(1+\nu)c_s t^3}{\pi}}. \tag{10.18}$$

	Theory		Simulation	
Mode	Linear $t_{\text{init}}^{\text{pred}}$	Nonlinear $t_{\text{init}}^{\text{pred}}$	Linear t_{init}	Nonlinear t_{init}
I	41.51	45.19	42.12	46.26
II	28.26	30.76	32.04	35.82

Table 10.1.: Griffith analysis of the atomistic models, for mode I and mode II cracks and different potentials. The predicted values based on continuum calculations agree well with the molecular-dynamics simulation results.

Equations (10.17), (10.18) and (10.12) can be used to derive an expression for the initiation time of crack motion:

$$t_{\text{init}}^{\text{pred}} = \sqrt[3]{\frac{9\pi\mu\gamma}{8c_s\left(\dot{\sigma}_{12}^2 + \sqrt{\frac{1-\nu}{2}}\dot{\sigma}_{11}^2\right)}}. \tag{10.19}$$

In the case of pure mode I cracks, the shear rate $\dot{\sigma}_{12}$ is set to zero in (10.19).

Crack initiation time predictions

The loading strain rate for the mode I simulations is $\dot{\varepsilon}_{xx} = 0.000\,05$. The predicted crack initiation time for the mode I linear crack is $t_{\text{init}}^{\text{pred}} = 41.51$. Assuming small perturbations, the crack initiation time for the nonlinear mode I crack is predicted to be $t_{\text{init}}^{\text{pred}} = 45.19$. We may assume that the nonlinearity is localized to the crack tip, and the slab region can be described by small perturbation elastic properties.

The values are summarized in Table 10.1. The initiation time decreases with stiffer systems (larger linear spring constants), faster loading and smaller values of the fracture surface energy.

For mode II, the loading rates are $\dot{\varepsilon}_{xx} = 0.000\,015$, and $\dot{\varepsilon}_{xy} = 0.000\,2$. We predict an initiation time for the crack in an harmonic solid $t_{\text{init}}^{\text{pred}} = 28.26$. For the nonlinear solid, we predict a slightly higher value $t_{\text{init}}^{pred} = 30.76$ because of the higher fracture energy. As before, we assume that the nonlinearity is localized to the crack tip, and the slab region can be described by small perturbation elastic properties. The values are summarized in Table 10.1.

10.4. Atomistic simulation results of a suddenly stopping mode I crack

In the following we present the results for a suddenly stopping mode I crack. The plan is to start with the linear system, and subsequently move on to the nonlinear system.

10.4.1. Harmonic systems

The crack propagating close to the Rayleigh velocity displays a distinct signature from cracks at lower speeds. We use the maximum principal stress field to analyze the simu-

lation results. We find this field to be a simple and powerful measure to be compared with continuum solutions, because it displays a significant dependence on the propagation speed (and can therefore distinguish a static field from a dynamic field). The stress field close to the crack tip is best described by the asymptotic solution of continuum mechanics [78]. The field shows only one maximum for low speeds, and exhibits another maximum for sufficiently high velocities. The stress state ahead of the crack at high velocities is more complicated than at low velocities. The asymptotic field obtained by atomistic simulation is shown in Figure 10.3 (a) for the quasi-static case ($v = 0$, and low velocities), and for the case $v = c_r$ in Figure 10.3 (b).

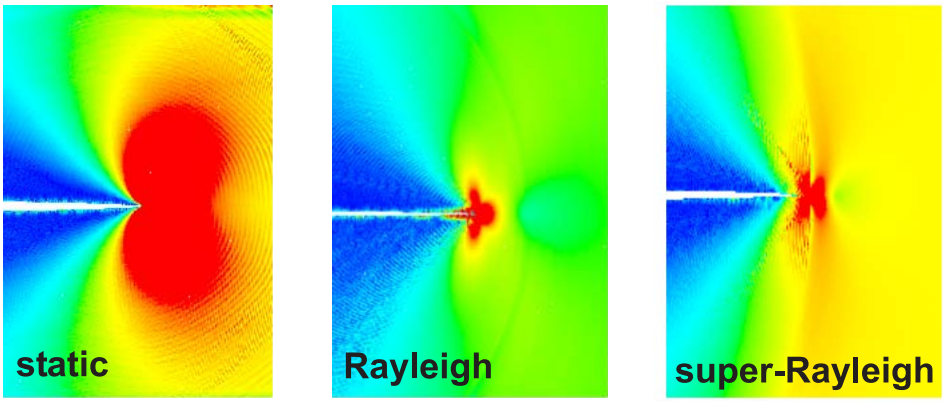

Figure 10.3.: The asymptotic field of maximum principal stress near a moving crack tip (a), when $v = 0$, (b) dynamic field for $v \approx c_r$, (c) dynamic field for super-Rayleigh propagation velocities ($v > c_r$).

Crack initiation time is determined as $t_{\text{init}} = 42.12$, in good agreements with the continuum theory prediction 41.51. The loading is stopped at $t^l = 72.8$ by setting the strain rate to zero. The crack has a velocity $v \approx 6.45$ before stopping, close to its limiting speed. The crack speed does not increase significantly even if the loading is kept for longer time. The maximum strain is $\varepsilon_{xx} = 0.0073$. The stress field, as well as numerical estimation of the crack velocity clearly identifies a crack propagating close to Rayleigh velocity. In Figure 10.4, the history of the crack length $a(t)$ is shown.

Once the mode I crack is stopped, two circular waves are emitted from the crack tip. The first wave front corresponds to the longitudinal wave front, while the second one is the shear wave front. The Rayleigh surface wave can be seen on the plane behind the crack. The static field was measured to spread out with a velocity $v \approx 7.05$, and the longitudinal wave emitted by the stopped crack is propagating at $v \approx 12.2$. Both values are, taking into account measurement errors, reasonably close to the continuum mechanics prediction.

In the prospective crack plane, the stress field takes on its static counterpart immediately after the shear wave has passed. Behind the crack tip, the static field is established after the Rayleigh wave has passed. In other areas, the static field is only reached in the long-time limit. We observe continuous wave emission and rapid attenuation in

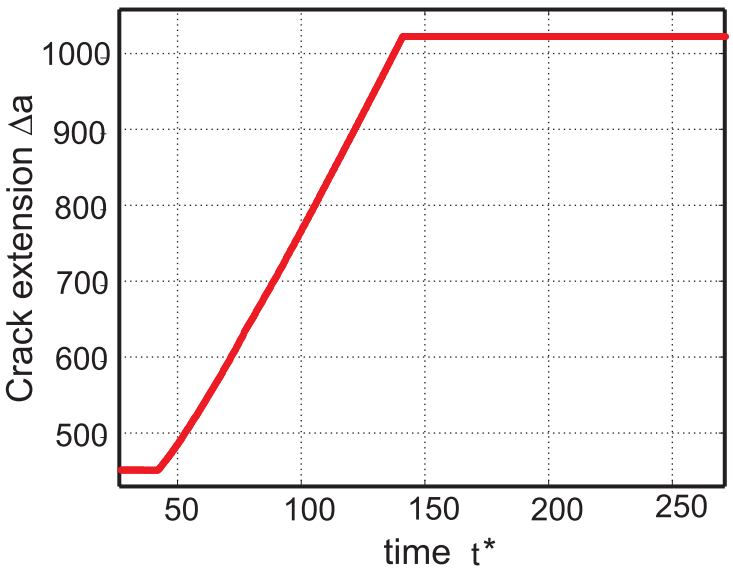

Figure 10.4.: Crack extension history versus time for the suddenly stopping linear mode I crack.

regions surrounding the crack tip. The frequency of these waves increases with time. The wave period attains atomic distance rapidly and elastic energy is dissipated as heat (thermalization). This is visualized in Figure 10.5.

It can be verified that at late stages (after the waves have attenuated), the static field inside the shear wave front remains constant, and no additional wave emission is identified (see lower right snapshot of Figure 10.5). The results confirm the experimental observations in [230]: In Figure 10.6 (a), the evolution of the maximum principal stress along the prospective crack line is shown. The evolution of potential energy is shown in Figure 10.6 (b). The first kink in the plots refers to the longitudinal wave front and a second kink corresponds to the shear wave front at which the static field is radiated. Additional evidence is provided by different snapshots of the stress field after the crack has been stopped. These are depicted in Figure 10.5.

The stresses ahead of the crack tip are closely related to the stress intensity factor K_I. We choose a fixed location to measure the stress over time. A similar approach was used in experiments [230]. The result is depicted in Figure 10.7. The plot also shows the results of experimental studies of a suddenly stopping mode I crack [230].

In both experiments and simulation, the stress decays slightly after the longitudinal wave has reached the measurement location, and increase again soon afterwards. This decrease in stress is related to the arrival of longitudinal wave and persists even when we change the measurement location to different y positions. The stresses continuously change until they reach the corresponding static solution. The result of Figure 10.7 agrees qualitatively with experimental data, as can be verified in the plot (see also Figure 2 in [230]). In particular, we note that the step at $t^* \approx 7$ and the minimum at $t^* \approx 3$ is qualitatively reproduced.

These results show good agreement among atomistic simulations, continuum theories and experiments. The atomistic simulation demonstrated that the rapid thermalization

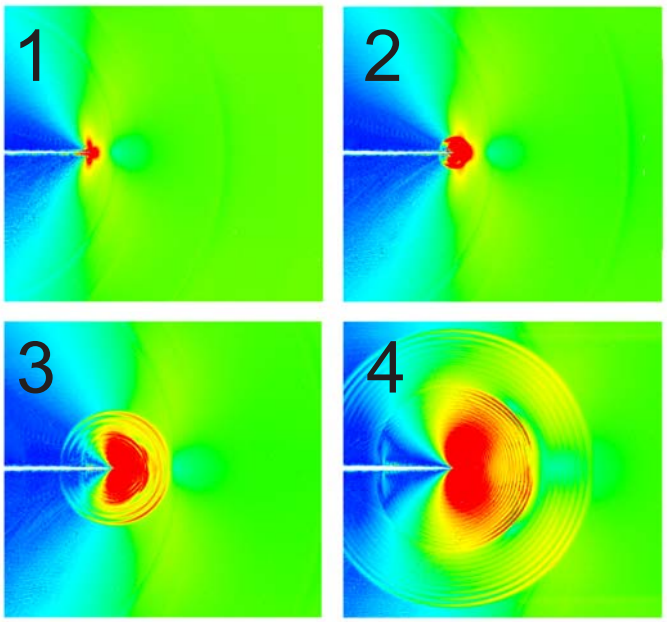

Figure 10.5.: Maximum principal stress field for various instants in time, mode I linear crack.

of elastic waves near the crack tip did not change the basic nature of crack tip stress fields predicted by continuum mechanics. This result would not have been possible by continuum mechanics alone.

10.4.2. Anharmonic systems

We have shown that the harmonic solid reproduces continuum mechanics solutions, and may serve as a reference system when we further probe into nonlinear material behaviors. Atomistic simulations provide an extremely helpful tool to investigate the nonlinear case – a situation which usually can not be solved in closed form. We present simulations to address the following questions:

- Does the result agree qualitatively and quantitatively with the linear solution?
- What is the "wave" speed in the nonlinear case, that is, how fast can the static field be established?

We start with a simple Griffith analysis to calculate the time for the onset of fracture due to the applied loading. Crack initiation time is found to be $t_{\text{init}} \approx 46.26$. The initiation time agrees well with the prediction $t_{\text{init}}^{\text{pred}} = 45.19$. The loading is kept up to $t^l = 144$. The maximum strain we achieve is $\varepsilon_{xx} = 0.0144$. The limiting speed observed is $v \approx 7.5$. As soon as loading is stopped, the velocity remains at the value it has at the moment where the strain rate is set to zero. We make a few remarks at this point:

1. The crack speed is significantly higher than in the linear case (7.5 versus 6.45; this is about 16 percent higher limiting speed than predicted by the linear theory).

2. The crack speed is also larger than the corresponding wave velocity in the far-field. This second finding is in good agreement with other results we have obtained with bilinear hyperelastic potentials (see chapter 7), as well as previous studies on the topic of hyperelastic brittle fracture [81, 82]. These results indicate that the *local* stress state at bond breaking is important [81, 82, 11]. The higher local wave speed leads to a higher limiting velocity. The crack can funnel energy faster than the far-field wave speeds would allow.

3. The dynamic maximum principal stress field provides signatures of nonlinear material response. For a super-Rayleigh crack, this field is shown in Figure 10.3 (c). The stresses are higher compared to the harmonic case, and the angular variation of the asymptotic field is different.

The histories of crack tip position and the velocity for the super-Rayleigh crack can be found in Figure 10.8 which plots the limiting speed calculated from our atomistic simulations and visualizes how the crack accelerates and approaches its limiting speed.

The history of maximum principal stress in the line ahead of the crack tip is shown in Figure 10.9 (a), and the potential energy field is shown in Figure 10.9 (b). Even in the nonlinear case, we can identify "bulk wave fronts" associated with a localized group of nonlinear waves. The distributions of stress and energy along y are different in the linear and nonlinear cases.

In very early stages, the shear wave front propagates with $v_y \approx 8.6$. Later, when the stress in y direction is reduced at the crack tip, we measure $v_y \approx 7.3$. The bulk of longitudinal waves emitted from the stopped crack is moving at $v_y \approx 15.3$ in early stages, and at $v_y \approx 12.3$ later, approaching the linear sound velocity. This can be attributed to the fact that the material ahead of the stopped crack is not strained as severely in the y direction. The propagation speed in the x direction (orthogonal to the crack) remains higher than that in the linear case. The longitudinal wave front orthogonal to propagating direction is moving faster than ahead of the crack at late stages. Similar finding applies qualitatively to the shear wave front. The results show that the wave velocity depends on the stress state, and is significantly affected by the loading condition. The fact that the wave fronts propagate faster orthogonal to the propagation direction leads to elliptical wave fronts. In particular, the local wave speeds differ significantly from the linear elastic wave speeds. This observation is found in all of our nonlinear simulations. The discontinuities of the longitudinal and shear wave front are smeared out compared to the corresponding harmonic simulation. This observation is again consistent with the idea that there is no unique wave speeds near the crack tip. There exists a train of "longitudinal" and "shear" waves associated with the rapidly changing stress state near the crack tip. Consequently, the static field is not established as soon as the crack has stopped behind the shear wave. In one of our simulations, it takes $\delta t \approx 61$ since stopping of the crack for the stresses to reach a static, constant value at $\delta y = 15$ ahead of the crack tip. This time is found to be shorter if the stresses are measured closer to the crack tip. For example, at $\delta y = 5$ ahead of the crack tip,

the time to establish the static field is determined to be $\delta t \approx 30$. The closer to the crack tip, the less the time required to establish the static field. The reason could be nonlinear wave dispersion. We emphasize that such large changes in the stress after the shear wave has passed are *not* observed in the linear case. The time it takes until the stresses do not change any more depends on the strength of the nonlinearity and on the amount of lateral loading. For our tethered LJ potential, we observe that for more compliant systems and longer loading time this effect becomes more severe, presumably due to larger displacements and more nonlinear dispersion. As in the harmonic case, emission of elastic waves occurs soon after crack arrest, and subsequent thermalization suppresses additional wave emission.

The maximum principal stress field is shown in Figure 10.10 for various instants in time. The discontinuities are smeared out, and it becomes evident that the definition of a unique wave front can be difficult. In comparing Figure 10.11 with Figure 10.5, it is evident that in the nonlinear case the shape of the wave fronts is different (elliptical versus circular).

The normalized maximum principal stress over time, recorded at a constant distance ahead of the crack tip, is plotted in Figure 10.12 for an anharmonic simulation. One can observe the difference in shape compared to the linear case shown in Figure10.7.

10.4.3. Discussion – mode I

One important observation in our simulation is that a large number of waves are generated after crack stopping. This effect is less significant in the prospective propagation direction and becomes more pronounced in other directions. The waves attenuate quickly after the crack is stopped, and in the long-time limit become dissipated as heat ("thermalizing"). In the nonlinear case, we summarize the following findings:

1. There is no unique wave velocity, and the static field does not spread out behind the shear wave front. We find that there exists a train of "longitudinal" and "shear" waves associated with the rapidly changing stress state near the crack tip. The static field is not established until all waves have passed.

2. There is an anisotropy effect. Ahead of the crack, the wave speed approaches the linear limit, and orthogonal to the crack, the wave speed is significantly larger. We see elliptical wave fronts instead of circular wave fronts.

10.5. Atomistic simulation results of a suddenly stopping mode II crack

We consider crack propagation under in-plane shear dominated loading, starting with the linear case and moving subsequently to the nonlinear case. For all mode II simulations, we observe a mother-daughter mechanism to overcome the forbidden velocity zone. This mechanisms is assumed to be governed by a Burridge-Andrew mechanism [16, 39]. A peak shear stress ahead of the crack continuously increases as the mother

crack propagates through the material. Once this peak of shear stress reaches the cohesive strength of the interface, the daughter crack nucleates at some distance ahead of the mother crack and starts to propagate at an intersonic speed. The observation regarding the mother-daughter mechanism and the limiting speed of c_l is consistent with the discussion in [10, 83].

10.5.1. Harmonic systems

The objective is to validate the theoretical results derived in [116, 117] using computer experiments. In particular, we will show that the static field does not spread out until the Rayleigh wave carrying the mother crack reaches the stopped daughter crack. We will determine the stresses slightly ahead of the crack tip from our molecular-dynamics data and show similarity to the continuum solution. The linear solution will serve as the reference system when we probe into nonlinear material behaviors.

Crack initiation time is found to be $t_{init} = 32.04$, in good agreement to the continuum theory prediction $t_{\text{init}}^{\text{pred}} = 28.26$. The daughter crack nucleates at $t = 82$, this is $\delta t \approx 50$ later than the initiation of the mother crack. The loading is stopped at $t^l \approx 84$ soon after the daughter crack is nucleated. The mother crack hits the stopped daughter crack at $t = 105$. The mother crack propagates at $v \approx 6.5$, and the daughter crack quickly attains a velocity $v \approx 12.3$. The suddenly stopping intersonic crack shows the following sequence of events. The daughter crack is stopped, and the mother crack continues until it reaches the end of the weak layer. For each crack stopping event, two wave fronts are emitted yielding a total number of four wave fronts. The mechanism of the suddenly stopping intersonic crack is visualized schematically in Figure 10.13 (a) and (b) [117].

The stresses continuously change after the daughter crack is stopped [117]. Once the mother crack hits the daughter crack, stresses begin to increase dramatically. The static field radiates out from the crack tip with a velocity $v \approx 7.4$. This velocity is the shear wave velocity and the observation provides good agreement to the prediction by continuum theory. Other propagation velocities measured from our data also agree with the continuum mechanics predictions. In Figure 10.14 (a), the maximum principal stress is shown, and in Figure 10.14 (b), the potential energy field is depicted some distance ahead of the crack tip. The potential energy field is shown in Figure 10.15 at several instants in time.

Figure 10.16 shows the normalized maximum principal stress at a fixed measurement location some distance ahead of the crack. When comparing this quantity to the stress intensity factor, care must be taken because the singularity changes continuously as the crack passes through the distinct intersonic velocity phases. The arrival of the shear wave front is characterized by a strong discontinuity induced by the Rayleigh wave[116, 117, 83]. As soon as the shear wave reaches the measurement location, the static field is established and the stress no longer changes afterwards.

The simulation results are not inconsistent with the analysis in [117].

10.5.2. Anharmonic systems

The linear solution has reproduced results similar to the continuum mechanics solution of the problem. We further consider the dynamics of a suddenly stopping crack in a nonlinear material.

Crack initiation time is determined to be $t_{\text{init}} = 35.82$, which is somewhat larger than the prediction $t_{\text{init}}^{\text{pred}} = 30.76$. The loading is stopped at $t^l = 129.6$, after nucleation of the daughter crack at $t \approx 112$. This leads to a far-field strain of $\varepsilon_{xx} = 0.0039$ and $\varepsilon_{xy} = 0.052$. The crack propagation speeds we measure are $v \approx 8$ for the mother crack, and $v \approx 16.8$ for the daughter crack. Both velocities are higher than the corresponding velocities of the linear case (22 percent higher, and 36 percent higher for mother and daughter crack respectively) due to material nonlinearities. The daughter crack propagates supersonically through the material. Figure 10.17 plots the crack extension history $a(t)$. In this Figure, the mother-daughter mechanism can be identified straightforwardly.

The mother crack hits the daughter crack at $t \approx 197$, $\delta t \approx 77$ after the nucleation of the daughter crack. This can also be estimated from Figure 10.17.

Like in the simulations of a mode I crack in nonlinear material, the wave fronts are smeared out, but we can still identify a localized group of nonlinear waves which may be interpreted as a "nonlinear wave front". The first waves emitted after stopping of the crack can be regarded as the longitudinal wave moving with a velocity $v \approx 16.4$ through the solid in the prospective crack line. The strong spike ahead of the crack corresponds to the shear wave induced by the stopped daughter crack and is propagating with a velocity $v \approx 10.5$. Both values are higher than the corresponding linear shear wave velocity. The propagation speed of the longitudinal wave is close to the velocity of the daughter crack before stopping. The stopping mother crack leads to nucleation of additional waves. We observe a discontinuity propagating at $v \approx 10.5$, emitted when the mother crack is stopped. We associate this with the shear wave front. It is difficult to observe the longitudinal wave front from our molecular-dynamics data in this case.

Plots of the maximum principal stress field and the potential energy field ahead of the crack tip in the prospective crack line are shown in Figures 10.18 (a) and 10.18 (b). The plots look quite different from the harmonic case. The shape we have observed in the harmonic counterpart, in particular the strong discontinuity before arrival of shear wave front seems to have disappeared. The discontinuity associated with the shear wave front of the daughter crack is more pronounced than in the linear case. The fact that the discontinuities are smeared out can lead to stresses changing significantly even after the bulk of the shear waves of the mother crack has passed. This effect is reminiscent of the phenomenon observed in the nonlinear mode I crack. In this simulation, the static stresses are reached soon after the bulk of shear waves has passed. The delay required to establish the static field after the shear waves have passed, which we have observed in the nonlinear mode I case, is not observed in this simulation, but appears in different simulations when the impact of nonlinearities is stronger due to higher lateral strains (see further discussion below).

The potential energy field around the crack tip is shown in Figure 10.19 for various times. The velocity of the wave fronts depends on the angle. This leads to elliptical shapes of the wave front, as also observed in the mode I case. Like in previous simula-

tions, a thermalization effect is observed. In particular, after stopping of the daughter crack, energy is found to be dissipated as heat, as can be verified from Figure 10.19 (right top). The normalized stresses σ^* versus time are shown in Figure 10.20 for an anharmonic simulation.

Comparing this result to the linear case, we find similarity until the shear wave arrives. Unlike the linear case in which stresses decrease strongly after the mother crack arrives, this stress remains constant until the mother crack arrives and then quickly increase to the steady state value.

To investigate the nonlinear dynamics further, we will briefly discuss a second simulation. To obtain softer elastic properties, we alter the tethered LJ potential and choose $\epsilon_0 = 1$. The corresponding harmonic wave velocities are $c_r = 4.8$, $c_s = 5.2$ and $c_l = 9$. As we mention in Section 10.4.2, this softening in combination with higher lateral strain allows us to study the nonlinear effect better. The loading is kept for a longer time than in previous simulations. All other parameters are kept constant. The daughter crack achieves a speed of $v \approx 12$ and is truly supersonic. The mother crack propagates at $v \approx 5.8$, which is super-Rayleigh. The wave fronts become very difficult to identify, because they are smeared out more than in the previous simulation. The shape of the discontinuities is clearly elliptical. The longitudinal wave front of the stopped daughter crack is propagating with $v \approx 11.95$, and the shear wave front is associated with a strong discontinuity propagating at $v \approx 7.80$ through the solid. We remark that the velocity of the longitudinal wave front is almost identical to the propagation velocity of the daughter crack. Once the mother crack reaches the stopped daughter crack, there is no more significant discontinuity. This is very different from the harmonic case where each wave front is clearly identified by a distinct discontinuity. We find that the mother crack, represented by a surface wave after the secondary crack is nucleated, is smeared out in the nonlinear case. Therefore the arrival of the mother crack is not the arrival of a singularity, but of a distributed stress concentration. The static field is not instantaneously established. The stress intensity is continuously increases from the point where the daughter crack has been stopped until the it becomes fully steady state. We observe a slight increase of stresses until all waves have passed, just as in the nonlinear mode I case.

This also helps to explain the difference in shape of energy and stress distribution in the prospective crack line, when we compare the harmonic with the anharmonic simulations. Moreover, the static field is not established until all waves have passed.

10.5.3. Discussion – mode II

We would like to start with the results for the linear case:

1. We have shown that static field does not establish until the mother crack reaches the stopped daughter crack for the linear reference system.

2. After the mother crack has reached the stopped crack tip, the stress field (as well as the energy field) ahead of the crack tip is static behind the shear wave front in, and is static behind the Rayleigh surface wave behind the crack. Both observations match the prediction by continuum mechanics.

In the nonlinear case, the definition and observation of the longitudinal wave front is difficult. The wave fronts are not as sharp and discontinuities not as strong, which may cause the field behind the shear wave front of the mother crack to change continuously during some transition time until all waves have passed.

10.6. Discussion

We have studied suddenly stopping cracks by atomistic simulations. We considered a plane-stress elastic solid consisting of a two-dimensional, triangular atomic lattice. For the interatomic interactions, we assumed a tethered Lennard-Jones potential, as well as a harmonic potential. We presented four simulations for mode I and mode II loading conditions, and linear and nonlinear simulation potentials. In addition to the atomistic simulations, we have done continuum analyses to determine the crack initiation time and wave velocities associated with the interatomic potentials.

The harmonic atomistic simulations have shown good agreement with the continuum mechanics and experiments. We would like to summarize the main results below.

1. In mode I, the static solution spreads out as soon as the crack is stopped. This is in agreement to the continuum theory [75].

2. In mode I, experiments and atomistic studies show similar results on very different scales [230] (see Figure 10.7).

3. In mode II, the static solution spreads out as soon as the mother crack has reached the stopped daughter crack. The nature of the mode II intersonic crack is very different from the sub-Rayleigh crack [117].

4. In both mode I and mode II, we observe emission of waves from the stopped crack. These waves attenuate quickly, in which process energy is dissipated as heat. This does not change the basic nature of stress fields near the crack tip as predicted by continuum mechanics.

The anharmonic simulations give somewhat different results, which can not be explained by linear elastic fracture mechanics only. For the nonlinear case, we would like to summarize the main findings as follows.

1. In both mode I and mode II, the wave fronts and discontinuities are not as sharp as in the linear case. This nonlinear dispersion effect could cause the field to change continuously even after the main wave discontinuities have passed.

2. For supersonic mode II cracks, the mother crack could transform from a stress singularity into a less localized stress distribution. The static field is not instantaneously established but stresses increase continuously, until they eventually reach steady state.

3. The nonlinearity can leads to an anisotropy effect of wave propagation. Instead of circular wave fronts, we find elliptical wave fronts.

Our simulations show that the linear model is a reasonable approximation even when moderate nonlinearities are present. The simulations provide evidence that the crack behaves like a massless particle only in the sub-Rayleigh regime. The Griffith criterion works well in all simulations we presented.

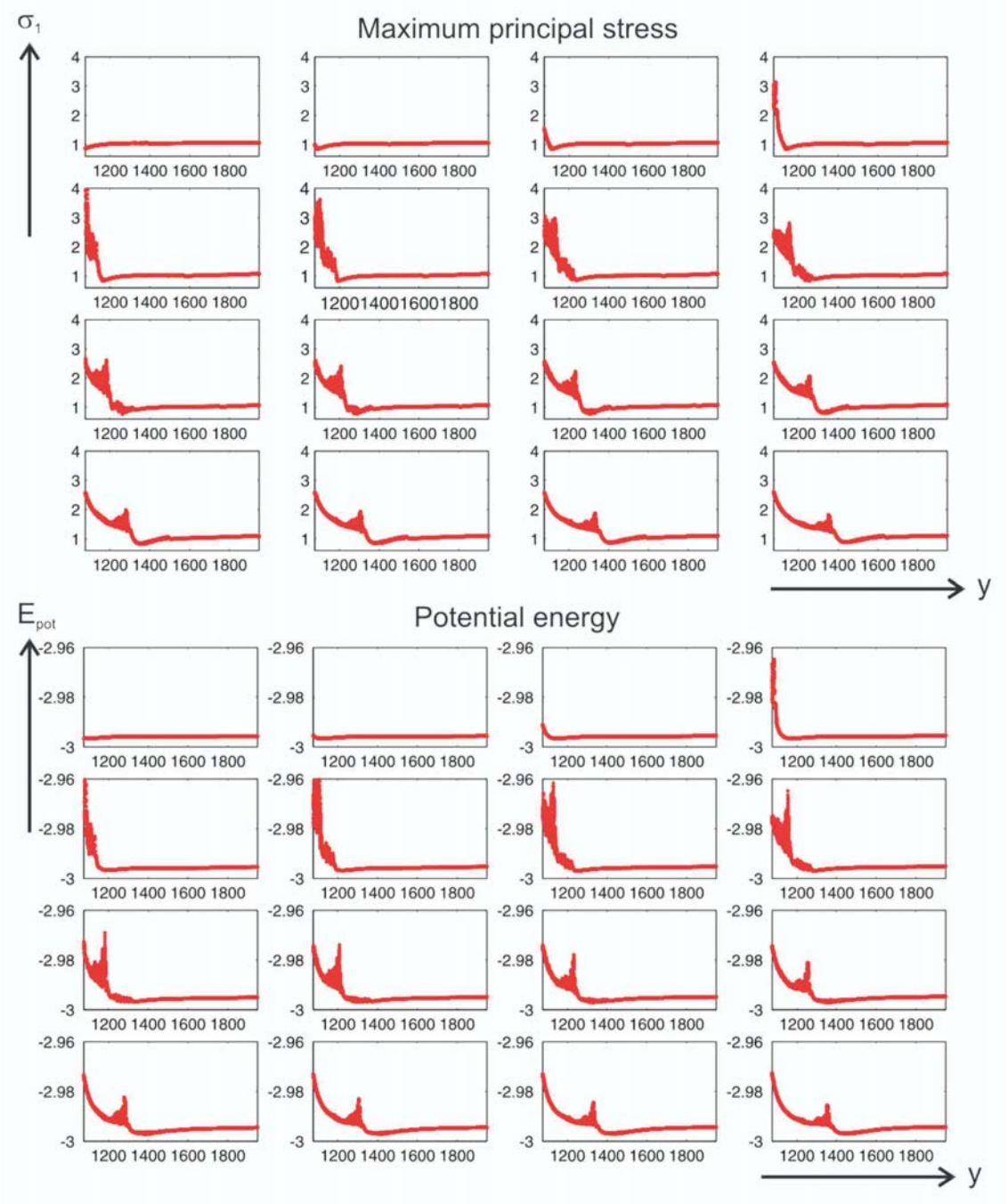

Figure 10.6.: Evolution of principal maximum stress and potential energy along the prospective crack line, for a linear mode I crack.

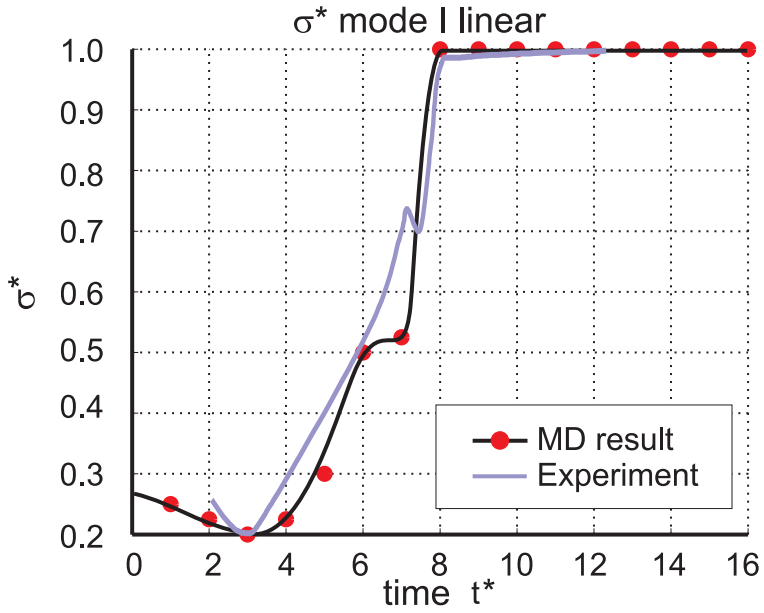

Figure 10.7.: Variation of stress at fixed distance ahead of the stopped linear mode I crack. At $t \approx 0$, the longitudinal wave arrives at the location where the stress is measured. At $t \approx 8$, the shear wave arrives and the stress field behind the crack tip is static. The plot also shows the results of experimental studies [230] of a suddenly stopping mode I crack for qualitative comparison (the time is fitted to the MD result such that the arrival of the shear wave and the minimum at $t^* \approx 3$ match).

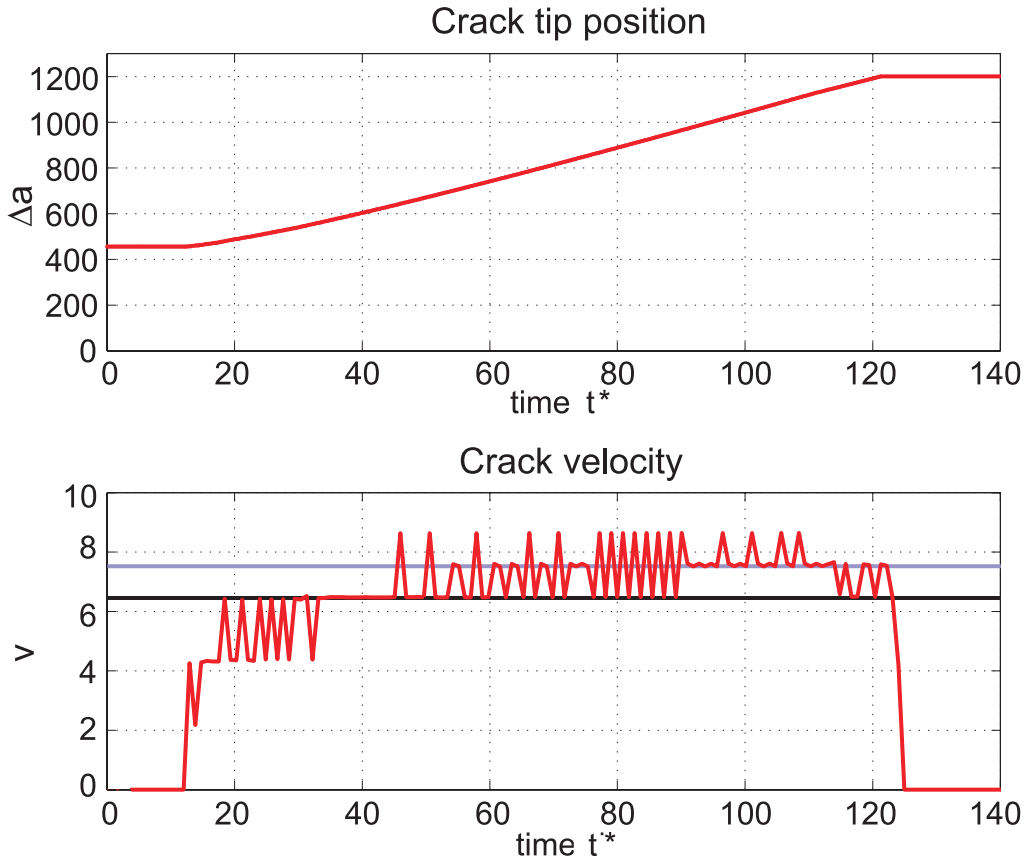

Figure 10.8.: Crack tip history $a(t)$ and crack tip velocity v as a function of time, suddenly stopping mode I crack. The limiting speed according to the linear theory is denoted by the black line (Rayleigh velocity), and the super-Rayleigh terminal speed of the crack in the nonlinear material is given by the blueish line. When the crack stops, the crack speed drops to zero.

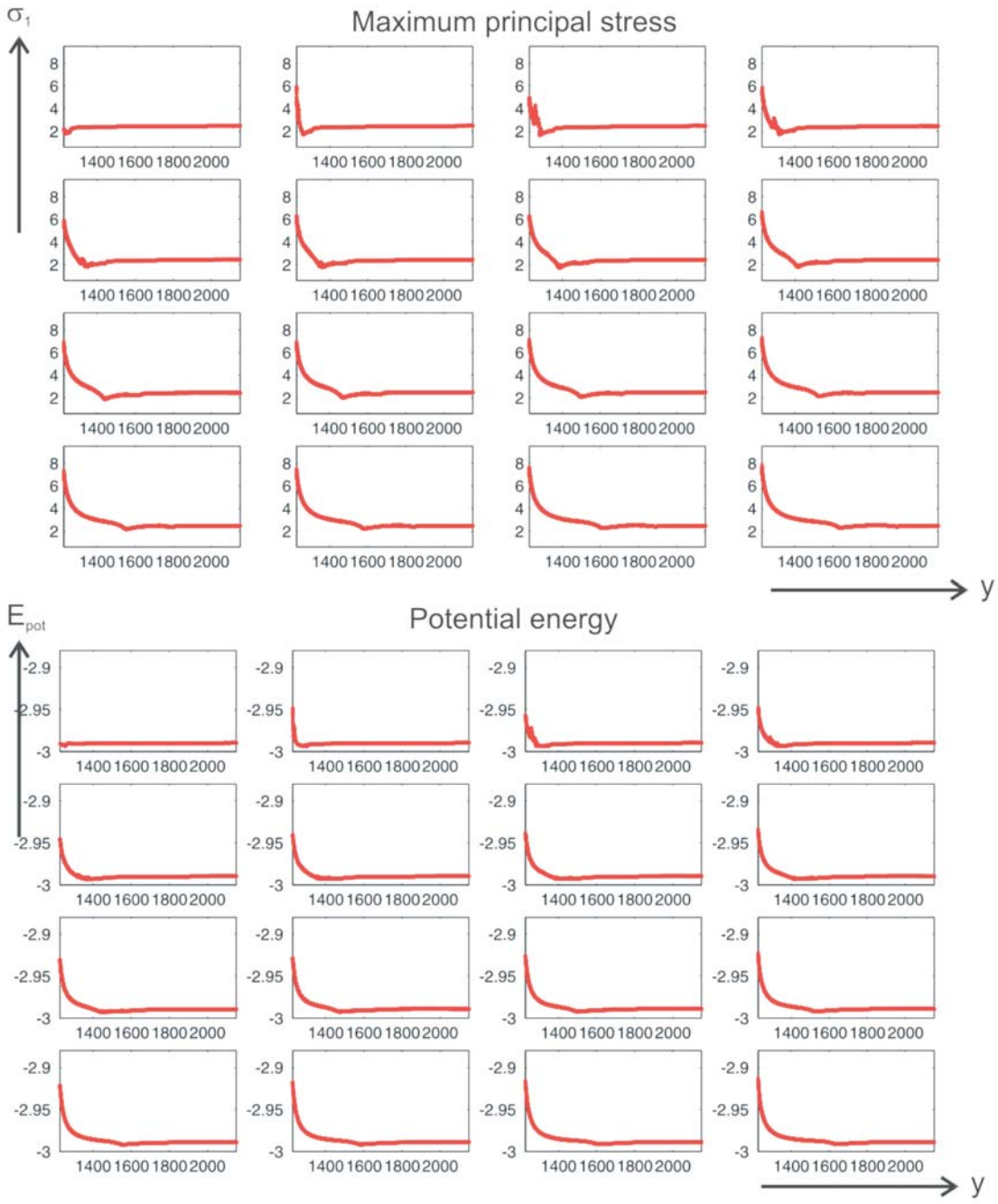

Figure 10.9.: Evolution of principal maximum stress and potential energy along the prospective crack line; for a mode I nonlinear crack.

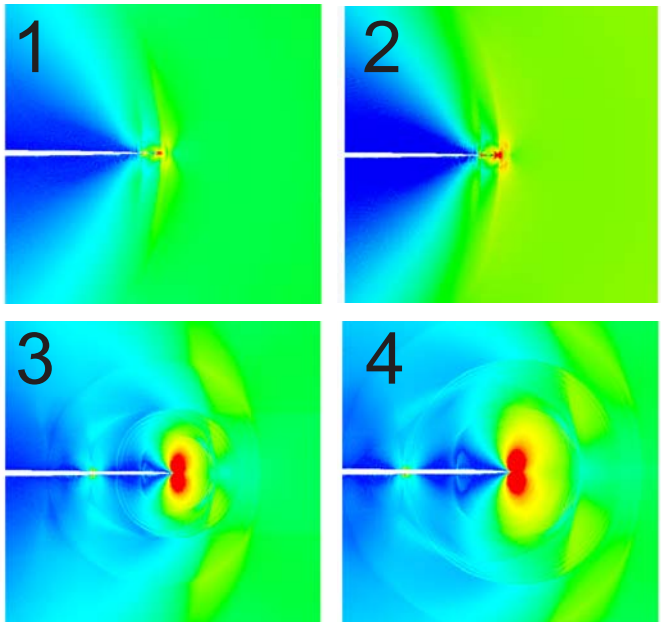

Figure 10.10.: Maximum principal stress field for various instants in time, for mode I nonlinear crack.

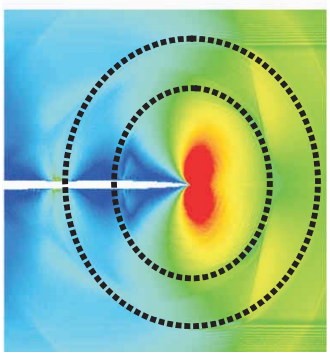

Figure 10.11.: Elliptical wave fronts in the mode I nonlinear crack.

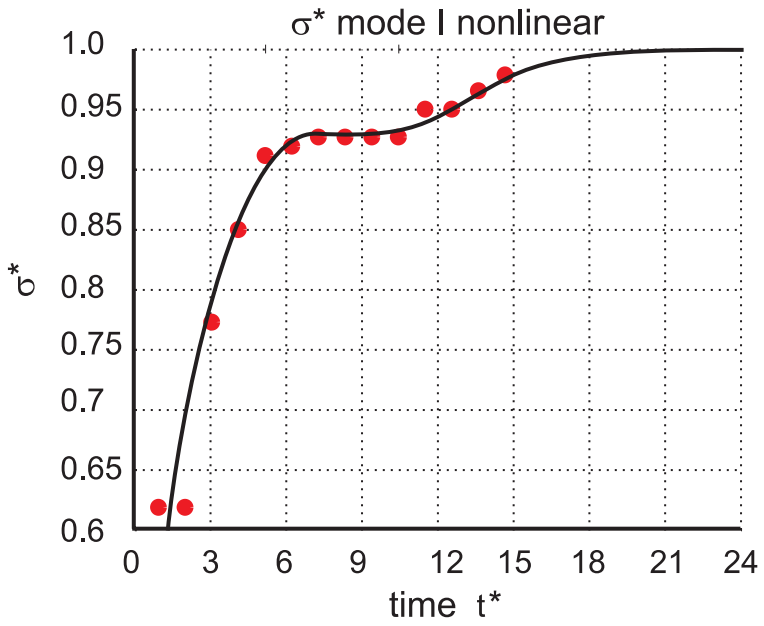

Figure 10.12.: Variation of stress at fixed distance ahead of the stopped nonlinear mode I crack.

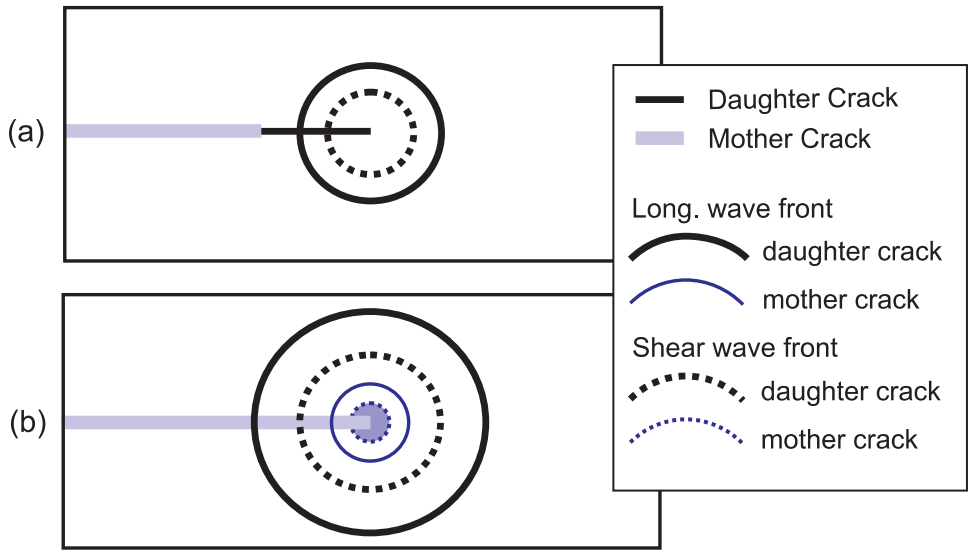

Figure 10.13.: Schematic of waves emitted at a suddenly stopping mode II crack; (a) stopping of daughter crack, (b) stopping of mother crack.

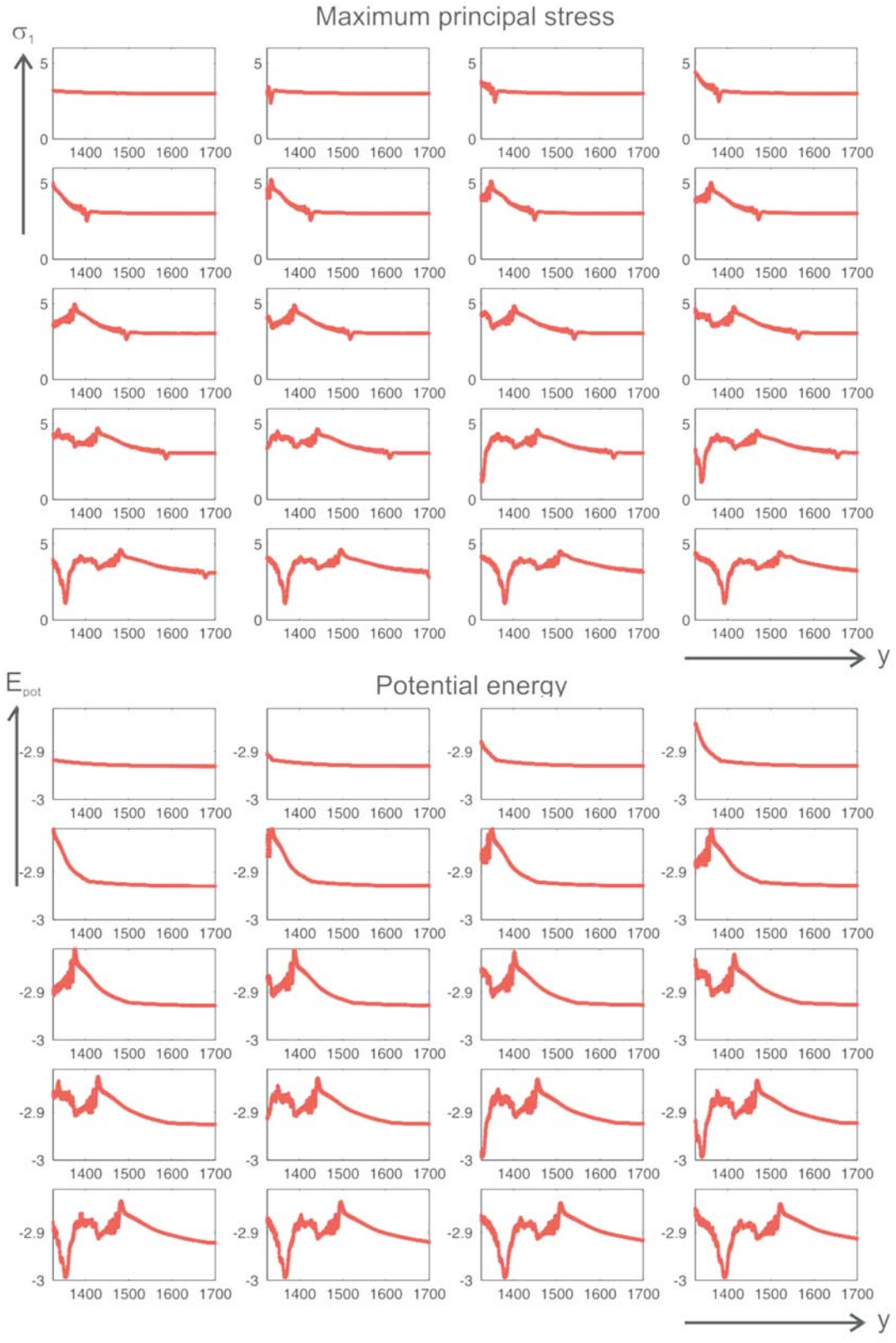

Figure 10.14.: Evolution of (a) principal maximum stress and (b) potential energy along the prospective crack line; for linear supersonic crack.

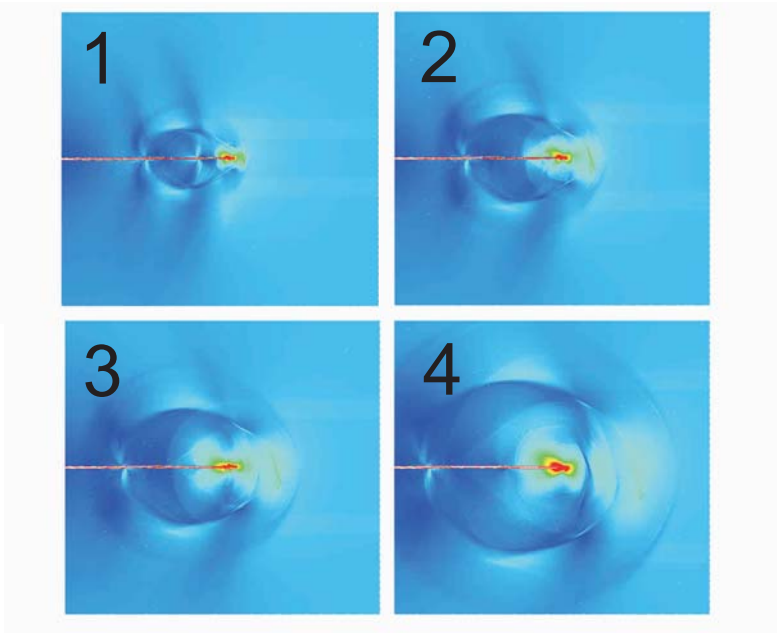

Figure 10.15.: Potential energy field for various instants in time, mode II linear crack.

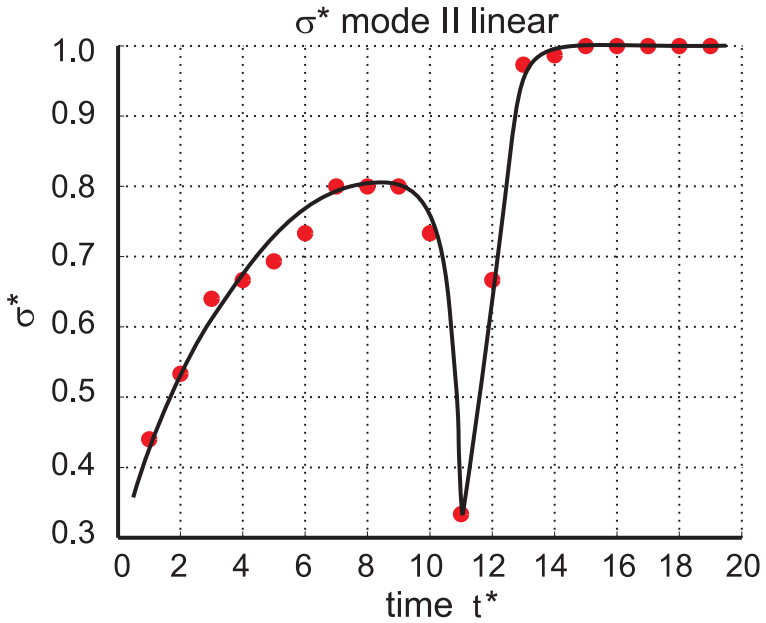

Figure 10.16.: Variation of stress at fixed distance ahead of the stopped intersonic mode II crack.

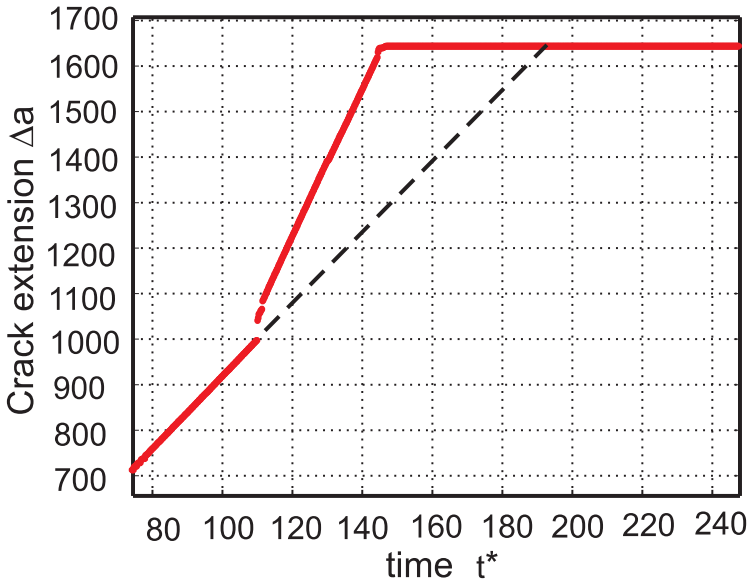

Figure 10.17.: Crack extension history versus time for the supersonic mode II crack. The dashed line is used to estimate the time when the mother crack comes to rest.

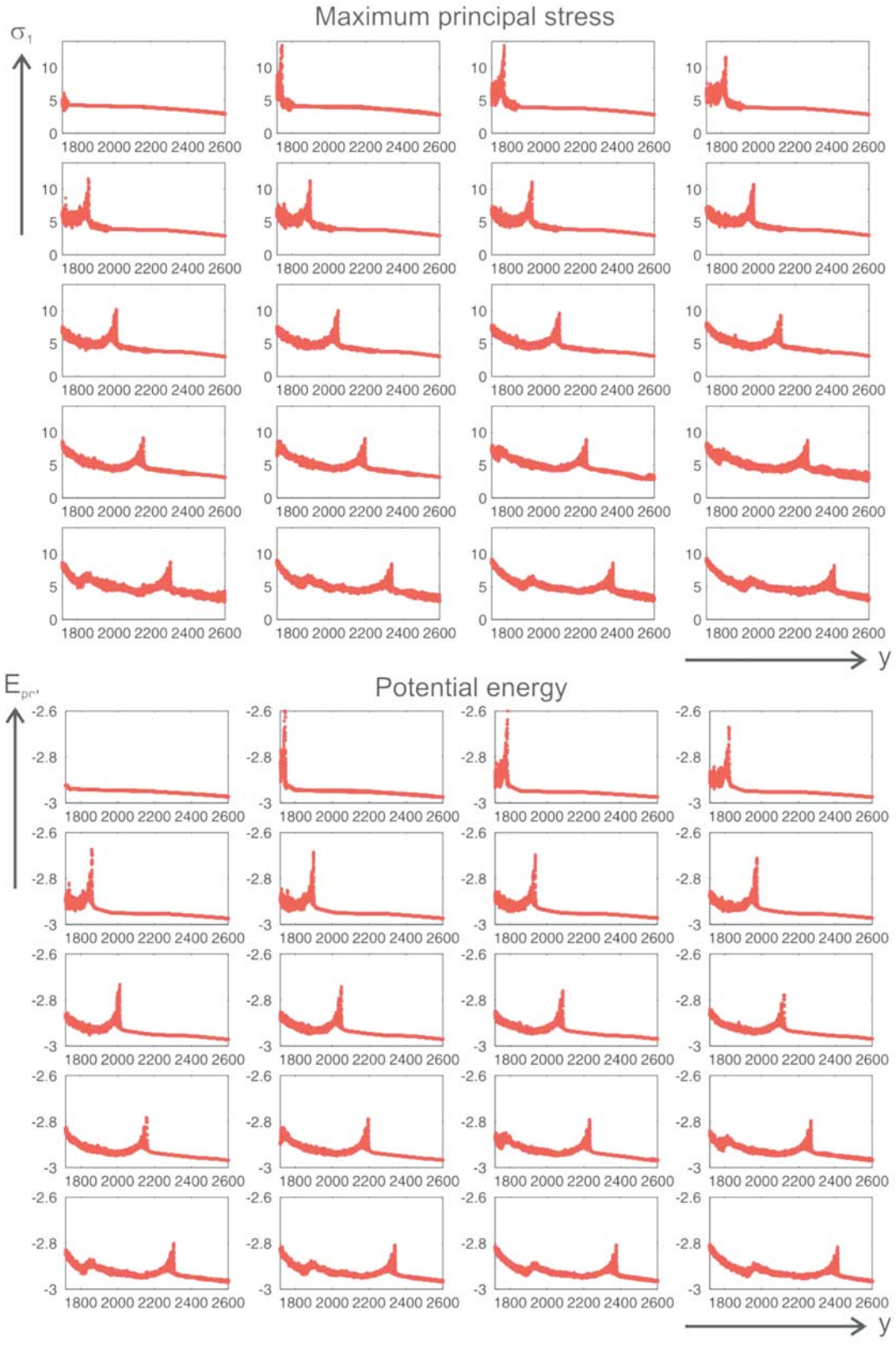

Figure 10.18.: Evolution of (a) principal maximum stress and (b) potential energy along the prospective crack line; for nonlinear supersonic crack.

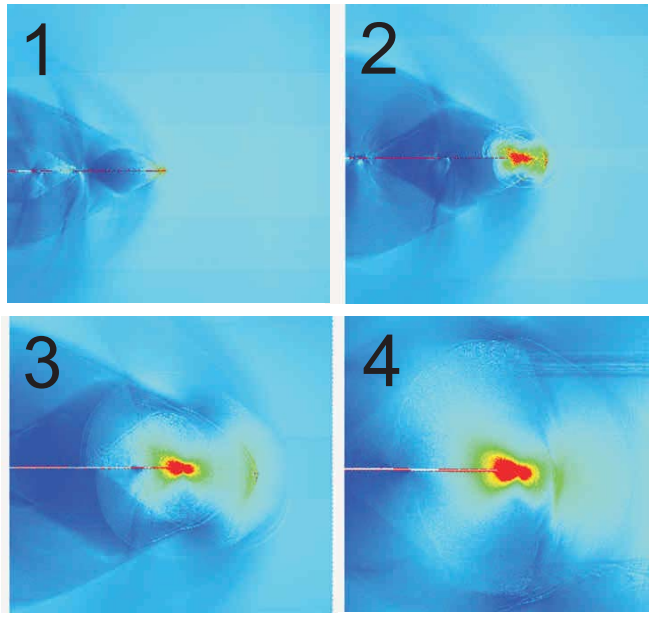

Figure 10.19.: Potential energy field around the crack tip for various times, suddenly stopping mode II crack.

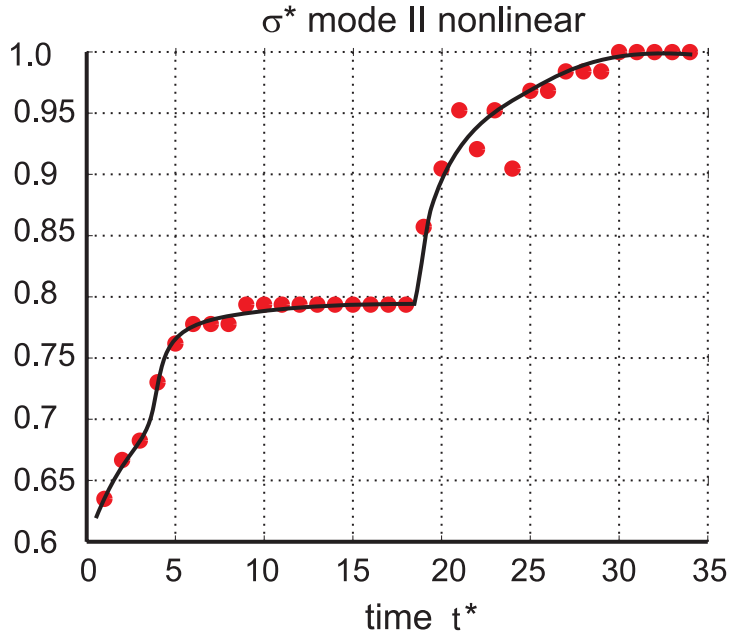

Figure 10.20.: Normalized stresses σ^* versus time, suddenly stopping supersonic mode II crack.

11. Mechanical and physical properties of three-dimensional solids

Thus far, we have focused attention to one- and two dimensional models of fracture. For cracks under mode I and mode II loading, the 2D setup is a reasonable choice since the elastic problem is of two-dimensional nature [78]. For mode III cracks under anti-plane shear loading, however, two dimensional models can not be used and three dimensional models are necessary.

We dedicate this chapter to the discussion of mechanical and physical properties of three-dimensional solids associated with a face-centered cubic lattice. The aim is to determine the elastic properties and fracture surface energy for computer experiments of mode III cracks, similarly as done in Chapter 5 for the two-dimensional solids.

11.1. Elastic properties, wave speeds and fracture surface energy for the harmonic potential

Here we focus on harmonic interactions between atoms as defined in equation (2.6). As in the two-dimensional models, atoms only interact with their nearest neighbors. Additional results for elastic properties will be given for LJ and EAM solids.

11.1.1. Elastic properties and wave speeds for cubical crystal orientation

We assume that nearest neighbor distance is $r_0 = 2^{1/6} \approx 1.12246$, so that the lattice constant $a_0 = \sqrt{2}r_0 = 2^{1/6}\sqrt{2} \approx 1.5874$. For mass $m = 1$, the density is given by $\rho \approx 1$, since the volume of one unit cell is $V = 4$, and there are four atoms per unit cell with mass unity. The atomic volume is $\Omega_0 = 1$.

In a fcc crystal with pair potential atomic interactions [26],

$$c_{1111} = b_{1111}/\Omega_0, \quad c_{1122} = c_{1212} = b_{1122}/\Omega_0. \tag{11.1}$$

The fact that $c_{1122} = c_{1212}$ shows that the Cauchy relation holds. For a cubical crystal orientation (that is, $x = [100]$ and $y = [010]$ and $z = [001]$), the nonzero factors b_{ijkl} are given by

$$b_{1111} = \frac{4\phi''\left(a_0/2\right)^4}{\left(a_0/\sqrt{2}\right)^2}, \quad b_{1122} = b_{1212} = \frac{2\phi''\left(a_0/2\right)^4}{\left(a_0/\sqrt{2}\right)^2}. \tag{11.2}$$

Crystal orientation	k	E	μ	ν	c_l	c_s	c_r
[100]	$36\sqrt[3]{2} \approx 28.57$	48	18	0.33	8.48	4.24	3.86
[100]	$72\sqrt[3]{2} \approx 57.14$	96	36	0.33	12	6	5.56

Table 11.1.: Elastic properties and wave speeds associated with the harmonic potential (see equation (2.6)) in a 3D solid for different choices of the spring constant k, cubical crystal orientation.

The second derivative of the potential $\phi'' = k$, where k is the spring constant associated with the harmonic potential. The shear modulus can be expressed in terms of the spring constant and the nearest neighbor distance as

$$\mu = \frac{r_0^2}{2} k. \tag{11.3}$$

For $k_0 = 28.57$ this leads to numerical values $c_{1111} \approx 36$, and $\mu = c_{1122} = c_{1212} \approx 18$. Note that $\lambda = 2\mu$, and therefore Young's modulus is

$$E = \frac{\mu\,(3\lambda + 2\mu)}{\lambda + \mu} = \frac{8}{3}\mu \approx 48, \tag{11.4}$$

and the shear modulus is $\mu = c_{1122} = c_{1212} \approx 18$. Poisson's ratio is determined to be

$$\nu = \frac{\lambda}{2(\lambda + \mu)} = 1/3. \tag{11.5}$$

This yields wave velocities

$$c_l = \sqrt{\frac{(1-\nu)}{(1+\nu)(1-2\nu)}\frac{E}{\rho}} \approx 8.48, \quad c_s = \sqrt{\frac{\mu}{\rho}} \approx 4.24, \tag{11.6}$$

and finally the Rayleigh wave speed is given by

$$c_r \approx 0.91 c_s \approx 3.86. \tag{11.7}$$

For $k_1 = 2k_0 \approx 57.14$, the wave speeds are a factor of $\sqrt{2}$ larger. The results are summarized in Table 11.1.

Figure 11.1 shows the numerically estimated elastic properties associated with the harmonic potential with $k_0 = 28.57$ in the [100] crystal orientation, with Poisson relaxation. The values for the elastic properties show good agreement. Additional results are shown in Figure 11.2 for uniaxial loading without Poisson relaxation, and in Figure 11.3 for triaxial loading. Note that under uniaxial loading as shown in Figure 11.1 and Figure 11.2, Young's modulus increases slightly with strain, while it decreases with strain under triaxial loading as shown in Figure 11.3.

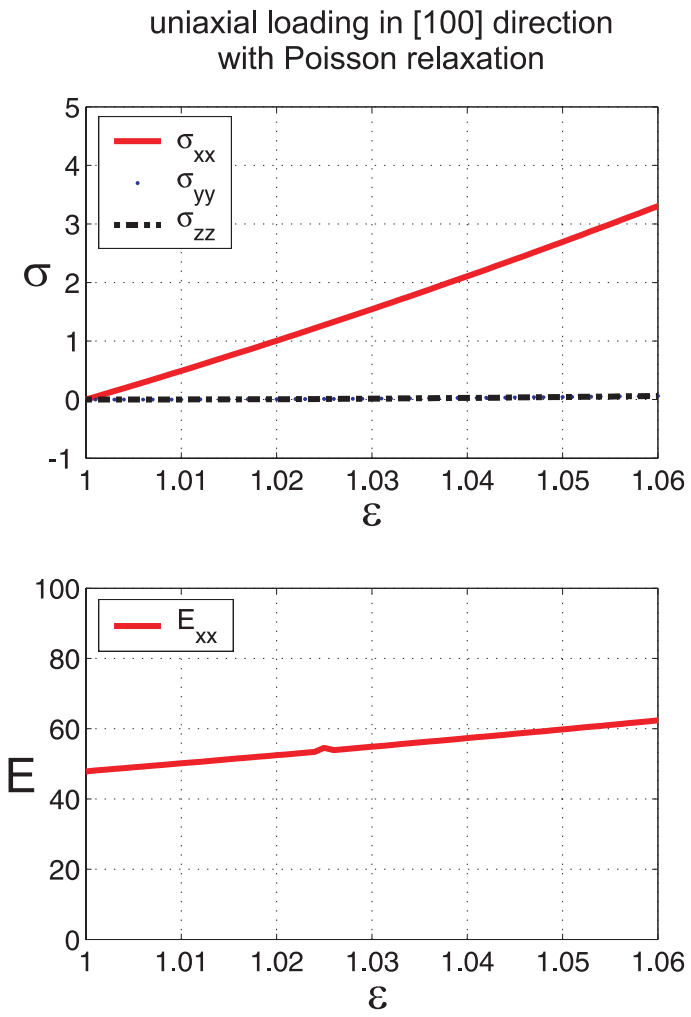

Figure 11.1.: Elastic properties associated with the harmonic potential, [100] crystal orientation, with Poisson relaxation. Poisson ratio is $\nu \approx 0.33$ and is approximately independent of the applied strain. The plot shows the elastic properties as a function of strain.

11.1.2. Elastic properties in different crystal orientations

Here we show some numerical results of elastic properties for uniaxial tension with Poisson relaxation in the [110] and the [111] direction.

Figure 11.4 (a) plots the results for uniaxial tension with Poisson relaxation in the [110] direction. Young's modulus is approximately $E \approx 72$. It is notable that Poisson's ratio is different in the y and the z direction. The relaxation in the z direction is $\nu_z \approx 0.5$, and in the y direction there is no relaxation. This result, as well as the values for Young's modulus can also be obtained from continuum mechanics theories based on generalized Hooke's law (calculation not shown here). Unlike the two-dimensional triangular lattice, the three-dimensional fcc lattice is not isotropic.

Figure 11.4 (b) plots the results for uniaxial tension with Poisson relaxation in the [111] direction. Young's modulus is approximately $E \approx 100$. Poisson's ratio is identical

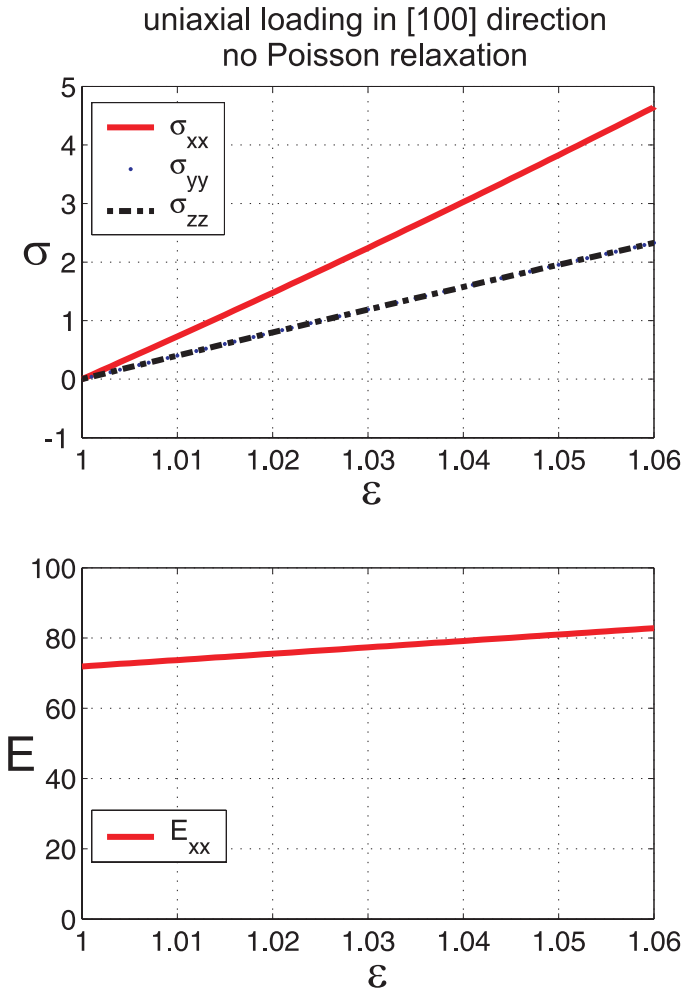

Figure 11.2.: Elastic properties associated with the harmonic potential, [100] crystal orientation, without Poisson relaxation. The plot shows the elastic properties as a function of strain.

in the y and z direction, and is found to be $\nu \approx 0.2$. As for the loading in [110], this result can also be obtained from continuum mechanics theories. The elastic properties in the [110] and [111] direction are summarized in Table 11.2.

11.1.3. Fracture surface energy

The fracture surface energy can be expressed as

$$2\gamma = N_b \rho_A \Delta\phi, \tag{11.8}$$

where $\rho_A = 2/a_0^2 \approx 0.794$ is the density of surface atoms along the fracture plane, and $\Delta\phi$ denotes the potential energy per bond. The factor $N_b = 4$ since each atom has 4 bonds across the [100] plane (thus (010) crack faces). The potential energy per bond is given by

$$\Delta\phi = \frac{1}{2} k_0 (r_{\mathrm{rbreak}} - r_0)^2 \tag{11.9}$$

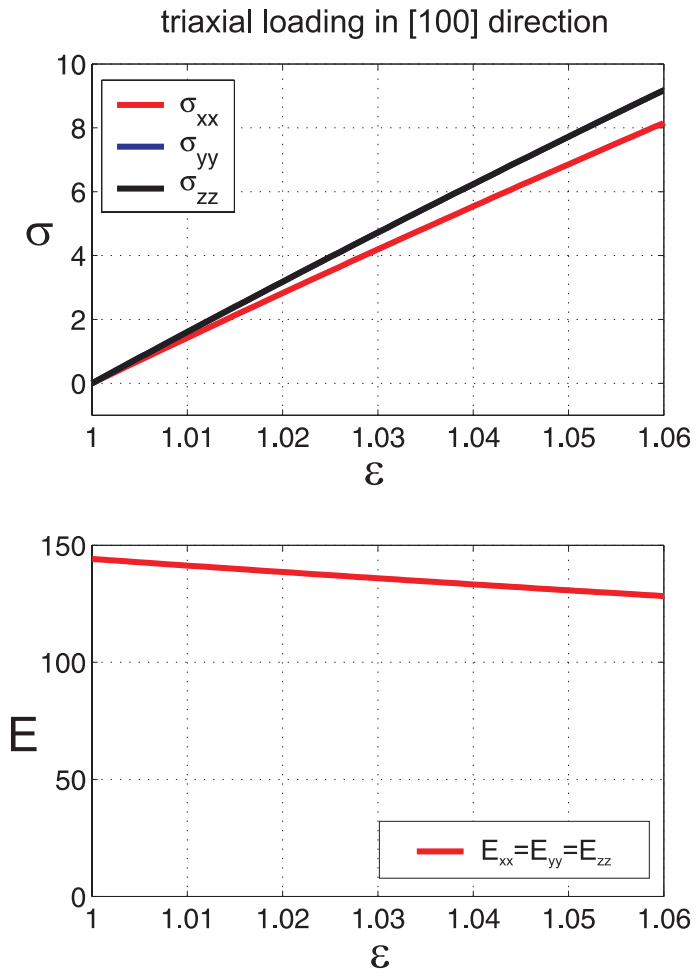

Figure 11.3.: Elastic properties associated with the harmonic potential, [100] crystal orientation, triaxial loading. The plot shows the elastic properties as a function of strain.

and is $\Delta\phi \approx 2.26 \times 10^{-3}$ for $r_{\text{rbreak}} = 1.17$ and $k_0 \approx 57.32$.

Therefore, the fracture surface energy $2\gamma \approx 0.21$. As in the two-dimensional case, note that $\gamma \sim k_0$ and therefore $\gamma \sim E$.

11.2. Elastic properties of LJ and EAM potentials

Figure 11.5 shows the stress-strain curves for a pair potential and a multi-body potential. Figure 11.5 (a) shows the results for a LJ potential with nearest neighbor interaction, and Figure 11.5 (b) shows the results for an EAM potential for nickel. In both cases, the [110] direction is very weak and fails at about 12 percent strain in the case of an LJ potential, and it fails at a strain of only 8 percent in the case of an EAM potential. In contrast to this, the cohesive strain in the [100] direction is largest in the EAM potential and smaller when the LJ potential is used. The critical cohesive strains are summarized in Table 11.3.

An important difference to the harmonic potentials studied in the previous section is

Loading direction	k	E	ν_y	ν_z
[110]	$36\sqrt[3]{2} \approx 28.57$	72	0	0.5
[111]	$36\sqrt[3]{2} \approx 28.57$	100	0.2	0.2

Table 11.2.: Elastic properties associated with the harmonic potential (see equation (2.6)) in a 3D solid for different choices of the spring constant k and [110] and [111] crystal orientation. The plot shows the elastic properties as a function of strain.

Potential	$\varepsilon_{\text{coh}}^{[100]}$	$\varepsilon_{\text{coh}}^{[110]}$	$\varepsilon_{\text{coh}}^{[111]}$
LJ	0.25	0.17	0.13
EAM	0.35	0.23	0.08

Table 11.3.: Cohesive strains $\varepsilon_{\text{coh}}^{[100]}$, $\varepsilon_{\text{coh}}^{[110]}$ and $\varepsilon_{\text{coh}}^{[111]}$ for the LJ potential and the EAM potential. In all potentials, the weakest pulling direction is the [110] direction. The plot shows the elastic properties as a function of strain.

that Young's modulus significantly decreases with strain, leading to a strong softening effect.

11.3. Summary and discussion

The results reported in this chapter provide analytical expressions for the elastic properties of three-dimensional solids with harmonic interatomic potentials. The analytical predictions were verified by numerical calculations of the elastic properties. We also report results of elastic properties of fcc solids with LJ interatomic potential and EAM potentials. An interesting observation was that when pulling in the [110] direction, the solid fails at a very low strain (and at very low stress) compared to other pulling directions ([100] and [111]). This phenomenon is likely due to the strong softening of the bonds in the LJ and EAM potential. In contrast, such phenomenon does not appear in the harmonic potential since the bonds do not weaken with stretching (see Figures 11.1 and Figure 11.4). In fact, Young's modulus in the [110] direction is in between the values of the [100] and [111] direction. Similar observations have been made in earlier studies for LJ pair potentials [6]. Our results show that this also applies to EAM potentials. Therefore, it is expected that this phenomenon should occur in metals.

The observation of this "weak" crystal orientation could potentially have impact on the design of nanowires or interconnects in integrated circuits. Future research would be necessary to clarify further impact of this finding.

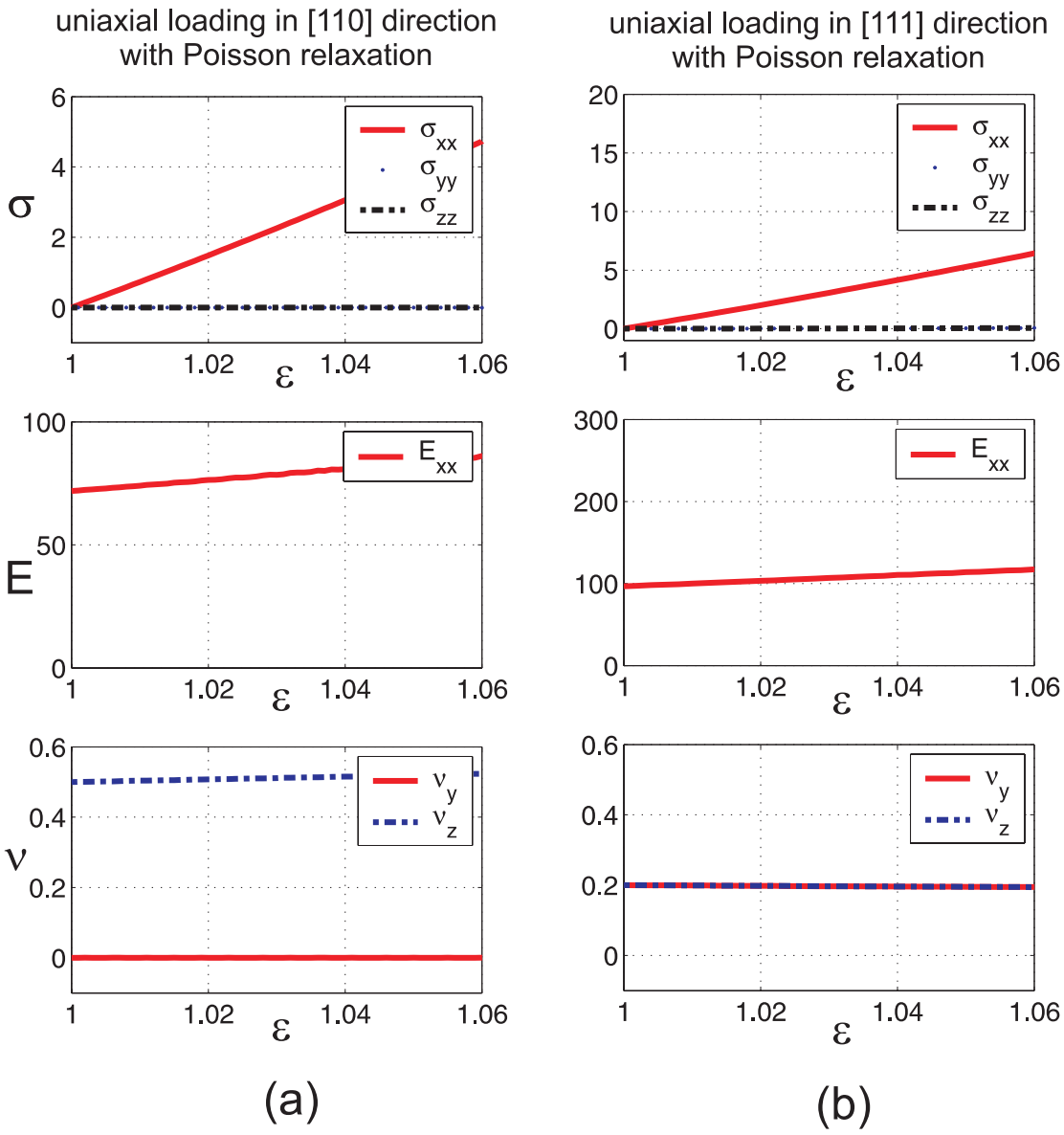

Figure 11.4.: Elastic properties associated with the harmonic potential, (a) [110] and (b) [111] crystal orientation, uniaxial loading with Poisson relaxation. The plot shows the elastic properties as a function of strain.

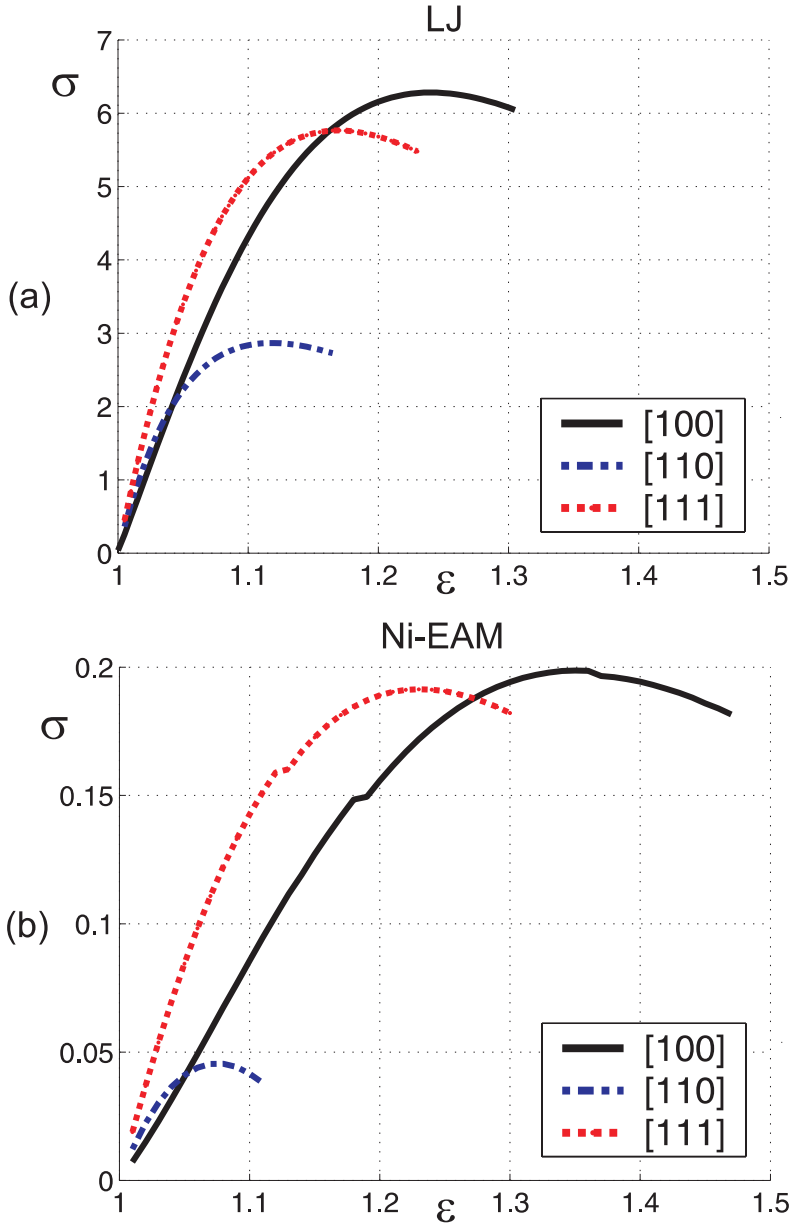

Figure 11.5.: Elastic properties associated with (a) LJ potential, and (b) an EAM potential for nickel [59], uniaxial loading in [100], [110] and [111] with Poisson relaxation. The plot shows the elastic properties as a function of strain.

12. Dynamic fracture under mode III loading

In this chapter, we study three-dimensional models of mode III cracks. A schematic of the mode III antiplane shear crack loading is shown in Figure 12.1.

The study of mode III cracks is motivated by the fact that in mode III, there exists only one wave speed associated with crack dynamics, the shear wave speed c_s. This simplifies the theoretical continuum mechanics analysis of the crack dynamics. Recently, a closed form solution for the crack speed of a crack propagating in a stiff material layer embedded in a soft matrix was derived [44]. The analysis revealed that the same concept of a characteristic energy length scale χ also holds for mode III cracks. The most important objective of this chapter is therefore to validate this finding using atomistic simulations similar to those presented in Section 7.5.

To our knowledge, mode III cracks have rarely been studied with molecular-dynamics methods before. Some simulations were reported in the literature, but these focused on cracks in ductile materials under mode III loading [249, 191].

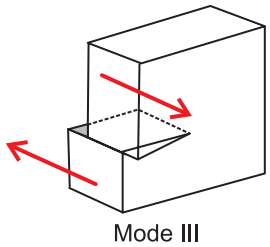

Figure 12.1.: Schematic of mode III crack loading.

According to classical linear elastic theories [78], for mode III cracks all velocities below the shear wave speed are admitted, thus

$$v \leq c_\mathrm{s}. \tag{12.1}$$

The allowed crack propagation speeds for mode III cracks in linear and nonlinear solids are shown in Figure 12.2. Similar to the results of mode I and mode II cracks where cracks can move faster than the wave speeds in the material, mode III cracks can also move faster than the shear wave speed and thus become supersonic once the material stiffens with strain. This phenomenon was verified using a tethered LJ potential (results not shown here).

The objectives of the studies in this chapter are summarized as follows. First, we verify that the limiting speed associated with a crack propagating in a harmonic lattice agrees with the theoretical prediction. We then discuss simulation results of crack

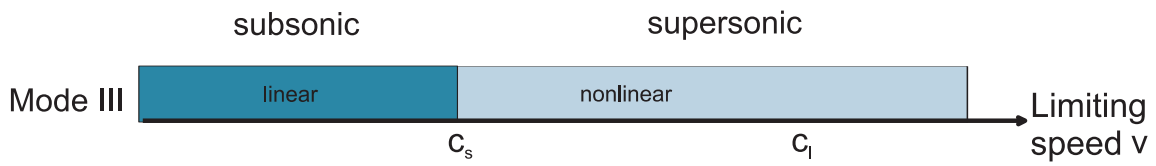

Figure 12.2.: Allowed velocities for mode III crack propagation, linear and nonlinear case.

motion in a thin stiff layer embedded in a soft matrix, also yielding supersonic crack motion (similarly to the Broberg problem discussed in Chapter 7). The recently derived analytical continuum mechanics solution of the problem is quantitatively compared with the molecular-dynamics results [44]. We find that the energy length scale described in Chapter 7 also applies to mode III cracks.

12.1. Atomistic modeling of mode III cracks

Previous studies have provided evidence that 3D molecular-dynamics is a good framework to investigate the dynamics of fracture. For instance, Abraham and coworkers [6] studied dynamic fracture in a three-dimensional solid with LJ interactions. They showed that unlike in two dimensions where the LJ potential yields a very brittle solid (see Figure 8.1), in three dimensions the LJ potentials leads to a very ductile solid [12]. The researchers studied the dynamics of fracture in different crystal orientation and provided a Schmidt factor analysis [9]. Later, a three-dimensional model using harmonic interactions in the bulk, and using the concept of a weak fracture path was adopted in simulations of dynamic crack propagation [11]. This model corresponds to a perfectly brittle system which allows to study the dynamics of fracture in a clean environment.

Here we adopt a similar approach and confine crack motion along a weak layer, which is characterized by a fracture surface energy much smaller than in the bulk. This confined fracture path helps to avoid crack branching and allows to purely focus on the dynamics of cracks. In previous studies, a weak LJ layer was used to model the weak fracture layer [11]. Here we assume a homogeneous material with harmonic interactions. The interactions are defined according to equation (5.1.3) in the bulk, and according to equation (5.19) across the weak fracture layer.

The slab is initialized at zero temperature and loaded according to mode III, and we also give a slight mode I loading. The loading rates are $\dot{\varepsilon}_{xx} = 0.000\,1$ for mode I and the (engineering) shear rate $\dot{\gamma}_{xz} = 0.000\,2$. The loading is kept up during a loading time t^l, and then the boundaries are held fixed.

12.2. Mode III cracks in a harmonic lattice–the reference systems

The results show that the limiting speed of mode III cracks in a harmonic lattice is given by the shear wave speed. This was verified for two choices of the spring constant

$k_1 \approx 57.32$ and $k_1 = k_0/2$. This observation is in agreement with the predictions by continuum mechanics theories [78]. The crack tip history for the soft and stiff reference system is shown in Figure 12.3. In both systems, the loading is stopped at $t^l = 135$. Both soft and stiff systems approach the theoretical limiting speeds. Fracture initiation times are $t_{\text{init}}^{\text{soft}} \approx 47$ for the soft system and $t_{\text{init}}^{\text{stiff}} \approx 41$.

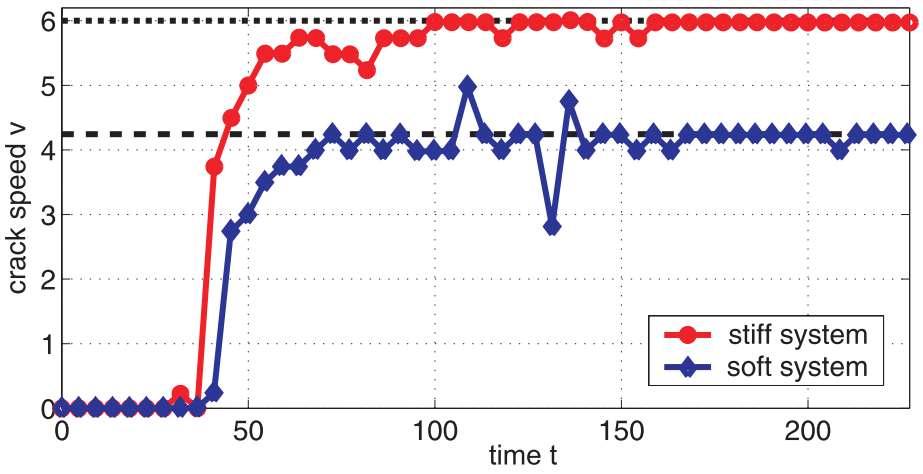

Figure 12.3.: Crack tip velocity history for a mode III crack propagating in a harmonic lattice for two different choices of the spring constant k_i. The dotted line shows the limiting speed of the stiff reference system, and the dashed line shows the limiting speed of the soft reference system. Both soft and stiff systems approach the corresponding theoretical limiting speeds.

12.3. Mode III crack propagation in a thin stiff layer embedded in a soft matrix

Here we use the same geometry as shown in Figure 7.9, with the difference that the slab is predominantly under mode III loading. The main objective is to compare the molecular-dynamics simulation results of the curve $v(h/\chi)$ with the theoretical prediction.

According to theory [44], the energy release rate for a crack propagating in a stiff layer with width h is given by

$$G = \frac{h\sigma_{xz}^2}{\mu} f(v, c_0, c_1) \tag{12.2}$$

where f is a function only of the elastic properties of the layer and matrix material as well as the crack propagation velocity. Using the Griffith condition $G = 2\gamma$, equation (12.2) can be numerically solved for v. Therefore, the crack velocity can be expressed as

$$v = \tilde{f}(c_0, c_1, h/\chi) \tag{12.3}$$

where

$$\chi = \beta \frac{\gamma\mu}{\sigma_{xz}^2} \tag{12.4}$$

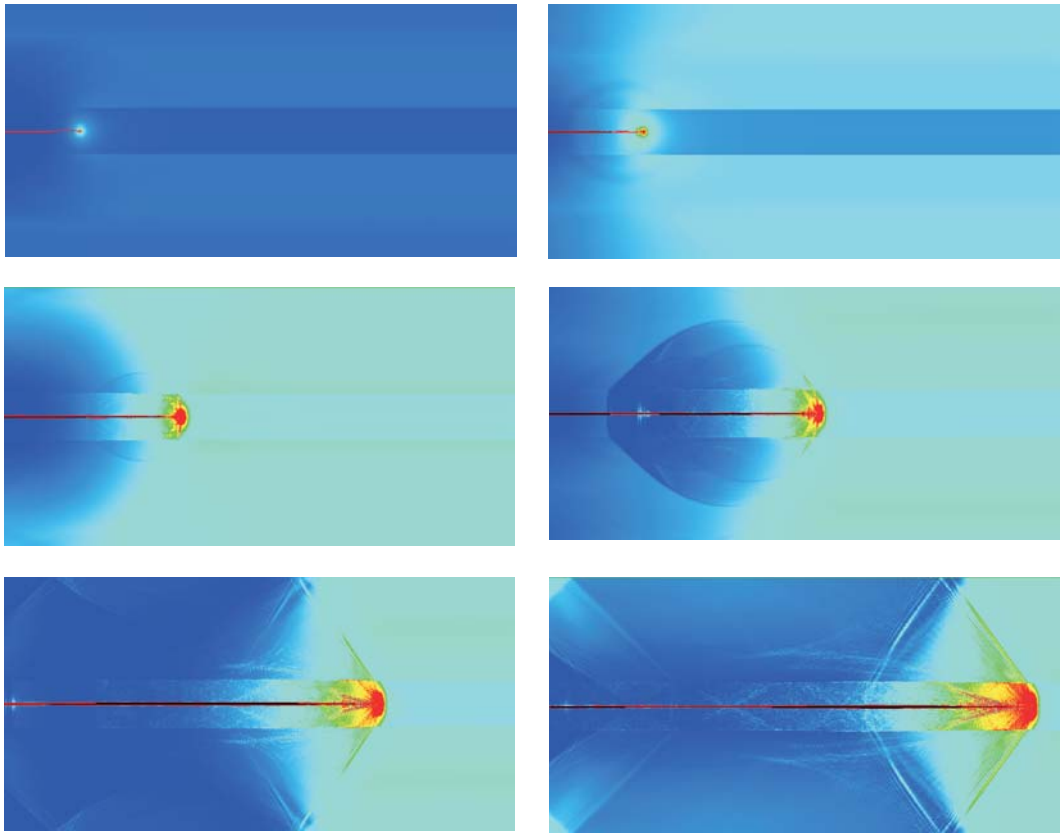

Figure 12.4.: Mode III crack propagating in a thin elastic strip that is elastically stiff. The potential energy field is shown while the crack propagates supersonically through the solid. The stiff layer width is $h = 50$.

denotes the characteristic energy length scale. The characteristic energy length scale is defined such that h/χ equals one when the increase in crack speed is 50 % of the difference between the shear wave speed of soft and stiff material. Most importantly, the crack speed should only depend on the ratio of the layer width h to the characteristic energy length scale χ.

According to the values of γ, μ and the applied shear stress σ_{xz} for loading time of $t^l = 135$, $\gamma\mu/\sigma_{xz}^2 \approx 1$.

Figure 12.4 shows a mode III crack propagating in a thin elastic strip which is elastically stiff. The crack propagates supersonically through the solid, and the stiff layer width is $h = 50$. Figure 12.5 depicts the results of a set of calculations to check of the scaling law for mode III dynamic fracture. The continuous line corresponds to the analytical continuum mechanics solution, and the data points are obtained for different simulation conditions. In the molecular-dynamics simulations, the loading σ_{xz}, the fracture surface energy γ as well the elastic properties E are changed independently. The results show that all velocities fall on the same curve. From comparison of molecular-dynamics results to the continuum solution, the parameter $\beta \approx 11$ and therefore $\chi \approx 11$. When the inner layer width h approaches this length scale, the crack speed has increased 50 % of the difference of soft and stiff shear wave speed.

For realistic experimental conditions under 0.1 % shear strain and a crack propagating within a thin steel layer, χ is on the order of millimeters. Further details will be included in a forthcoming publication [43].

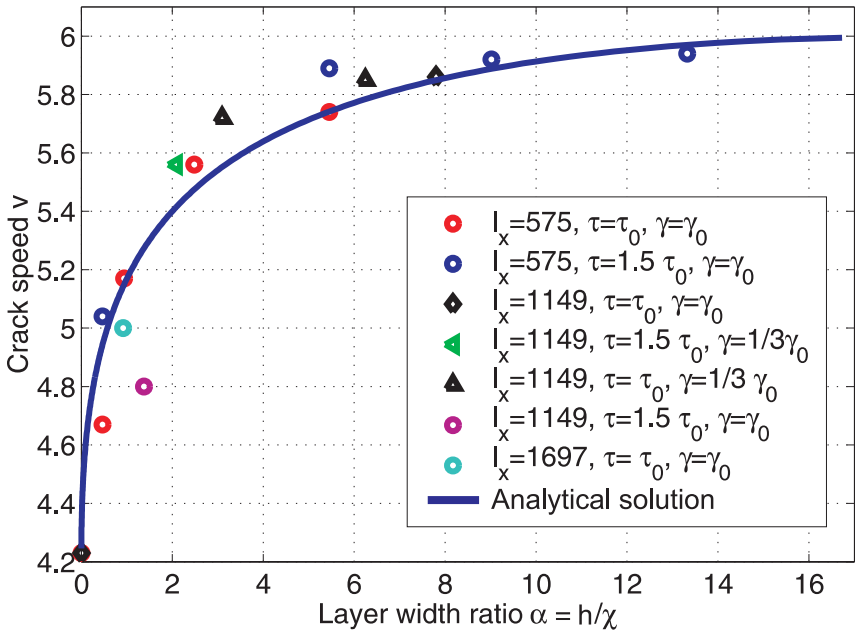

Figure 12.5.: Check of the scaling law of the mode III Broberg problem. The continuous line refers to the analytical continuum mechanics solution [44] of the problem. The parameters $\gamma_0 = 0.1029$ and $\tau_0 = 0.054$.

12.4. Suddenly stopping mode III crack

In Chapter 10, we discussed suddenly stopping mode I and mode II cracks in linear and nonlinear materials. We have conducted similar studies for a suddenly stopping mode III crack. Theory predicts that the dynamics of the suddenly stopping mode III crack is very similar to the mode I crack [78]. An important difference of the suddenly stopping mode III crack to the mode I case is that the static field spreads out in the whole area around the crack tip, and not only in the line ahead of the crack tip as in mode I [78].

Figure 12.6 shows the potential energy field close to a suddenly stopping mode III crack. The simulation technique is the same as described in Chapter 10 with the only difference that a three-dimensional model is used.

The result is very reminiscent of the mode I simulation results discussed in Chapter 10. The static field spreads out with the shear wave speed as soon as the crack is stopped. In snapshot "1" of Figure 12.6, the crack propagates at a velocity close to the shear wave speed prior to stopping. Behind the crack, the static field is transported with the Rayleigh wave speed. The Rayleigh surface wave can clearly be observed in Figure 12.6, snapshots "3" and "4". The static stress field spreads out in the whole area around the crack tip, and not only in the line ahead of the crack tip as in mode I [78].

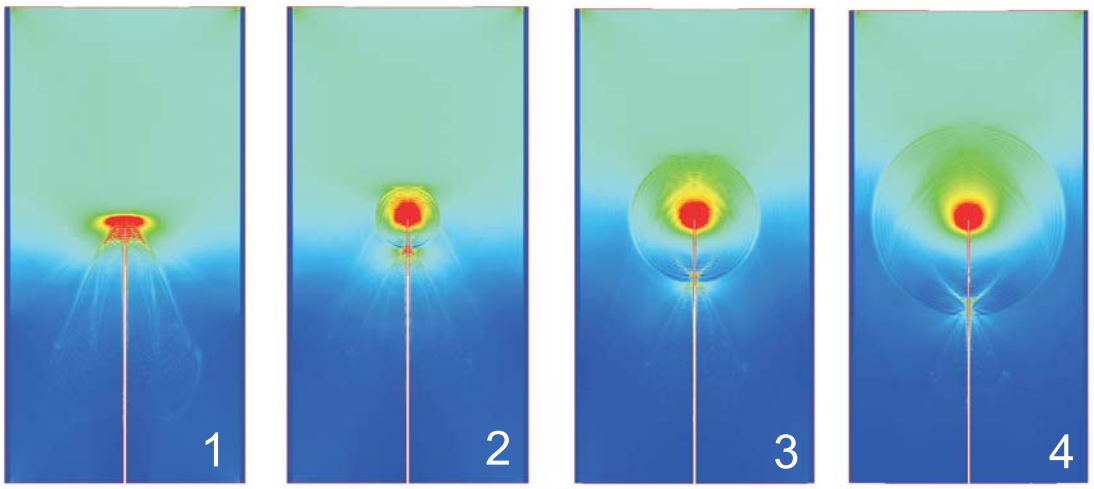

Figure 12.6.: Suddenly stopping mode III crack. The static field spreads out behind the shear wave front after the crack is brought to rest.

12.5. Discussion

The limiting speeds of mode III cracks are found to be in agreement with the predicted velocities from the continuum mechanics analysis. With the results reported in this chapter, we conclude that for all three modes of loading, the predicted limiting speeds agree well with the observation in atomistic simulations.

The most important result of this chapter is that the scaling law found for mode I cracks also holds for the mode III case. A quantitative comparison with the theory provided good agreement. This result strongly corroborates the concept of the energy length scale proposed earlier. The results also suggest, in accordance with the continuum analysis of the problem, that supersonic mode III crack motion is possible [44]. The results are also in agreement with recent theoretical analysis of supersonic mode III crack propagation in nonlinear stiffening materials [99]. Preliminary molecular-dynamics simulations of crack motion in a material defined by the tethered LJ potentials have also shown supersonic mode III crack propagation (the results will be discussed in a forthcoming publication).

Further results of a suddenly stopping mode III crack agree qualitatively with the continuum mechanics prediction of a suddenly stopping mode III crack. The static field is found to spread out behind the shear wave front nucleated by the stopping crack. In harmonic lattices, the mode III carries no inertia, as the mode I crack and the sub-Rayleigh mode II crack.

13. Summary and discussion of the results in the area of brittle fracture

The studies in the area of dynamic fracture focused on the following points.

- Comparison of atomistic results with continuum mechanics theory predictions (in particular crack limiting speed, crack tip instability speed and deformation fields).
- Investigation of hyperelastic effects in dynamic fracture (in particular crack limiting speed and crack tip instability speed).
- Effect of geometric confinement (cracks in thin layers) and crack propagation along interfaces of dissimilar materials.

The first study discussed in Chapter 4 centered on a one-dimensional model of dynamic fracture. The appeal of the one-dimensional model is that many of the physical phenomena of dynamic fracture, such as maximum crack speed and a condition for crack initiation similar to the Griffith theory, also appear in this simple model. An important aspect was that analytical expressions for the nonlinear dynamics of fracture could be derived (see Section 4.3). The analytical model predicted crack motion faster than the speed of sound, if there is an elastically stiff zone near the crack tip. The atomistic model with harmonic interactions is found to reproduce the predictions of the linear elastic continuum theory well. The simulations carried out with nonlinear interatomic potentials revealed that a small zone with stiff elastic properties at the crack tip significantly changes the dynamics and allows the crack to break through the sound barrier. This observation is in agreement with the theoretical predictions of the model described in Section 4.3. As shown in Figure 4.11 (a), the crack propagation speed depends critically on the onset strain of the hyperelastic effect and therefore, the crack speed is highly sensitive to the size of the hyperelastic region. The deformation fields near the one-dimensional crack in nonlinear materials agrees reasonably well with the predictions by continuum theory, as shown in Figure 4.11 (b).

After studying the one-dimensional crack, we moved on to two-dimensional models. The first problem studied was the elastic properties of two-dimensional solids in Chapter 5. We demonstrated that the choice of the potential allows to construct model materials with the objective to probe the effect of specific material properties on the dynamics of fracture. One of the examples of such model materials is the biharmonic potential. This potential yields a solid composed of two linear elastic materials, with one Young's modulus associated with small strains and one with large strains, representing a

simplistic model material for hyperelasticity. Further, we calculated the fracture surface energy for different choices of the interatomic potential serving as input parameter for the prediction of crack initiation time by the Griffith model [78].

A quantitative comparison of the deformation fields near a rapidly propagating mode I crack in a harmonic lattice revealed that the continuum theory predictions of angular variation of stress and strain agree well with the results of atomistic simulations (Chapter 6). We find that the prediction that the hoop stress becomes bimodal [246] at a critical crack propagation speed is reproduced in atomistic calculations. The occurrence of the bimodal hoop stress is an important aspect in the theories of crack tip instabilities. In summary, the studies in Chapter 6 (together with the results of the one-dimensional crack reported in Chapter 4) reveal that atomistic simulations with harmonic potentials are a good model for the linear elastic continuum theory. The results in this chapter and the results of the one-dimensional model with harmonic interactions both show reasonable agreement with the linear elastic continuum theory [78].

In Chapter 7, we changed the large-strain elastic properties while keeping the small-strain elastic properties constant to systematically investigate the effect on crack dynamics. The main finding is that the elasticity of large strains can dominate the dynamics of fracture, in contrast to the predictions by many existing theories [78]! With the new concept of the characteristic energy length scale χ in dynamic fracture we could explain experimental and computational results. This length scale immediately explains under which conditions hyperelasticity is important and when it can be neglected. Cracks moving in solids absorb and dissipate energy from the surrounding material. The new length scale characterizes the zone near the crack tip from which the crack draws energy to sustain its motion. When materials are under extreme stress, this length scale extends only a few dozens nanometers. One of the important consequences of this is that cracks can move supersonically in contrast to existing theories. The finding that the crack speed increases continuously as the size of the hyperelastic region expands (shown in Figure 7.4 and Figure 7.5) can be explained by the interplay of the hyperelastic region size and the characteristic energy length scale, and is in qualitative agreement with the findings in the one-dimensional model depicted in Figure 4.11 (a). Stimulated by the results reported in Chapter 7 [32], intersonic mode I cracks as shown in Figure 7.6 have recently been verified in the laboratory [172].

In the following chapter, we investigated the effect of hyperelasticity on the stability of cracks. It is known that cracks propagate straight at low velocities, but start to wiggle when the crack speed gets larger [5, 70]. One of the theoretical explanations [78, 246] is that the hoop stress becomes bimodal at a speed of 73 % of Rayleigh-wave speed. Indeed, we find in our atomistic simulation that a crack in a harmonic lattice becomes unstable at a speed of about 73 % of Rayleigh-wave speed, in good agreement with the continuum theory. However, if a softening potential is used, the instability occurs at lower speeds! In contrast, we demonstrated that if material stiffens with strain, the instability occurs at higher speeds than predicted by theory (see Figure 8.5). We therefore conclude that hyperelasticity governs the dynamic crack tip instability. Another observation is the nucleation of intersonic daughter cracks from sub-Rayleigh mother cracks as shown in Figure 8.11. Such deformation mode has, to our knowledge, not been described before. This underlines the fact that sub-Rayleigh cracks may serve

as ready sources for secondary cracks similarly to the mother-daughter mechanism known from mode II cracks [83].

Additional studies focused on cracks at interfaces. We carried out studies of mode I and mode II cracks along interfaces of elastically dissimilar materials. In mode I, we observed that cracks are limited by the Rayleigh-wave speed of the stiffer of the two materials provided that sufficient loading is applied. A mother-daughter mechanism, similar as known to exist at interfaces of identical materials under mode II loading [83], is observed that allows the crack to break through the sound barrier. In mode II, we find that the crack speed is limited by the longitudinal wave speed of the stiff material and observe a mother-daughter-granddaughter crack mechanism. Whereas a mother-daughter mechanism has not been observed in mode I cracks, the mother-daughter-granddaughter mechanism has been observed in mode II cracks along interfaces of elastically harmonic and anharmonic materials [11]. Most importantly, experimental evidence was reported for the existence of such mechanisms for crack propagation along interfaces of aluminum (stiff) and PMMA (soft) [182] corresponding to our atomistic model. Our molecular-dynamics simulations reproduce some of the experimental findings.

The next chapter was devoted to a discussion of suddenly stopping cracks. The main result was that mode I cracks in harmonic lattices carry no inertia, and the static field spreads out behind the shear wave front immediately after the crack is stopped. This result matches the prediction by continuum theory [78]. A comparison of the suddenly stopping mode I cracks with experimental results [230] also reveals good agreement. The results in reported in this Chapter are in accordance with the results of a suddenly stopping one-dimensional crack shown in Figure 4.7. As soon as the crack stops, the strain field of the solution corresponding to zero crack velocity is spread out. We have then shown that mode II cracks behave differently than mode I cracks: In agreement with the predictions by continuum mechanics theories of suddenly stopping intersonic cracks [117], an intersonic mode II crack does carry inertia and the static field does not spread out until the mother crack has reached the stopped daughter crack. In the nonlinear cases of mode I and mode II cracks, the wave fronts are smeared out and the static field is not instantaneously reached but after all trails of waves have passed.

In the last two remaining chapters we focused on the dynamics of mode III cracks by using three-dimensional atomistic simulations. Firstly, we considered the mechanical and physical properties of three-dimensional solids. We discussed the elastic properties and compare theoretical predictions with numerical estimates for various crystal orientations in an fcc crystal. As in the two-dimensional case, we also calculated the fracture surface energy. The results of the preceding chapter on the mechanical and physical properties of three-dimensional solids provide important information for the studies discussed in Chapter 12. After studying cracks in harmonic lattices and showing agreement of the corresponding limiting speed (the shear wave speed), we focused on the critical energy length scale χ. We find that the same concept as that discovered in Chapter 7 also holds for mode III cracks. A quantitative comparison with an analytical continuum theory solution [44] showed good agreement. For realistic experimental conditions and cracks propagation within a thin steel layer, the characteristic energy length scale was estimated to be on the order of millimeters. Further studies of mode III cracks included suddenly stopping cracks. We have shown that, as for sub-Rayleigh mode I and mode

II cracks, mode III cracks in harmonic lattices carry no inertia [78].

13.1. Hyperelasticity can govern dynamic fracture

In this thesis, the effect of the elasticity of large strains on the dynamics of fracture was was one of the main points of interest. Here we discuss the role of hyperelasticity in more general terms.

Our results suggest that hyperelasticity has (1) an effect on the crack speed as well as (2) on the instability dynamics of cracks. Unlike in some previous studies (e.g. [5]), we used the concept of the weak fracture layer to separate the two problems of limiting speed and instability from one another to obtain clean simulation and analysis conditions. This allowed us to investigate the conditions under which hyperelasticity governs the dynamics of fracture.

Our approach of defining model materials seems to be a reasonable method to investigate some of the fundamentals of dynamic fracture, and may be considered advantageous over methods where the peculiarities of a specific material are accounted for. In several previous studies, due to the complexities of the potential it was difficult to draw general conclusions about crack dynamics in brittle solids (e.g. [111, 104]).

13.1.1. Limiting speed of cracks

We have shown that the key to understand the dynamics of cracks in hyperelastic materials is a new length scale that characterizes the zone near the crack tip from which the crack draws energy to sustain its motion.

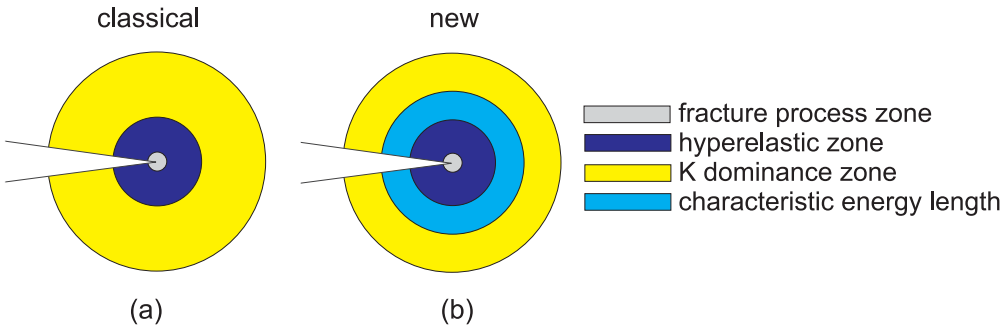

Figure 13.1.: Different length scales associated with dynamic fracture. Subplot (a) shows the classical picture [78], and subplot (b) shows the picture with the new concept of the characteristic energy length χ.

This characteristic length scale is found to be proportional to the fracture surface energy and elastic modulus, and inversely proportional to the square of the applied stress,

$$\chi \sim \frac{\gamma E}{\sigma^2}. \tag{13.1}$$

Contrary to the common belief, the crack does not need to transport energy from regions far away from its tip, rather only from a small local region described by the characteristic

length scale. The assumption of linear elasticity, and hence the classical theories, fails if the hyperelastic zone becomes comparable to the local energy flux zone. This is because in soft materials energy is transported slower, in stiff materials faster. Correspondingly, the crack velocity becomes slower or larger once the hyperelastic region is sufficiently large. If the region around the crack tip becomes stiff due to hyperelasticity, more energy can flow to the crack tip in shorter time. In the opposite, energy transport gets slower when there is a local softening zone around the crack tip. Therefore, hyperelasticity is crucial for understanding and predicting the dynamics of brittle fracture.

When hyperelasticity dominates, cracks can move faster than all elastic waves as shown in Figure 7.8. This is in clear contrast to the classical theories in which it is believed that the longitudinal elastic wave speed is an impenetrable upper limit of crack speed. Such phenomenon can only be understood from the viewpoint of hyperelasticity.

Hyperelasticity dominates fracture energy transport when the size of the hyperelastic zone approaches the energy characteristic length. Under normal experimental conditions, the magnitude of stress may be one or two orders of magnitude smaller than that under atomic simulations. In such cases, the characteristic length is relatively large and the effect of hyperelasticity on effective velocity of energy transport is relatively small. At about one percent of elastic strain, the energy characteristic length is on the order of a few hundred atomic spacing and significant hyperelastic effects are observed. It seems that hyperelasticity can play the governing role especially in nanostructured materials such as thin films, or under high-impact conditions where huge stresses occur, so that the region from which the crack needs to draw energy is small.

In the classical picture of dynamic fracture, there exist three important length scales near the crack tip, as shown in Figure 13.1 (a). The fracture process zone in which atomic bonds are broken is usually very small and extends only a few Angstroms in perfectly brittle systems. Another important length scale is the K-dominance zone, which is relatively large. In between the fracture process zone and the K-dominance zone is the region where material response is hyperelastic. We proposed that there exists an additional length scale near the dynamic crack, the characteristic energy length scale. This new energy length scale is shown in Figure 13.1 (b), and it is in between the K-dominance zone and the hyperelastic region. If the size of the hyperelastic region becomes comparable to the energy length scale, hyperelasticity governs dynamic fracture. If it is much smaller, hyperelasticity can be neglected.

13.1.2. Crack tip instabilities

We find that the large-strain elastic properties have a strong impact on the stability of dynamic cracks. Therefore, the dynamics of fracture is predominantly governed by the large-strain elastic properties of the interatomic potential.

This was exemplified in a study of a harmonic versus softening and stiffening potentials. Whereas the crack becomes unstable at 73 % of the Rayleigh-wave speed in materials with harmonic interactions, the crack becomes unstable at speeds much smaller than the Rayleigh-wave speed in softening materials. In contrast, stiffening material behavior allowed cracks close to Rayleigh-wave speed to propagate stable. Based on systematically varying the ratio of large-strain elastic properties while keeping the

small-strain elastic properties constant, we showed that the instability speed depends on the local wave speed (see correlation depicted in Figure 8.5). A generalized Yoffe criterion [246] and Gao's analysis [81] of local limiting speed helped to explain some of the simulation results.

With respect to the governing mechanism of the dynamic crack tip instability, the stiffening and softening case need to be distinguished. We illustrated that in softening systems, the reduction in local energy flow governs the instability, and in stiffening systems, the change in deformation field near the crack tip is responsible for the crack to leave its straight forward motion and branch. Analysis of the stress and strain field support these assumptions (Figures 8.9 and 8.10). Figure 8.6 summarizes the effect of a local stiff and soft zone on the energy flux.

13.1.3. Main conclusion

The main conclusion of the studies on the role of hyperelasticity in dynamic fracture is that hyperelasticity is crucial in order to form a clear picture of the failure process: Both the maximum crack speed and the dynamic instability are strongly influenced by the large-strain elastic properties.

13.2. Interfaces and geometric confinement

Interfaces and geometric confinement play an important role in the dynamics of cracks. Crack propagation constrained along interfaces can significantly change the associated maximum speeds of crack motion. This is illustrated for instance by the studies using the concept of a weak fracture layer where the Rayleigh-wave speed of cracks can be attained by cracks (see Chapter 6), versus the studies of cracks in homogeneous materials where the crack starts to wiggle at 73 % of the theoretical limiting speed (see Figure 8.3).

If cracks propagate along interfaces of elastically dissimilar materials, the maximum crack speed can significantly change and new mechanisms of crack propagation such as daughter and granddaughter cracks appear. Geometric confinement as cracks moving inside thin strips (the Broberg problem) has proven to provide strong impact on the dynamics of cracks. If the crack propagates in a small strip with different elastic properties, a significant effect on the propagation speed of the crack is observed as illustrated in Figure 7.10 for mode I and in Figure 12.5 for mode III cracks. An implication of crack motion within a thin stiff layer is that mode I cracks can break through the shear wave speed barrier and propagate at intersonic velocities as shown in Figure 7.11, and that mode III cracks become supersonic as shown in Figure 12.4.

In summary, our studies suggest that geometric confinement has strong impact on how cracks propagate. This is potentially important in composite materials where understanding of crack dynamics may be critical in designing robust and reliable devices.

The results presented in this thesis suggest that the definition of wave speeds according to the small-strain elastic properties is questionable in many cases and should be replaced by a local wave speed. Similar thoughts apply to the definition of wave speeds across interfaces: When the elastic properties are discontinuous, no unique definition of the

wave speed and therefore the crack limiting speed is possible.

Part III.

Plasticity of submicron thin copper films

14. Mechanical properties of ultra thin films

The study of the mechanical properties of materials at nano- and sub-micrometer scales is motivated by increasing need for such materials due to miniaturization of engineering and electronic components, development of nanostructured materials, thin film technology and surface science. When the material volume is lowered, characteristic dimensions are reduced that control the material properties and this often results in deviation from the behavior of bulk materials. Small-scale materials are often referred to as materials in small dimensions, and they are defined as materials where at least one dimension is reduced. For instance, thin films bond to substrates are a relevant example of materials in small dimensions since the film thickness h_f is small compared to the planar extension of the film and the thickness of the substrate. Thin films bond to substrates have become an increasingly active area of research in the last decades. This can partly be attributed to the fact that these materials are becoming critically important in today's technologies, whereas changes in material behavior due to the effects of surfaces, interfaces and constraints are not completely understood.

The focus of this part is on mechanical properties of ultra thin sub-micron copper films on substrates. We will show that in such materials, important effects of the film surface and grain boundaries are observed and that the constraint by the film-substrate interface governs the mechanical behavior [222, 132, 127, 88, 131, 25, 223].

Polycrystalline thin copper films as shown schematically in Figure 14.1 are frequently deposited on substrate materials to build complex microelectronic devices. In many applications and during the manufacturing process, thin films are subjected to stresses arising from thermal mismatch between the film material and the substrate. This can have a significant effect on the production yield as well as on the performance and reliability of devices in service. In past years, an ever increasing trend of miniaturization in semiconductor and integrated circuit technologies has been observed, stimulating a growing interest to investigate the deformation behavior of such ultra thin films with film thicknesses well below 1 μm.

Different inelastic deformation mechanisms are known to operate relaxing the internal and external stresses in a thin film. Experiment shows that for films of thicknesses between approximately 2 and 0.5 μm, the flow stress increases in inverse proportion to the film thickness (see for example [127, 132, 222]). This has been attributed to dislocation channelling through the film [77, 167, 168], where a moving threading dislocation leaves behind an interfacial segment. The relative energetic effort to generate these interfacial dislocations increases with decreasing film thickness, which explains the higher strength of thinner films. This model, however, could not completely explain the high strength of thin films found in experiments [127]. More recent theoretical and experimental work

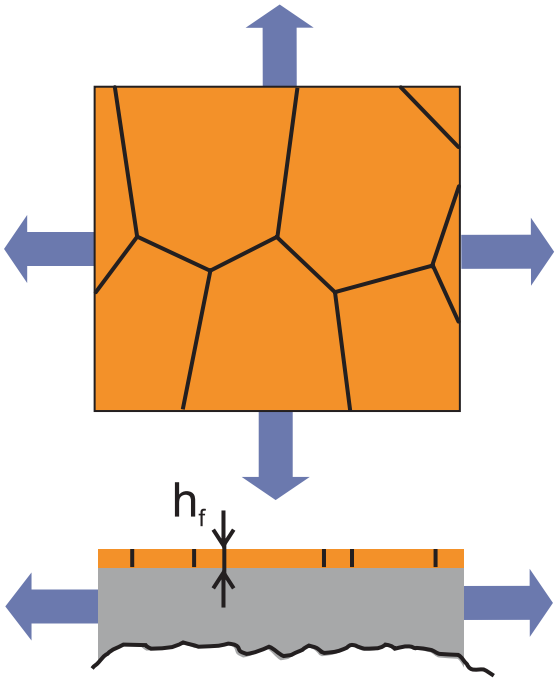

Figure 14.1.: Polycrystalline thin film geometry. A thin polycrystalline copper film is bond to a substrate (e.g. silicon). The grain boundaries are predominantly orthogonal to the film surface.

[25, 55, 223, 143, 224] indicates that the strength of thin metal films often results from a lack of active dislocation sources rather than from the energetic effort associated with dislocation motion.

In copper films, the regime where plastic relaxation is limited by dislocation nucleation and carried by glide of threading dislocations reaches down to film thicknesses of about $h_\mathrm{f} \approx 400$ nm [25]. For yet thinner films experiments reveal a film-thickness-independent flow stress [24, 55, 25]. This observation is in clear contrast to the existing theories of plasticity in thin films. *In-situ* transmission electron microscopy observations of the deformation of such ultra thin films reveal dislocation motion parallel to the film-substrate interface [25, 55]. This glide mechanism is unexpected, because in the global biaxial stress field there is no resolved shear stress on parallel glide planes. This indicates that there must be a mechanism involving long-range internal stresses that decay only slowly on the length scale of the film thickness. For sufficiently thin films these internal stresses have a pronounced effect on the mechanical behavior. It has been proposed that constrained diffusional creep may be the origin of this novel deformation mechanism [88]. This deformation mechanism by parallel glide dislocations is not well understood as of today. In this thesis, we therefore propose atomistic and continuum studies to investigate the behavior of such thin films below 400 nm. The final objective is to draw a deformation map that summarizes all relevant deformation mechanisms in submicron thin films.

This review chapter features three main sections. The first section discusses mechanical properties of materials under confinement, including nanostructured materials. In

this section we discuss one of the key references for our modeling, a recent report of modeling of Coble creep in nanocrystalline palladium with classical molecular-dynamics [240]. The second section reviews research activities in the field of mechanical properties of submicron thin metal films with a focus on diffusional processes. The third section discusses atomistic modeling activities of plasticity, providing a basis for the modeling of plasticity in submicron thin films reported in this work. Finally, we provide an outline of the studies contained in this part.

14.1. Deformation mechanisms in materials under geometric confinement

It is known that the strength of materials depends on their microstructure [19]. It has been established that in most metals, by decreasing the grain size, the strength of the material can be increased. Therefore, fine-grained materials are usually stronger than coarse-grained materials. The yield strength increases according to

$$\sigma_{\mathrm{Y}} \sim \frac{1}{\sqrt{d}} \tag{14.1}$$

where d is the grain size. This is referred to as Hall-Petch behavior, and can be derived based on considerations of dislocation pileups in the grains [19, 51]. It is a prominent example of a geometric confinement effect.

However, materials can not get infinitely strong as suggested by equation (14.1). For instance, at elevated temperatures [162, 50, 19, 51] deformation by creep plays an important role in materials with small grain sizes. Fine-grained materials thus tend to fail rapidly under loading, and can not get infinitely strong contradicting the prediction of equation (14.1).

More recent research results suggest that even at low temperatures, materials with ultra fine grain sizes behave quite differently from coarse-grained materials. For instance, in nanostructered materials, the role of grain boundaries becomes increasingly important leading to previously unknown deformation mechanisms. Even though it is generally accepted that grain boundaries provide sources and sinks for dislocations, its role in doing so is still not well understood. One of the reasons for the increasing importance of grain boundaries is that classical mechanisms of dislocation generation (e.g. Frank-Read-sources) can not operate in nanocrystals, because they would not fit within the grain. In addition, defects such as grain boundaries interact in complicated ways with other defects like dislocations. An important consequence of this is that despite the prediction by equation (14.1), the strength of nanomaterials does not increase continuously with decreasing grain size. Below a critical grain size, experiments have shown that the strength decreases again [166]. This is referred to as the inverse Hall-Petch effect [166, 19, 241]. In this regime, it was proposed that the yield stress scales as

$$\sigma_{\mathrm{Y}} \sim \sqrt{d}, \tag{14.2}$$

although physical foundation of such material behavior is yet to be explored [235]. Such behavior indicates that there may exist a maximum of strength for a certain grain size,

described as "the strongest size" by Yip in 1998 [245]. One of the major objectives of recent research is to quantify this critical condition and understand the underlying principles.

Applying classical molecular-dynamics to investigations of nanostructured materials is particularly attractive because of the fact that the length scale of several tens of nanometers fall well within the range accessible to molecular-dynamics simulation. Indeed, classical molecular-dynamics methods have proven to be a very powerful tool for these materials. Studying deformation of nanocrystalline materials with molecular-dynamics still requires significant computer power. Atomistic studies of nanostructured materials were reported by several groups (see, for example [216, 217, 66, 243, 240, 241, 121]). In most of the molecular-dynamics studies, polycrystalline samples at nanoscale were created (for example by a Voronoi construction), annealed, relaxed and then exposed to tensile loading. In the following paragraphs we summarize the main results in this field obtained for different geometries, materials and simulation conditions (e.g. variation of temperature and loading conditions). Coble creep is a well-known mechanism for creep of polycrystalline materials [50]. The characteristic time for exponential stress relaxation scales as

$$\tau \sim d^3 \tag{14.3}$$

where d is the grain diameter. Appreciating that the grain size in nanostructured materials is on the order of tens of nanometers (in contrast to micrometer grain sizes in coarse-grained materials), this scaling suggests that at very small grain size, diffusive mechanisms at grain boundaries may play a dominating role in nanomaterials even at moderate temperatures!

In recent publications, this was investigated using molecular-dynamics simulations at elevated temperature [240, 235, 236]. The temperature was increased to render the process of diffusion accessible to the molecular-dynamics time scale. The authors [240, 235] used a fully three dimensional model of palladium with 16 grains having a truncated-octahedral shape arranged on a three-dimensionally periodic bcc lattice. Grain sizes range from $d \approx 3.8$ nm to $d \approx 15$ nm, and the grain boundary misorientations are chosen such that only high-energy grain boundaries are present in the model. A multi-body EAM potential was used to model the atomic interactions. They find that grain boundary processes indeed play a dominating role and conclude that grain boundary diffusion fully accounts for plasticity. Under lower strain rates than in molecular-dynamics simulation, this result could be valid even at room temperature, once microcracking and dislocation nucleation are suppressed. Dislocation mechanisms are shut down due to the small grain size and moderate loading of the sample! The authors derive a generalized Coble-creep equation, and show that the grain-size dependence of the strain rate decreases from the $1/d^3$ scaling law appropriate for large grain size towards a $1/d^2$ scaling law as expected in the limit of a very small grain size (critical grain size $d \approx 7$ nm in palladium). The grain size scaling observed in molecular-dynamics simulations indeed agrees with this prediction [240]. It is also concluded that grain boundary diffusion creep must be accommodated by grain boundary sliding (also referred to as Lifshitz sliding) to avoid micro-cracking.

Experimental reports of the inverse Hall-Petch behavior inspired numerous simulation studies by Schiotz and coworkers [188, 190] and Swygenhoven and coworkers [215, 219,

218, 216, 56]. In contrast to the above research of Coble creep, these simulations are all performed at low temperatures making it basically impossible to observe any Coble creep at the present (molecular-dynamics-) time scale. In these studies, very large stresses in the range of 1-3 GPa were applied. Schiotz *et al.* [188, 190] determined the yield stress σ_Y as a function of the grain size d. In contrast, the group around van Swygenhoven focused attention on the strain rate. Both groups concluded that the deformation mechanism is controlled by grain boundary processes and that the material softens with decreasing grain size (inverse Hall-Petch effect). Nucleation of numerous partial dislocations was observed in their simulations.

Schiotz and coworkers [188, 190] considered nanocrystalline copper with grain sizes from 3.3 to 6.6 nm and showed that grain boundary sliding occurs together with grain rotation. When the grain size was larger than about 5 nm, nucleation of partial dislocation was identified under very large stresses. Similar observations were also reported by van Swygenhoven and coworkers [218, 219] in simulations of nickel at average grain sizes of about 5 nm at a temperature of 70 K. The results were confirmed with simulations at higher temperature and for larger grain sizes [216]. The authors suggested that grain boundary sliding occurs through atom shuffling and stress induced athermal grain boundary diffusion. In a later paper by Wolf *et al.* [235], the missing issue of the rate-limiting deformation mechanism was addressed. The authors suggest that the accommodation mechanism in the simulations described by van Swygenhoven's and Schiotz's group is the same as that in Coble creep, with the difference that there is no activation energy for this athermal process. Therefore, the Coble creep equation should apply. They verified this proposal by an analysis of the data in [218], proving that the data points for the three smallest grain sizes fall on a straight line with a slope 2.73 in a log-log plot of the $\dot{\epsilon}/\sigma$ versus the grain size d (Figure 4 in [235]). It was concluded that the athermal mode of Coble creep is due to the fact that the simulations are carried out in a regime where molecular-dynamics can not be used. The fact that Coble creep still dominates may indicate that grain boundary diffusion is a very robust mechanism for stress relaxation [235].

Recent work by Hasnaoui *et al.* [103] discussed the influence of the grain boundary misorientation on the ductility of nanocrystalline materials. It was shown that at specific low-energy grain boundaries (e.g. twins), several neighboring grains can be effectively immobilized, creating structures that offer significant resistance to plastic deformation. The authors finally discuss the possibility to design more ductile nanostructured materials that feature less low-energy grain boundaries and therefore lead to a more homogeneous deformation.

Other studies were carried out on dislocation processes of nanocrystalline aluminum [242]. The authors demonstrate that deformation twinning may play a very important role in the deformation of nanocrystalline aluminum. The simulations demonstrate that molecular-dynamics simulations have advanced to predict deformation mechanisms of materials at a level of detail not yet accessible to experimental techniques. Observation of twinning is quite surprising because of the small grain size and the high stacking fault energy of aluminum [260]. The predictions by these simulations have recently been verified experimentally [41]. Experimentalists conclude that twinning in aluminum only occurs in nanocrystalline materials, while it is not observed in coarse-grained aluminum.

The findings support the hypothesis that in the nanograin-regime, a transition occurs from normal slip of complete dislocations to activities dominated by partial dislocations. The critical stress for nucleation of dislocations in nanocrystalline aluminum was estimated to be 2.3 GPa.

Not only has research focused on polycrystalline nanoscale materials, but also on the mechanics of single crystals with nanometer extension. Such structures may become increasingly important for example as interconnects in complex integrated circuits or bio-electrical devices. Studies of defect-free single nano-crystals under tension (the crystals had dimensions of several nanometers) have been carried out by Komanduri *et al.* [135]. Due to the small structural size of the nanocrystals, the dislocations glide quickly through the specimen leaving surface steps, and repeated glide admits plastic deformation. Similar research of mechanical properties of copper were carried out by Heino and coworkers [106].

14.2. Continuum modeling of constrained diffusional creep in thin metal films

Similarly as in bulk nanostructured materials, it has also been hypothesized that grain boundary processes dominate the mechanical properties in ultra thin films [88, 234, 24, 55, 25].

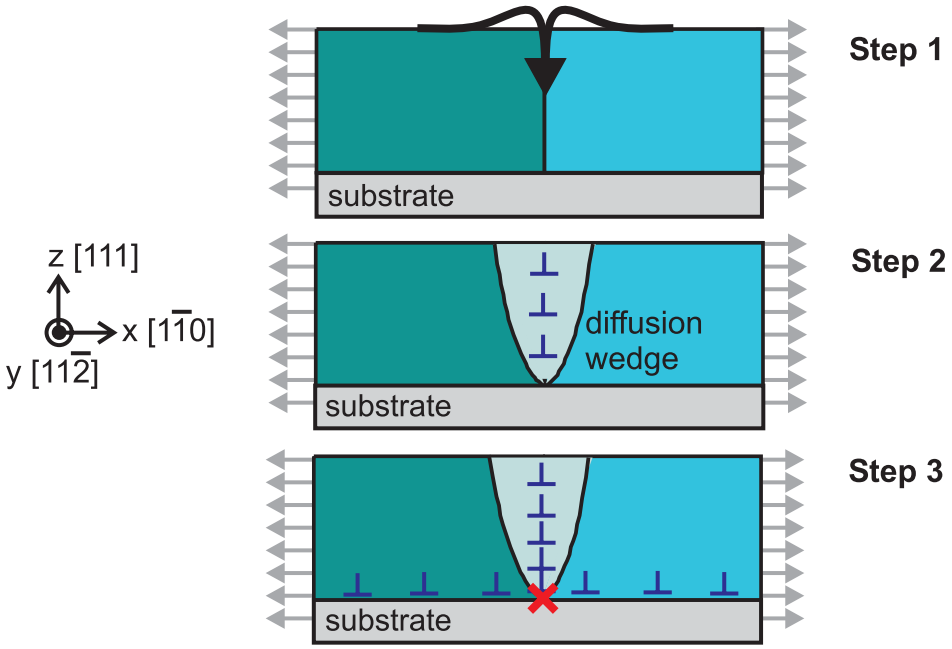

Figure 14.2.: Mechanism of constrained diffusional creep in thin films as proposed by Gao *et al.* [88].

In recent theoretical studies of diffusional creep in polycrystalline thin films deposited on substrates, a new class of defects called the grain boundary diffusion wedges was predicted [88]. These diffusion wedges are formed by stress driven mass transport between

the free surface of the film and the grain boundaries during the process of substrate-constrained grain boundary diffusion. The diffusion wedges feature a crack-like opening displacement, and due to the strong bonding between film and substrate, a stress concentration at the root of the grain boundary builds up. This leads to a singular, crack-like stress field in the film as the grain boundary tractions are relaxed. Because the material inserted into the grain boundary by diffusion takes the shape of a wedge, this new class of defects has been referred to as a diffusion wedge [88, 251]. An important implication of the crack-like stress field at the diffusion wedges is that dislocations with Burgers vector parallel to the interface may be nucleated at the root of the grain boundary, at the location with highest shear stress. This is a new dislocation mechanism in thin films that contrasts to the well known Mathews-Freund-Nix mechanism of threading dislocation propagation [77, 167, 168].

Indeed, results of recent TEM experiments show that, while threading dislocations dominate in passivated metal films, parallel glide dislocations begin to dominate in unpassivated copper films with thickness below 400 nm. The discovery of parallel glide dislocations [24] provided experimental support for the constrained diffusional creep model [88]. In turn, constrained diffusional creep provided the basis for interpretation of certain experimental results, especially in regard to the mechanisms for the creation and emission of parallel glide dislocations.

Figure 14.2 summarizes this model including the occurrence of parallel glide dislocations in three stages: In stage one, material is transported from the surface into the grain boundary. In stage two, mass transport leads to the formation of a diffusion wedge, as more and more material flows into and accumulates in the grain boundary. The continuum model predicts that the traction along the grain boundary diffusion wedge becomes fully relaxed and crack-like on the scale of a characteristic time τ. The time scale at that diffusion takes place is usually much larger than that of dislocation glide. However, in the nano-scaled structures investigated here, the model can explain the observed deformation rates even at room temperature, because the time scale of diffusional creep is inversely proportional to the cube of the characteristic structural length (similarly to Coble creep, see equation (14.3)).

14.2.1. Mathematical basics

We review the continuum model since its predictions will later be compared to atomistic simulation results. In the continuum model [88], diffusion is modeled as dislocation climb in the grain boundary. The solution for a single edge dislocation near a surface is used as the Green's function to construct a solution with infinitesimal Volterra edge dislocations [205, 109, 63]. The basis for the continuum modeling is the solution for the normal traction σ_{xx} along the grain boundary due to insertion of a single dislocation (material layer of thickness b) along $(0, \zeta)$ (corresponding to a climb edge dislocation). The coordinate system is given in Figure 14.3.

The traction is then

$$\sigma_{xx}(\zeta, \xi) = \frac{Eb}{4\pi(1-\nu^2)} K(\zeta, \xi), \tag{14.4}$$

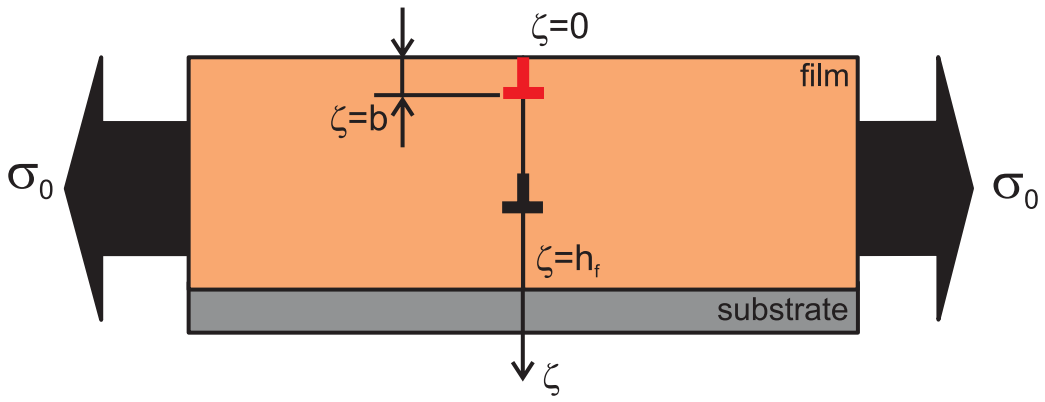

Figure 14.3.: Geometry and coordinate system of the continuum mechanics model of constrained diffusional creep.

where

$$K(\zeta,\xi) = \frac{1}{\zeta-\xi} - \frac{1}{\zeta+\xi} - \frac{2\zeta(\zeta-\xi)}{(\zeta+\xi)^3} \tag{14.5}$$

is the Cauchy kernel function for this particular problem. Further, E is Young's modulus, and ν is Poisson's ratio. For an arbitrary opening function $2u(\zeta)$ in a film with thickness h_f and applied stress σ_0 in the absence of diffusion, the stress along the grain boundary is given by

$$\sigma_{xx}(\zeta,t) = \sigma_0 - \frac{E}{2\pi(1-\nu^2)} \int_0^{h_\mathrm{f}} S(\zeta,\xi)\frac{\partial u(\xi,t)}{\partial \xi}\mathrm{d}\xi, \tag{14.6}$$

where $S(\zeta,\xi)$ is a Green's function kernel for the continuous dislocation problem (Cauchy kernel) and corresponds to the elasticity solution of a single array of dislocations near a surface. For a dislocation near a free surface, $S(\zeta,\xi) = K(\zeta,\xi)$. The kernel function $S(\zeta,\xi)$ can also be established for a dislocation near a bimaterial interface [88, 251] or for periodic wedges [88].

The chemical potential relative to the flat free surface (with atomic volume $\Omega = a_0^3/4$ in face centered cubic crystals where a_0 is the lattice parameter) is given by

$$\mu(\zeta,t) = \mu_0 - \sigma_{xx}(\zeta,t)\Omega. \tag{14.7}$$

The corresponding atomic flux per unit thickness in the ζ direction in the boundary is

$$j(\zeta,t) = -\frac{\delta_\mathrm{gb}D_\mathrm{gb}}{\mathrm{k}T}\frac{\partial\mu(\zeta,t)}{\partial\zeta} = \frac{\delta_\mathrm{gb}D_\mathrm{gb}}{\mathrm{k}T}\frac{\partial\sigma_{xx}(\zeta,t)}{\partial\zeta} \tag{14.8}$$

where $\delta_\mathrm{gb}D_\mathrm{gb}$ is the grain boundary diffusivity, and $\mathrm{k}T$ is the Boltzmann constant multiplied by the absolute temperature. Equations (14.7) and (14.8) are coupled by arguments of mass conservation, since the flux divergence for any ζ is related to the displacement rate through

$$2\frac{\partial u}{\partial t} = -\Omega\frac{\partial j(\zeta,t)}{\partial\zeta}, \tag{14.9}$$

which can be combined with equation (14.8) to obtain

$$\frac{\partial u}{\partial t} = -\frac{\delta_{\mathrm{gb}} D_{\mathrm{gb}} \Omega}{2\mathrm{k}T} \frac{\partial^2 \sigma_{xx}(\zeta, t)}{\partial \zeta^2}. \tag{14.10}$$

The derivative of $\sigma_{xx}(\zeta, t)$ with respect to time is given by

$$\frac{\partial \sigma_{xx}(\zeta, t)}{\partial t} = -\frac{E}{2\pi(1-\nu^2)} \int_0^{h_{\mathrm{f}}} S(\zeta, \xi) \frac{\partial^2 u(\xi)}{\partial \xi \partial t} \mathrm{d}\xi, \tag{14.11}$$

and inserting equation (14.10) into equation (14.11) yields

$$\frac{\partial \sigma_{xx}(\zeta, t)}{\partial t} = \frac{E \delta_{\mathrm{gb}} D_{\mathrm{gb}} \Omega}{4\pi(1-\nu^2)\mathrm{k}T} \int_0^{h_{\mathrm{f}}} S(\zeta, \xi) \frac{\partial^3 \sigma_{xx}(\xi, t)}{\partial \xi^3} \mathrm{d}\xi \tag{14.12}$$

for the grain boundary traction. Boundary and initial conditions are given as follows. For the continuity of the chemical potential near the free surface,

$$\sigma_{xx}(\zeta = 0, t) = 0, \tag{14.13}$$

and for no sliding and no diffusion at the interface,

$$\frac{\partial \sigma_{xx}}{\partial \zeta}(\zeta = h_{\mathrm{f}}, t) = \frac{\partial^2 \sigma_{xx}}{\partial \zeta^2}(\zeta = h_{\mathrm{f}}, t) = 0. \tag{14.14}$$

Finally,

$$\sigma_{xx}(\zeta, t = 0) = \sigma_0 \tag{14.15}$$

sets the initial condition for the transient problem.

The problem given by equation (14.12) can be expressed by the method of separation of variables in the form of an expansion series

$$\sigma_{xx}(\zeta, t) = \sigma_0 \sum_{n=1}^{\infty} c_n \exp\left(-\lambda_n t/\tau\right) f_n(\zeta/h_{\mathrm{f}}) \tag{14.16}$$

where

$$\tau = \frac{4\pi(1-\nu^2)\mathrm{k}T h_{\mathrm{f}}^3}{E D_{\mathrm{gb}} \delta_{\mathrm{gb}} \Omega} \tag{14.17}$$

is a characteristic time, and λ_n and f_n are eigenvalues and eigenfunctions. It is important to note that $\tau \sim h_{\mathrm{f}}^3$, as in the classical Coble creep equation [50]. To solve the equations numerically, the problem is transformed into a standard Cauchy-type singular equation for f_n''' [88]. The Gauss-Chebyshev quadrature, developed by Erdogan *et al.* [61, 60] can be used to solve the equations. The solution for the opening displacement $u(z, t)$ is given by

$$u(\zeta, t) = -\frac{2\pi(1-\nu^2) h_{\mathrm{f}} \sigma_0}{E} \sum_{n=1}^{\infty} c_n \lambda_n^{-1} \left(1 - \exp\left(-\lambda_n t/\tau\right)\right) f_n''(\zeta/h_{\mathrm{f}}). \tag{14.18}$$

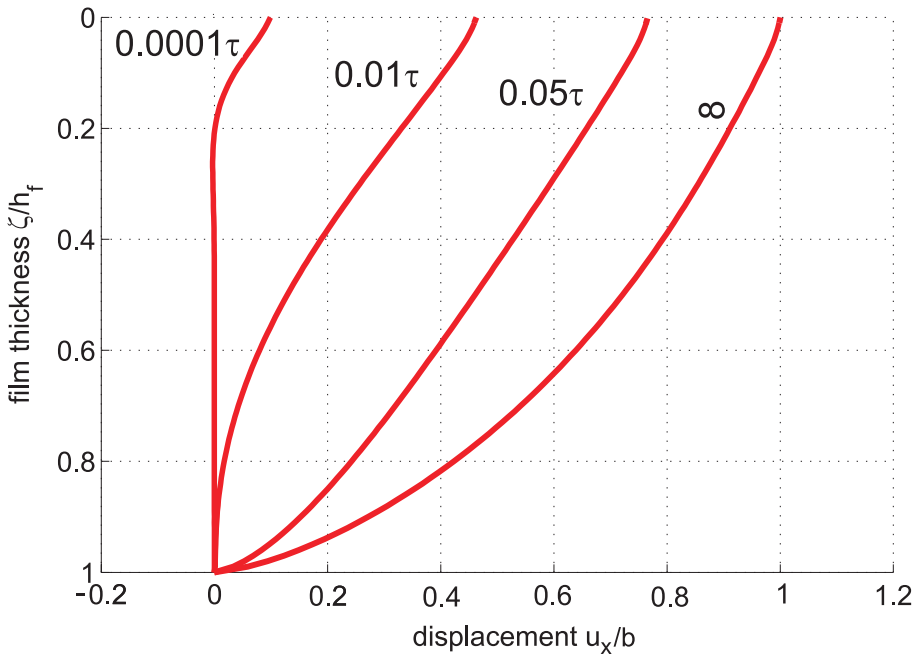

Figure 14.4.: Development of grain boundary opening u_x normalized by a Burgers vector over time, for the case of a copper film on a rigid substrate. The loading σ_0 is chosen such that the opening displacement at the film surface ($\zeta = 0$) at $t \to \infty$ is one Burgers vector [88].

The solution procedure can be summarized as follows. Steps: (1), find eigenvalues and eigenfunctions, (2) find the coefficients c_n and (3) calculate the traction and displacement from equations (14.16) and (14.18).

The dislocations "stored" in the grain boundary are a measure of additional material in the grain boundary. With respect to the lattice distortion around the diffusion wedge, the dislocations in the grain boundary exemplify a type of geometrically necessary dislocations [84] that cause nonuniform plastic deformation in the thin film. The eigenvalues measure the rate of decay of each eigenmode. The results show that the higher eigenmodes decay much faster than the first eigenmode, so that the diffusion process is dominated by the first eigenmode.

The continuum mechanics model was further advanced to capture the effect of surface diffusion [251]. No difference in the qualitative behavior was found, and stress decay in the film is still exponential with a characteristic time proportional to the cube of the film thickness. Further details could be found in [251].

In all cases considered in the literature [88, 251], with the proper definition of the characteristic time τ, stress decay could be described by an exponential law of the form

$$\sigma_{\mathrm{gb}}(t) = \sigma_0 \exp\left(-\lambda_0 \frac{t}{\tau}\right) \tag{14.19}$$

with a geometry-dependent constant

$$\lambda_0 = 8.10 + 30.65 h_{\mathrm{f}}/d. \tag{14.20}$$

Note that d characterizes the grain size, and σ_0 stands for the laterally applied stress as discussed above. Equation (14.20) is an empirical formula and is valid for $0.2 \leq h_f/d \leq 10$.

14.2.2. Numerical examples

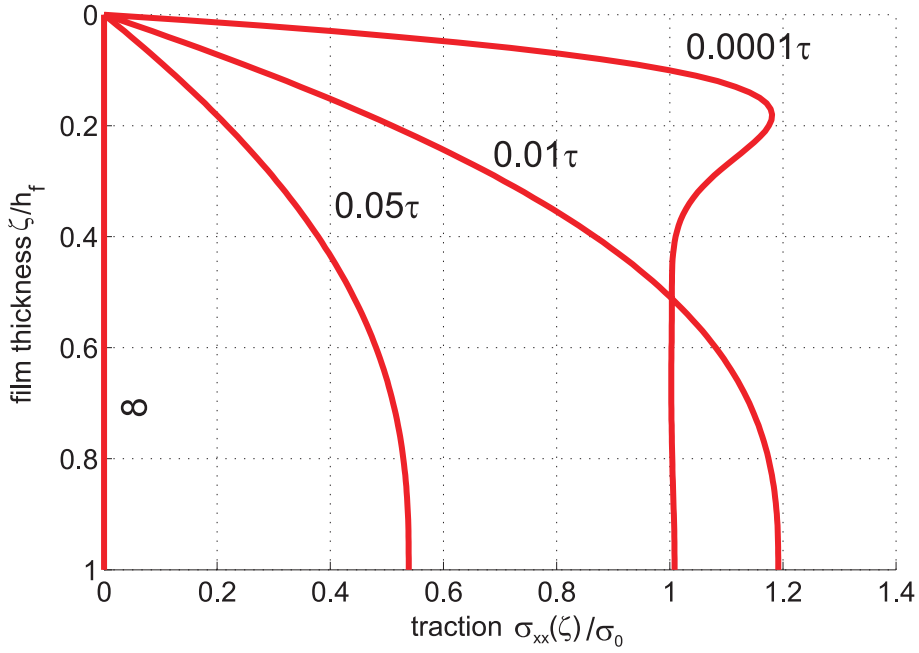

Figure 14.5.: Traction along the grain boundary for various instants in time [88].

Figures 14.4, 14.5 and 14.6 show several numerical examples. Figure 14.4 shows the opening displacement along the grain boundary for several instants in time. Figure 14.5 shows the traction along the grain boundary for various instants in time. These examples show that in the long time limit $t \to \infty$, the solution approaches the displacement of a crack.

Figure 14.6 shows the stress intensity factor normalized by the corresponding value of a crack over the reduced time $t^* = t/\tau$ for identical elastic properties of substrate and film material (isotropic case), rigid substrate (copper film and rigid substrate) and soft substrate (aluminum film and epoxy substrate). The results indicate that in a film on a soft substrate, the stress intensity factor of a crack is reached faster compared to the homogeneous case. Similarly, the stress intensity factor of a crack is reached slower in the case of a film on a soft substrate compared to the homogeneous case. Table 14.1 summarizes the material parameters used for the calculation.

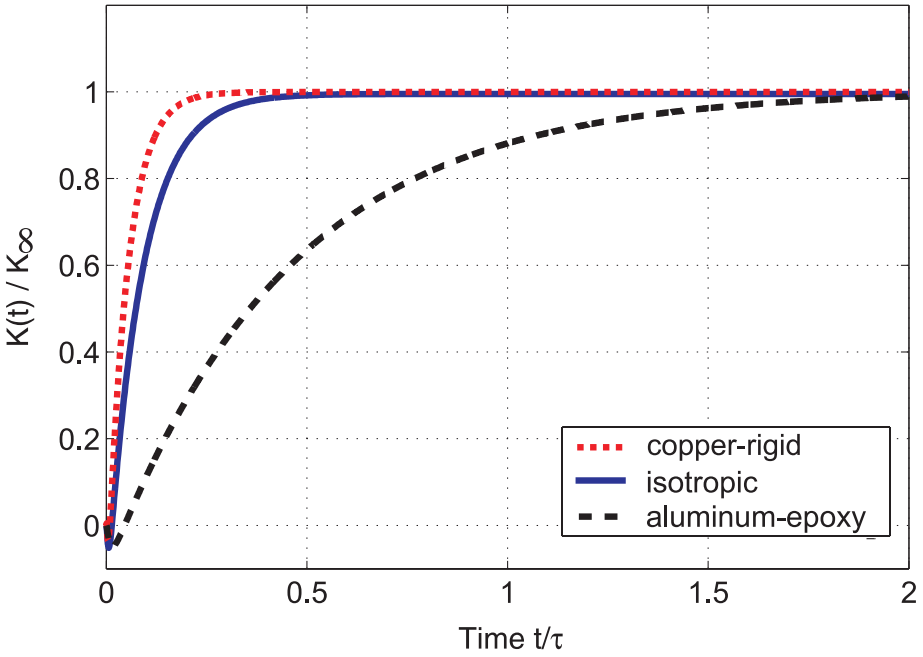

Figure 14.6.: Stress intensity factor normalized by the corresponding value of a crack over the reduced time $t^* = t/\tau$ for identical elastic properties of substrate and film material (isotropic case), rigid substrate (copper film and rigid substrate) and soft substrate (aluminum film and epoxy substrate) [88, 250, 251].

	ν_{film}	ν_{subs}	$\mu_{\text{film}}/\mu_{\text{subs}}$
Cu/rigid	0.32	-	0
Al/epoxy	0.3	0.35	23.08
isotropic	-	-	1

Table 14.1.: Material parameters for calculation of stress intensity factor over the reduced time.

14.3. Modeling plasticity using large-scale atomistic simulations

Plastic deformation of metals is often described using continuum mechanics techniques, such as crystal plasticity theories [200, 198, 161] or strain gradient formulations [72, 84]. Significant research effort has also been put into the development of mesoscopic discrete dislocation dynamics techniques [147, 223, 47, 48, 49, 136, 137, 101]. Yet another, unconventional approach that could be taken is to study plasticity using large scale atomistic simulations [12, 186].

Unlike continuum mechanics approaches, atomistic techniques require no *a priori* assumptions and no formulation of constitutive laws to model the behavior of dislocations and thus describe mechanical properties of materials. "Everything", that is the complete material behavior, is determined once the atomic interactions are chosen. Atomic interactions can be defined for a specific material such as copper based on quantum

mechanics calculations. Alternatively, they can also be chosen such that generic properties common to a large class of materials are incorporated. This allows to develop "model materials" to study specific materials phenomena. Models for ductile materials, for example, thus allow studying the generic features of ductile material behavior.

The length and time range accessible to molecular-dynamics is suitable for studying dislocation nucleation from defects such as cracks, as well as complicated dislocation reactions. The method also intrinsically captures dynamics of other topological defects, such as vacancies or grain boundaries and its interaction with dislocations. This is an advantage over mesoscopic methods that require picking parameters and rules for defect interaction. Also, using multi-body EAM potentials (e.g. [71]), reasonably good models for some metals can be obtained. With sufficient computer resources it is possible to study the collective behavior of a large number of dislocations in systems with high dislocation density. Systems under large strain rates can be readily simulated. In discrete dislocation dynamics methods, such conditions are difficult to achieve.

Two distinct length scales are involved in the mechanics of networks of crystal defects. The micrometer length scale is characteristic of the mutual elastic interaction among dislocations, but dislocation cores and formation of junctions and other reaction products is characterized by the length scale of several Burgers vectors and occur at the atomic length scale [109]. The two length scales span over several orders of magnitude, indicating the computational challenge associated with modeling. The rapidly advancing computing capabilities of supercomputers approaching TFLOPs and beyond now allow simulations ranging from nanoscale to microscale within one simulation [12]. The state-of-the-art of of ultra large scale simulations can model billion atom systems [185, 11, 12, 221].

We will continue with a review of some of the activities and the historical development of atomistic simulations of dislocations and dislocation interactions in metals, and illustrate that progress in this field was highly coupled to advances in computer resources.

Early studies by Hoagland *et al.* [110] and deCelis *et al.* [54] treated only a few hundred atoms. The researchers studied the competition of ductile versus brittle behaviors of solids using quasi-static methods and investigated how and under which conditions dislocations are generated at a crack tip. Such micro-cracks can be found in virtually any real materials (referred to as material flaws), and serve as seeds for defect generation (see also Figure 1.1 and the associated discussion). The studies were small in size, and only a few dislocations could be simulated. Due to the lack of dynamic response and the system size limitations, the treatments were valid only until the first dislocation moved a small fraction of the sample size away from the crack tip.

Computational resources rapidly developed during the 1990s (see Figure 2.2). Cleri *et al.* [46] studied the atomic-scale mechanism of crack-tip plasticity using around $80,000$ atoms. They investigated dislocation emission from a crack tip by extracting the atomic-level displacement and stress fields, so as to link the molecular-dynamics results to continuum mechanics descriptions of brittle versus ductile behavior in crack propagation [178, 179, 181]. Zhou and coworkers [254] performed large-scale molecular-dynamics simulations and carried out simulations of up to 35 million atoms to study ductile failure. In these simulations, the atoms interact with Morse pair potentials as well as more

realistic EAM potentials. They observed emission of dislocation loops from the crack front, and find that the sequence of dislocation emission events strongly depends on the crystallographic orientation of the crack front. They assumed that systems comprising of 3.5 million atoms are sufficient to study the early stages of dislocation nucleation (since they observed the same feature independent of the system size).

In 1997, Abraham and coworkers [7] performed simulations using 100 million atoms and showed generation of "flower-of-loop" dislocations at a moving crack tip. It was observed that generation of dislocation loops in a rapidly propagating crack occurs above a critical crack speed, suggesting a dynamic brittle-to-ductile transition.

Other studies focused on the creation, motion and reaction of very few dislocations in an fcc lattice, with the objective to understand the fundamental principles. Research activity was centered on atomistic details of the dislocation core making use of the EAM method [91, 53]. Zhou and Hoolian [255] performed molecular-dynamics simulations of up to 3.5 million atoms interacting with EAM potentials (they used up to 35 million atoms with pair potentials). They studied the intersection of extended dislocations in copper and observed that the intersection process begins with junction formation, followed by an unzipping event and partial dislocation bowing and cutting. These are unique studies, whose results can be immediately applied in mesoscopic simulations. Additional research was carried out to investigate the screw dislocation structure and interaction in a nickel fcc lattice by Qi *et al.*[174], using a QM-Sutton-Chen many body potential. The researchers studied the core geometry of partial dislocations, as well as the motion and annihilation of oppositely signed dislocations, and discussed cross-slip and associated energy barriers. Atomistic simulations have also been applied to study the interaction of dislocations with other defects.

Further studies focused on the ductility of quasicrystals (see also discussion in Section 3.1) [153, 154, 211]. Atomistic simulation particularly helped to explain the mechanism of dislocation motion in quasicrystals. An important contribution was the observation of phason-walls that are attached to each moving dislocation. These phason-walls helped to clarify some of the perplexing properties of quasicrystals found in experiments, such as a brittle-to-ductile transition at about 80 % of the melting temperature. Most recently, three-dimensional atomistic simulations at elevated temperatures were carried out [187] where it was found that dislocation climb processes play an increasingly important role.

In summary, molecular-dynamics simulations of plasticity have advanced to a quite sophisticated level. We propose that atomistic simulations with multi-body EAM potentials can also be applied to describe mechanical properties of thin metal films.

14.4. Outline of the studies presented in this part

The main focus of this work can be summarized as follows.

- Further development of the continuum mechanics model. We address some missing features of the existing continuum theory including a quantitative description of diffusion initiation, and a model for nucleation process of parallel glide dislocations from diffusion wedges.

- Analysis of the atomistic details of parallel glide dislocation nucleation from grain boundaries, diffusion wedges and cracks and comparison with the continuum mechanics model.

- Summary of the different deformation mechanisms that appear in ultra thin copper films in a deformation map (e.g. threading dislocations versus diffusional creep).

Chapter 15 focuses on continuum mechanics modeling of constrained diffusional creep. We discuss some missing features of the existing continuum theory, such as an initiation condition for diffusion and dislocation nucleation from diffusion wedges. An initiation condition for diffusion is proposed based on the consideration of discrete dislocations close to the film surface. This concept has the important consequence that diffusion can not operate below a threshold stress. Further discussion is devoted to the role of single dislocations under nano-scale geometric confinement. We continue with a Rice-Thomson model for nucleation of parallel glide dislocations from diffusion wedges.

In Chapter 16, a continuum mechanics model incorporating the concept of a threshold stress for diffusion is presented. The model is then used to calculate the stress in the thin film during thermal cycling experiments. Several numerical examples are provided showing some qualitative agreement with the experimental results.

The following Chapter 17 is devoted to atomistic modeling of constrained diffusional creep in a quasi-two dimensional bicrystal model under plain strain conditions. We show that diffusional mass transport from the surface along the grain boundary leads to build up of a new material defect referred to as diffusion wedge [88]. We also illustrate that the deformation field near a diffusion wedge becomes crack like and causes emission of parallel glide dislocations. We analyze and describe the atomic details of parallel glide dislocation nucleation near a diffusion wedge and a crack and compare the results to the continuum model presented in Chapter 15.

In the following chapters we will focus on plasticity of polycrystalline thin films. In Chapter 18 we discuss dislocation nucleation from a grain triple junction where grain boundary tractions are relieved by constrained diffusional creep. Atomistic simulation are used to focus on the nucleation process of parallel glide dislocations from different types of grain boundary structures.

Chapter 19 is dedicated to simulations of polycrystalline thin films. Our hexagonal atomistic models feature a geometry similar to the microstructure found in the experiments [25]. We show that traction relaxation along the grain boundaries by diffusional creep leads to a fundamentally different mechanism of deformation. We study the transition from threading to parallel glide dislocations. Extending the quasi-two dimensional modeling with the bicrystal, we report results of a study of constrained diffusional creep in polycrystalline thin films. We observe nucleation of parallel glide dislocations from grain boundary diffusion wedges.

Finally, Chapter 20 contains a discussion of the results of modeling in the part on thin films and summarizes the findings in a deformation map of plasticity of ultra thin films. We propose that beyond the classical regime of threading dislocations, there exist several novel mechanisms that become active once the film thickness approaches nano-scale.

15. Continuum modeling of constrained diffusional creep in thin submicron copper films

The review in Section 14.2 suggests that some important aspects are missing in the existing continuum model. For instance, continuum theory neglected the fact that once climb of edge dislocations occurs in the grain boundary, the view of discrete dislocations becomes increasingly important. In particular when the film thickness reaches nanoscale, single dislocations may play a governing role in the deformation mechanism.

A missing aspect is further a condition for initiation of diffusion. The continuum theory [88] assumes that diffusion initiates at an infinitesimal stress and can thus completely relax tractions in the film. In contrast to these predictions, experimental results have reported a threshold stress for diffusion in several studies by Kobrinsky *et al.* [132, 133, 131].

Another important point is the nucleation condition for parallel glide dislocations. Although continuum theory predicts that the deformation field near a diffusion wedge becomes crack-like [88], no quantitative criterion for nucleation of dislocations was proposed so far.

This chapter proceeds as follows. We discuss models for initiation of diffusion and nucleation of parallel glide dislocations. We also discuss the energetical stability of a single dislocation in a thin nano-sized film.

15.1. Initiation condition for diffusion

Here we propose a criterion for the initiation of grain boundary diffusion following the spirit of the Rice-Thomson model. The main assumption is that grain boundary diffusion initiates when spontaneous insertion of a climb dislocation into the grain boundary from the free surface occurs. It is therefore postulated that the condition for initiation of diffusion is a local criterion, independent of the film thickness.

Considering the force balance on the critical configuration of an edge dislocation one Burgers vector away from the free surface (see also Figure 14.3), a critical lateral stress

$$\sigma_0^{\mathrm{cr}} > \frac{E}{8\pi(1-\nu^2)} \tag{15.1}$$

for initiation of grain boundary diffusion could be obtained. Note that E should here be interpreted as the local modulus of the grain boundary near the surface that could be much smaller than the bulk modulus. Another possible formulation that could be

used is assuming that the critical stress level for a dislocation to exist in equilibrium at distance d_{src} from the surface is given as [109, 101]

$$\sigma_0^{\mathrm{cr}} = \frac{E}{8\pi(1-\nu^2)} \frac{b}{d_{\mathrm{src}}}. \tag{15.2}$$

The parameter d_{src} could be fitted to experimental or numerical results.

In any case, if the applied stress is smaller than that threshold, the image force will drag the dislocation immediately to the free surface. The most important result of this analysis is that a critical stress, independent of the film thickness, is required for the onset of grain boundary diffusion. This is in contrast to the existing continuum modeling of constrained diffusional creep where diffusion operates at infinitesimal stresses [88].

15.2. Single edge dislocations in nanoscale thin films

Mass transport from the surface into the grain boundary toward the substrate is modeled as climb of edge dislocations [88]. Previous studies ([88, 251]) had neglected the discrete atomistic viewpoint and therefore the fact that diffusion into the grain boundary has to proceed with at least one atomic column, with a finite width. At nanoscale, the fact that dislocation climb in the grain boundary is a discrete process becomes more evident. Grain boundary diffusion requires insertion of climb dislocations into the grain boundary one by one.

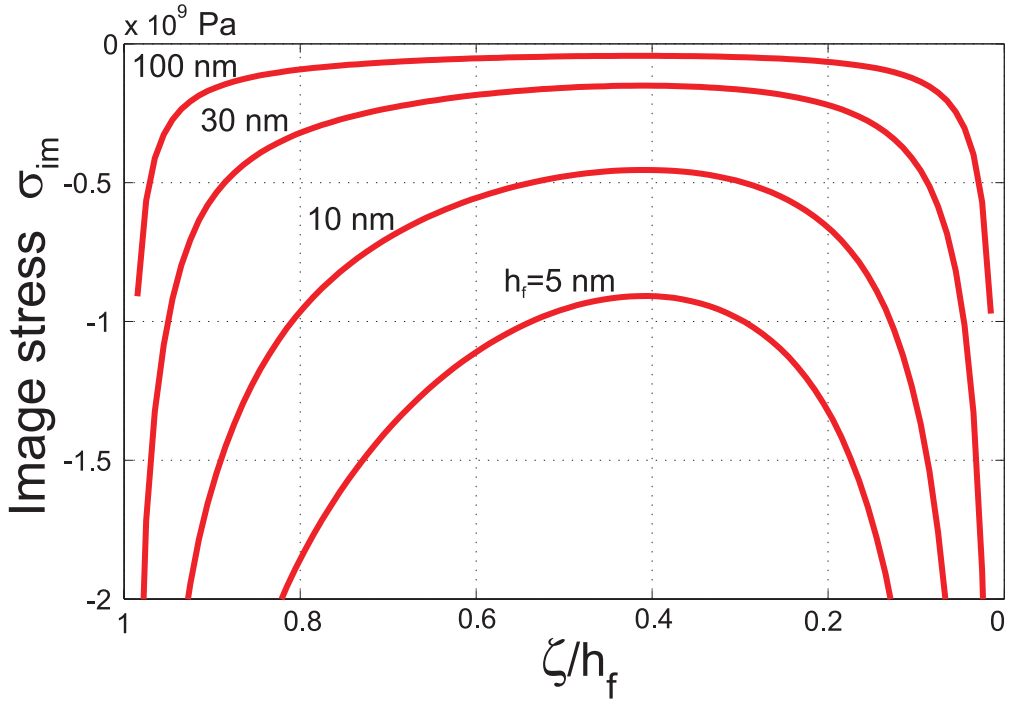

Figure 15.1.: Image stress on a single edge dislocation in nanoscale thin film constrained by a rigid substrate.

To investigate the effect, we consider a single edge dislocation climbing in a grain boundary in an elastic film of thickness h_{f} on a rigid substrate. The elastic solution

of edge dislocations in such a film can be obtained using the methods described in [205, 250]. The geometry, as well as the coordinate system is shown in Figure 14.3. In such a geometry, a dislocation placed inside the film is subject to image forces due to the surface and the film-substrate interface.

The image stress on the dislocation for different film thicknesses is shown in Figure 15.1. The thinner the films, the stronger gets the effect of the geometric confinement.

Between the film surface and the film-substrate interface, the image force is found to attain a minimum value at $\zeta_{\mathrm{EQ}} \approx 0.4h_{\mathrm{f}}$. Therefore, from the energetic point of view, a minimum critical stress is required to allow even a single climb edge dislocation to exist in the grain boundary. The thicker the film, the smaller this critical stress.

This analysis suggests that consideration of single, discrete dislocations can become very important for the nanoscale thin films. The requirement that an edge dislocation in the film is in a stable configuration could be regarded as a necessary condition for constrained grain boundary diffusion to initiate and proceed. If more than one dislocations are stored in the grain boundary, even stronger image forces are expected since different dislocations repel each other.

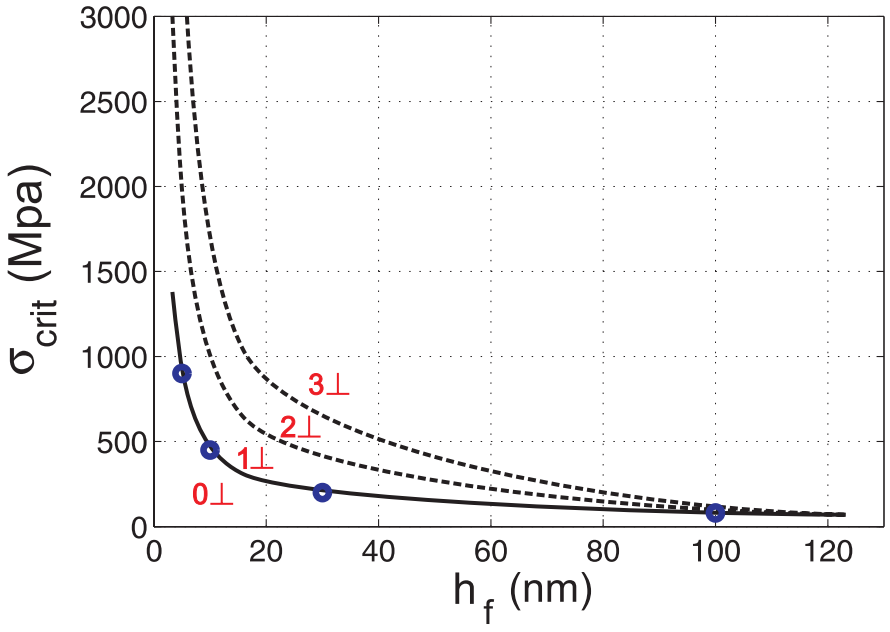

Figure 15.2.: Critical stress as a function of film thickness for stability of one, two and three dislocations in a thin film. The critical stress for the stability of one dislocation (continuous line) is taken from the analysis shown in Figure 15.1. The curves for more dislocations (dashed lines) in the grain boundary are estimates.

Another consequence of the geometric confinement of dislocations is that discrete dislocation effects can lead to quantization of stresses in nano-structured devices. Figure 15.2 shows the critical stress as a function of film thickness for stability of one, two and three dislocations in a thin film. The critical stress for the stability of one dislocation is taken from the analysis shown in Figure 15.1. The curves for two and more dislocations in the grain boundary are estimates. For a given film thickness, for at least

one dislocation to be stable inside the film, the critical stress needs to exceed a critical value. For two dislocations to be stable inside the film, the critical stress is even higher. Consequently, the stress relief due to insertion of dislocations will also be quantized. Most importantly, as the film thickness increases the critical stresses for stable dislocations in the film get smaller and smaller, eventually approaching the limit when the role of single dislocations can be neglected and the quantization is negligible. Similar observations have been made in discrete dislocation modeling of constrained diffusional creep in thin films [101].

15.3. Rice-Thompson model for nucleation of parallel glide dislocations

To characterize the nucleation condition of parallel glide dislocations, a criterion based on a critical stress intensity factor K^{PG} is proposed. The motivation is that the concept of stress intensity factor is commonly used in the mechanics of materials community and provides a possible link to mesoscopic simulation methods.

The critical value for nucleation of parallel glide dislocations from a diffusion wedge could be thought of as a new material parameter. The stress intensity factor is defined as

$$K = \lim_{\zeta \to h_{\mathrm{f}}} \left\{ [2\pi(\zeta - h_{\mathrm{f}})]^s \, \sigma_{xx}(0, z) \right\} \tag{15.3}$$

where s refers to the stress singularity exponent determined by [248]

$$\cos(s\pi) - 2\frac{\alpha - \beta}{1 - \beta}(1 - s)^2 + \frac{\alpha - \beta^2}{1 - \beta^2} = 0. \tag{15.4}$$

It is assumed that the diffusion wedge is located close to a rigid substrate and the corresponding Dundurs parameters for this case are $\alpha = -1$ and $\beta = -0.2647$. The Dundurs parameter measure the elastic mismatch of film and substrate material [250]. The singularity exponent is found to be $s \approx 0.31$ for the material combination considered in our simulations (comparing to $s = 0.5$ in the case of a homogeneous material). Close to the bimaterial interface, we calculate the stress intensity factor

$$K = A \times \lim_{\zeta \to h_{\mathrm{f}}} \left(\frac{\partial u_x(\zeta)}{\partial \zeta} (1 - (\zeta / h_{\mathrm{f}})^2)^s \right) (\pi h_{\mathrm{f}})^s, \tag{15.5}$$

where

$$A = \frac{E}{1 - \nu^2} \frac{(1 - \alpha)}{4 \sin(\pi s)} \left(\frac{3 - 2s}{1 + \beta} - \frac{1 - 2s}{1 - \beta} \right). \tag{15.6}$$

The stress intensity factor provides an important link between the atomistic results and continuum mechanics. To calculate the stress intensity factor from atomistic data, the atomic displacements of the lattice close to the diffusion wedge are calculated and the stress intensity factor is then determined using equation (15.5).

The Peach-Koehler force on a dislocation can be written as $F_d = (\sigma \cdot \mathbf{b}) \times \mathrm{d}l$, where $\mathrm{d}l$ is a dislocation element and σ the local stress [109]. The variable b_x stands for the

magnitude of the Burgers vector in the $x = [1\bar{1}0]$ direction, and $b_x \approx 3.615/\sqrt{2} \times 10^{-10}$ m for copper at 0 K. A dislocation is assumed to be in an equilibrium position when $F_d = 0$. Following the approach of the Rice-Thomson model [181], we consider the force balance on a probing dislocation in the vicinity of a dislocation source to define the nucleation criterion. The probing dislocation is usually subject to an image force attracting it toward the source and a force due to applied stress driving it away from the source. The image force dominates at small distances and the driving force due to applied stress dominates at large distances. There is thus a critical distance between the dislocation and the source at which the dislocation is at unstable equilibrium. Spontaneous nucleation of a dislocation can be assumed to occur when the unstable equilibrium position is within one Burgers vector of the source.

15.3.1. Nucleation mechanism of parallel glide dislocations

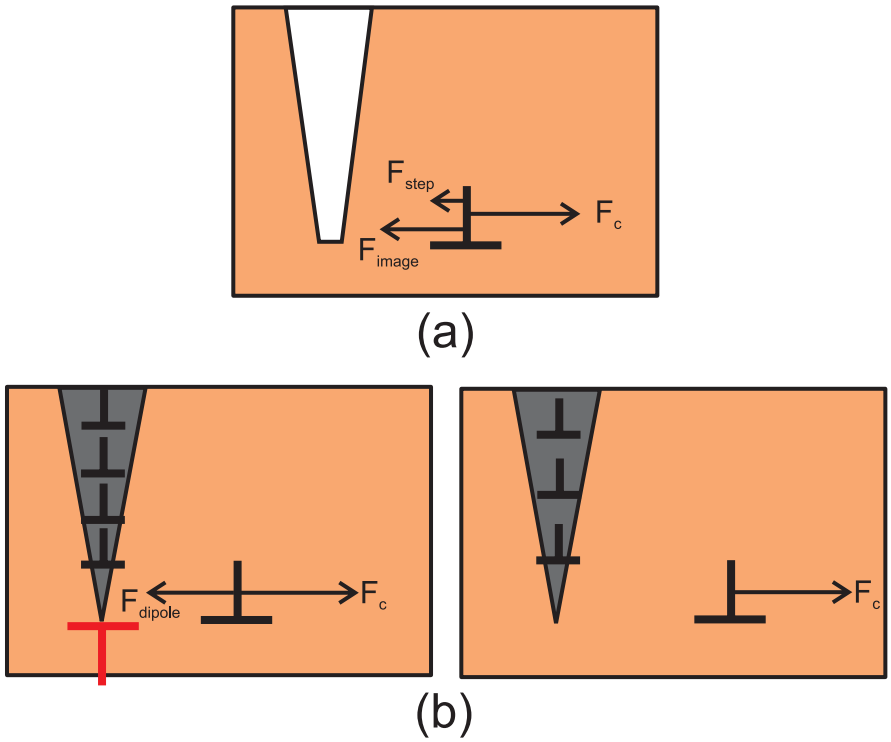

Figure 15.3.: Rice-Thomson model for nucleation of parallel glide dislocations. Subplot (a) shows the force balance in case of a crack, and subplot (b) depicts the force balance in case of a diffusion wedge.

Nucleation of parallel glide dislocations from a crack in comparison to that from a diffusion wedge is shown in Figure 15.3. The crack is treated as by [181], and forces involved are F_c due to the crack tip stress field, F_image because of the free surface (image dislocation) and F_step due to creation of a surface step (in the following, we assume $F_\mathrm{step} \ll F_\mathrm{image}$).

Close to a diffusion wedge, $F_\mathrm{step} = 0$ since no surface step is involved and a dipole must be created in order to nucleate a parallel glide dislocation from the wedge. This leads to

a dipole interaction force F_{dipole}. The dipole consists of a pair of dislocations of opposite signs, one pinned at the source and the other trying to emerge and escape from the source. The pinned end of the dipole has the opposite sign to the climb dislocations in the diffusion wedge and can be annihilated via further climb within the grain boundary. The annihilation breaks the dipole free and eliminates the dipole interaction force so that the emergent end of the dipole moves away to complete the nucleation process. Therefore, it seems that there could be two possible scenarios for dislocation nucleation at a diffusion wedge. In the first scenario, the nucleation condition is controlled by a critical stress required to overcome the dipole interaction force. In the second scenario, the nucleation criterion is controlled by the kinetics of climb annihilation within the grain boundary which breaks the dipole interaction by removing its pinned end and setting the other end free. No matter which scenario controls the nucleation process, the climb annihilation of edge dislocations in the grain boundary must be completed and will be the rate limiting process. The force balance on the dislocation is illustrated in Figure 15.3 (b) for two different, subsequent instants in time.

15.3.2. Critical stress intensity factor for dislocation nucleation in homogeneous material

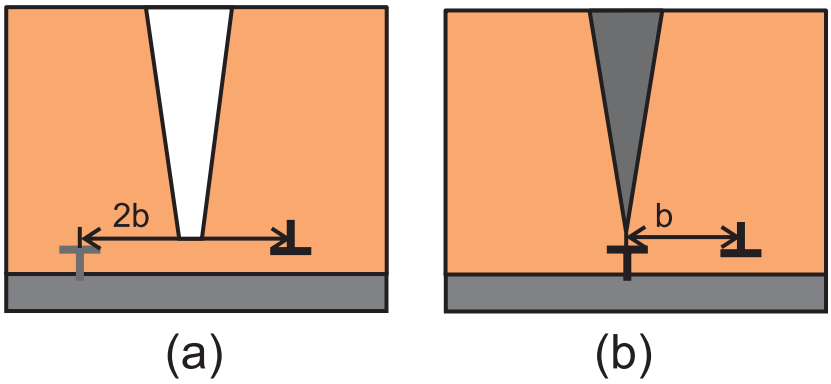

Figure 15.4.: Dislocation model for critical stress intensity factor for nucleation of parallel glide dislocations.

It is now assumed that dislocation nucleation at a diffusion wedge is stress controlled (rather than kinetics controlled) and adopt the first scenario of dislocation nucleation as described above. This assumption will later be verified by molecular-dynamics simulation results. With this assumption, it is possible to define a nucleation criterion in terms of a critical stress intensity factor for both cracks and diffusion wedges. We illustrate the critical condition for dislocation nucleation in Figure 15.4. A force balance on a dislocation near a crack tip leads to the critical stress intensity factor for dislocation nucleation from a crack

$$K_{\text{cr}}^{\text{PG}} = \frac{E(2\pi b_x)^s}{8\pi(1-\nu^2)}. \tag{15.7}$$

In comparison, a balance of critical stress required to break the dipole interaction in

front of a diffusion wedge yields a similar nucleation criterion

$$K_{\mathrm{dw}}^{\mathrm{PG}} = \frac{E(2\pi b_x)^s}{4\pi(1-\nu^2)}. \tag{15.8}$$

For copper with $E = 150$ GPa, $s = 0.31$ and $\nu = 0.33$ the predicted values are $K_{\mathrm{cr}}^{\mathrm{PG}} \approx 12.5\,\mathrm{MPa} \times \mathrm{m}^s$ and $K_{\mathrm{dw}}^{\mathrm{PG}} \approx 25\,\mathrm{MPa} \times \mathrm{m}^s$, and we note a factor of 2 difference in critical K-values, $K_{\mathrm{dw}}^{\mathrm{PG}}/K_{\mathrm{cr}}^{\mathrm{PG}} = 2$, for dislocation nucleation at a diffusion wedge and at a crack tip.

15.4. Discussion and summary

The main results of this chapter are summarized as follows.

- By considering climb of single edge dislocations in the grain boundary (as opposed to taking the infinitesimal viewpoint assumed in equation (14.6)), we showed that there exists a critical stress to initiate diffusion. This critical stress in independent of the film thickness. An important implication is that diffusion can not relax stresses in the film completely. This is in contradiction to the stress decay to zero as predicted by equation (14.19). In the next chapter we will thus present a modified continuum model that accounts for this difference.

- The study of single edge dislocation showed that in film thicknesses of several nanometers, image stresses on climb edge dislocations can be as large as 1 GPa. This further supports the hypothesis that single dislocations become important in small dimensions and that the discrete viewpoint of dislocation climb needs to be adapted. It also supports the view of a critical stress for diffusion initiation described above.

- A criterion in the spirit of the Rice-Thomson model was proposed to describe the conditions under which parallel glide dislocations are nucleated from diffusion wedges and cracks. The most important prediction of this model is that the critical stress intensity factor for parallel glide dislocation nucleation from a diffusion wedge is twice as large compared to the case of a crack.

16. Continuum modeling of thermal cycling experiments

It is known that mechanical stresses in thin films are often significantly higher than those in the bulk form of the same material. At low temperatures, this has (as discussed in Chapter 14) been mostly attributed to geometric confinement or lack of dislocation sources. At higher temperatures, several experimental results indicate that diffusional creep may play an increasingly important role [234].

Gao's model of constrained diffusional creep [88] has been further developed in light of experimental results to directly model the average stress in the film during the thermal cycling experiments by introducing a convolution procedure [234, 25]. Weiss *et al.* [234] invoked the constrained diffusional creep model to explain the occurrence of a stress drop observed during the first heating cycle of thin copper films. They also used constrained diffusional creep to model the stress-temperature curves measured during thermal cycling of several films and found good agreement for a 500 nm copper film, albeit by assuming a very large grain size.

In this chapter we propose a modification of the continuum model including a threshold stress for diffusion initiation. The assumption of the threshold stress is motivated by experimental results and the theoretical considerations about diffusion initiation discussed in Section 15.1. We will show that the modified model including the threshold stress provides better agreement of the experimental results with the theory particularly for higher temperatures.

The outline of this chapter is as follows. We first report the modified continuum model to capture the threshold stress. We then compare thermal cycling curves predicted by the new continuum mechanics model featuring a threshold stress with the experimental results.

16.1. Continuum model of constrained grain boundary diffusion with threshold stress

Equation (14.12) is the governing equation for the problem of constrained diffusional creep. Assuming a threshold stress σ_t for grain boundary diffusion, the boundary conditions are now modified as

$$\sigma_{xx}(\zeta = 0, t) = \sigma_t, \tag{16.1}$$

and

$$\frac{\partial \sigma_{xx}}{\partial \zeta}(\zeta = h_\mathrm{f}, t) = \frac{\partial^2 \sigma_{xx}}{\partial \zeta^2}(\zeta = h_\mathrm{f}, t) = 0. \tag{16.2}$$

The initial condition remains the same

$$\sigma_{xx}(\zeta, t = 0) = \sigma_0. \tag{16.3}$$

We consider the possibility that σ_t may be different under tension and compression. That is, no grain boundary diffusion can occur when

$$\sigma_t^- < \sigma_{xx}(0, t) < \sigma_t^+, \tag{16.4}$$

where $\sigma_{xx}(0, t)$ is the stress at the site of initiating climb edge dislocations near the entrance to the grain boundary.

Using superposition,

$$\sigma_{xx}(\zeta, t) = \sigma_t + \tilde{\sigma}(\zeta, t), \tag{16.5}$$

we obtain the governing equation for $\tilde{\sigma}(\zeta, t)$ as

$$\frac{\partial \tilde{\sigma}_{xx}(\zeta, t)}{\partial t} = \frac{ED_{\mathrm{gb}}\delta_{\mathrm{gb}}\Omega}{4\pi(1-\nu^2)\mathrm{k}T} \int_0^{h_\mathrm{f}} S(\zeta, \xi) \frac{\partial^3 \tilde{\sigma}_{xx}(\xi, t)}{\partial \xi^3} \mathrm{d}\xi. \tag{16.6}$$

The boundary conditions are

$$\tilde{\sigma}_{xx}(\zeta = 0, t) = 0, \tag{16.7}$$

$$\frac{\partial \tilde{\sigma}_{xx}}{\partial \zeta}(\zeta = h_\mathrm{f}, t) = \frac{\partial^2 \tilde{\sigma}_{xx}}{\partial \zeta^2}(\zeta = h_\mathrm{f}, t) = 0. \tag{16.8}$$

and the initial condition is

$$\tilde{\sigma}_{xx}(\zeta, t = 0) = \sigma_0 - \sigma_t \tag{16.9}$$

These equations are identical to those of [88] except that the initial condition is effectively reduced. Therefore, we can simply use the previous solution to obtain the average stress along the grain boundary as

$$\hat{\sigma}_{\mathrm{gb}}(t) = (\sigma_0 - \sigma_t) \exp\left(-\lambda_0 t/\tau\right) + \sigma_t \tag{16.10}$$

with a geometry-dependent constant defined in equation (14.20).

Figure 16.1 shows a numerical example of the decay of the average stress in the film as given by equation (16.13) with and without threshold stress (the characteristic time is fitted to experimental results). The parameter σ_t^+ is assumed to be 65 MPa. For comparison, experimental stress relaxation curves for 200 and 800 nm Cu films are presented in Figure 16.1. The experimental results show that the film stress does not decay to zero but instead approaches a plateau value.

We can now generalize the convolution procedure described by Weiss *et al.* [234]

$$\frac{\mathrm{d}\sigma_0}{\mathrm{d}T} = -\Delta\alpha M_\mathrm{f} \tag{16.11}$$

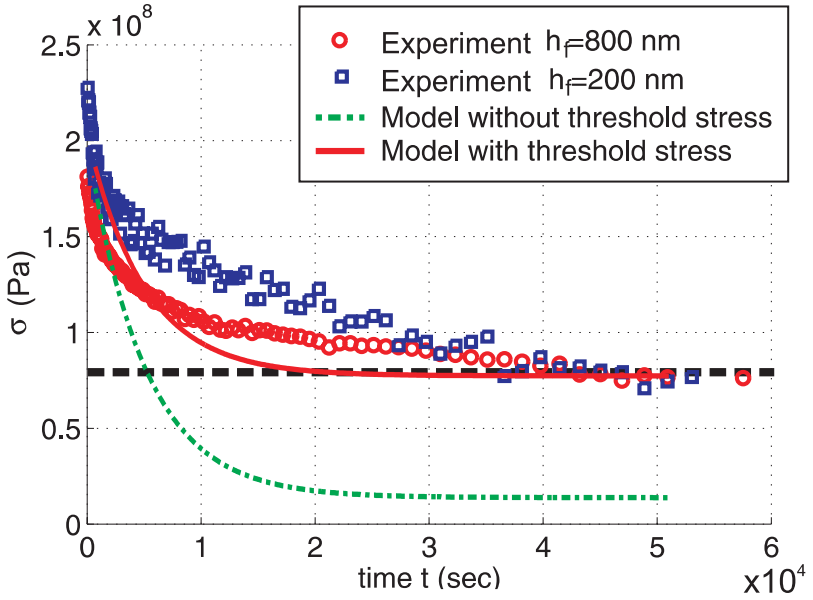

Figure 16.1.: Experimental results of stress decay at 250 °C for $h_\mathrm{f} = 200$ nm and $h_\mathrm{f} = 800$ nm [23, 33], and prediction of stress decay by the continuum model with and without threshold stress.

where $M_\mathrm{f} = E/(1-\nu)$ is the biaxial modulus and $\Delta\alpha$ refers to the thermal mismatch of film and substrate material. Then,

$$\begin{aligned}\hat{\sigma}_\mathrm{gb}(t) =& \sigma_t + \left(\sigma_0^\mathrm{start} - \sigma_t\right) \exp\left[-\lambda \int_{T_\mathrm{start}}^{T} \frac{\mathrm{d}\zeta}{\dot{T}\tau(\zeta)}\right] \\ &- M_\mathrm{f}\Delta\alpha\dot{T} \int_{T_\mathrm{start}}^{T} \exp\left[-\frac{\lambda}{\dot{T}}\left(\int_{\zeta}^{T} \frac{\mathrm{d}\xi}{\tau(\xi)}\right)\right] \frac{1}{\dot{T}}\mathrm{d}\zeta.\end{aligned} \tag{16.12}$$

The average stress σ in the film is related to σ_0 and $\hat{\sigma}_\mathrm{gb}$ as

$$\sigma = \sigma_0 - (\sigma_0 - \hat{\sigma}_\mathrm{gb})\Theta \tag{16.13}$$

where

$$\Theta = \frac{4h_\mathrm{f}}{d}\tanh\left(\frac{d}{4h_\mathrm{f}}\right). \tag{16.14}$$

For a given experimentally measured stress σ, the average stress in the grain boundary $\hat{\sigma}_\mathrm{gb}$ is given by

$$\hat{\sigma}_\mathrm{gb} = \frac{1}{\Theta}(\sigma - \sigma_0) + \sigma_0. \tag{16.15}$$

The average film stress depends on the ratio of grain size to film thickness.

16.2. Modeling of thermal cycling experiments by the continuum theory

As reported in [234, 79], the grain boundary diffusivity for copper is given by

$$\delta_{\mathrm{gb}} D_{\mathrm{gb}}(T) = 5 \times 10^{-15} \exp\left(-\frac{Q_b}{\mathrm{R}T}\right) \mathrm{m}^3\mathrm{s}^{-1} \tag{16.16}$$

with activation energy $Q_b = 104$ kJ/mole. We consider two film thicknesses of 100 and 600 nm. The threshold stresses for the grain boundary average stress is estimated from the experimentally measured average stress in the film by equation (16.15), and are chosen to be $\sigma_t^+ = 65$ MPa and $\sigma_t^- = -65$ MPa [33] (see also Figure 16.1). In the following, we assume that $E = 124$ GPa, $\nu = 0.34$ and the difference in thermal expansion coefficients of film and substrate is $\Delta\alpha = 1.3 \times 10^{-5}$ K^{-1} (same parameters as chosen in [234]).

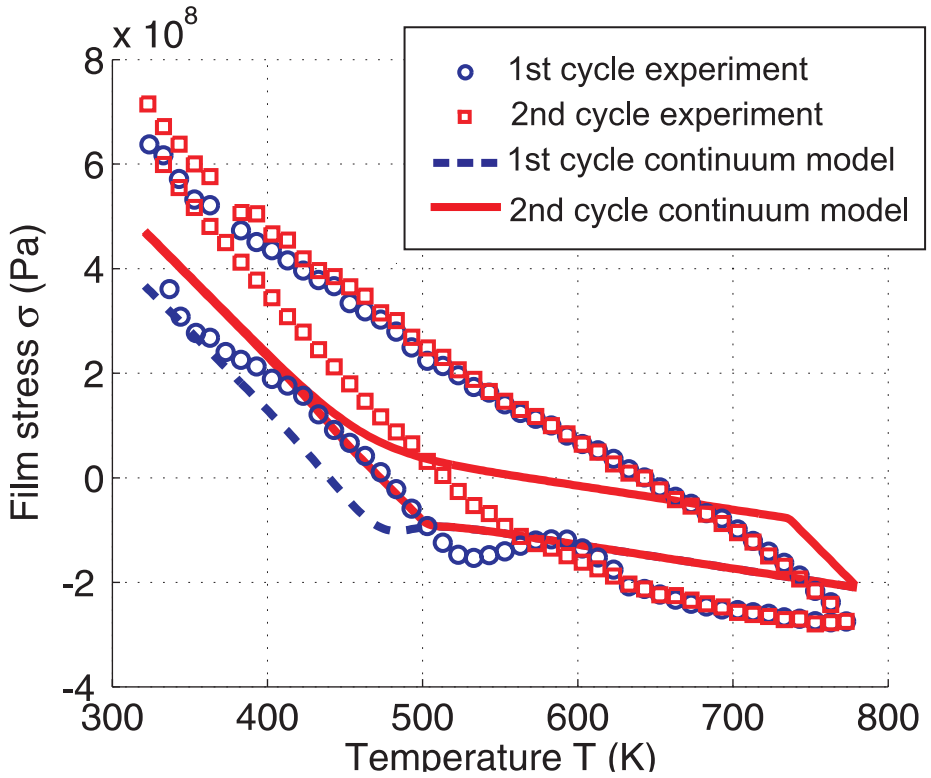

Figure 16.2.: Fit of continuum model with threshold stress to the experimental data of thermal cycling [23]. The film thickness is $h_{\mathrm{f}} = 100$ nm and grain boundary diffusivities are as in [79].

In Figure 16.2 we show a comparison of experiment and the continuum model with threshold stress for steady-state thermal cycling of thin films of thickness $h_{\mathrm{f}} \approx 100$ nm. In Figure 16.3 we show a comparison of experiment and the continuum model with threshold stress for steady-state thermal cycling of a 600 nm film. The experimental data is taken from [33, 23].

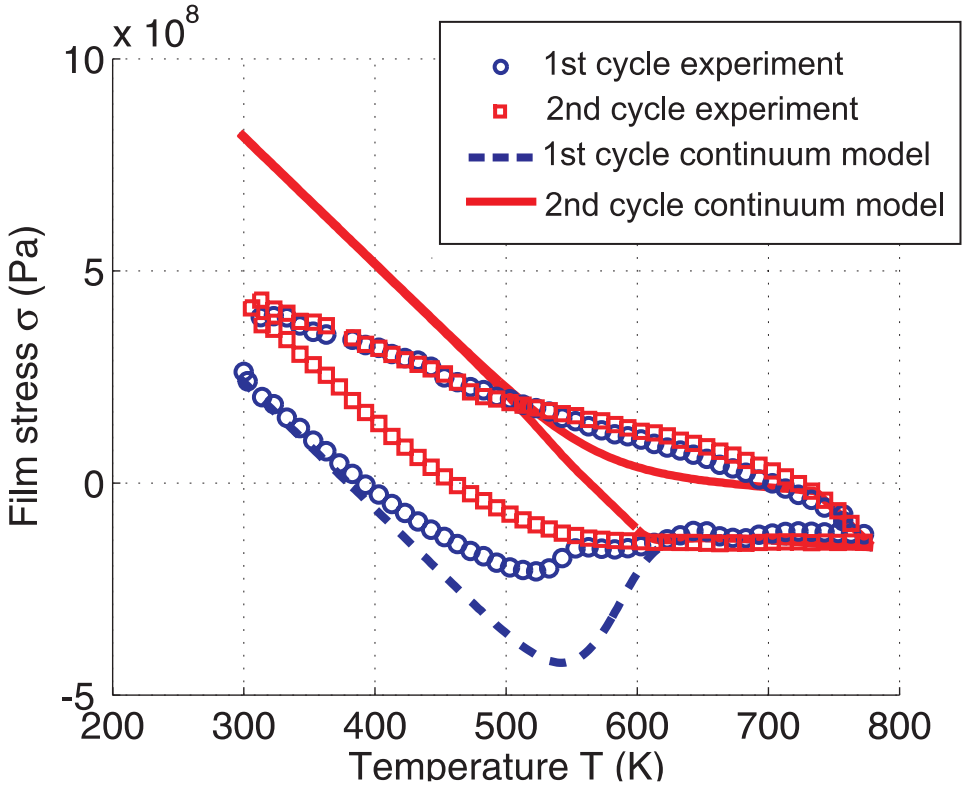

Figure 16.3.: Fit of continuum model with threshold stress to experimental data of thermal cycling [23]. The film thickness is $h_f = 600$ nm and grain boundary diffusivities are as in [79].

In both cases, some qualitative agreement is found, especially at elevated temperatures. For the 600 nm film, the results at low temperatures during the cooling cycle (upper curve) do not match as good as for high temperatures. This could partly be explained by the fact that, due to the rather large film thickness, not only parallel glide dislocations are present. In addition, threading dislocations are nucleated and relieve stresses as has been confirmed experimentally [25]. Experiment clearly shows that threading dislocations are nucleated in this regime [24, 55, 25]. Therefore, during cooling of the film, diffusional creep dominates at high temperatures, but threading dislocations dominate at low temperatures. Since the continuum model does not account for threading dislocations, the stresses at low temperatures (upper left corner in the plot) are overestimated. At high temperatures during the heating cycle, the stress relaxes to the value associated with the threshold stress σ_t^-, and the experimental measurements and continuum modeling agree quite well.

16.3. Estimation of diffusivities from experimental data

Another interesting aspect that we explored is the estimation of diffusivities from the experimental data. It can be observed in Figure 16.3 that the stress decay in the first heating cycle is larger in the experiment than in the simulation. When the classical

diffusivities as reported in the literature are used, the maximum compressive stress is overestimated by a factor of two (similar observation was also made in the paper by Weiss *et al.* [234], Figure 10). This could be due to the fact that the diffusivities used in the continuum mechanics model are smaller than the actual experimental value.

Figure 16.4 shows a fit of the continuum mechanics model to the experimental data, with a threshold stress $\sigma_t^- = -65$ MPa for a 600 nm film as obtained from experiment (see discussion above). Fitting the maximum compressive stress to the experimental results by adjusting the diffusivity yields a diffusivity 80 times higher than in the literature. Possible reasons for this could be the fact that the grain boundary structure strongly influences the diffusivities. This point that was not addressed in most classical theories of grain boundary diffusion. However, a strong dependence of the diffusivities on the grain boundary structure has been proposed [235]. Taking such considerations into account may explain the observations in the current studies.

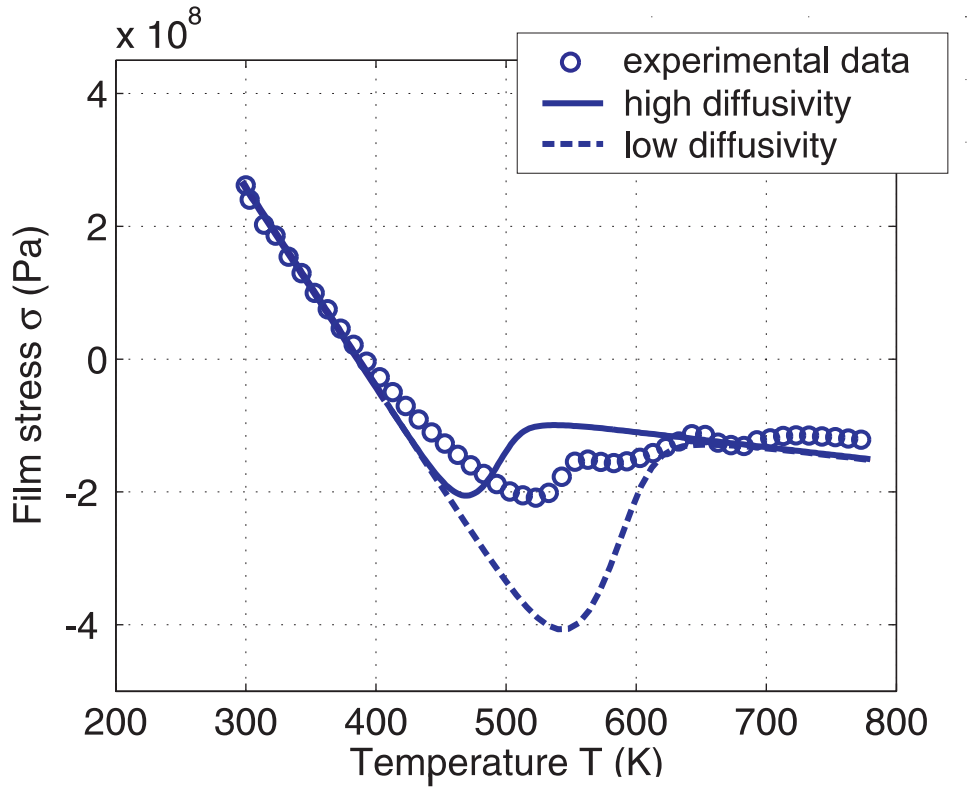

Figure 16.4.: Fit of diffusivities to the experimental data based on the first heating curve of the 600 nm film [23].

The fitted grain boundary diffusivity is given by

$$\delta_{\mathrm{gb}} D_{\mathrm{gb}}(T) = 4 \times 10^{-13} \exp\left(-\frac{Q_b}{\mathrm{R}T}\right) \mathrm{m}^3\mathrm{s}^{-1}. \tag{16.17}$$

The characteristic time for a film with $h_{\mathrm{f}} = 20$ nm at a temperature of about 90 percent of the melting point is then on the order of 10^{-8} seconds. This supports the idea that constrained grain boundary diffusion can be modeled with classical molecular-dynamics, since such simulations are typically limited to a time scale of around 10^{-8} seconds.

Finally, we compare thermal cycling experiments with the new estimate for diffusivities to the experimental results. In Figure 16.5 we show a comparison of experiment and the continuum model with threshold stress for steady-state thermal cycling of thin films with film thickness $h_f \approx 100$ nm. In Figure 16.6 we show a comparison of experiment and the continuum model with threshold stress for steady-state thermal cycling with film thickness $h_f \approx 600$ nm.

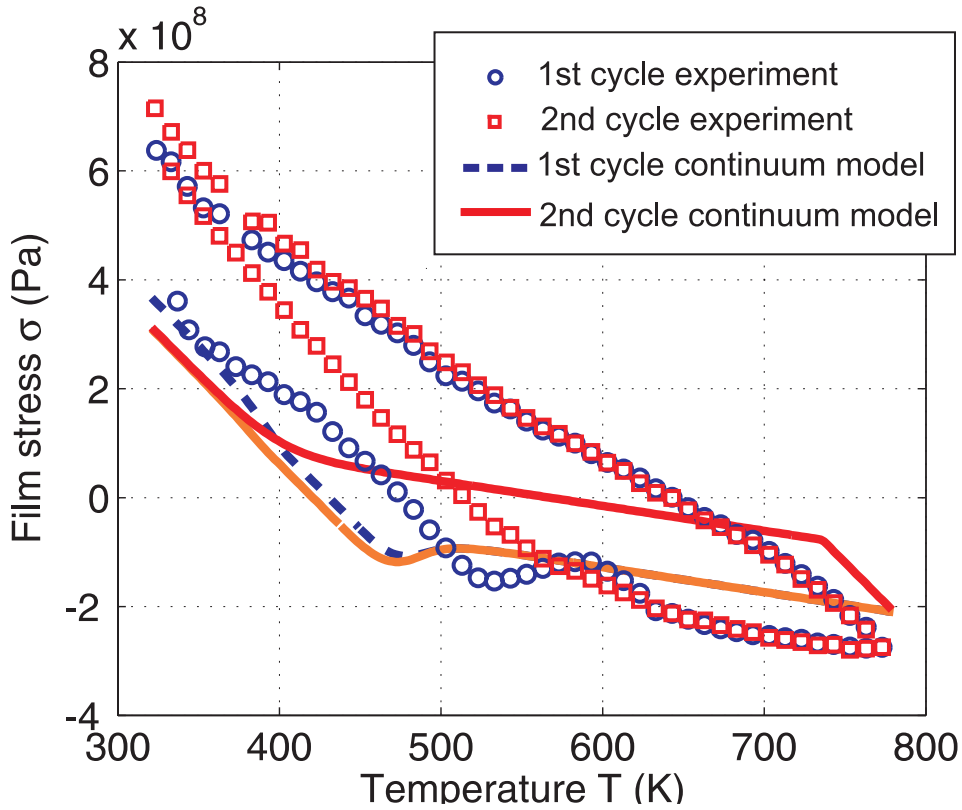

Figure 16.5.: Fit of continuum model with threshold stress to experimental data of thermal cycling [23]. The film thickness is $h_f = 100$ nm and grain boundary diffusivities are fitted to experimental data.

16.4. Discussion

The most important result reported in this chapter is the new concept of a threshold stress for diffusional creep in thin films. With this modified continuum theory, we could qualitatively reproduce results of the average film stress during thermal cycling experiments.

The modeled thermal cycling curves show that the introduction of a threshold stress based on experimental data represents some improvement of the previous model. Unlike in [234] where the grain size was changed in order to improve agreement, the parameters used here are identical to those in the experiments (same grain size, same ratio of grain size to grain diameter, same cooling and heating rates, etc.).

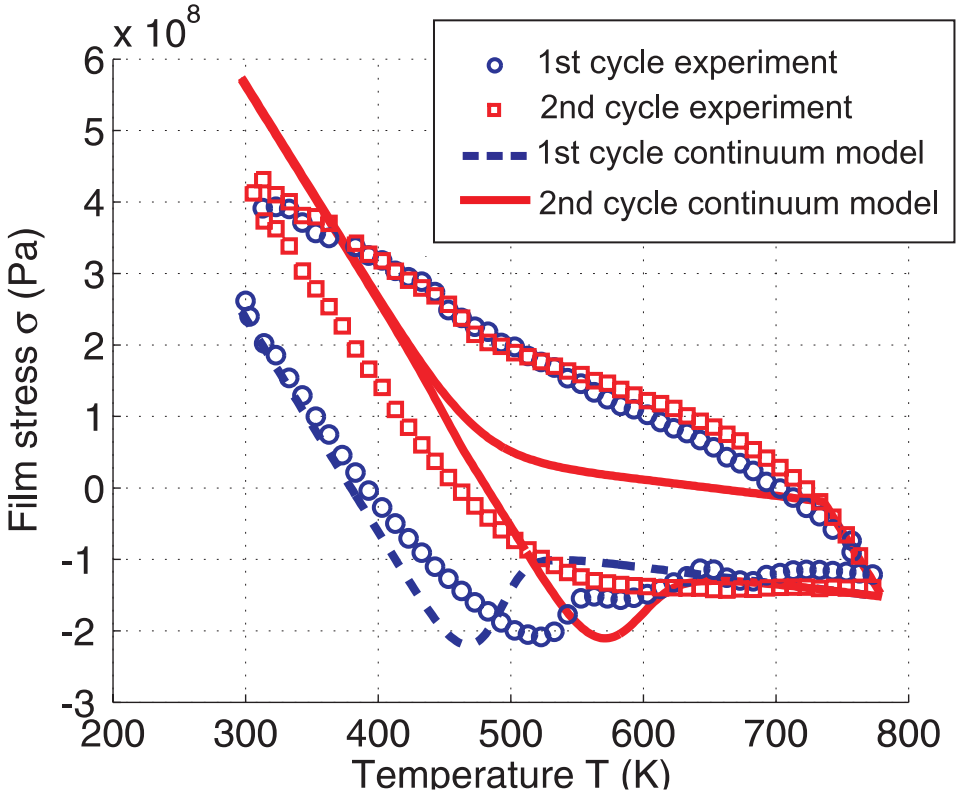

Figure 16.6.: Fit of continuum model with threshold stress to experimental data of thermal cycling [23]. The film thickness is $h_\mathrm{f} = 600$ nm and grain boundary diffusivities are fitted to experimental data.

The most important difference is that without the threshold stress, the numerically estimated curves are very "thin" in contrast to the experimental results where the curves are wider. Most importantly, the thermal slope, which is apparent at high temperatures during the cooling cycle, can only be reproduced with a model featuring a threshold stress.

Additional discussion was devoted to estimates of the grain boundary diffusivity from experimental data. It was found that diffusivities may be higher than reported in the literature [79]. It was proposed that this may be attributed to the dependence of diffusivities on the grain boundary structure.

17. Atomistic modeling of constrained grain boundary diffusion in a bicrystal model

While the continuum model [88, 251] of constrained diffusional creep has been very successful in explaining the origin of the internal stresses in thin films, it can neither yield a description of the nucleation process of parallel glide dislocations from the diffusion wedge, nor can it incorporate the parallel glide mechanism into the prediction of residual stresses in a film. Under the guidance of the continuum model [88, 250, 251], atomistic simulations are an ideal tool to provide a detailed description of how parallel glide dislocations are nucleated near a diffusion wedge.

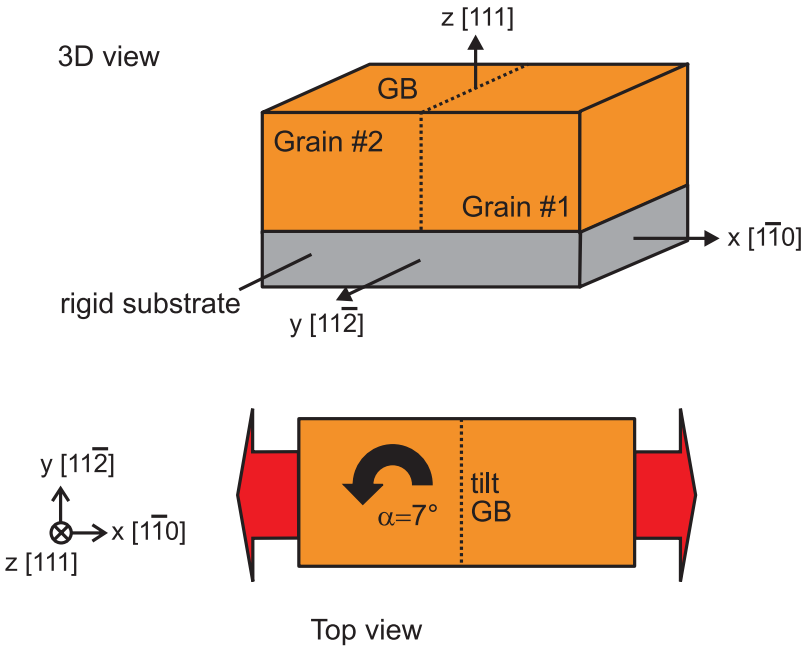

Figure 17.1.: Sample geometry of the atomistic simulations of constrained diffusional creep in a bicrystal model.

In this chapter, we describe large-scale atomistic simulations to study plastic deformation in sub-micron thin films on substrates. The simulations reveal that stresses in the film are relaxed by mass diffusion from the surface into the grain boundary. This leads to formation of a novel material defect referred to as the diffusion wedge. A crack-like stress field is found to develop around the diffusion wedge as the traction along the grain boundary is relaxed and the adhesion between the film and the substrate prohibits strain

relaxation close to the interface. The diffusion wedge causes nucleation of dislocations on slip planes parallel to the plane of the film. We find that nucleation of such parallel glide dislocations from a diffusion wedge can be described by a critical stress intensity factor similar to the case of a crack. Atomistic simulations of parallel glide dislocations associated with the crack-like grain boundary diffusion wedge represent a significant progress in the theory of diffusional creep in thin films on substrates since they close the theory-experiment-simulation linkage.

17.1. Introduction and modeling procedure

Atomistic modeling of thin film mechanics becomes feasible with the advent of massively parallel computers on time and length-scales comparable with those usually attained in experimental investigations. Due to the time limitation of the classical molecular-dynamics method (time intervals are typically $< 10^{-8}$ s), we perform simulations at elevated temperatures to accelerate the dynamics of grain boundary diffusion. To make the diffusive processes accessible to the molecular-dynamics time scale, the simulations are carried out at temperatures between 80 and 90 percent of the melting temperature. Luckily, we find that the phenomenon of grain boundary diffusion wedge and the associated dislocation mechanisms persist at very high temperatures. This makes it possible to simulate this specific phenomenon. Generally, it is still very difficult to simulate diffusion related phenomena by molecular-dynamics.

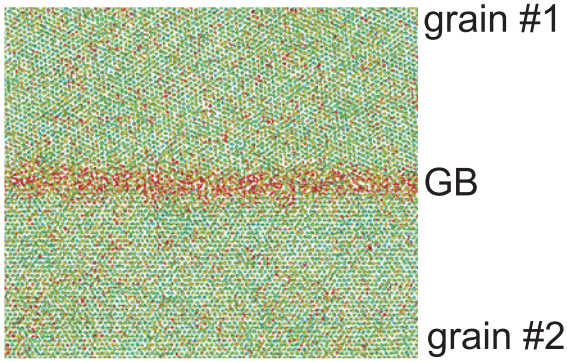

Figure 17.2.: Disordered intergranular layer at high-energy grain boundary in copper at elevated temperature (85 % of melting temperature).

At elevated temperatures, grain boundary diffusion in a bulk material was successfully modeled recently [240, 241, 235], where grain sizes up to 15 nm were considered in a model system of Pd. Recent work [240, 124, 125] suggests that at elevated temperatures, the grain boundary structure of metals may transform into a liquid like structure with a width of 1-2 nm referred to as “glassy phase”.

Glassy phases in grain boundaries were found in copper at homologous temperatures as low as $T_h \approx 0.4$ [139, 125]. Experimental evidence for glassy intergranular phases was discussed by [31]. We expect such phase transformation at the grain boundary to play a significant role in the plastic properties at elevated temperatures because the different grain boundary structure has significant influence on the diffusivities [125, 124]. Further

discussion on the topic is found in a recent review article [235]. Figure 17.2 plots such a disordered intergranular phase obtained in a thin film of copper.

17.1.1. Computational method and interatomic potential

We use a massively parallel classical molecular-dynamics code to model the problem of constrained grain boundary diffusion. A multi-body potential [155] derived using the embedded atom scheme is used, and we integrate the equations of motion using a velocity verlet algorithm [15, 207]. The studies are carried out using a microcanonical NVE ensemble.

The potential [155] shows good agreement with *ab initio* calculations in terms of elastic properties, stacking fault energies and excited phases of copper [155]. We determine the melting point to be close to the experimental value of $T_m = 1360$ K with this potential.

17.1.2. Modeling of a thin film on substrate

We establish the simulation sample by creating a $< 111 >$ fcc lattice, rotating one half counterclockwise and cutting out two rectangular pieces. This procedure leads to an asymmetric $< 111 >$ tilt grain boundary with approximately $\alpha \approx 7^\circ$ mismatch. Note that the choice of this geometry and the tilt angle is motivated by recent experimental results [25].

The simulation geometry is depicted in Figure 17.1. In some simulations, we further rotate the tilted grain counterclockwise around its [112] axis, creating a higher energy grain boundary.

The structure is periodic in the y-direction. We impose a homogeneous strain throughout the sample to account for thermal expansion [155]. The boundary and substrate atoms are chosen such that atoms inside the film do not sense the existence of the surface. The atoms of the boundary and the substrate are held pinned at a prescribed location by introducing an additional term in the potential energy of the form

$$\phi^p = \frac{1}{2}\, k_0 r^2_{x^d - x^c}, \tag{17.1}$$

where x^d is the prescribed location of an atom, and x^c is its current position. The expression $r_{x^d - x^c} =\mid x^d - x^c \mid$ stands for the radius of separation of the desired and present location, while k_0 is a harmonic spring constant which is chosen $k_0 = 20$ in reduced atomic units. We prescribe locations of atoms in the substrate only in the x and z direction, and leave the y direction unconstrained. The atoms in the boundary are only constrained in the x direction, so that the boundary is allowed to relax in the y and z direction.

In terms of a continuum mechanics interpretation of the simulation cell, this resembles a plane strain case with a thin compliant (copper) film on a rigid substrate, with no sliding and no diffusion at the film-substrate interface. The choice of the rigid substrate is partly motivated by the finding that the stress intensity factor of a crack is reached faster in the case of a rigid substrate than in the isotropic case or when the film is

attached to a compliant substrate (see Figure 14.6 and associated discussion). After the "raw" sample is created, a global energy minimization scheme is applied to relax the structure. Subsequently, the sample is heated up to an elevated temperature and annealed for a longer time so that the grain boundary structure relaxes and takes its equilibrium configuration. We wait until the virial stresses [212] relax to zero in this initial configuration.

To make the diffusive processes accessible to the molecular-dynamics time scale, the simulations are carried out at elevated temperatures. The simulations to investigate dislocation nucleation in conjunction with diffusional creep are performed at a homologous temperature of $T_h \approx 0.8$ and $T_h \approx 0.9$, while studies on diffusion alone are done at temperatures as low as $T_h \approx 0.6$. At elevated temperature, the grain boundary exhibits a highly confined glassy intergranular phase of less than 1 nm width, in accordance with [125].

After annealing we proceed with applying a lateral strain. The prescribed positions x_d are calculated according to a homogeneous strain throughout the simulation sample. We use a time step of $\Delta t \approx 3 \times 10^{-15}$ s for integration. The strain rate is on the order of 10^7 s^{-1} corresponding to approximately 1 percent strain per nanosecond. The strain rate is adjusted during the simulation such that the stress in the film remains low to avoid nucleation of dislocations on inclined slip planes, similar to the procedure adopted by [240]. The only deformation mechanism allowed is diffusional creep in the grain boundary. Whenever activation of a different mechanism such as threading dislocations is observed, the simulation is restarted at a lower stress and the strain rate is lowered. This procedure has proven to allow more time for diffusive processes and effectively shut down competing mechanisms. In the simulation with $T_h \approx 0.8$, the grain boundary width remains less than 1 nm and increases slightly at higher temperatures when the sample is loaded. In the simulation with $T_h \approx 0.9$ the grain boundary width is further increased and is found to be around 1-2 nm.

The systems contain more than $1,000,000$ particles, which is a significant number since simulations are carried out over several nanoseconds. The film thickness ranges from 4.5 nm to 35 nm, the latter value becoming comparable to experimental investigations where films between 35 and 50 nm were investigated [24, 55].

17.2. Formation of the diffusion wedge

In this section we discuss the change of the displacement field as the diffusion wedge builds up and show that the displacement field becomes crack-like. Further, we show the diffusive displacement of atoms and hence prove that diffusional mass transport from the surface along the grain boundary leads to formation of a diffusion wedge.

17.2.1. Crack-like displacement near a diffusion wedge

We find in our simulations that a minimum stress around $\sigma_{xx} \approx 1.6$ GPa independent of the film thickness is required to initiate diffusion. In addition, we observe that the grain boundary traction can not be relaxed below $\sigma_{xx} \approx 1.6$ GPa for films thinner than ten

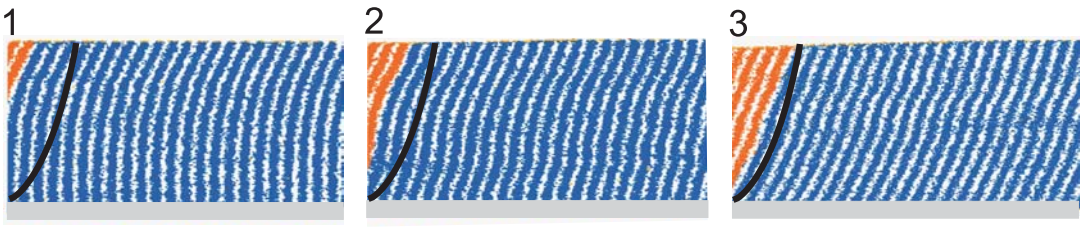

Figure 17.3.: Change of displacements in the vicinity of the diffusion wedge over time. The continuous dark line corresponds to the continuum mechanics solution discussed in Chapter 14.2.1.

nanometers. Diffusion can not relax stresses in such thin films completely! These facts seem to be qualitatively consistent with the predictions of equation (15.1). The fact that we have calculated stress by averaging over a finite region in the atomistic model can not explain this finding. Similar calculations in a sample with a crack show that the traction along the crack face approaches zero.

The snapshots in Figure 17.3 show how the displacement changes as material diffuses into the grain boundary. The horizontal coordinates have been stretched by a factor of ten in the x direction to make the crystal lines clearly visible

$$[x, y, z]^{new} = [10 \cdot x, y, z]^{orig}. \tag{17.2}$$

This visualization technique is applied throughout this chapter. We highlight the additional half planes of atoms close to the grain boundary. The continuous dark line corresponds to the continuum mechanics solution in the long-time limit $t \to \infty$ discussed in Chapter 14.2.1. The results suggest that the displacement field near the diffusion wedge approaches the continuum mechanics solution.

17.2.2. Diffusive displacement of atoms in the grain boundary

To illustrate diffusional motion of atoms in the grain boundary, we color each atom with diffusive displacement δz larger than a few Burgers vectors. Figure 17.4 plots these fields for several instants in time. Diffusion leads to significant surface grooving, with groove depths up to several nm. One can clearly identify the wedge-shape of the diffused atoms. The atomistic simulations show that atoms inserted into the grain boundary instantaneously crystallize, rendering the structure of the grain boundary invariant (this was observed for temperatures below 1150 K; at higher temperatures, the width of the grain boundary increases slightly).

The atoms transported along the grain boundary add to either one of the two grains. This result illustrates that the continuum mechanics assumptions [88, 250, 251] are valid also on the atomistic level.

We also observe "classical" threading dislocations which become operative when stresses in the film are high enough to allow nucleation of dislocations [240, 217]. A frequently observed phenomenon is the emission of dislocations from the grain boundary on inclined $< 111 >$ glide planes [168, 217]. In the sample with $h_f \approx 30$ nm, such threading dislocations are nucleated at a stress level of $\sigma_{xx} \approx 2.4$ GPa. We observe that thinner

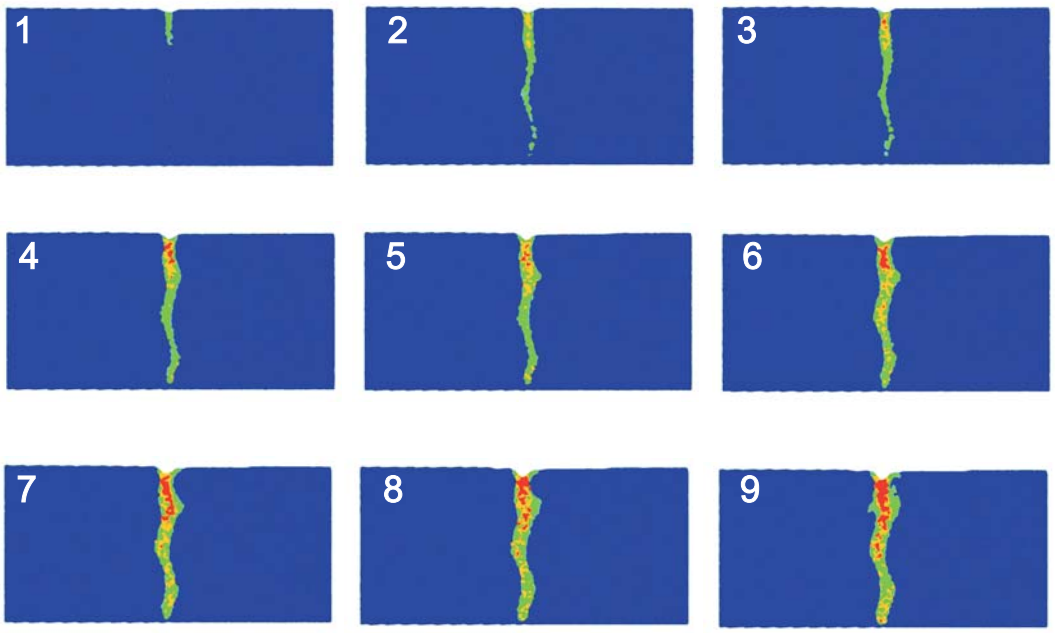

Figure 17.4.: Diffusional flow of material into the grain boundary. Atoms that diffused into the grain boundary are highlighted.

films require a higher critical stress for dislocation nucleation from the grain boundary, in qualitative agreement with the prediction by the $1/h_{\mathrm{f}}$ scaling law for the yield stress. In films thinner than 10 nm it requires extremely high stresses to nucleate inclined dislocations, which renders this mechanism almost impossible. The studies show that grain boundaries are, as proposed in the literature, fertile sources for dislocations in small-grained materials [240, 217].

Another issue in terms of dislocation nucleation is the stability and mobility of the grain boundary. We observe that the grain boundary forms jogs at elevated temperatures and relatively low stresses (contrary to our intuition, at high stresses the grain boundary remains straight). The diffusion path can be severely suppressed and the local stress concentration at the kink serves as a ready source for dislocations. The grain boundary does not remain straight and oscillates around the initial, straight position.

17.3. Development of the crack-like stress field and nucleation of parallel glide dislocations

Here we summarize the main results of the atomistic simulations focused on nucleation of parallel glide dislocations from diffusion wedges and cracks.

T (K)	h_f (nm)	K^PG (MPa $\times$ m^s)
Crack		
300	27.2	4.95
Diffusion wedge		
1150	27.2	11.91
1250	27.2	11.35
1250	34.2	11.23

Table 17.1.: Critical stress intensity factors K^PG for nucleation of parallel glide dislocations under various conditions, for a diffusion wedge and a crack.

17.3.1. Nucleation of parallel glide dislocations from a diffusion wedge

Continuum theory assumes that dislocations are nucleated when the stress field around the diffusion wedge becomes crack-like. Critical stress intensity factors for dislocation nucleation measured from the atomistic simulations are shown in Table 17.1 for different simulations. We use equation (15.5) to determine the stress intensity factor. The stress intensity factor is found independent of geometry (film thickness) and also has similar values at $T_h = 0.8$ and $T_h = 0.9$. We observe that nucleation of parallel glide dislocations depends on the film thickness. In the present quasi-two-dimensional setup with rigid boundaries, we observe that dislocations from the boundaries are nucleated when very large strains are applied, thus imposing a condition on the minimum thickness for nucleation of parallel glide dislocations.

Dislocation nucleation at a diffusion wedge can be divided into different stages shown in Figure 17.5. After the critical stress intensity factor is achieved, a dislocation dipole is formed. One end of the dipole is pinned in the grain boundary, while the dislocation at the other end of the dipole slides away from the grain boundary. Subsequently, the pinned dislocation is annihilated or "dissolves into" the grain boundary, while the dislocation at the right end of the dipole begins to move away from the nucleation site. As usually found in fcc metals, the dislocation is decomposed into two Shockley partials. The parallel glide dislocation glides on a slip plane parallel to the plane of the film at a distance of a few Burgers vectors above the film-substrate interface (and is therefore completely inside the film material). The core width of the partials extends to about 6 Burgers vectors around 1.6 nm. The dislocation moves a small distance away from the grain boundary to its equilibrium position. When stresses in the film become larger, it responds by moving further away from the grain boundary. The nucleation process is highly repeatable. Every time one parallel glide dislocation is nucleated, one climb edge dislocation is annihilated, leading to a decay in stress intensity. The additional time required to nucleate another parallel glide dislocation is determined by the time required for diffusion to recover the critical stress intensity. This time is much less than the initial time required to form the diffusion wedge. After the first dislocation is nucleated, more and more parallel glide dislocations are observed. In our confined, finite simulation geometry, the emitted parallel glide dislocations form a "secondary pileup" close to the

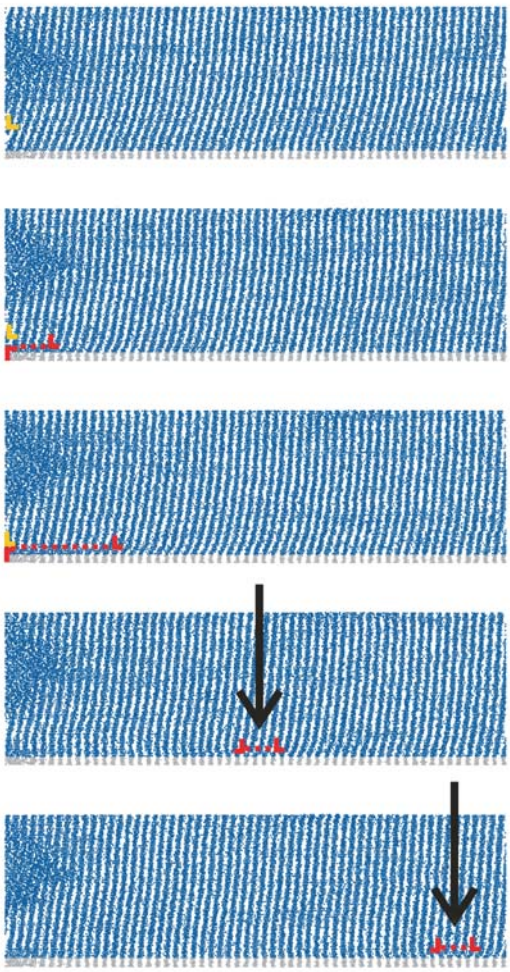

Figure 17.5.: Nucleation of parallel glide dislocations from a diffusion wedge.

boundary of the simulation cell. In simulations at lower temperatures ($T \approx 800$ K), we also observe constrained grain boundary diffusion and the formation of a diffusion wedge with a lattice displacement field similar to that of a crack. However, due to the time constraints of molecular-dynamics, nucleation of parallel glide dislocation is not observed.

17.3.2. Nucleation of parallel glide dislocations from a crack

The nucleation of parallel glide dislocations from a crack in a bimaterial layer is shown in Figure 17.6. For numerical reasons, the loading rate is chosen higher than in the previous case and the temperature in the simulations is about 300 K.

After an incipient dislocation is formed, a dislocation nucleates and moves away from the crack tip. The crack tip is blunted, and each time a parallel glide dislocation is nucleated, one surface step is formed. This process is also highly repeatable, as lateral strain is increased. The nucleation of parallel glide dislocations from a crack tip is observed at loading rate a few orders of magnitude higher than in the case of a diffusion

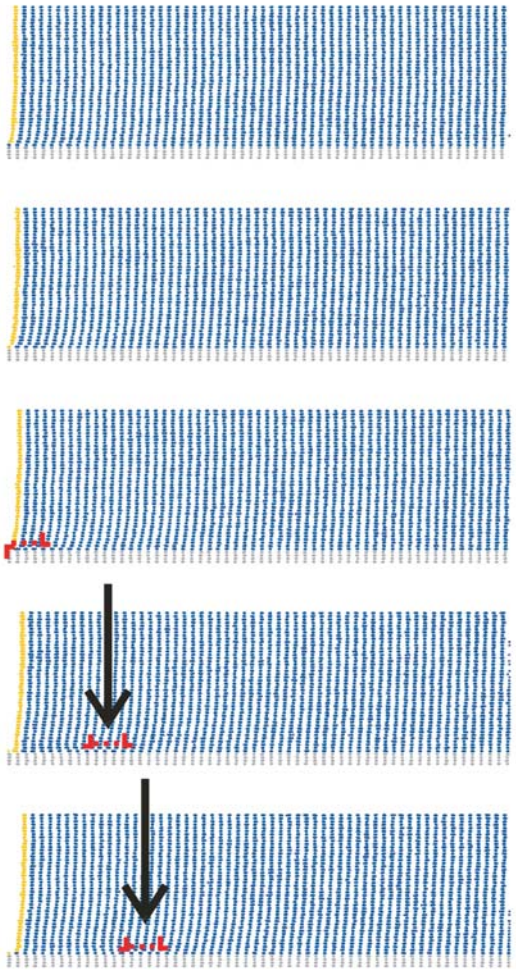

Figure 17.6.: Nucleation of parallel glide dislocations from a crack.

wedge and there seems to be no rate limitation in the case of a crack. As in the case of a diffusion wedge, the dislocation glides on a parallel glide plane a few Burgers vectors above the film-substrate interface. For a crack, nucleation of parallel glide dislocations is observed in films as thin as 5 nm. This may be because the critical stress intensity factor is smaller than that for a diffusion wedge, as indicated in Table 17.1. The critical stress intensity for parallel glide dislocation nucleation from a diffusion wedge is about 2.3 times larger than that for a crack. This value is in good agreement with the estimate based on the Rice-Thomson model.

17.4. Discussion

When classical mechanisms of plastic deformation based on the creation and motion of dislocations are severely hindered in thin films on substrates, constrained diffusional creep becomes a major mechanism for stress relaxation, leading to the formation of a new class of defects called the grain boundary diffusion wedge. Large-scale atomistic simulations are performed to investigate the properties of such diffusion wedges. We

have shown by atomistic simulations that material is indeed transported from the surface into grain boundaries and that such transport leads to a crack-like stress field causing nucleation of a novel dislocation mechanism of parallel glide dislocations near the film-substrate interface. The atomistic simulations of parallel glide dislocations being emitted near the root of the grain boundary have further clarified the mechanism of constrained grain boundary diffusion in thin films and provided an important link between theory and experiments.

17.4.1. Theoretical, experimental and simulation results

The experimental data suggests that nucleation occurs only at specific grain boundaries. This can partially be explained by the strong dependence of diffusion coefficients on the structure of the grain boundary [240, 125]. Using different types of grain boundaries, we have verified that high-energy grain boundaries exhibit faster diffusivities than low-energy grain boundaries. The viewpoint proposed in [125] is thus consistent with our simulation results. The fact that this concept was shown to hold in covalently bonded system, palladium as well as copper (the present study) shows that the transformation of grain boundaries into liquid-like structures may be a more general concept independent of the details of the atomic bonding. Experimentalists [55, 24] have found that nucleation of parallel glide dislocation occurs repeatedly from grain boundary sources near the film-substrate interface while strain is increased during thermal cycling. The same phenomenon is observed in the atomistic simulations reported in this chapter, although the conditions are quite different. Repeatedly emitted parallel glide dislocations form a pileup when they move towards an obstacle, which can be other grain boundaries (e.g. twins) in the experiments or boundary atoms in the simulations. Repeated nucleation is possible because by each parallel glide nucleation, only one climb edge dislocation in the grain boundary is annihilated while many of them remain "stored" in the grain boundary. The total Burgers vector stored in the grain boundary is found to remain constant.

Computer simulations provide evidence that diffusion initiation occurs at a critical applied stress $\sigma_0 \approx 1.6$ GPa, independent of the film thickness. Continuum analysis in equation (15.1) at $T = 0$ K for initiation of diffusion support this finding and predict a critical stress $\sigma_0 \approx 6$ GPa, also independent of the film thickness. The fact that the continuum analysis suggests a higher value could be explained by the higher temperature used in the simulations. In other publications [181] it is proposed that the critical stresses for dislocation nucleation are about five times smaller at room temperature, thus attaining the value measured in the atomistic simulations. It has recently been shown that stress distribution in thin films over different grains is highly inhomogeneous [201]. In some grains, extremely high stresses of several GPa are observed. This readily provides sufficiently large stresses to initiate diffusion, and also helps to explain why parallel glide dislocation nucleation only occurs at specific grain boundaries in the experiments. Alternatively to equation (15.1), the critical stress for diffusion initiation can be defined based on equation (15.2). In this case, the critical stress for the initiation of grain boundary diffusion resulting from the molecular-dynamics simulations agrees well with a value of $d_{\mathrm{src}} = 3\,b = 0.78$ nm. Even in the molecular-dynamics simulation that does

not *a priori* assume grain boundary diffusion to occur in form of dislocation climb, there exists such a critical stress which is independent of the film thickness. From the thermodynamic point of view, this is unexpected since diffusion should start at infinitesimal stresses provided that sources for the diffusive processes are present. We note here that the observed finite threshold stress could, in principle, be a consequence quasi-two-dimensional geometry used in the simulations. However, in experiment it is also observed that for stresses below a threshold magnitude of several hundred MPa, no diffusion occurs even at elevated temperatures [55, 132]. We briefly note that the concept of a threshold stress in diffusional creep has also been proposed by Arzt and coworkers, due to the discreteness of the dislocations participating in the creep process [18]. Further research may be necessary to clarify this point.

As discussed in Section 15.2, in films thinner than ten nanometers, image stresses on climb dislocations can be as large as 1 GPa. This can severely hinder climb mediated diffusional creep, suggesting that the behavior of discrete dislocations needs to be considered for the nanoscale thin films. This is also supported by the atomistic results showing that stress can not be relaxed completely in extremely thin films. In addition to the theoretical and computational evidence, our results are not contradicting experimental results which often show large residual stresses in extremely thin films [132].

Employing our molecular-dynamics result that nucleation occurs at a critical stress intensity factor K^{PG}, we estimate the necessary lateral stress σ_0 in order to achieve this stress intensity factor at $t \to \infty$. In films thinner than a critical thickness between 10 and 20 nm, the analysis predicts stresses reaching the cohesive strength of the material. Hence, before nucleation of parallel glide dislocations the simulation sample will be destroyed by homogeneous decohesion. In the present quasi-two-dimensional setup with rigid boundaries, an additional issue is that dislocations from the boundaries are nucleated when very large strains are applied.

These considerations suggest a minimum thickness for parallel glide dislocation nucleation. The critical stress intensity factor for dislocation nucleation from a crack and a diffusion wedge at 0 K are about three times larger than the values calculated from atomistic simulation results at elevated temperature. This can be explained by the finite temperature in the simulations. Yet it is important that both approaches suggest that $K^{\mathrm{PG}}_{\mathrm{dw}}/K^{\mathrm{PG}}_{\mathrm{cr}} \approx 2$.

The discussion reveals that the diffusion wedge has similar properties as a crack, but requires a larger stress intensity factor to nucleate a dislocation. The reason for this is that in the case of a diffusion wedge, a dislocation dipole needs to be formed and the dipole interaction force is twice as strong the image force on an emergent dislocation near a crack tip. This is an important result of atomistic modeling that corroborates the assertion made in the development of the Rice-Thomson model in Section 15.3.

17.4.2. Diffusion wedge versus crack

We discuss some of the common and distinct properties observed in atomistic simulations for the two kinds of defects (crack versus diffusion wedge), both are assumed to lie along the grain boundary under elevated temperatures. For a *crack*, we observe

- As the applied stress σ_0 is increased, the normal stress σ_{xx} along the grain boundary

remains zero throughout the film thickness, in consistency with the traction free crack condition.

- The loading rate for dislocation nucleation can be much higher than in the case of diffusional creep; there is no rate limiting factor.
- Dislocation nucleation occurs at relatively small stress intensity factor.
- Dislocation nucleation starts with an incipient dislocation close to the crack tip.

In contrast, for a *diffusion wedge*, we observe

- The loading rate must be slow enough to allow for diffusion as a dominant relaxation mechanism. Otherwise dislocation activities on inclined planes are observed instead of grain boundary diffusion.
- The stresses in the film are determined by the competition of processes causing stresses to be generated and inelastic deformation mechanisms that allow the stresses to be relaxed.
- The nucleation process proceeds much slower, because in order to nucleate a parallel glide dislocation, dislocation climb in the grain boundary has to take place to annihilate part of the newly created dipole. On atomistic time scales, nucleation is an extremely slow process (for a crack, nucleation is very fast).
- Dislocation nucleation starts when the stress intensity factor is sufficiently large to create a dislocation dipole near the diffusion wedge.
- There exists a minimal thickness for parallel glide dislocation nucleation. If the film is very thin, the applied stress reaches the cohesive strength of the material before the critical stress intensity factor K^{PG} for dislocation nucleation is reached.

The two defects have major differences in the time scale associated with creation of dislocations. A crack is a ready source for dislocations, while a diffusion wedge has an intrinsic characteristic time associated with dislocation climb. We finally note that no difference in the mechanism of parallel glide dislocation nucleation is observed at different temperatures. We propose further investigations on discrete dislocation effects at the nanoscale. In particular, it is important to develop continuum level solutions for dislocation nucleation in the spirit of Rice's analysis based on Peierls concept [178, 171]. It should also be interesting to study thin films creep using mesoscopic methods such as discrete dislocation dynamics. Results of the molecular-dynamics simulations can be used as input parameter in a multi-scale modeling procedure.

17.5. Conclusions

We have reported large scale atomistic simulations of constrained diffusional creep in thin films on substrates. The following objectives have been achieved.

1. We have confirmed the formation of diffusion wedges using atomistic simulations, and have shown, in agreement with theory and experiment, that the flow of matter from the film surface into grain boundaries represents a significant mechanism of plasticity in submicron thin films.

2. We have verified that the diffusion wedge exhibits crack-like stress field at the atomistic level, and this mechanism occurs even if the background stress in the film is insufficient to create dislocations.

3. From the simulations, we have observed a critical stress intensity factor for nucleation of parallel glide dislocations from the diffusion wedge. The critical stress intensity is found to be independent of the film thickness and does not significantly change in the temperature range of our investigation (from $T_h = 0.9$ to $T_h = 0.8$). We have proposed a critical stress intensity as the nucleation criterion for dislocations near both a crack and a diffusion wedge. We have shown that such criterion yields predictions in reasonable agreement with atomistic simulation results.

The most important result of these simulations is that when grain boundary diffusion is active, the grain boundary can be treated as a crack in a first approximation. In the present chapter, we have only studied a two-dimensional geometry. In the following the chapters we will show that the condition of traction relaxation along grain boundaries also has dramatic consequences on the dislocation mechanisms in polycrystalline thin films.

18. Dislocation nucleation from grain triple junction

In this chapter we focus on the details of dislocation nucleation close to a triple junction between three grains misoriented with respect to one another. The simulation geometry is shown in Figure 18.1.

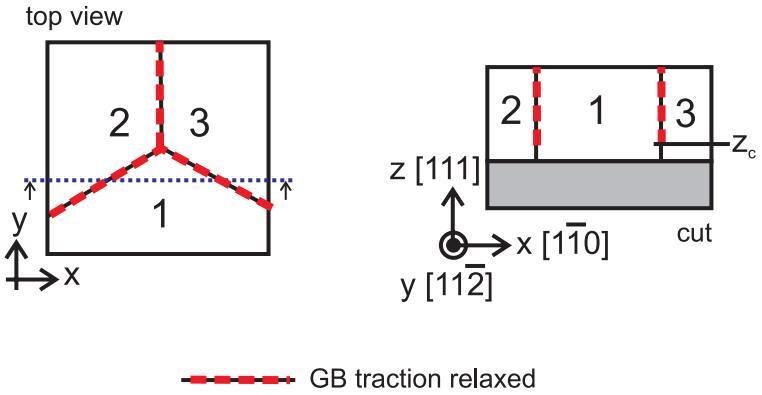

Figure 18.1.: Geometry for studies of plasticity in grain triple junctions.

In contrast to the simple bicrystal geometry used in numerical studies discussed in the preceding chapter, experiments are carried out in polycrystalline thin films [55, 25]. The first goal of this and the following chapter is hence to extend the quasi-two dimensional studies of constrained diffusional creep to more realistic polycrystalline microstructures.

We will investigate plasticity of thin films with traction relaxation along the grain boundaries due to constrained diffusional creep. The continuum model and the quasi-two dimensional geometry of previous atomistic simulation of plasticity in thin films could not provide a clear understanding of dislocation nucleation processes from different types of grain boundaries. Yet, experiments show a high selectivity of dislocation nucleation from different grain boundaries [24, 25]. Understanding the features of the grain boundaries as sources for dislocation nucleation is critically important to form a clear picture of thin film plasticity. Therefore, an important objective of this chapter is to study the details of the dislocation nucleation process near the grain boundary-substrate interface. We show that the grain boundary structure indeed has a significant influence on the dislocation nucleation process. Another interesting result is that the role of partial dislocations is important in very thin films with very small grain diameters.

18.1. Atomistic modeling of the grain triple junction

Here we summarize the details of the atomistic modeling procedure. To focus on the nucleation process of dislocations and the effect of different types of grain boundaries in detail, we consider a tri-crystal model with a triple junction between three grains. The model is constructed such that it features two high-energy and one low-energy grain boundary. The schematic geometry is shown in Figure 18.1. As indicated in Figure 18.1, cracked grain boundaries with traction-free surfaces along $z_c < z < h_\mathrm{f}$ are used to mimic the existence of diffusion wedges in all of the grain boundaries. We choose $z_c \approx 1.5$ nm so that the crack does not reach the substrate ($z = 0$ at the substrate). This is motivated by the results of molecular-dynamics simulations showing that the glide plane of dislocations is not directly at the substrate but a few atomic layers above.

Loading is applied by prescribing a displacement to the outermost rows at the boundary of the quadratic slab. Grain 1 has the reference configuration ($[1\overline{1}0]$ in the x direction, $[11\overline{2}]$ in the y direction). Grain 2 is rotated counterclockwise by 7.4 degrees, and grain 3 is rotated by 35 degrees with respect to grain 1. The low-energy grain boundary is situated between grains 1 and 2, and the two high-energy grain boundaries are between grains 2 and 3 and between 3 and 1.

The structure of the low-energy grain boundary is significantly different from that of the high-energy ones. The former is essentially composed of a periodic array of misfit dislocations, with a strongly inhomogeneous distribution of strain energy along the grain boundary. In contrast, the strain energy along the high-energy grain boundaries is more homogeneously distributed. After creation of the sample, the structure is annealed for a few picoseconds and then relaxed for a few thousand integration steps using an energy minimization scheme.

18.1.1. Boundary conditions and integration scheme

The boundary conditions of all models are chosen such that atoms close to the film-substrate interface are pinned to their initial locations (and also moved according to the applied strain field), mimicking perfect adhesion of a film on a stiff substrate. After the initial atomic configuration is created, a global energy minimization scheme is applied to relax the structure.

The studies are carried out using a microcanonical NVE ensemble with a quasi-static energy minimization scheme. The strain in the samples is gradually increased up to 2.5 percent. The simulations are performed using the ITAP-IMD molecular-dynamics code [203, 185] suitable for large-scale simulations. We use the same multi-body embedded atom potential (EAM) potential for copper developed by Mishin and coworkers [155] as in the studies on diffusion in the previous chapter.

18.1.2. Analysis techniques

The simulation results are analyzed with the centrosymmetry technique [126] which is a convenient way to discriminate between different defects such as partial dislocations, stacking faults, grain boundaries, surfaces, and surface steps. In some cases, we will

also use the slip vector technique proposed recently [258]. This method allows us to extract quantitative information about the Burgers vector and slip plane of dislocations immediately from the simulation data.

18.2. Atomistic simulation results

We will investigate the details of parallel glide dislocation nucleation process near the grain boundary-substrate interface. Dislocation mechanisms associated with grain boundary cracks will be compared and related to experimental results.

18.2.1. Nucleation of parallel glide dislocations from a grain triple junction

In this section we focus on the details of dislocation nucleation close to a triple junction between three grains misoriented with respect to one another.

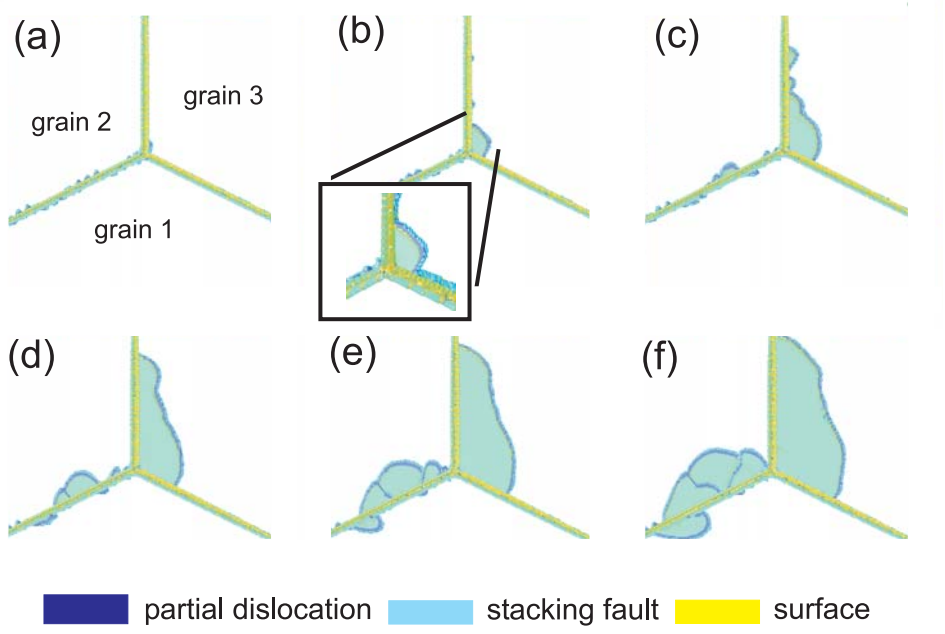

Figure 18.2.: Nucleation of parallel glide dislocations from a grain triple junction. The plot shows a time sequence based on a centrosymmetry analysis.

As soon as a threshold stress is overcome during loading, the generation of parallel glide dislocations from the grain boundaries is initiated. Snapshots of this processes are shown in Figure 18.2.

We begin with a description of the nucleation process from the low-energy grain boundary between grains 1 and 2. This boundary is composed of an array of misfit grain

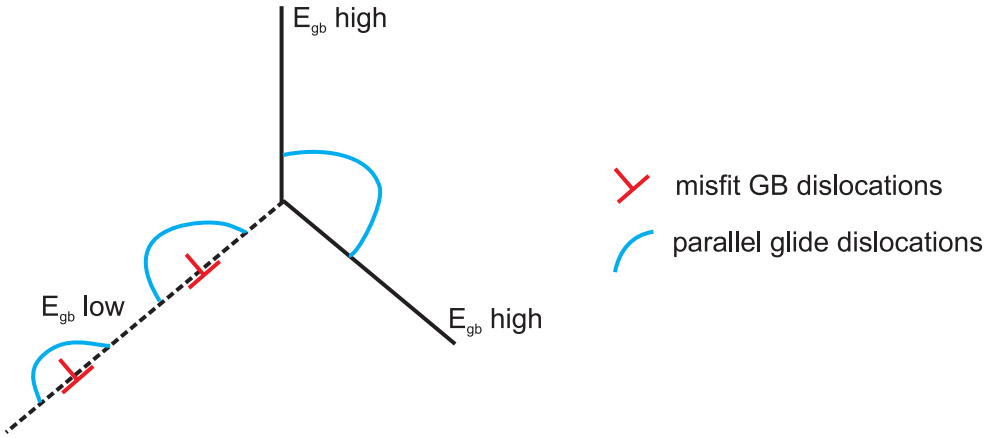

Figure 18.3.: Schematic of dislocation nucleation from different types of grain boundaries. Misfit dislocations at low-energy grain boundaries serve as sources for dislocations. At high-energy grain boundaries, there is not inherent nucleation site so that the point of largest resolved shear stress serves as nucleation point.

boundary dislocations which serve simultaneously as multiple nucleation sites for new dislocations. The nucleation sites are therefore not necessarily located close to the triple junction, the region of largest shear stresses. This observation could be reproduced in different geometries. A small number of incipient dislocations grow along the low-energy grain boundary and coalesce to form dislocation half-loops. This mechanism is also visualized schematically in Figure 18.3. In Figure 18.4 we show that deformation twinning occurs due to repeated nucleation of partial dislocations with the same Burgers vector.

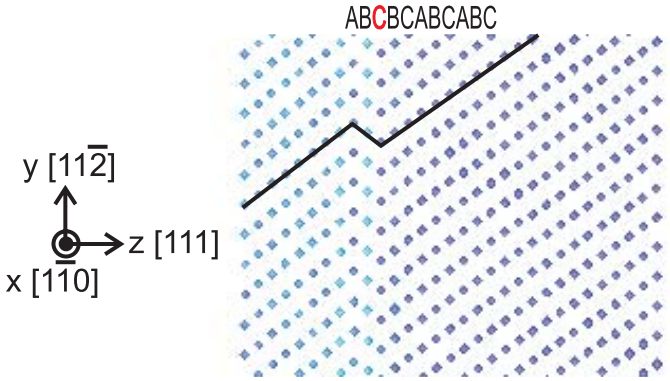

Figure 18.4.: Deformation twinning by repeated nucleation of partial dislocations. Repeated slip of partial dislocations leads to generation of a twin grain boundary.

18.2.2. Jog dragging

An interesting observation in our simulations is that some dislocations are strongly bowed at defect junctions. Dislocation junctions obstructing further glide motion are highlighted in Figure 18.5. The reason for this effect is that the glide planes of the incipient half-loops of partial dislocations are different, but have the same Burgers vector.

Using the slip vector approach proposed by Zimmerman and coworkers [258], we have verified that the Burgers vector of the dislocations nucleated in each grain are indeed identical.

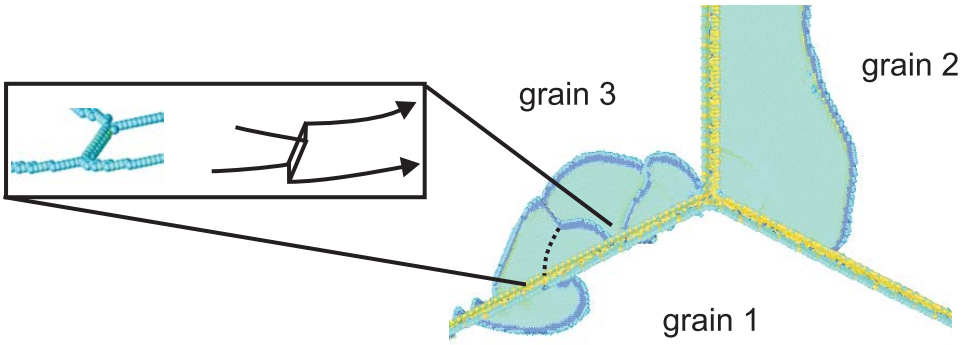

Figure 18.5.: Dislocation junction and bowing of dislocations by jog dragging. A trail of point defects is produced at the jog in the leading dislocation, which is then repaired by the following partial dislocation.

Once different half loops grow, they combine with each other while forming jogs since they glide on different glide planes. The jog has a non-glissile component, and can not move conservatively [109] thus causing generation of point defects. This, in turn, exerts a drag force on dislocations causing the dislocation lines to bow.

A similar mechanism of jog dragging due to point defect generation is known from dislocation cutting processes as depicted in Figure 18.6. As discussed in the literature on dislocation mechanics [109], when two dislocations intersect each acquires a jog equal in direction and length to the Burgers vector of the other dislocation. If two screw dislocations intersect, this jog can not glide conservatively since it features a sessile edge segment. However, if the applied stress is large enough, the dislocation with the jog starts to glide and the jog leaves a trail of vacancies, or a trail of interstitials depending on the line orientation and the Burgers vector of the reacting dislocations.

The mechanism observed in the simulations is similar. The difference is that no dislocation cutting process occurs, but instead the jog in the dislocation line develops due to nucleation of incipient dislocations on different glide planes. We observe that the sessile component of the jog is rather small and is only a fraction of the partial Burgers vector. Therefore, not a complete point defect is generated but only a trail of "partial point defects". Trails of "partial point defects" have recently also been observed in large-scale computer simulations of work-hardening in ductile materials [35]. As shown by calculations in [35], the dragging force of the partial point defects is estimated to be about 20 % of the dragging force exerted by generation of complete vacancy tubes. If these appear in large numbers, the effect on dislocation motion can be significant.

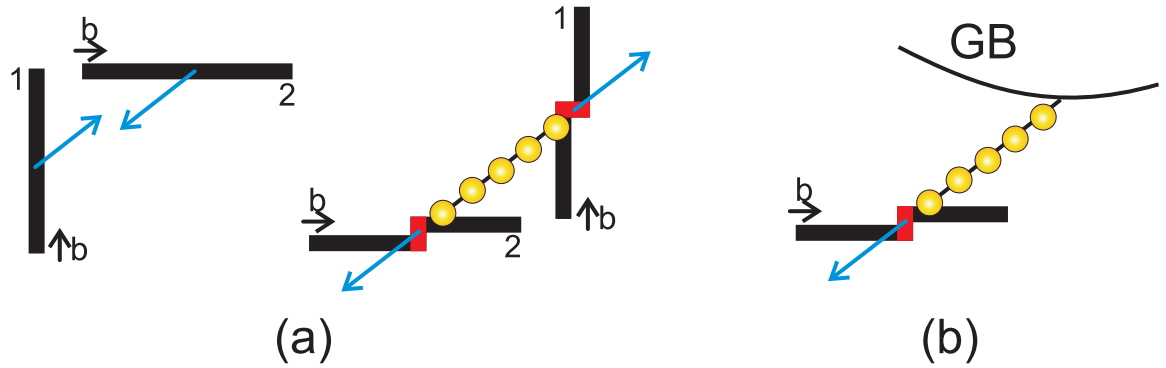

Figure 18.6.: Generation of trails of point defects. Subplot (a): Dislocation cutting processes with jog formation and generation of trails of point defects. Both dislocations leave a trail of point defects after intersection. The blue arrows indicate the velocity vector of the dislocations. Subplot (b): Nucleation of dislocations on different glide planes from grain boundaries generate a jog in the dislocation line that causes generation of trails of point defects.

18.2.3. High-energy versus low-energy grain boundaries

In the case of high-energy grain boundaries (as between grains 2 and 3) with a more homogeneous structure, nucleation of parallel glide dislocations is found to occur preferably at the triple junction. The process proceeds with an incipient dislocation growing until the second partial is emitted. The parallel glide dislocations often have semi-circular shapes as observed in early stages of dislocation nucleation in experiment [24, 55].

In contrast to the low energy grain boundary where misfit dislocations serve as nucleation sites for new dislocations, the triple junction acts as the main nucleation source at high energy grain boundaries.

18.3. Discussion

Dislocation nucleation depends on the grain boundary structure: We observe that low-energy grain boundaries composed of a periodic array of misfit dislocations provide more fertile sources for threading dislocation nucleation.

At low-energy grain boundaries, dislocations are often observed to nucleate close to grain boundary misfit dislocations. This can be referred to as an intrinsic condition, because the concentration of internal grain boundary stresses serve as nucleation site for dislocations. Since the incipient dislocations are often nucleated at different glide planes, complex dislocation reactions take place when several of them combine to form a single dislocation line. Such mechanisms can hinder dislocation motion and cause bowing of the dislocation line. The observation of such nucleation induced jogs with subsequent generation of trails of point defects has not been described in the literature. In other computer simulation of ductile materials [35] similar mechanisms have been observed, suggesting that this mechanism may play a role in hardening of materials.

In the more homogeneous high-energy grain boundaries there is inherently no preferred nucleation site. Therefore, triple junctions of grain boundaries are preferred as nucleation

sites. The overall stress field governs dislocation nucleation, since such a triple junction provides a location with highest stress concentration. Different parallel glide dislocations can interact in a complex way to form networks of dislocations, as shown in Figure 18.5.

Another finding is that partial dislocations dominate plasticity in the simulations, as can be verified in Figure 18.4 where deformation twinning is depicted. This indicates that partial dislocations dominate plasticity at nanoscale. Similar observations have been reported by other groups [217, 235].

19. Atomistic modeling of plasticity of polycrystalline thin films

Atomistic modeling of plasticity in polycrystalline thin films is just at its beginning. Few studies of such systems have been reported in the literature. Recently, atomistic simulations of two-dimensional systems were reported by Shen [195]. In this study, the increase in yield strength was investigated and nucleation and motion of threading dislocations was in the focus. However, the model did not contain grain boundaries despite the fact that grain boundaries can serve as fertile sources for dislocations. In contrast to this simplistic model, we propose a three-dimensional model of thin films with a more realistic microstructure. The model studied in this chapter is a polycrystalline thin film consisting of hexagonal shaped grains, as shown in Figure 19.1. The choice of this geometry is motivated by the grain microstructure found in experiments [24, 55]. An advantage of this model over the geometry studies in the preceding chapter is that fully-periodic boundary conditions in the x- and y-direction can be assumed.

Here we will focus on dislocation nucleation and motion from grain boundaries and a crack-grain boundary interface. One of the important objectives will be to study the effect of grain boundary traction relaxation by diffusional creep on the dislocation mechanism that operate in the film. Further studies will be focused on the details of dislocation nucleation from different type of grain boundaries. As known from the preceding chapter, the structure of the grain boundaries has strong influence on the nucleation of dislocations.

The plan of this chapter is summarized as follows. After presenting details about the atomistic modeling procedure, we will continue with a discussion of the results of several large-scale atomistic studies comprising of up to 35 million particles. Even for today's supercomputers, this represents a significant system size. We will show that grain boundary relaxation by diffusional creep gives rise to dominance of parallel glide dislocations, in accordance with experiment. In contrast, if grain boundary tractions are not relaxed, threading dislocations dominate plasticity. We show that low-energy grain boundaries are more fertile sources for plasticity than more homogeneous high-energy grain boundaries. This hypothesis is further supported by a set of atomistic simulations of bulk nanocrystalline copper.

19.1. Atomistic modeling of polycrystalline thin films

As indicated in Figure 19.1, cracked grain boundaries with traction-free surfaces (along $z_c < z < h_\mathrm{f}$ where $z_c \approx 1.5$ nm) are used to mimic the existence of diffusion wedges in some of the grain boundaries. Grain 1 is in the reference configuration ($[1\overline{1}0]$ in the x

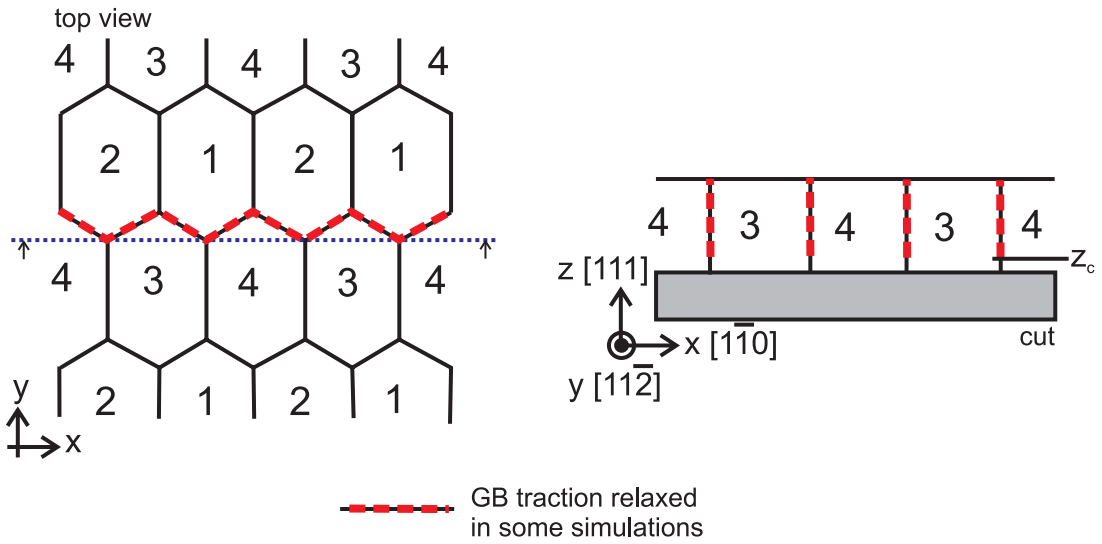

Figure 19.1.: Geometry for the studies of plasticity in polycrystalline simulation sample.

direction, [11$\bar{2}$] in the y direction). Grain 2 is rotated counterclockwise by 7.4 degrees, grain 3 is rotated by 35 degrees, and grain 4 is rotated by 21.8 degrees with respect to grain 1. The model contains up to 35 million particles. With this procedure, a low-energy grain boundary is constructed between grains 3 and 4. After creation of the sample, the structure is relaxed for a few thousand integration steps using an energy minimization scheme. Figure 19.2 shows the atomistic model of the polycrystalline thin film. Only surfaces (yellowish color) and grain boundaries (bluish color) are shown.

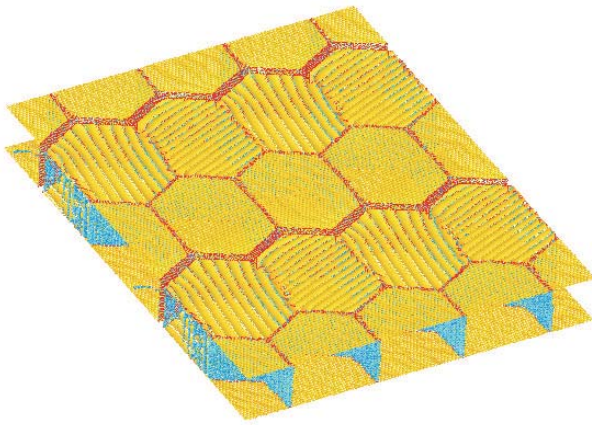

Figure 19.2.: Atomistic model of the polycrystalline thin film. Only surfaces (yellowish color) and grain boundaries (bluish color) are shown.

In contrast to the modeling with the tri-crystal model, the simulation cell is fully periodic in the x and y direction. Loading is applied by homogeneously straining the sample in the desired direction. Further details on the modeling technique can be found in Section 18.1.

19.2. Atomistic simulation results

We will investigate plasticity of thin films with and without traction relaxation and study the details of the dislocation nucleation process near the grain boundary-substrate interface. Dislocation mechanisms associated with grain boundary cracks will be compared and related to experimental results.

The model of constrained diffusional creep [88] predicts that due to mass transport from the surface into the grain boundary, the tractions along the grain boundary are relaxed, and thus a crack-like stress field develops. This change should significantly alter the dislocation microstructure that develops in the film under mechanical deformation. While threading dislocations dominate plasticity in films where grain boundary diffusion is shut down, in films where grain boundary diffusion is active parallel glide dislocations are expected to dominate. Indeed, since the continuum model was proposed [88], an experimental group has reported the observation of parallel glide dislocations in copper films with thicknesses below 400 nm [25]. The researchers concluded that grain boundary traction relaxation by diffusional creep leads to change in the deformation field near the crack tip. Experimental results suggest that threading and parallel glide dislocations are competing mechanisms [24, 55, 25] in submicron, uncapped thin films on substrates.

In this section we want to probe this hypothesis by large-scale atomistic simulations. Atomistic modeling of thin film plasticity at the nanoscale provides an ideal tool to study such competing mechanisms and to determine conditions under which they are active.

It is known that grain boundaries are important sources for dislocations in nanostructured materials. We illustrate that the structure of the grain boundaries has significant influence on the motion of dislocations into the grain interior. Furthermore, we find that the role of partial dislocations seems to be increasingly important as the grain size approaches nanoscale.

19.2.1. Threading dislocations

We start with the polycrystalline sample without relaxation of tractions along the grain boundaries, corresponding to the case when grain boundary diffusion is not active. The simulation results are depicted in Figures 19.3 and 19.4. In this case, the dominating inelastic deformation mechanism is clearly glide of threading dislocations on inclined glide planes. No dislocations on glide planes parallel to the film surface are observed, as expected because there is no resolved shear stress and thus no driving force for dislocation nucleation on parallel glide planes.

Figure 19.3 (a) reveals a complex dislocation structure in the interior of the film. The dislocation structure is analyzed with the centrosymmetry technique. Figure 19.3 (b) shows a more detailed magnified view of a section of the film. Threading dislocations are observed to leave behind interfacial dislocation segments at the film-substrate interface and atomic steps at the film surface. Figure 19.4 shows snapshots of a top view of the film surface at different times, including a magnified view of the surface at snapshot 4 in Figure 19.5. The surface steps emanate from the grain boundaries, suggesting that dislocations are nucleated at the grain boundary-surface interface. From the direction of the surface steps it is evident that different glide planes are activated.

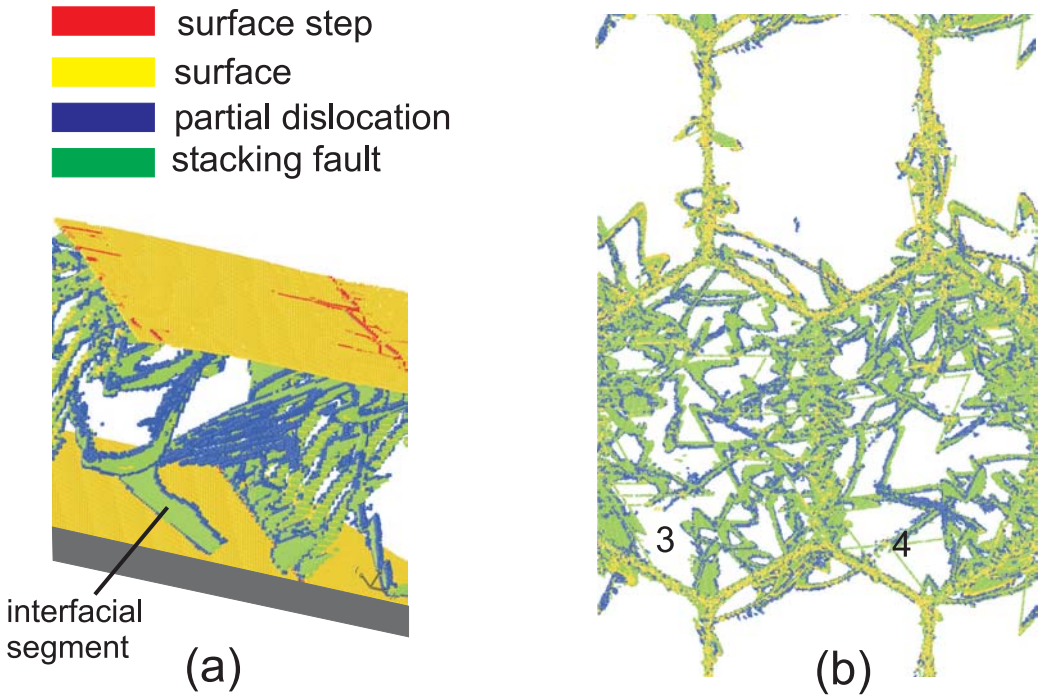

Figure 19.3.: Nucleation of threading dislocations in a polycrystalline thin film. Subplot (a) shows a view into the interior, illustrating how threading dislocations glide by leaving an interfacial segment. Subplot (b) shows a top view into the grain where the surface is not shown. The plot reveals that the dislocation density is much higher in grains 3 and 4.

From the number of surface steps (colored in red) created during plastic deformation, it seems that dislocation motion concentrates in grains adjacent to low-energy grain boundaries which apparently provide more fertile sources for dislocation nucleation (within grains 1 and 2). This can also be verified in Figure 19.3 (b). The dislocation density in grains 3 and 4 is several times higher than that in grains 1 and 2.

Figure 19.6 shows a sequence of a nucleation of a threading dislocation from the grain-boundary surface interface. The plot indeed shows that threading dislocations are nucleated at the grain boundary surface interface and then the half loops grow into the film until they reach the substrate. Due to the constraint by the substrate, threading dislocations leave an interfacial segment. This observation is in agreement with the classical understanding of threading dislocation nucleation and with experimental results [127, 132, 222]. The threading dislocations intersect the surface at an angle of 90 degrees [109].

19.2.2. Parallel glide dislocations

In the following, some of the grain boundaries are treated as traction-free cracks, as shown in Figure 19.1. In Figure 19.7, we show several snapshots of the dislocation structure. Parallel glide dislocations are generated close to the film-substrate interface. Figure 19.7 (a) shows a top view while Figure 19.7 (b) shows a perspective side view of

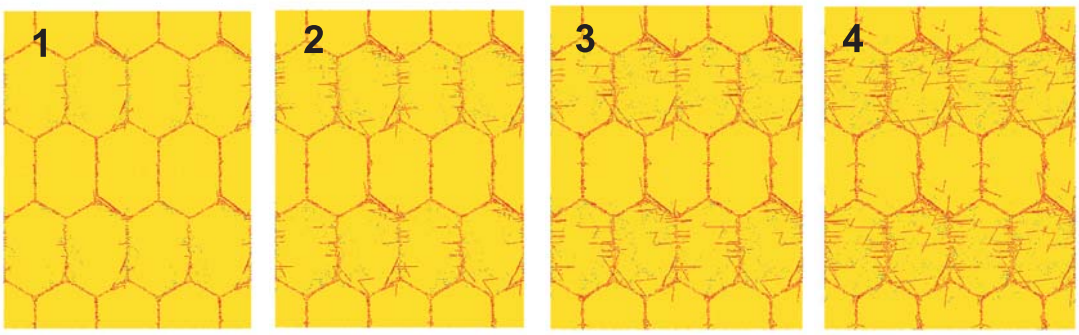

Figure 19.4.: Surface view of the film for different times. The threading dislocations inside the film leave surface steps that appear as red lines in the visualization scheme (color code see Figure 19.3). This plot further illustrates that the dislocation density in grains 3 and 4 is much higher than in the two other grains.

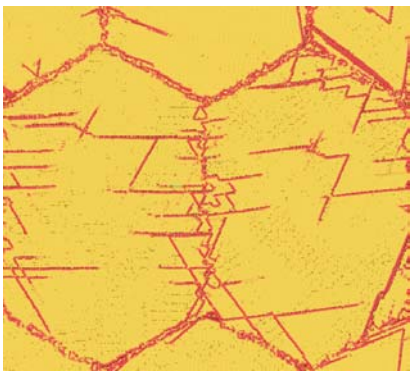

Figure 19.5.: Detailed view onto the surface (magnified view of snapshot 4 in Figure 19.4). The plot shows creation of steps due to motion of threading dislocations (color code see Figure 19.3). The surface steps emanate from the grain boundaries, suggesting that dislocations are nucleated at the grain boundary-surface interface. From the direction of the surface steps it is evident that different glide planes are activated.

the interior of the film.

The section shown has dimensions of approximately 120 nm × 150 nm, and the film thickness is $h_\mathrm{f} \approx 15$ nm. The grain diameter in the x-direction is approximately $d_x \approx 40$ nm. This plot reveals that not only parallel glide but also some threading dislocations are generated at the grain boundary-surface interface. The plot shows that dislocation activity centers on the grain boundary whose traction is relaxed. Due to the crack-like deformation field, large shear stresses on glide planes parallel to the film surface develop and cause nucleation of parallel glide dislocations. A complex dislocation network develops on a time scale of several picoseconds after dislocation nucleation.

Figure 19.8 shows the simulation results for a larger grain size. The section shown has dimensions of approximately 300 nm × 400 nm; the film thickness is $h_\mathrm{f} \approx 15$ nm. The grain diameter in the x-direction is approximately $d_x \approx 180$ nm, about four times larger than in Figure 19.7 while the film thickness is kept constant at $h_\mathrm{f} \approx 15$ nm.

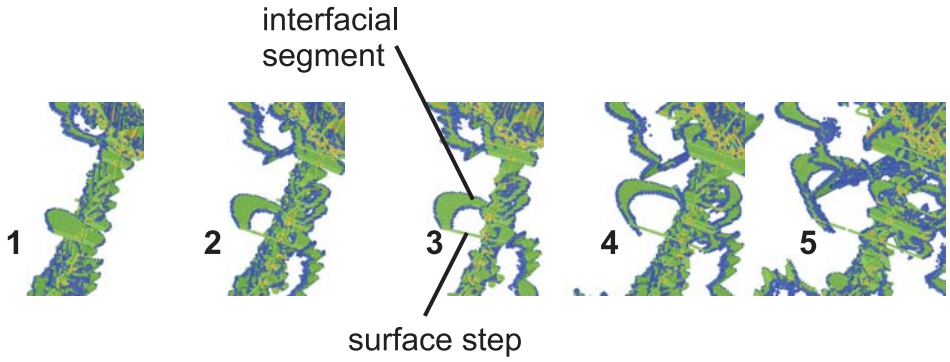

Figure 19.6.: Sequence of a nucleation of a threading dislocation, view at an inclined angle from the film surface. Threading dislocations are preferably nucleated at the grain boundary surface interface and half loops grow into the film until they reach the substrate. Due to the constraint by the substrate, threading dislocations leave an interfacial segment.

More dislocations are observed to nucleate than in Figure 19.7, indicating that more dislocations "fit" into the larger grain, and consequently, a more complex dislocation microstructure develops. As the laterally applied strain is continuously increased, the first dislocations to be nucleated are occasionally complete dislocations, while the following dislocations are often pure partial dislocations. Figure 19.9 shows a view of the surface of the results shown in snapshot 2 of Figure 19.8, revealing surface steps generated from the motion of threading dislocations. Even when the traction of some of the grain boundaries are relaxed, threading dislocations occur. The figure shows that threading dislocations are predominantly nucleated at the junction between traction-free grain boundaries and normal grain boundaries where traction is not relaxed.

We observe that dislocations can not glide as easily along the low-energy grain boundaries as along the more homogeneous high-energy grain boundaries between grains 1 and 2. This can be verified in Figure 19.7 (a). While an extended dislocation (marked by "PG") in grain 1 is almost a straight line, all dislocations in grains 3 and 4 are strongly curved.

Figure 19.10 shows the complex dislocation network of partial parallel glide dislocations that develops inside the grains. In this plot, the stacking fault planes are not shown. The bowing of the dislocations indicates that their motion is hindered by mutual interaction. We observe that formation of jogs and creation of trails of point defects play a very important role, as already discussed in Section 18.2.2.

19.3. Plasticity of nanocrystalline materials with twin lamella

In the preceding sections, the role of low-energy versus high-energy grain boundary was discussed. The importance of this concept is further underlined by the studies reported in this section. Here we focus on polycrystalline bulk copper, where the grain size is on the order of several nanometers to tens of nanometers.

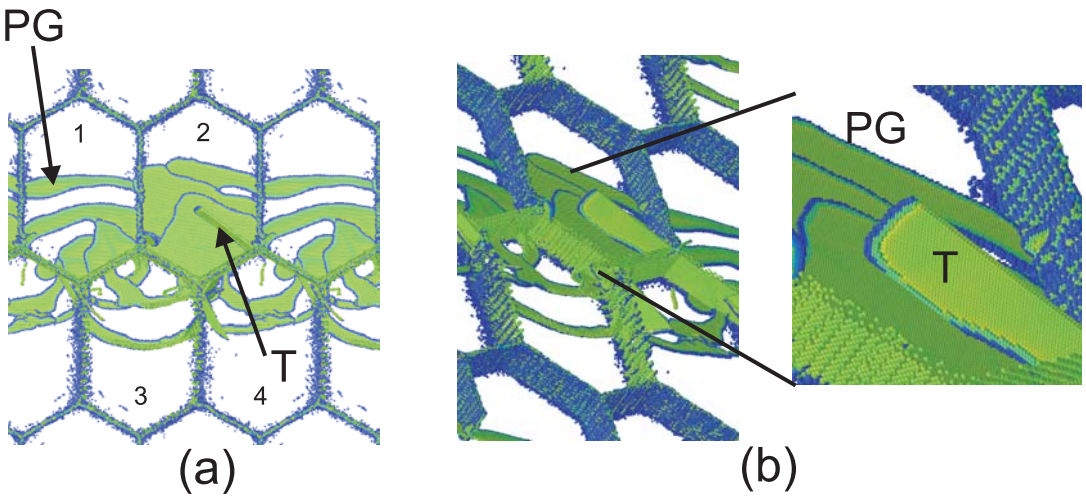

Figure 19.7.: Nucleation of parallel glide dislocations, small grain sizes. The plot shows that dislocation activity centers on the grain boundary whose traction is relaxed. Due to the crack-like deformation field, large shear stresses on glide planes parallel to the film surface develop and cause nucleation of parallel glide (PG) dislocations. Subplot (a) shows a top view, and subplot (b) a perspective view. The plot reveals that there are also threading (T) dislocations nucleated from the grain triple junctions.

We consider a polycrystalline microstructure with hexagonal grains, but with different grain orientations as in the previous case (see Figure 19.11 for details). To further study the effect of geometric confinement on plasticity, we introduce a sub-nano structure in the grains. This sub-nanostructure is established by assuming twin grain boundaries forming very thin twin-lamella. Such microstructure can be produced experimentally in copper [146]. With this model, we pursue two main objectives:

1. We show that in bulk nanostructured materials, the type of the grain boundary plays a very important role for dislocation nucleation, as it was found for thin films.

2. We show that the sub-nanostructure composed of twin grain boundaries provides a very effective barrier for dislocation motion and therefore leads to a very "strong" nanostructured material.

19.3.1. Modeling

To underline the first point regarding dislocation nucleation, we consider two samples. The first sample (i) has the same grain misorientations as in Section 19.2 (and therefore features a low-energy grain boundary between grains 3 and 4), and we construct a second sample (ii) where all grain boundaries are of the same type. If the proposed concept is correct that dislocation nucleation occurs predominantly from low-energy grain boundaries, the dislocation density in sample (i) should be higher in grains 3 and 4, and should be comparable in all grains in sample (ii).

The simulation geometry is depicted in Figure 19.11. The blue lines inside the grains

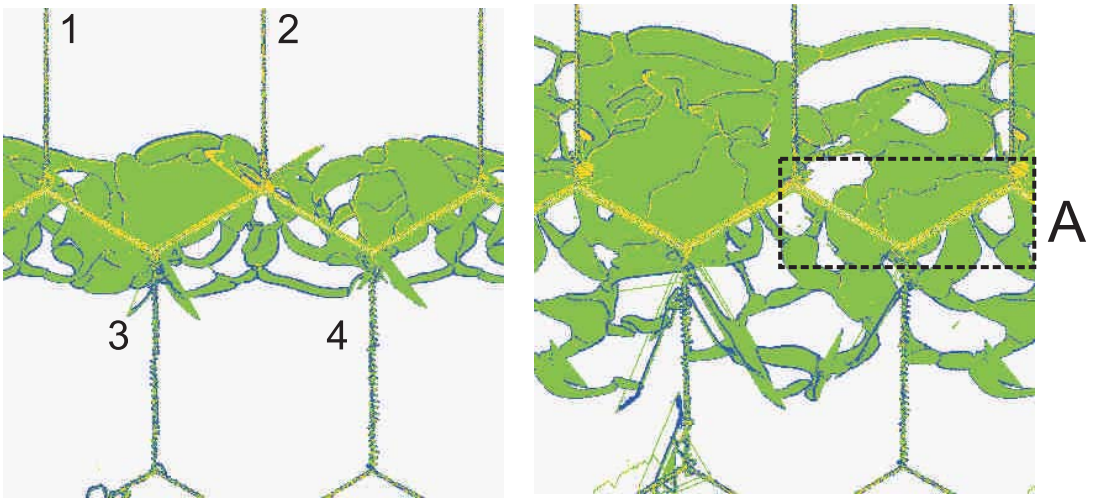

Figure 19.8.: Nucleation of parallel glide dislocations, large grains. The plot shows a top view of two consecutive snapshots. The region "A" is shown as a blow-up in Figure 19.10.

refer to the intra-grain twin grain boundaries. The thickness of the twin lamella is denoted by d_{T}.

19.3.2. Simulation results

The material is loaded uniaxially in the x-direction. We start with sample (i), and we consider is a grain size of 12.5 nm $\times$ 16.5 nm. The grains have the same misorientation as in the study described above. We perform the simulation for two different lamella sizes d_{T}. The results are shown in Figure 19.12.

We observe that dislocations are generated exclusively from the low-energy grain boundaries between grains 3 and 4. This is in agreement with the results of the polycrystalline thin films. The fact that we use a different grain orientation in this study with different boundary conditions suggests that the nucleation conditions discussed previously is a more general concept. The results indicate that the twin grain boundaries are an effective barrier for further dislocation motion, since we observe dislocation pileups at the twin grain boundaries. An important consequence is that the thinner the lamella structure (small d_{T}), the less plasticity can transmitted via the motion of dislocations. This indicates that grains with a nano-substructure of twin grain boundaries is an effective hardening mechanism for materials.

We report another study with the same microstructure, but different grain misorientation angles, sample (ii). In this case, we choose the grain boundary misorientation identical in all grains. Grain 1 is in its reference configuration, grain 2 is rotated by 30°, grain 3 by 60° and grain 4 is misoriented by 90°. All grain boundaries are now high-angle grain boundaries.

The results of this calculation are shown in Figure 19.13 (a). Unlike in Figure 19.12, dislocations are now nucleated at all grain boundaries and the nucleation of dislocations is governed by the resolved shear stress on different glide planes. We observe that dislocations can easily penetrate through the stacking fault planes generated by motion

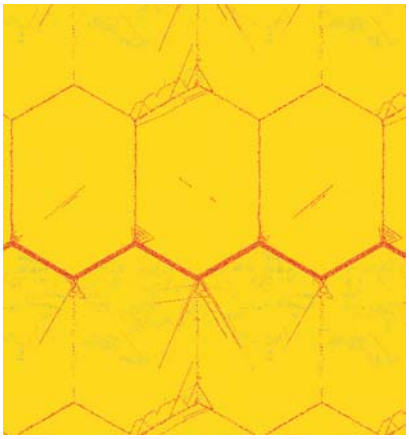

Figure 19.9.: Nucleation of parallel glide dislocations, large grains. The plot shows a view of the surface. From the surface view it is evident that threading dislocations are nucleated in addition to the parallel glide dislocations. These emanate preferably from the interface of grain boundaries, traction-free grain boundaries and the surface.

of other partial dislocations, but build pileups at the twin grain boundaries. We also observe that dislocations with opposite Burgers vector annihilate. Further, dislocations cross slip (see highlighted region in the center of Figure 19.13 (b), region i.) in regions with high dislocation densities. The activated primary and secondary glide planes are highlighted in the plot. The primary glide planes are parallel to the twin grain boundaries so that dislocation glide is not restricted. In contrast, once dislocations have cross-slipped to the secondary glide plane their motion is restricted due to the twin grain boundaries (see Figure 19.13 (b) ii.). Figure 19.13 (b) iii. shows intersection of dislocations. A defect is left at the intersection of the stacking fault planes.

As in the previous studies of nanostructured materials [235], we also observe that partial dislocations dominate plasticity. Dominance of partial dislocations is verified by the fact that dislocations leave behind a stacking fault.

19.4. Modeling of constrained diffusional creep in polycrystalline films

We have also modeled constrained grain boundary diffusion in polycrystalline thin films, thus extending the two-dimensional studies reported in Chapter 17 to the three-dimensional case. We apply biaxial loading rate on the order of 1 percent strain per nanosecond. The temperature is, as in the two-dimensional studies, chosen around 90 % of the melting temperature.

High-energy grain boundaries transform into liquid-like intergranular layers, while low-energy grain boundaries establish as arrays of misfit dislocations.

We will show that the basic mechanism of parallel glide dislocation nucleation is identical to the results observed in the two-dimensional case. The simulations provide direct evidence that the diffusivities depend on the grain boundary structure.

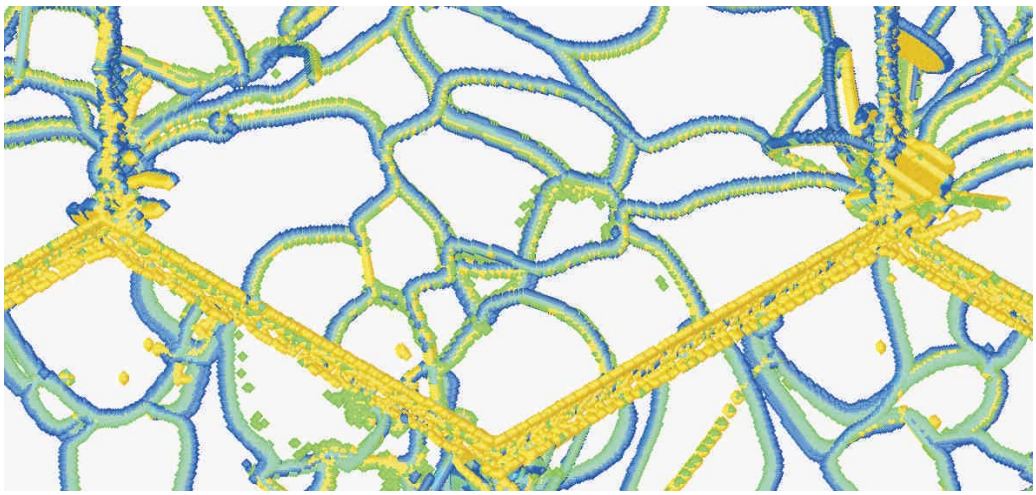

Figure 19.10.: Nucleation of parallel glide dislocations. The plot shows an analysis of the complex dislocation network of partial parallel glide dislocations that develops inside the grains (magnified view of the region "A" marked in Figure 19.8). All defects besides stacking fault planes are shown in this plot.

19.4.1. Constrained grain boundary diffusion and dependence on grain boundary structure

We model a film of thickness $h_\mathrm{f} \approx 11$ nm with a grain diameter of about 22 nm in the x-direction. The simulation sample is constructed such that we have high-energy as well as low-energy grain boundaries. This is motivated by our desire to investigate the effect of grain boundary structure on the deformation mechanisms. Grain 1 is completely surrounded by high-energy grain boundaries, and the other grains feature low-energy grain boundaries (grain 1 is in its reference configuration, grain 2 is rotated by 35.4 degrees, grain 3 by 44.7 degrees and grain 4 by 53.4 degrees). We observe that, in agreement with the predictions in the literature [235] that high-energy grain boundaries provide very fast diffusion paths, in contrast to low-energy grain boundaries. This strongly underlines the notion that the grain boundary structure needs to be taken account when diffusivities are determined.

Formation of grain boundary diffusion wedges is accompanied by surface grooving at the grain boundary interface. Therefore, the surface height profile provides a reasonable indication of diffusive activities in the grain. Figure 19.14 (a) plots the surface profile of a polycrystalline sample in early stages of the simulation. The observation of surface grooves is in agreement with recent experimental reports [234].

Compared with all other diffusion paths, grain triple junctions provide the fastest paths for diffusion. This is verified since at grain triple junctions, the surface grooves are deepest. As in the two-dimensional case, we observe that the grain boundaries become curved along the z-direction.

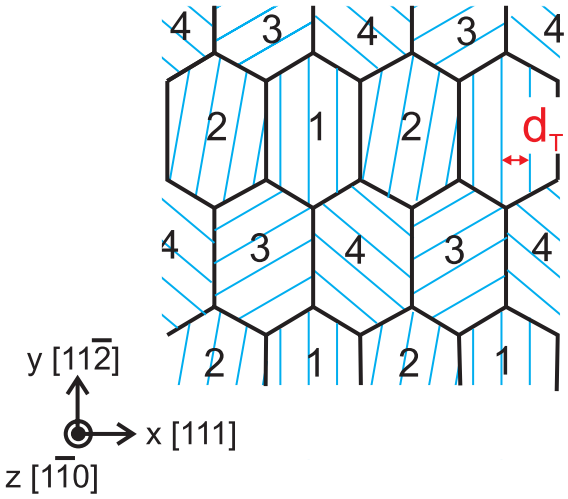

Figure 19.11.: Nanostructured material with twin grain boundary nano-substructure. The blue lines inside the grains refer to the intra-grain twin grain boundaries. The thickness of the twin lamella is denoted by d_{T}.

19.4.2. Nucleation of parallel glide dislocations

According to the hypothesis by continuum theory [88], parallel glide dislocations should only be nucleated along grain boundaries whose tractions are relaxed by diffusional creep. Since high-energy grain boundaries are predominant paths for diffusion, in grains neighboring high-angle grain boundaries parallel glide dislocations should dominate plasticity. In other grains, where tractions along the grain boundaries are not relaxed threading dislocations should dominate.

This prediction is verified by our atomistic simulations. Nucleation of parallel glide dislocation only occurs in grains that are completely surrounded by high-energy grain boundaries. In our sample, there is no other dislocation activity than parallel glide dislocations after diffusion has proceeded sufficiently long. We observe nucleation of parallel glide dislocations at a biaxial strain of about $\varepsilon_{xx} = \varepsilon_{yy} \approx 1.6$ %. In other grains where little grain boundary relaxation is possible by diffusional creep, threading dislocations are easily nucleated. Predominant nucleation site are, in agreement with previous results, misfit dislocations at the grain boundary. The observation of threading dislocations in other grains is consistent with the studies where some grain boundaries were assumed traction free (see Figure 19.8).

This result of the study of constrained grain boundary diffusion in polycrystalline films is documented in Figure 19.14 (b) and (c). The nucleated parallel glide dislocation is shown in Figure 19.14 (c) as a black line. Its shape was determined using the energy method shown in the blow-up of Figure 19.14 (c). Additional analysis was performed based on geometrical methods identical to those applied in Chapter 17. After the first parallel glide dislocation is nucleated, additional dislocations appear as the loading is increased and the dislocations form a network that is similar to the results shown in Figure 19.7. Note that even at higher loads, there are exclusively parallel glide disloca-

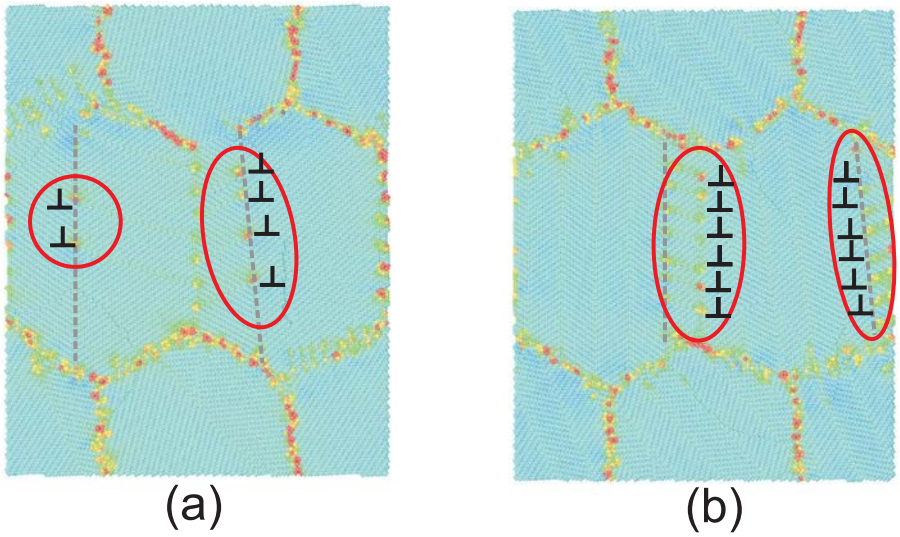

Figure 19.12.: Simulation results of nanostructured material with twin lamella substructure under uniaxial loading for two different twin lamella thicknesses. Subplot (a) shows the results for thick twin lamella ($d_{\mathrm{T}} \approx 15\ nm > d$) and subplot (b) for thinner twin lamella ($d_{\mathrm{T}} \approx 2.5$ nm). Motion of dislocations is effectively hindered at twin grain boundaries.

tions in grain 1 as shown in Figure 19.7 (d). In other grains, we observe parallel glide dislocations at later stages in addition to the threading dislocations.

The most important result of this section is that constrained diffusional creep and nucleation of parallel glide dislocations can also be modeled in a polycrystalline model. Further discussion on the simulation results will be left to future publications.

19.5. Discussion

The simulation results can be summarized as follows.

1. Threading dislocations dominate deformation when tractions along the grain boundaries are not relaxed. However, if the grain boundary tractions are relaxed, parallel glide dislocations dominate the plasticity of ultrathin films ($h_{\mathrm{f}} \approx 15$ nm). Almost all plasticity is carried on glide planes that are very close to each other. This transition of the maximum shear stress from inclined planes to planes parallel to the film surface is illustrated in Figure 19.15.

2. Dislocation nucleation depends on the grain boundary structure: Low-energy grain boundaries composed of an array of misfit dislocations provide more fertile sources of dislocations than high-energy grain boundaries with a more homogeneous structure. We find that the dislocation density is a few times higher in grains connected by low-angle grain boundaries. This assertion is further supported by the studies of nanostructured bulk material described in Section 19.3.

3. Different parallel glide dislocations can interact in a complex way to form networks

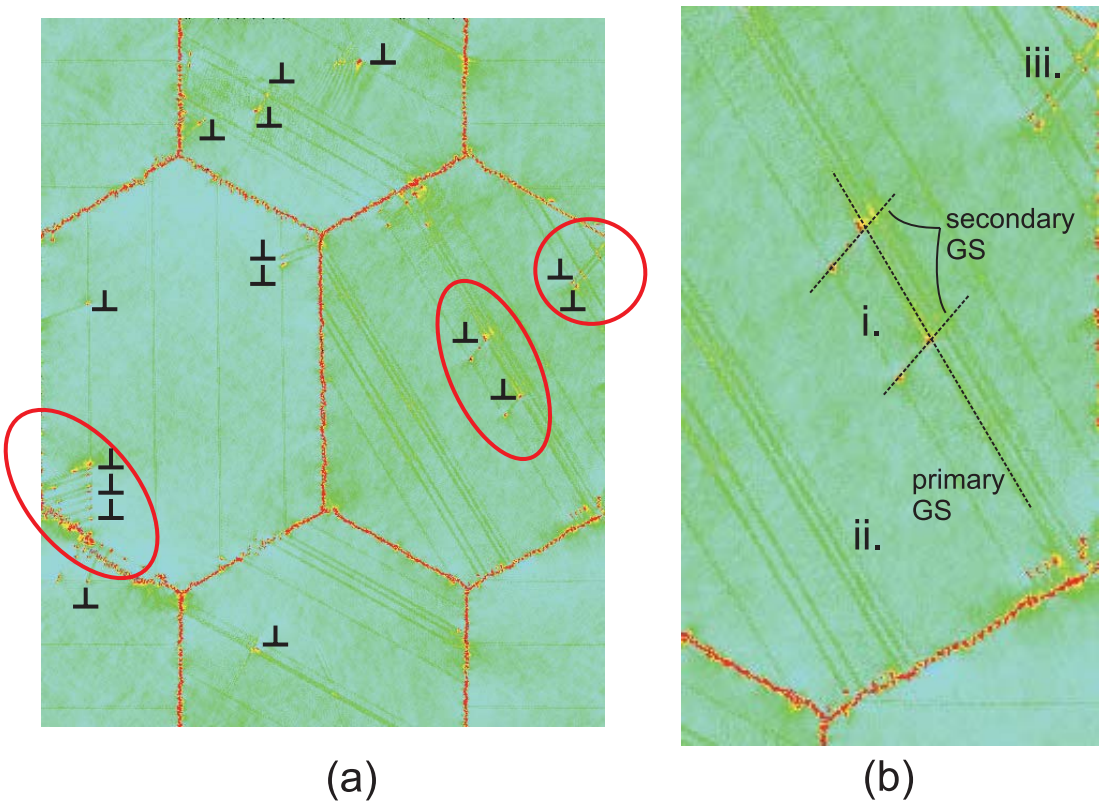

Figure 19.13.: Simulation results of nanostructured material with twin lamella substructure under uniaxial loading for two different twin lamella thicknesses, all high-energy grain boundaries. Subplot (a) shows the potential energy field after uniaxial loading was applied. Interesting regions are highlighted by a circle. Unlike in Figure 19.12, dislocations are now nucleated at all grain boundaries. The nucleation of dislocations is now governed by the resolved shear stress on different glide planes. Subplot (b) highlights an interesting region in the right half where i. cross-slip, ii. stacking fault planes generated by motion of partial dislocations and iii. intersection of stacking fault planes left by dislocations is observed.

of dislocations, as shown in Figure 19.10 (a blow-up picture, showing only partial dislocations and grain boundaries while filtering out the stacking faults).

Our simulations show that relaxation of grain boundary tractions changes the dislocation microstructure and triggers completely different stress relaxation mechanisms in thin films. We have also investigated nucleation of parallel glide dislocations from diffusion wedges using the quasi-continuum method. The results of this simulation are discussed in Section 2.3.3 and results were shown in Figure 2.7, for instance. The same behavior was observed in these simulations as with purely atomistic methods.

Without relaxation of grain boundary tractions, threading dislocations dominate thin film plasticity, while under grain boundary diffusion, dislocations on parallel glide planes dominate. Threading dislocations are found to be mostly complete dislocations, while we see a strong tendency to nucleate partial dislocations in the case of parallel glide dislocations in the nanometer-sized grains investigated here. This is qualitatively con-

sistent with results of atomistic modeling of deformation of nanocrystalline materials [217, 242, 235]. At nanoscale, the role of partial dislocations becomes increasingly important! Twinning along parallel planes might become an important deformation mechanism at high strain rates, as it is shown in Figure 18.4.

The transition of the deformation mechanism from threading dislocations to parallel glide dislocations is also observed in recent experimental investigations [24, 55]. Experiment clearly shows that once grain boundary diffusion is shut down in very thick films or by a capping layer, threading dislocations dominate plasticity [24, 55, 25]. When grain boundary diffusion is active because there is no capping layer or the film thickness is sufficiently small, parallel glide dislocations dominate. This indicates that mechanisms relaxing the grain boundary tractions are active during the deformation of ultra-thin films. Experimental results are in good qualitative agreement with the molecular-dynamics results reported in this work.

Another important feature is that parallel glide dislocations do not glide as easily along inhomogeneous low-angle grain boundaries as they do along homogeneous high-energy grain boundaries, as shown in Figure 19.8. This is explained by the fact that the low-energy grain boundaries are composed of an array of misfit dislocations and thus rather inhomogeneous. Similar mechanism has been observed in experiment. In [25], it was reported that dislocations are effectively repelled from certain type of grain boundaries causing significant bowing.

Figure 19.7 (b) reveals that not only parallel glide but also some threading dislocations are generated at the grain boundary-surface interface. This observation is in qualitative agreement with experiment [25]. Our studies of constrained grain boundary diffusion in polycrystalline samples led to similar results and are also in qualitative agreement with experiment.

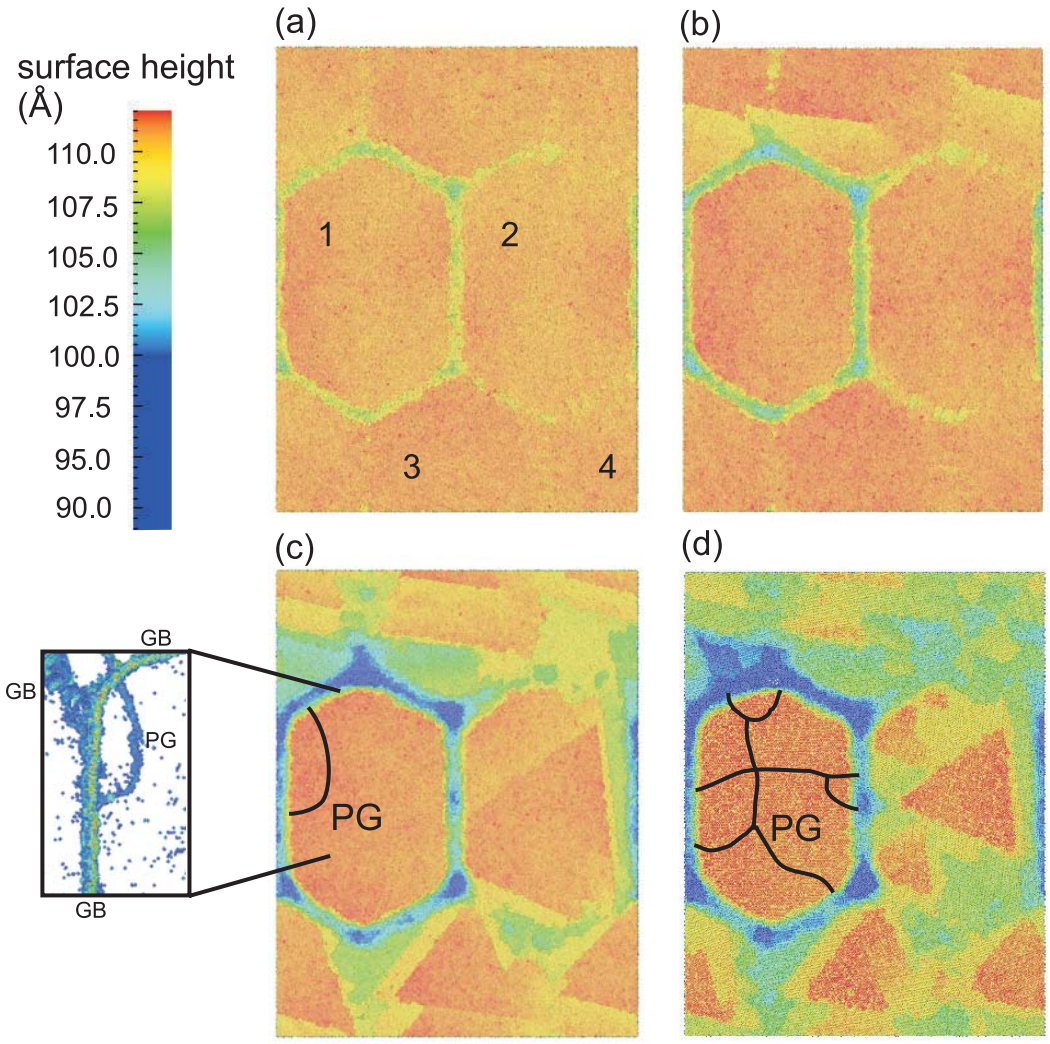

Figure 19.14.: Modeling of constrained diffusional creep in polycrystalline samples; nucleation of threading versus parallel glide dislocations. The blowup in panel (c) shows an energy analysis of the dislocation structure, and visualizes a parallel glide dislocation nucleated from a grain boundary diffusion wedge. The surface steps indicate that threading dislocations have moved through the grain, and no threading dislocations exist in grain 1. The black lines show the network of parallel glide dislocations in grain 1 (in other grains we also find parallel glide dislocations in snapshot (d) but they are not shown).

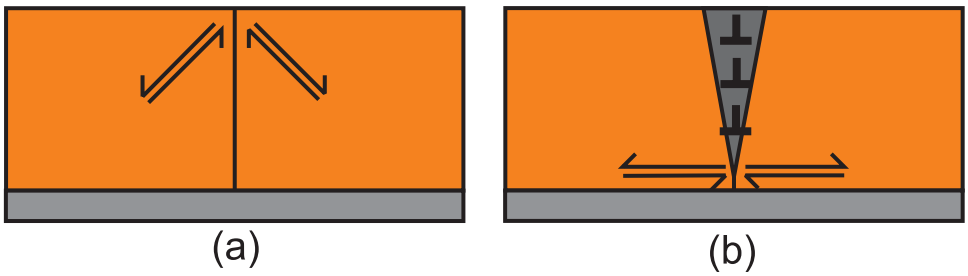

Figure 19.15.: Change of maximum shear stress due to formation of the diffusion wedge. In the case of no traction relaxation along the grain boundary, the largest shear stress occur on inclined glide planes relative to the free surface. When tractions are relaxed, the largest shear stresses occur on glide planes parallel to the film surface.

20. Summary and discussion of the results of modeling of thin films

We have described a new deformation mechanism in submicron thin copper films referred to as constrained diffusional creep with subsequent parallel glide dislocation nucleation. Together with experimental observations [25], the results of atomistic modeling of constrained grain boundary diffusion provide evidence that it is an important deformation mechanism in very thin uncapped copper films. The observation of parallel glide dislocations nucleated at grain boundary diffusion wedges (shown in Figure 17.5) agrees with experimental investigations of deformation of ultra thin copper films [24, 55, 25]. The results also agree well with the predictions by recently developed continuum mechanics theory [88, 251], thus closing the experiment-theory-simulation linkage. The most important result is that once other stress relaxation mechanisms (e.g. by dislocation motion) are shut down, diffusional flow of matter along grain boundaries dominate the mechanical properties of thin metal films on substrates.

An important contribution of this work is the atomistic study of constrained diffusional creep and subsequent parallel glide dislocation nucleation. We find that grain boundary diffusion could be modeled by classical molecular-dynamics, in agreement with reports in previous studies [240, 235]. However, modeling of grain boundary diffusion is difficult with classical molecular-dynamics and is only possible under large stress and high temperatures. In our simulations, we apply several GPa stress and study diffusion at elevated temperatures on the order of 90 % of the melting temperature of copper.

Modeling at the atomic scale helped to identify the key mechanism of dislocation nucleation from a diffusion wedge. The simulations allowed to establish a detailed understanding of the dislocation nucleation process close to a diffusion wedge. This led to the definition of a critical stress intensity factor for parallel glide dislocation nucleation. The critical value for dislocation nucleation from a diffusion wedge is twice as large compared to a crack. This was explained by the difference in force balance on the incipient dislocation: For dislocation nucleation near a diffusion wedge, a dislocation dipole needs to be generated where the dislocations are one Burgers vectors apart. In the case of a crack, the incipient dislocation senses the image force of the surface corresponding to a "virtual" dislocation dipole where the dislocations are two Burgers vectors apart (see Figure 15.4 for a schematic visualization of these considerations). The atomic simulation results support this theoretical model since the ratio of critical stress intensity factor of a diffusion wedge to a crack is found to be around two.

As discussed in Section 17.4.2, a crack and a diffusion wedge have major differences in the time scale associated with creation of dislocations. A crack is a ready source for dislocations, while a diffusion wedge has an intrinsic characteristic time associated with dislocation climb. In the long-time limit on the order of a characteristic time τ,

the diffusion wedge behaves as a crack in agreement with theoretical considerations [88]. The change of maximum resolved shear stress due to climb of edge dislocations into the grain boundary is schematically visualized in Figure 19.15.

Our studies also corroborate the hypothesis of a threshold stress for constrained grain boundary diffusion. Unlike as proposed in the existing theories [88], we postulate that diffusion can not completely relax stresses in the film and introduce the concept of a threshold stress in the continuum theory. Experimental evidence of a threshold stress [132, 133, 131] as well as our atomistic modeling support this concept. The modified continuum theory was applied to modeling of the average stress in the film during thermal cycling experiments, and this new concept of the threshold stress allowed for some improvement in the agreement of the theory and the experimental data. In particular at high temperatures where constrained diffusional creep dominates, the new model describes the stress-temperature curves better (see, for instance in Figures 16.2 and 16.3). This suggests that the threshold stress for diffusion initiation is a useful concept.

Atomistic studies of polycrystalline thin films helped to clarify the nucleation mechanisms of dislocations from different types of grain boundaries. We find that low-energy grain boundaries provide more fertile sources for dislocations than high-energy grain boundaries. This concept helps to explain why the dislocation density is several times higher in grains neighboring to low-energy grain boundaries in our simulations.

We observe that mostly partial dislocations are nucleated from the grain boundaries in nanostructured thin films. This contradicts the classical theories of deformation [109] where it is predicted that complete dislocations dominate, but it is in agreement with other studies of deformation of nanostructured bulk materials [215, 242, 217, 66, 41]. A detailed investigation of the dislocation nucleation process from low-energy and high-energy grain boundaries provided insight into the atomic mechanisms of this process. One of the important observations is that dislocation half loops are generated on different glide planes causing formation of sessile jogs in the dislocation line that generate point defects as they move.

Additional simulations of constrained grain boundary diffusion in polycrystalline films suggested that there is a strong dependence of the diffusivities on the grain boundary structure. We could also show that parallel glide dislocations are nucleated along grain boundaries with highest diffusivities. This result shows that diffusion and nucleation of parallel glide dislocations are highly coupled, thus supporting the theoretical understanding of the process [88].

20.1. Usage of atomistic simulation results in hierarchical multi-scale modeling

Classical molecular-dynamics is rather constrained with respect to the accessible time scale. One of the drawbacks is that parameter studies with varying film thickness are difficult, if not impossible to carry out with today's computers. Therefore, hierarchical multi-scale modeling may serve as a useful tool to reach higher length-and timescales. Such studies are now being frequently applied in materials modeling (see, e.g. [102, 157, 224]). Here we briefly describe how a coupling of molecular-dynamics with mesoscopic

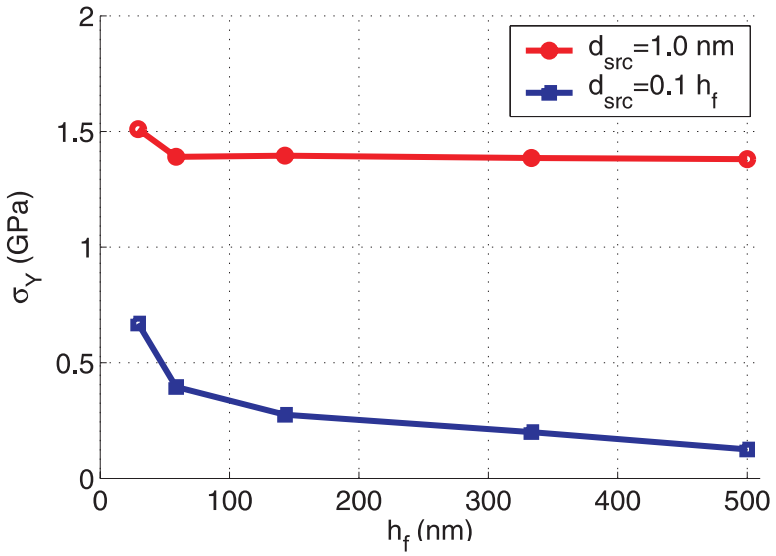

Figure 20.1.: Flow stress σ_Y versus the film thickness h_f, as obtained from mesoscopic simulations of constrained diffusional creep and parallel glide dislocation nucleation (data taken from [101]). The results are shown for two different initiation criteria for diffusion (constant source and therefore local criterion as proposed in equation (15.2), and a film-dependent source). In the case of a local criterion for diffusion initiation, the yield stress is film-thickness independent as observed in experiment [25].

simulations was achieved and review the results of a mesoscopic study that was carried out based on the molecular-dynamics results discussed in this thesis.

Mesoscopic methods must rely on phenomenological input parameters or rules. The most important contribution by the molecular-dynamics simulations was the concept of a critical stress intensity factor which could be translated into a discrete dislocation formulation of diffusional creep [101]. The mesoscopic model reported in [101] follows the well-known discrete dislocation models in two and three dimension described in the literature (see for example [192, 223, 224, 165] for thin film plasticity). In such models dislocations are considered sources of stress and strain in a linear elastic continuum.

The proposed discrete dislocation model for diffusional creep in ultra-thin films proved to be capable of predicting experimentally measurable quantities like the flow stress [101]. The two-dimensional model reveals the existence of a threshold stress for grain boundary diffusion, in agreement with atomistic simulations and experimental results. The investigation of different conditions for nucleation of climb and glide dislocations, as well as their interaction with grain boundaries, allowed to conclude that the diffusion threshold stress should only depend on the strain in the top layer of the film, and thus be independent of the film thickness. This gives rise to a thickness-independent flow stress for ultra-thin films, in good agreement with the relevant experimental results [25].

An important point is that only a local criterion for initiation of diffusion as proposed in equation (15.1) or equation (15.2) leads to a film thickness-independent yield stress. If the source for diffusion initiation is chosen film-thickness dependent, the yield stress

is also a function of the film thickness. Since the yield stress is found independent of the film thickness in experiment [25], there is reason to believe that our assertion of a *local* criterion for diffusion initiation is correct. This is in contrast to the nucleation criterion for parallel glide dislocations, which is a *global* criterion dependent on the film thickness. The results for the yield stress obtained from mesoscopic simulation are summarized in Figure 20.1 [101]. The yield stress as a function of film thickness is shown for two different initiation criteria for diffusion (constant source and therefore local criterion as proposed in equation (15.2), and film-dependent source). In the case of a local criterion for diffusion initiation, the yield stress is film-thickness independent as observed in experiment [25]. The yield stress increases slightly for very thin films.

The results obtained by this hierarchical multi-scale simulation method illustrate the usefulness of the atomistic approach and its possible transferability to other materials phenomena for which fully atomistic simulations are not yet feasible.

20.2. Mechanisms of plastic deformation of ultra-thin uncapped copper films

Prior to this study, no comprehensive overview over the deformation mechanisms in ultra thin films was reported. The results of atomistic simulations, experiments, continuum modeling as well as mesoscopic modeling have advanced to a level that they allow drawing general conclusions about the deformation mechanism in ultra thin films. Here we summarize the main results in a deformation map of thin films. The objective of this is to provide a clear overview over the different deformation mechanisms in ultra thin films.

20.2.1. Deformation map of thin films

The results from the numerical modeling reported in this thesis and in [101] together with experimental findings reported by different authors [25] allow us to qualitatively describe different deformation mechanisms that occur in thin films in the sub-micron regime. We propose that there exist four different deformation regimes. These are

- Regime (A): Deformation with threading dislocations,
- Regime (B): Constrained diffusional creep with subsequent parallel glide,
- Regime (C): Constrained diffusional creep without parallel glide, and
- Regime (D): No stress relaxation mechanism with no diffusion and no dislocation motion.

A schematic "deformation map" is plotted in Figure 20.2. This plot shows the critical applied stress to initiate different mechanisms of deformation as a function of the film thickness. We assume that the loading is applied very slowly, and the temperature is sufficiently high such that diffusive processes are generally admitted.

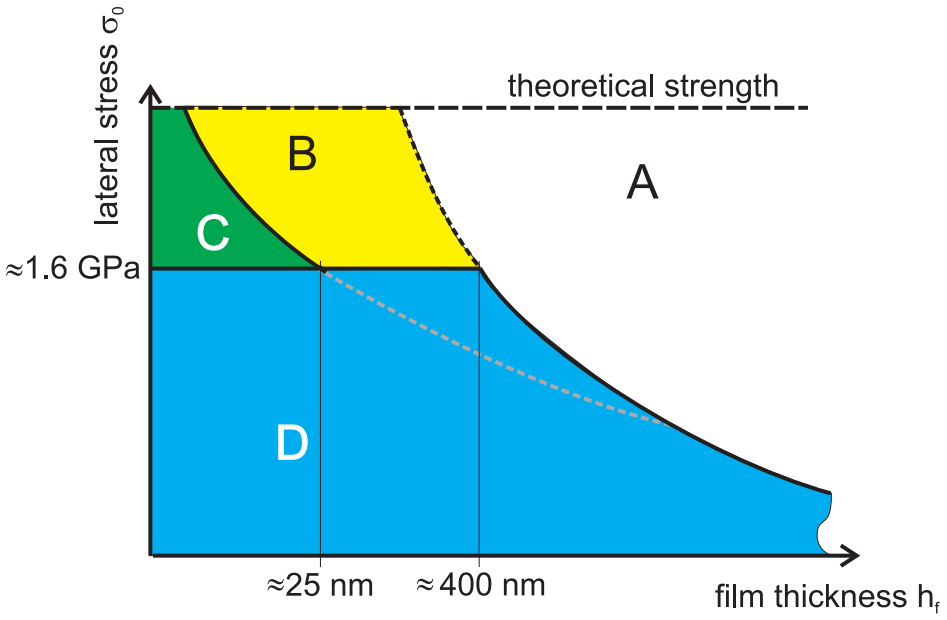

Figure 20.2.: Deformation map of thin films, different regimes. Thin films with thicknesses in the sub-micron regime feature several novel mechanisms next to the deformation by threading dislocations (A). For example, plasticity can be dominated by diffusional creep and parallel glide dislocations (B), purely diffusional creep (C) and no stress relaxation mechanism (D).

The critical applied stress to nucleate threading dislocations scales with $1/h_\mathrm{f}$ [77, 167, 169]. We note that the $1/h_\mathrm{f}$-scaling has been found in two-dimensional molecular-dynamics simulations [195] recently. Two-dimensional mesoscopic studies [165] revealed qualitatively that the flow stress increases with decreasing film thickness.

For films thicker than a material dependent value, regime (A) is the dominating deformation mechanism. For thinner films, the stress necessary to nucleate threading dislocations must be assumed larger than the stress to initiate grain boundary diffusion. In this regime (B), diffusion dominates stress relaxation and causes a plateau in the flow stress as shown by the discrete dislocation modeling.

Parallel glide helps to maintain grain boundary diffusion until the overall stress level is below the diffusion threshold which is independent of the film thickness. For yet thinner films grain boundary diffusion stops before a sufficient stress concentration to trigger parallel slip is obtained, as suggested by our molecular-dynamics simulations.

The onset of regime (C) can be described with the scaling of the critical nucleation stress for parallel glide with $1/h_\mathrm{f}^s$ ($s \approx 0.5$). In this regime, the flow stress increases again for smaller films, due to the back stress of the climb dislocations in the grain boundary, effectively stopping further grain boundary diffusion. If the applied stress is lower than the critical stress for diffusion, no stress relaxation mechanism is possible. This is referred to as regime (D). The critical film thickness of 25 nm is estimated based on the result for the critical $K_\mathrm{dw}^\mathrm{PG}$ from molecular-dynamics simulations.

Our investigations of ultra thin films show the richness of phenomena that occur as the dimensions of materials are shrunk to nanometer scale. For tomorrow's engineers,

such knowledge may be the key to successful design.

20.2.2. Yield stress in ultra thin copper films

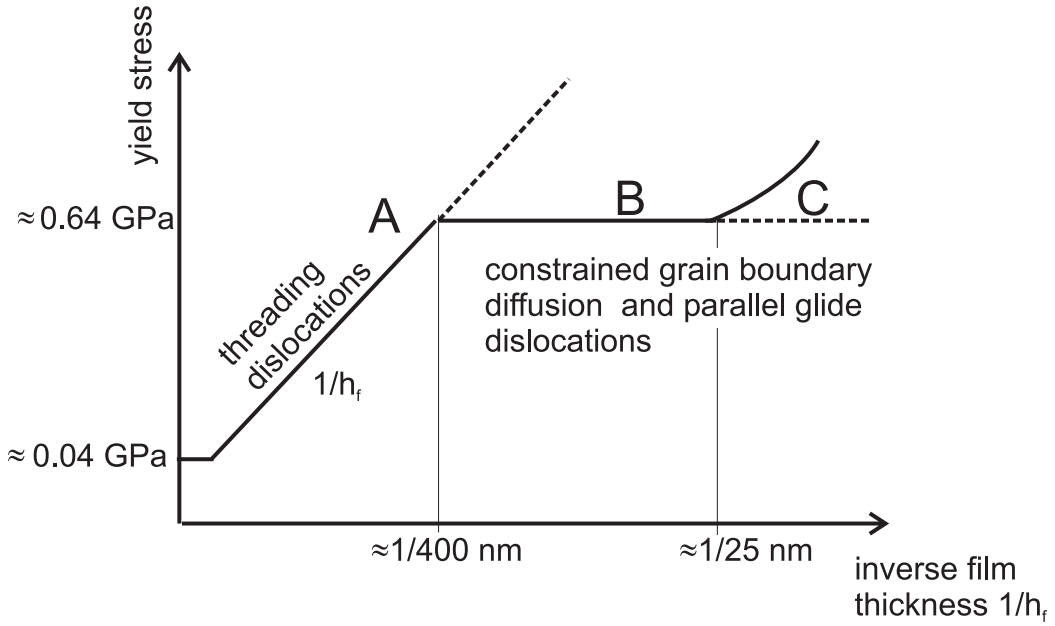

Figure 20.3.: Deformation map of thin copper films, yield stress. For films in the submicron regime (thinner than about 400 nm), the yield stress shows a plateau. This is the regime where diffusional creep and parallel glide dislocations dominate (regime (B) in Figure 20.2).

The yield stress of thin films resulting from these considerations is summarized in Figure 20.3 for different film thicknesses. For thicker films, the strength increases inversely proportional to the film thickness as has been shown in many theoretical and experimental studies [127, 25, 167, 223]. If the films thickness is small enough such that grain boundary diffusion and parallel glide are the prevailing deformation mechanisms, the film strength is essentially independent of h_f, as shown by the discrete dislocation model (reviewed in Section 20.1) and seen in experiment [25]. However, for films thinner than $h_\mathrm{f} \approx 25$ nm, the modeling predicts an increase in strength with decreasing film thickness (see also Figure 20.1).

In Figure 20.3, the film thickness of $h_\mathrm{f} \approx 400$ nm below which the yield stress remains constant, as well as the plateau yield stress of 0.64 GPa are taken from experimental results of copper thin films [55, 25].

20.3. The role of interfaces and geometric confinement

Our studies show that interface properties and geometric confinement can govern the deformation mechanisms in thin films. Important interfaces in thin films are

- the film surface,

- the grain boundary between two neighboring grains,
- and the interface of film and substrate (geometrical constraint).

In the following paragraphs, we will discuss the role of these different interfaces and constraints on the mechanical behavior.

20.3.1. Film surface

The film surface is important since it allows that atoms diffuse along the surface into the grain boundary. As shown in [251], the slower of the processes surface or grain boundary diffusion controls the dynamics of constrained diffusional creep.

20.3.2. Grain boundary structure

The governing character of the grain boundary structure in thin films is found either when deformation is mediated by diffusional creep, or by dislocation motion: As discussed in [240], the grain boundary structure has a significant influence on the diffusivities, and therefore determines how fast the tractions along the grain boundaries are relaxed and a singular stress field develops. This is also shown in Figure 19.14 where the depth of grain boundary grooves is deepest at high-energy grain boundaries corresponding to the fastest diffusion paths. Another indication of this is that high-energy grain boundaries lead to more pronounced surface grooves than low-energy grain boundaries when grain boundary diffusion is active. If deformation is carried by nucleation and motion of dislocations, the structure of the grain boundaries also has a significant influence on the details of deformation: Low-energy grain boundaries composed of arrays of misfit dislocations are more fertile sources for dislocation nucleation than homogeneous high-energy grain boundaries. On the other hand, motion of parallel glide dislocations through grains may be hindered due to pinning of dislocations when such a inhomogeneous grain boundary structure is present (see discussion in Section 19.2.2).

20.3.3. Geometrical constraints

The geometrical constraint of no sliding at the interface of film and surface is the reason for the singular stress field to develop around the diffusion wedge and is therefore responsible for the occurrence of parallel glide dislocations [88].

The geometrical constraint imposed by the grain size strongly influences the dislocation network that develops inside the grain. In very small grains of a few tens of nanometers, only one or two dislocations fit into a grain. In larger grains of several hundred nanometers, a much larger number of dislocations fit into each grain and may form a more complicated network (see Figure 19.10). Similar considerations apply to the Hall-Petch hardening [51].

20.3.4. Deformation mechanisms of small-scale materials

The dominance of grain boundary processes during deformation of ultra thin films is in qualitative agreement with recent investigations of other small-scale materials, such as nanostructured materials [235].

The preliminary study on nanostructured materials discussed in Section 19.3 showed that an intergranular nano-substructure constituted by twin lamellas could play an important role in effectively strengthening materials. Since twin grain boundaries are relatively poor diffusion paths (since they are low-energy grain boundaries), such materials could potentially be successfully employed at elevated temperatures where "usual" materials with ultra-fine grains can not be utilized since creep becomes the dominant deformation mechanism. The study supports the notion that geometric confinement has strong impact on the deformation, and could potentially be utilized to create materials with superior mechanical properties.

20.4. Linking atomistic simulation results to continuum mechanics theories of plasticity

Atomic measures for quantities like stress or elastic strain are well-described in the literature and it has been shown in several cases that good agreement of continuum mechanics theories and atomistic simulation results can be obtained, even in the dynamic cases as shown in this thesis (see, for instance the studies reported in Chapter 6). However, no direct link between continuum mechanics concepts of plasticity such as strain gradient theories of plasticity has been established so far. In this section we discuss how such coupling could in principle be achieved.

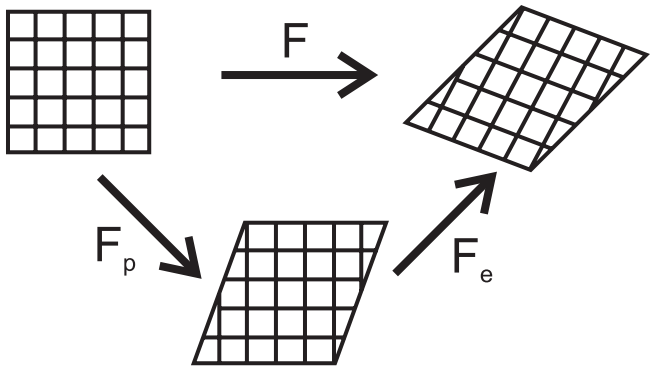

Figure 20.4.: The multiplicative decomposition $\mathbf{F} = \mathbf{F}_e\mathbf{F}_p$ in continuum theory of plasticity.

We assume that the deformation gradient is multiplicatively decomposed, thus $\mathbf{F} = \mathbf{F}_e\mathbf{F}_p$ where the lattice distortion is assumed to be contained in the elastic part $\mathbf{F}_e$, and the plastic slip is contained in $\mathbf{F}_p$ [142]. Such deformation mapping is illustrated in Figure 20.4. In the continuum theory of plasticity, the geometrically necessary dislocation

density tensor $\mathbf{A}$ is defined as [161, 100, 142]

$$\mathbf{A} = \det(\mathbf{F_e})\mathbf{F}_e^{-1}(\mathrm{curl}\mathbf{F}_e^{-1})^T = \frac{1}{\det(\mathbf{F}_e)}\mathbf{F}_p(\mathrm{Curl}\mathbf{F}_p^{-1})^T. \tag{20.1}$$

Note that Curl is the curl differential operator with respect to the material point in the reference configuration, while curl is the curl operator with respect to a material point in the current configuration.

From an atomistic point of view, the dislocation density can be expressed as [142, 161, 100]

$$\mathbf{A} = \mathbf{l} \otimes \mathbf{b}\frac{\Delta l}{\Delta v} \tag{20.2}$$

where $\mathbf{l}$ denotes the unit tangent vector along the dislocation line segment, Δl is the element of the dislocation line and Δv is the elementary volume. The operator $\otimes$ denotes a dyad product. Under the assumption of infinitesimal deformation and negligible elastic strain, the dislocation density tensor is directly linked to the plastic distortion [161]. In the case of multiple dislocation segments within a representative volume element, the dislocation density tensor is defined by a linear combination of dislocations

$$\mathbf{A} = \sum_k \eta_k \mathbf{l_k} \otimes \mathbf{b_k} \tag{20.3}$$

where

$$\eta_k = \frac{\mathrm{d}l_k}{\mathrm{d}v}b. \tag{20.4}$$

An integral formulation of equation (20.3) is given by

$$\mathbf{A} = \frac{1}{\Delta v}\int\limits_{\perp \text{ in } \Delta v} \mathbf{dl} \otimes \mathbf{b}. \tag{20.5}$$

Note that statistically stored dislocations do not contribute to $\mathbf{A}$ in crystal plasticity since dislocation dipoles cancel. Curved dislocation lines can be approximated by straight dislocation segments.

Equation (20.3) could be used to calculate the dislocation density tensor from atomistic data. The slip vector approach, as described in Section 2.5.3 is a possible candidate for this purpose. As discussed earlier, Figure 2.10 shows the result of a slip vector analysis of a single dislocation in copper. The quantitative information obtained from atomistic results described in Section 2.5.3 can be used to calculate the dislocation density tensor.

20.5. Far-reaching implications and outlook to future research

As illustrated in the studies carried out in this thesis, a complex interplay of diffusion and "classical" dislocation mediated plasticity exists and governs the mechanical properties.

In view of technological applications, this could lead to the question of how strong can materials get? In thin films, experimental and numerical studies [101, 25] reveal that the strength saturates at a plateau at the nanoscale, and the results suggest that grain boundary processes such as grain boundary diffusion play an increasingly important role, the smaller the relevant length scales in materials get.

This suggests that if means to inhibit grain boundary processes such as diffusion could be found, the strength of nanostructured materials could be significantly increased. One possible solution for thin film systems would be to design effective capping layers that shut down grain boundary diffusion. The effect of capping layers on shutting down diffusion in thin films has been demonstrated in experiment [234].

Considerations of how strong can materials get have recently also been carried out to investigate the fracture strength of biological materials such as bones and teeth with a nano-substructure [85]. Assisted by studying nature's design of these materials, it was found that at a critical characteristic length scale of several nanometers, brittle materials become intolerant to flaws since the stress magnification at cracks vanishes at a critical length scale. This concept could be employed to address an important open question in the literature, which is to understand the fundamentally different behavior of coarse-grained versus nano-grained metals [217, 242, 235]. A systematic study, possibly with a microstructure as described in Section 19.2, could be used to investigate the transition from dominance of partial dislocations to complete dislocations depending on the grain size.

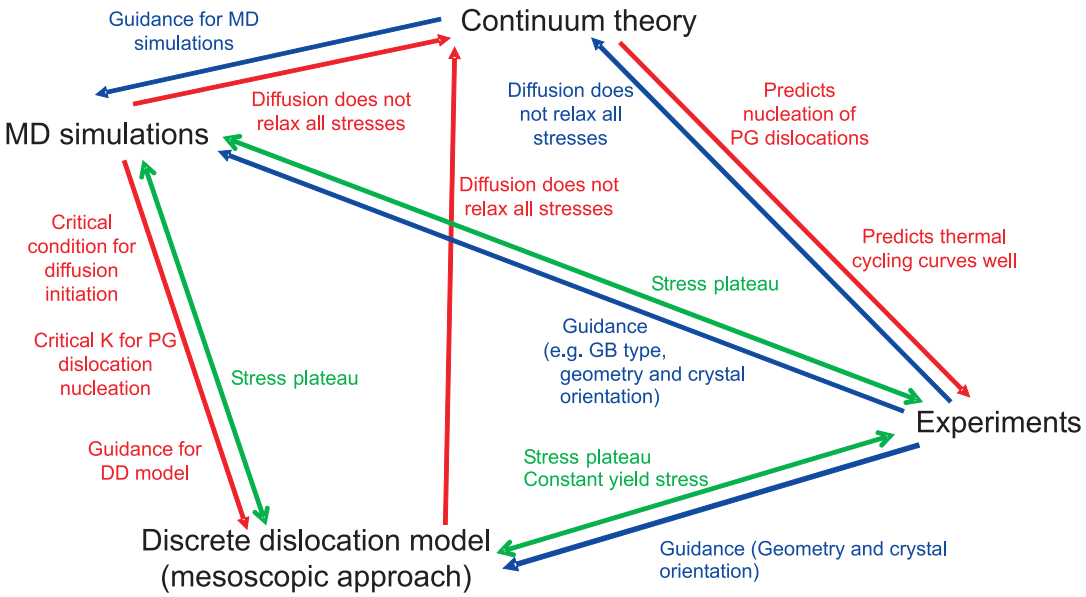

Figure 20.5.: The figure shows a summary of the investigation of constrained diffusional creep of thin films with different approaches [101, 24, 55, 25, 88, 250, 251]. The green arrow indicates agreement of the results obtained by different methods, the red arrow refers to transport of information and predictions, and the blue arrows correspond to general guidance for model development.

From a more philosophical viewpoint, the grain boundary appears to be behave somewhere in between a free surface (crack) and bulk material [88]. Indeed, from the energy

point of view it is well-known that the grain boundary energy is usually between the free surface and the bulk material. The present study shows that constrained diffusional creep provides a mechanism that slowly transforms the grain boundary into a crack-like object due to applied stress.

Together with the work reported in the literature [24, 55, 101, 25], constrained diffusional creep was investigated with a variety of methods, where each of the approaches contributed an important part to the understanding of the mechanisms. A schematic overview is depicted in Figure 20.5, and we summarize some important points:

- *Continuum theory:* Continuum theory predicted the existence of diffusion wedges, which was later verified in experiment. Continuum theory also served as guidance to develop molecular-dynamics simulations. In turn, molecular-dynamics simulations helped to advance continuum theory, for instance by introducing the concept of the threshold stress for diffusion initiation.

- *Experiment:* Experiment helped to guide development of continuum theory with the new concept of a threshold stress. Experiments also confirmed the predictions by the continuum modeling that crack-like diffusion wedges lead to parallel glide dislocations.

- *Atomistic simulations:* The results in molecular-dynamics simulations confirmed the conclusions that were drawn from experimentalists, for instance that diffusion wedges are created featuring a crack-like stress field leading to nucleation of parallel glide dislocations. Molecular-dynamics simulations guided mesoscopic simulations that used the results of molecular-dynamics simulations as input parameters for phenomenological rules. Atomistic simulations also confirmed the predicted Rice-Thomson continuum model for nucleation of parallel glide dislocations.

- *Mesoscopic simulations:* The most important result of mesoscopic discrete dislocation dynamics simulations is the prediction of a film thickness-independent yield stress [101]. This observation is in direct agreement with experimental results, even though no input parameters from experiments were used! This also validates the molecular-dynamics simulation results.

Similar joint theoretical, experimental and numerical studies could be applied to other materials phenomena in a similar manner.

Part IV.

Discussion

21. Discussion and summary

We have presented a set of studies where atomistic simulations were used in conjunction with continuum mechanics concepts. The studies included

- dynamic fracture,
- diffusional creep in thin films and
- dislocation nucleation from grain boundaries and cracks.

It was illustrated that joint application of atomistic with continuum mechanics methods can be a fruitful approach in studying materials phenomena at small scales: For instance, continuum theory can guide atomistic simulations (e.g. modeling of constrained diffusional creep), and simulation can also help to develop new continuum theories and concepts (e.g. characteristic energy length scale in dynamic fracture). In some cases, computer simulation results can also stimulate experimental work as in the case of intersonic mode I cracks [32, 172]. This exemplifies that due to increasing computer power, new physical phenomena may be discovered by computer simulation!

In this final chapter, we present a discussion of the approaches taken to solve the problems reported in this thesis. We proceed as follows. We start with a critical assessment of the simulation tools that we used in our studies. Then, we focus on possible ways of coupling atomistic simulation results to other materials modeling concepts and experimental data, and discuss the predicability of atomistic simulations. We conclude with an outlook to possible future research.

21.1. Potential and limitations of the molecular dynamics method

A critical limitation of applicability of atomistic methods is the available computer power: Huge computers are required to simulate systems on a sufficiently long time scale, or model systems that comprise of a large number of atoms. Lack of computer power inhibits application of atomistic methods in many cases. Nevertheless, the enormous increase in computer power in recent years allowed for very large atomistic simulations. Recent reports of billion-atom simulations [12, 185, 193] show that such ultra-large scale simulations are in principle feasible. Particularly during the analysis of these ultra-large scale simulations [36], it has become apparent that methods to analyze and link atomistic results to other modeling techniques and experimental results need to be further developed [34]. The analysis of terabytes of data and extracting "useful" information is a highly non-trivial task.

21.1.1. Length- and timescale limitations

A simulation comprising a billion atoms undoubtedly represents a new level of achievement in atom system size. However, the crystal studied in [12], for example, still represents a very small solid, only 0.3 microns on a side. This illustrates that it is important to further advance computing power in the future. The analyses described in [12, 36] illustrate that despite certain shortcomings of the molecular-dynamics method, it can, with the limitations understood, be used to study plasticity in crystals approaching the micrometer scale. Recent reports of application of molecular-dynamics to study diffusion [240, 235] in polycrystals with grain sizes of several tens of nanometers (as well as the studies presented in this thesis) further illustrate to what level atomistic simulations have advanced. Miniaturization of technology, while at the same time computer power increases dramatically, will soon result in an overlap of the scale that is technologically relevant, with the scale that is accessible to molecular-dynamics. We thus believe that for tomorrow's engineering applications, molecular-dynamics simulations will provide an important tool: In some of tomorrow's technology components, not 10^{23} atoms will be contained, but only 10^{10} atoms, which is within the regime accessible to molecular-dynamics simulations, but, however not within the scope of continuum methods!

The time scale limitation is more severe than the limitations with respect to system size: In the classical molecular-dynamics schemes, it is in principle possible to simulate arbitrarily large systems, provided sufficiently powerful computers are available. However, the time scale always remains confined to several nanoseconds. Surprisingly, this is also true for very small systems independent of how large computers we use. The reason is that very small systems can not be effectively parallelized. In addition, time can not easily be parallelized. Surprisingly there exists little tradeoff between desired simulation time and desired simulation size. This problem was recently referred to as the "time-scale dilemma of molecular-dynamics" by Voter [229]. Many systems of interest spend a lot of time in local free energy minima before a transition to another state occurs. In such cases, the free energy surface has several local minima separated by large barriers. This is computationally highly inefficient for simulations with classical molecular-dynamics methods since the thermal vibrations of all atoms have to be simulated. An important field where classical molecular-dynamics is difficult to apply are diffusive processes. Although we were able to model grain boundary diffusion with classical molecular-dynamics in this thesis, we could only achieve this at very high temperatures and under unrealistically high strain rates and stresses. Luckily, we find that the mechanism of parallel glide dislocations is still active under these conditions. However, in some other cases this may not be the case and therefore classical molecular-dynamics may not be applicable at all. Advanced molecular-dynamics simulation methods as described in Section 2.3.2 could be a possible approach to overcome the limitations. As an example, we applied the temperature accelerated dynamics method to calculate the surface diffusivity of copper, and to calculation of the atomic activity near a surface step at a copper surface in Section 2.3.2. Development of such methods should, in our opinion, be a very important future research objective. Advancing methods that would be more generally applicable than today's tools and yet overcome the time scale limitations could potentially revolutionize the way how atomistic simulations are applied.

21.1.2. Multi-scale simulations

A possible way to overcome the time-scale restrictions of purely atomistic simulations is to take advantage of multi-scale simulations. As discussed in Section 2.3.3, in particular the development of hierarchical multi-scale simulation techniques is an emerging field. Hierarchical multi-scale simulation consist of a series of simulation tools that feed information to the next level of modeling. For instance, dislocation reactions could be investigated on a fundamental level using classical molecular-dynamics and then inserted into phenomenological rules. For hierarchical multi-scale simulations, the most difficult issue is to couple the different simulation tools. The study of diffusional creep in thin films using mesoscopic methods provided further evidence that such an approach is feasible [101] and can lead to useful results. The study reported in [101] used the results of atomistic simulations reported in this thesis as input parameters to define empirical rules for parallel glide dislocation nucleation (see Section 20.1). The most important result presented in [101] was the observation of a film thickness independent flow stress, a finding in direct agreement with experimental results [25] (see Figure 20.1). Mesoscopic simulations fed by atomistic simulation results are virtually the only way to perform such studies. We believe that hierarchical multi-scale simulations that base upon atomistic simulation results could be an important future modeling approach for a variety of complex materials phenomena. This could be considered an important "niche" for classical molecular-dynamics. Molecular-dynamics could play a role in helping to understand atomic mechanisms (such as the details of nucleation of parallel glide dislocations, for instance) as well as providing quantitative numbers (like the critical stress intensity factor for nucleation of parallel glide dislocations).

Another promising area are concurrent multi-scale methods such as the quasi-continuum method [208]. The method was exemplified in Section 2.3.3 to study parallel glide dislocation nucleation in thin copper films constrained by substrates. The results of this calculation are shown in Figure 2.7. The analysis shows good agreement with the results in purely atomistic simulations, for instance shown in Figure 17.6. The advantage of the quasi-continuum method is that the simulation time required to carry out such studies is significantly reduced and that the simulations can be performed on a LINUX workstation, instead of using a supercomputer! Compared to classical molecular-dynamics simulations, concurrent multi-scale methods are often based on complicated numerical procedures, and certainly much future research needs to be carried out to make them applicable to more general cases. For instance, most of the available techniques are only for quasi-static cases and are restricted to simulations at 0 K. Nevertheless, such techniques have great potential and are expected to play an important role in the future.

21.1.3. Applicability and predicability of atomistic methods

Despite the appeal of atomistic methods, it is misleading to assume that molecular-dynamics could be applied to any problems. One needs to be very critical where atomistic methods can be utilized. Given that the bonding between atoms can be described sufficiently accurate, in the field of dynamic fracture molecular-dynamics is undoubtedly one of the methods with the greatest appeal. This is because the relevant time- and

	yes	yes w/ limitations	no
Fracture in model materials	×		
Fracture in real materials		×	
GB diffusion at high temperatures		×	
GB diffusion at low temperatures			×
Plasticity in model materials	×		
Plasticity in real materials		×	

Table 21.1.: Applicability of classical molecular-dynamics simulations to a selection of problems in materials science.

length scales are well within the regime accessible to molecular-dynamics.

In other areas, for instance where activated events play a governing role, the usage of classical molecular-dynamics may be questionable and its application needs to be critically assessed. Other simulation techniques like finite element methods or mesoscopic simulations may be advantageous in some cases. Applicability of molecular-dynamics to different problems in materials science is summarized in Table 21.1.

An important issue in atomistic modeling is the description of the interatomic bonding. Many researchers tried modeling the interatomic bonding according to specific materials. A more unconventional, alternative approach is the development of "model materials" for computer experiments as used in some parts of this thesis (see Chapter 5, for instance). In such cases, interatomic potentials are not fit to model a specific material (e.g. copper), but instead aim on describing *generic features* of a whole class of materials. Such model materials have been developed for ductile and brittle materials (e.g. [12]), and are becoming increasingly popular particularly in the mechanics community. However, one needs to be critical with respect to the validity of the results when using such model materials. For a discussion on the role of interatomic bonding in describing the dynamics of fracture in different materials, see [3].

An important conclusion is that atomic simulations should be used with care: Although they can be predictive in some cases, the severe length- and time scale limitations can provide a serious burden. It is often only a small window where atomistic simulations can be used. In order to carry out useful simulations, one needs to have good understanding of this window. For instance, since diffusional creep can be studied with classical molecular-dynamics only in the high-temperature regime close to the melting temperature, it may be questionable to extrapolate the results (e.g. the critical stress intensity factor) to lower temperatures. This fact also underlines the importance of validating the results of atomistic simulations with experimental work.

21.2. Coupling between continuum theories and atomistic methods

We have shown that continuum theories can be coupled to atomistic methods by a variety of concepts. The most prominent concept is to use quantities like the virial stress and virial strain as done in Chapter 6, for instance. Other quantities like energy flux, particle velocity or potential energy field could also be directly used to link continuum to atomistic methods.

In Chapter 17, the concept of a critical stress intensity factor was employed to define critical conditions for nucleation of parallel glide dislocations. Essentially, this approach relies on determination of displacements at the atomic scale and fitting the results to continuum mechanics solutions. The stress intensity factor also served as a method to couple atomistic and mesoscopic simulations [101].

For the analysis of dislocations, energy filtering techniques and more advanced methods such as the centrosymmetry parameter proved to be helpful as outlined in Chapter 18, for instance. However, the analysis of networks of dislocations is generally not as straightforward as the study of elastic deformation fields. In particular, the linkage of atomistic simulation results to continuum theories of plasticity is not understood well and remains yet to be explored. The development of analysis tools should thus be in the focus of future research. In particular, tools to analyze the three-dimensional data of complex dislocation topologies more conveniently and methods to express the results in terms of quantities used in the continuum mechanics community should be further developed [36]. A possible approach for coupling of dislocation simulation results with continuum theories of plasticity is calculation of the dislocation density tensor from the atomistic simulation results, as outlined in Section 20.4. We believe that due to the complexity of the problem, the development of numerical tools to couple atomic scale plasticity is just at its beginning and much further research needs to be completed.

21.3. Applicability of continuum mechanics concepts to study materials phenomena at very small scales

Historically, the coupling of continuum mechanics with the atomistic viewpoint has often been neglected. It is only in recent years that the increasing interest in nanoscale phenomena has led to attempts to use continuum theories to describe deformation at the nanoscale. This was exemplified for instance in numerous studies of the mechanical properties of carbon nanotubes [239]. Most of the studies were confined to the static case.

The studies in this thesis showed that continuum mechanics concepts can also be applied to study dynamic materials phenomena at very small scales. Linear elastic concepts can only be used when material nonlinearities are small, and they can not be applied when nonlinearities are present, as illustrated in Chapter 7.

In the field of thin film mechanics, continuum theory proved to be a helpful guidance to atomistic modeling. Some of the predictions by continuum theory, as for instance the

crack-like displacement field near a diffusion wedge could be qualitatively reproduced at the atomic scale as discussed in Chapter 17 (see Figure 17.3).

21.4. Outlook to future research

The studies reported in this thesis could lead to several new topics of research.

A possible area of future investigations would be the investigation of the Broberg problem (crack propagating in a thin layer embedded in a matrix material with different elastic properties) when the inner layer is softer than the surrounding material. The existing solution for a mode I crack [30] suggests that there is no stress concentration any more. It would be interesting to study the atomic details of failure in such a system.

From the theoretical viewpoint, development of analytical solutions treating cracks at interfaces would be of interest. In particular the observed mother-daughter-granddaughter mechanism (see Section 9.2) and the observation of daughter cracks in mode I cracking along interfaces remain yet to be analyzed analytically. In addition, experimental evidence of this dynamical phenomena needs to be provided.

In the field of mechanical properties of thin films, an interesting point of study would be to investigate diffusional creep under compressive loading. This is motivated by experimental thermal cycling experiments (see Figure 16.2, for instance) where the stress at the grain boundary changes from compressive to tensile during cycling. A point of particular interest is to study if there is a net mass transport out of the grain boundary, possibly because of an asymmetry in the diffusional mass transport. Recent experimental observations suggest that similar mechanisms may occur in thin films and could possibly be explained by an asymmetry of mass transport [57].

The area of plasticity of polycrystalline materials is another point of future research. As we have illustrated in this thesis, plasticity is dominated by partial dislocations in grains with several tens of nanometers diameter. In contrast, it is known from experiment that in larger grains complete dislocations prevail (e.g. [109, 118]). In the literature, this issue has not been clarified so far. A systematic study with varying grain size could shed light on this problem, if it would be possible to cover the transition from one to the other mechanism by a series of molecular-dynamics simulations. Based on the atomistic simulation results, new continuum mechanics theories could be developed.

A more unconventional approach is to combine classical materials science concepts with biology and nanotechnology. We believe that classical molecular-dynamics could also be a very useful approach in these fields. In recent years, a trend to combine studies of classical materials science areas with biological applications became apparent. Numerous studies focused on modeling of carbon nanotubes. In a recent paper by Gao *et al.* [87], interaction of DNA with carbon nanotubes was studied. The authors showed that upon a critical CNT radius, the DNA is spontaneously encapsulated into the carbon nanotube.

Other studies could focus on the mechanical properties of carbon nanotubes (see, for instance [239]). When the CNTs approach sizes close to micrometer dimensions, large-scale computers become suitable tools for investigation. In Figure 21.1 we show several snapshots of CNTs under compression. The plot shows an overview of deformation

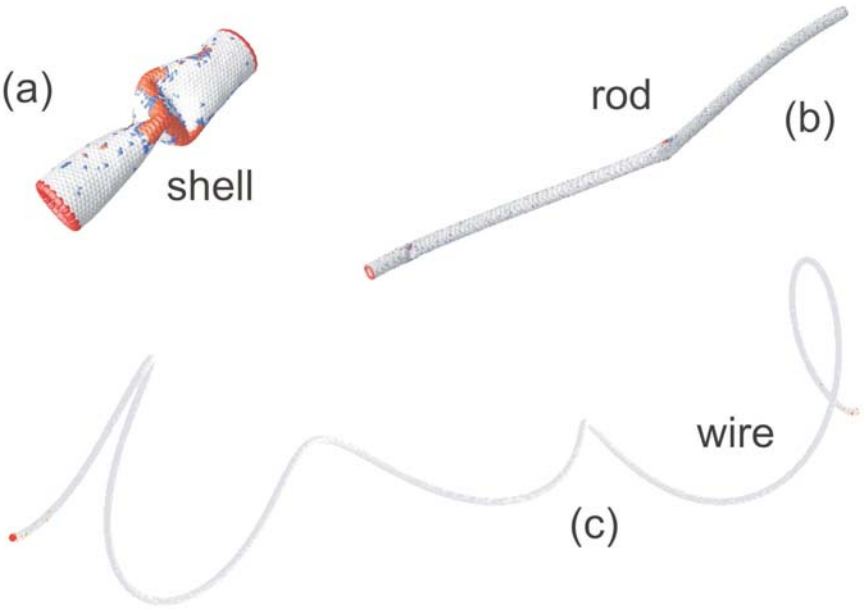

Figure 21.1.: Shell-rod-wire transition of carbon nanotubes as a function of length-to-diameter ratio.

mechanisms of single wall carbon nanotubes in compression [37]. This could be referred to as a shell-rod-wire transition as a function of the length-to-diameter aspect ratio of the CNT. The plot shows different modes of deformation, (a) buckling of the cylindrical shell structure, (b) rod-like behavior with localized buckling along the length of the tube, and (c) a flexible macromolecule. Statistical mechanics and entropic forces may play a role in the third class, the wire-like behavior of nanotubes with very large aspect ratios. Statistical theories of macromolecules may be used to analyze the dynamics of such nanostructures on the mesoscale. Thermodynamical properties of very long and thin CNTs could be an interesting subject for further study. The observation of a "self-folding" mechanism where different parts of the same CNT are brought into adhesive contact indicates that CNTs become very flexible at very large aspect ratios. In this case, different parts of the CNTs attract each other due to the van der Waals interaction. It could be interesting to further study such self-folding under entropical forces. An example of such a self-folded state is shown in Figure 21.2.

21.5. Summary

The main achievements are summarized as follows. In the area of brittle fracture

- We proposed an atomistic model of one-dimensional fracture, showing many of the

Figure 21.2.: Self-folding of carbon nanotubes. Our simulation results suggest that the folded state is in thermodynamical equilibrium at low temperature and unfolds at a critical elevated temperature [37].

features of higher-dimensional models. The one-dimensional model could be used to derive an analytical solution for cracks propagating in nonlinear materials, and the solution predicted the deformation field near supersonic cracks.

- We studied the stress and strain fields, particle velocity fields and the energy flux fields near rapidly propagating cracks in two-dimensional harmonic lattices and showed that the predictions by linear elastic fracture mechanics [78] could well be reproduced in atomistic simulations of cracks propagating in harmonic lattices.

- It was established that hyperelasticity can govern dynamic fracture, once the size of the hyperelastic region becomes comparable to a critical length scale χ associated with energy flux toward the crack tip. The new concept of the critical energy length scale χ provides an immediate explanation of different experimental and numerical results. One of the consequences of the results is the prediction of intersonic mode I cracks and supersonic mode II cracks. The prediction by our simulations [32] was recently verified in experiment [172] where intersonic mode I cracks were observed.

- We showed that hyperelasticity governs the dynamic crack tip instability. Cracks in harmonic lattices propagate straight up to a critical velocity of 73 % of the Rayleigh-wave speed, in agreement with linear elastic fracture mechanics [78, 246]. Hyperelasticity can significantly change the dynamics of cracks in homogeneous materials. We found that mode I cracks in stiffening solids could propagate straight with perfect mirror-like cleavage up to speeds close to the Rayleigh-wave speed. In contrast, cracks in softening materials show a strong tendency to become unstable at low velocities. The onset of instability is explained based on arguments of energy flow in the softening case, and based on the change in deformation field near the crack tip in the stiffening case.

- We showed that cracks at interfaces between dissimilar materials show a significant different dynamics than cracks in homogeneous materials or along weak fracture layers between identical materials. We observed that there exists a mother-daughter mechanism for mode I cracks, and that the limiting speed for mode I cracks is given by the Rayleigh-wave speed of the stiffer material. For mode II cracks, we observed a mother-daughter-granddaughter mechanism. The limiting

speed of mode II cracks along interfaces is given by the longitudinal wave speed of the stiffer material, in agreement with recent experimental observation [182].

- We showed that mode I cracks carry no inertia, in agreement with experimental results [230] and linear elastic fracture theories [78]. Intersonic mode II cracks carry inertia, as predicted by recent theoretical progress [117]. In the nonlinear cases, we find that the definition of a unique wave front is difficult and a trail of waves appears. A consequence is that the crack can no longer assumed to be inertia-less.

- We showed that the concept of the critical energy length scale χ also holds for mode III cracks under anti-plane shear loading. A quantitative comparison of the crack speed calculated from molecular-dynamics with recently developed continuum mechanics theory [44] provides additional evidence of the characteristic energy length scale.

In the area of mechanical properties of thin films

- We proposed a criterion for initiation of diffusion. In contrast to previous studies, we believe that constrained grain boundary diffusion can not operate below a threshold stress. Recent experimental evidence [132, 33] supports our assumption.

- We showed that at nanoscale, the role of single dislocations becomes important. A study of the image stress on climb edge dislocations in the GB of ultra thin films revealed that the image stress can be on the order of GPa for extremely thin films. Another result was that the critical stress for storage of dislocations in the GB is quantized.

- A Rice-Thomson model was proposed to model the nucleation of parallel glide dislocations from diffusion wedges and cracks in thin films. The model predicts that the ratio of critical stress intensity of diffusion wedge to crack is two. This was verified by atomistic simulations.

- We proposed a modified continuum model incorporating the concept of the threshold stress and used this model to predict the stress during thermal cycling experiments of thin films. A quantitative comparison with experimental results provided some agreement. Compared to earlier modeling [234], the concept of a threshold stress improved the agreement of the curves particularly for high temperatures.

- Using large-scale atomistic simulations we showed that mass transport from the surface along the grain boundaries leads to formation of diffusion wedges, as predicted by theory [88]. A crack-like deformation field develops near the diffusion wedge leading to high resolved shear stresses on glide planes parallel to the film surface. This causes emission of dislocations that glide on glide planes parallel to the film surface, therefore referred to as parallel glide dislocations. This simulation result provides an immediate explanation of the experimental observation of parallel glide dislocations. [24, 55, 25]. The observation of parallel glide dislocations from diffusion wedges closes the theory-experiment-simulation linkage. An

important result is that grain boundaries can be treated as traction free cracks in a first approximation once constrained grain boundary diffusion is active.

- We studied dislocation nucleation from grain triple junctions, and showed that the nucleation process strongly depends on the grain boundary structure. Dislocations nucleate preferably at the grain boundary misfit dislocations of low-energy grain boundaries.

- Large-scale atomistic simulations of polycrystalline thin films revealed that the deformation mechanism changes completely when tractions along grain boundaries are relaxed by diffusional creep. Whereas threading dislocations dominate in thin films with no diffusion [127, 132, 222], parallel glide dislocations dominate in films where diffusion is active. This finding is in agreement with recent experimental progress [24, 55, 25]. We also observed that low-energy grain boundaries are more fertile sources for dislocations than high-energy grain boundaries. The dislocation density in grains neighboring low-energy grain boundaries is several times larger. This was also confirmed in a study of nanocrystalline bulk copper.

- Different modes of deformation active in ultra thin copper films confined by substrates were summarized in a deformation map. We propose that beyond the classical regime of threading dislocations, there exists several new mechanisms, one of them being constrained diffusional creep with parallel glide dislocation nucleation. Additionally, we plot the yield stress as a function of film thickness. Recent results of mesoscopic modeling [101] used the critical conditions for nucleation of parallel glide dislocations obtained from molecular-dynamics simulations as input parameters and could successfully reproduce the experimental observation of a thickness-independent yield stress when constrained diffusional creep dominates plasticity.

Bibliography

[1] F.F. Abraham. Computational statistical mechanics-methodology, applications and supercomputing. *Advances in Physics*, 35(1):1–111, 1986.

[2] F.F. Abraham. Dynamics of brittle fracture with variable elasticity. *Phys. Rev. Lett.*, 77(5):869, 1996.

[3] F.F. Abraham. How fast can cracks move? A research adventure in materials failure using millions of atoms and big computers. *Advances in Physics*, 52(8):727–790, 2003.

[4] F.F. Abraham, N. Bernstein, J.Q. Broughton, and D. Hess. Dynamic fracture of silicon: Concurrent simulation of quantum electrons, classical atoms, and the continuum solid. *MRS Bulletin*, 25(5):27–32, 2000.

[5] F.F. Abraham, D. Brodbeck, R.A. Rafey, and W.E. Rudge. Instability dynamics of fracture: A computer simulation investigation. *Phys. Rev. Lett.*, 73(2):272–275, 1994.

[6] F.F. Abraham, D. Brodbeck, W.E. Rudge, J.Q. Broughton, D. Schneider, B. Land, D. Lifka, J. Gerner, M. Rosenkranz, J. Skivira, and H. Gao. *Ab-initio* dynamics of rapid fracture. *Modelling Simul. Mater. Sci. Eng.*, 6:639–670, 1998.

[7] F.F. Abraham, D. Brodbeck, W.E. Rudge, and X. Xu. A molecular dynamics investigation of rapid fracture mechanics. *J. Mech. Phys. Solids*, 45(9):1595–1619, 1997.

[8] F.F. Abraham, J.Q. Broughton, N. Bernstein, and E. Kaxiras. Spanning the length scales in dynamic simulation. *Computers in Physics*, 12(6):538–546, 1998.

[9] F.F. Abraham and H. Gao. Anamalous brittle-ductile fracture behaviors in FCC crystals. *Phil. Mag. Lett.*, 78:307–312, 1998.

[10] F.F. Abraham and H. Gao. How fast can cracks propagate? *Phys. Rev. Lett.*, 84(14):3113–3116, 2000.

[11] F.F. Abraham, R. Walkup, H. Gao, M. Duchaineau, T.D. de La Rubia, and M. Seager. Simulating materials failure by using up to one billion atoms and the world's fastest computer: Brittle fracture. *P. Natl. Acad. Sci. USA*, 99(9):5788–5792, 2002.

[12] F.F. Abraham, R. Walkup, H. Gao, M. Duchaineau, T.D. de La Rubia, and M. Seager. Simulating materials failure by using up to one billion atoms and the world's fastest computer: Work-hardening. *P. Natl. Acad. Sci. USA*, 99(9):5783–5787, 2002.

[13] B.J. Alder and T.E. Wainwright. Phase transformations for a hard sphere system. *J. Chem. Phys.*, 27:1208–1209, 1957.

[14] B.J. Alder and T.E. Wainwright. Studies in molecular dynamics. 1. General method. *J. Chem. Phys.*, 31:459–466, 1959.

[15] M.P. Allen and D.J. Tildesley. *Computer Simulation of Liquids*. Oxford University Press, 1989.

[16] D.J. Andrews. Rupture velocity of plane strain shear cracks. *J. Geophys. Res.*, 81:5679–5687, 1976.

[17] R.J. Archuleta. Analysis of near-source static and dynamic measurements from the 1979 imperial valley earthquake. *Bull. Seismol. Soc. Am.*, 72:1927–1956, 1982.

[18] E. Arzt. Interface controlled diffusional creep. *Acta Mater.*, 31:1977–1989, 1983.

[19] E. Arzt. Size effects in materials due to microstructural and dimensional constraints: A comparative review. *Acta Mater.*, 46:5611–5626, 1998.

[20] W.T. Ashurst and W.G. Hoover. Microscopic fracture studies in 2-dimensional triangular lattice. *Phys. Rev. B*, 14(4):1465–1473, 1976.

[21] B.A. Auld. *Accoustic Fields and Waves in Solids*. R.E. Krieger Publishing Company, 2nd edition, ISBN 0-89874-783-X edition, 1990.

[22] B.R. Baker. Dynamic stresses created by a moving crack. *Journal of Applied Mechanics*, 29:567–578, 1962.

[23] T.J. Balk. Personal communication.

[24] T.J. Balk, G. Dehm, and E. Arzt. Observations of dislocation motion and stress inhomogeneities in thin copper films. *Mat. Res. Soc. Symp. Proc.*, 673:2.7.1–2.7.6, 2001.

[25] T.J. Balk, G. Dehm, and E. Arzt. Parallel glide: Unexpected dislocation motion parallel to the substrate in ultrathin copper films. *Acta Mat.*, 51:4471–4485, 2003.

[26] M.I. Baskes. Embedded-atom method: Derivation and application to impurities, surfaces and other defects in metals. *Phys. Rev. B*, 29(12):6443–6543, 1984.

[27] A. Boresi and K.P. Chong. *Elasticity in Engineering Mechanics*. Wiley-Interscience, New York, 2nd edition, 2000.

[28] M. Born and K. Huang. *Dynamical Theories of Crystal Lattices*. Clarendon, Oxford, 1956.

[29] K.B. Broberg. *Cracks and Fracture*. Academic Press, 1990.

[30] K.B. Broberg. Dynamic crack propagation in a layer. *Int. J. Solids Struct.*, 32(6-7):883–896, 1995.

[31] E. Budke, C. Herzig, S. Prokofjev, and L. Shvindlerman. Study of grain-boundary diffusion of Au in copper within $\Sigma 5$ misorientation range in the context of structure of grain boundaries. *Defect and Diffusion Forum*, 156:21–33, 1998.

[32] M.J. Buehler, F.F. Abraham, and H. Gao. Hyperelasticity governs dynamic fracture at a critical length scale. *Nature*, 426:141–146, 2003.

[33] M.J. Buehler, T.J. Balk, H. Gao, and E. Arzt. *Handbook of Theoretical and Computational Nanotechnology*, chapter Constrained grain boundary diffusion in thin copper films. American Scientific Publishers (ASP), 2005.

[34] M.J. Buehler and H. Gao. *Handbook of Theoretical and Computational Nanotechnology*, chapter Ultra-large scale simulations of dynamic materials failure. American Scientific Publishers (ASP), 2005.

[35] M.J. Buehler, A. Hartmaier, F.F. Abraham, and H. Gao. Multi-million atom simulation of work-hardening in ductile metals with multi-body potentials. *To be submitted*.

[36] M.J. Buehler, A. Hartmaier, H. Gao, F.F. Abraham, and M. Duchaineau. Atomic plasticity: Description and analysis of a one-billion atom simulation of ductile materials failure. *In the press: Comp. Meth. in Appl. Mech. and Engrg.*, 2004.

[37] M.J. Buehler, Y. Kong, and H. Gao. Deformation mechanisms of very long single-wall carbon nanotubes subject to compressive loading. *Journal of Engineering Materials and Technology*, 126(3), 2004.

[38] V. Bulatov, F.F. Abraham, L. Kubin, B. Devincre, and S. Yip. Connecting atomistic and mesoscale simulations of crystal plasticity. *Nature*, 391:669–672, 1998.

[39] R. Burridge. Admissible speeds for plain-strain self-similar cracks with friction but lacking cohesion. *Geophys. J. Roy. Astron. Soc.*, 35:439–455, 1973.

[40] R. Car and M. Parrinello. Unified approach for molecular dynamics and density functional theory. *Phys. Rev. Lett.*, 55:2471, 1985.

[41] M.W. Chen, E. Ma, K.J. Hemker, Y. Wang H. Sheng, and C. Xuemei. Deformation twinning in nanocrystalline aluminum. *Science*, 300:1275–1277, 2003.

[42] S. Chen. Personal communication.

[43] S. Chen, M.J. Buehler, and H. Gao. The mode III broberg problem: Supersonic cracking in a stiff strip. *Under submission*.

[44] S. Chen, M.J. Buehler, and H. Gao. Supersonic mode III cracks propagating in a stiff strip embedded in a soft matrix. *Submitted to: Int. J. Fracture*, 2004.

[45] F.J. Cherne, M.I. Baskes, and P.A. Deymier. Properties of liquid nickel: A critical comparison of EAM and MEAM calculations. *Phys. Rev. A*, 65(2):024209, 2002.

[46] F. Cleri, S. Yip, D. Wolf, and S. Philpot. Atomic-scale mechanism of crack-tip plasticity: Dislocation nucleation and crack-tip shielding. *Phys. Rev. Lett*, 79:1309–1312, 1997.

[47] H. H. M. Cleveringa, E. van der Giessen, and A. Needleman. Comparison of discrete dislocation and continuum plasticity predictions for a composite material. *Acta Mater.*, 45:3163–3179, 1997.

[48] H. H. M. Cleveringa, E. van der Giessen, and A. Needleman. A discrete dislocation analysis of mode I crack growth. *J.Mech. Phys. Solids*, 48:1133–1157, 2000.

[49] H.H.M. Cleveringa, E. Van der Giessen, and A. Needleman. A discrete dislocation analysis of bending. *Int. J. of Plasticity*, 15:837–868, 1999.

[50] R.L. Coble. A model for boundary controlled creep in polycrystalline materials. *J. of Applied Physics*, 41:1679–1682, 1963.

[51] T.H. Courtney. *Mechanical behavior of materials.* McGraw-Hill, 1990.

[52] T. Cramer, A. Wanner, and P. Gumbsch. Energy dissipation and path instabilities in dynamic fracture of silicon single crystals. *Phys. Rev. Lett.*, 85:788–791, 2000.

[53] J. Cserti, M. Khantha, V. Vitek, and D.P. Pope. An atomistic study of the dislocation core structures and mechanical-behavior of a model alloy. *Mat. Science and Engrg. A*, 152(1-2):95–102, 1998.

[54] B. deCelis, A.S. Argon, and S. Yip. Molecular-dynamics simulation of crack tip processes in alpha-iron and copper. *J. Appl. Phys.*, 54(9):4864–4878, 1983.

[55] G. Dehm, T.J. Balk, B. von Blanckenhagen, P. Gumbsch, and E. Arzt. Dislocation dynamics in sub-micron confinement: Recent progress in Cu thin film plasticity. *Z. Metallk.*, 93(5):383–391, 2002.

[56] P.M. Derlet, A. Hasnaoui, and H. van Swygenhoven. Atomistic simulations as guidance to experiments. *Scripta Mater.*, 49:629–635, 2003.

[57] C. Eberl. Personal communication.

[58] A.H. England. A crack between dissimilar media. *J. Appl. Mech.*, 32:400–402, 1965.

[59] F. Ercolessi and J.B. Adams. Interatomic potentials from 1st principle-calculations – the force matching method. *Europhys. Lett.*, 28(8):583–588, 1994.

[60] F. Ergodan and G.D. Gupta. On numerical solution of singular integral equations. *Q. Appl. Math.*, 30:525–534, 1972.

[61] F. Ergodan, G.D. Gupta, and T.S. Cook. *Methods of Analysis and Solutions of Crack Problems*, chapter Numerical solution of singular integral equations, pages 168–425. Nordhoff Leyden, 1973.

[62] J.D. Eshelby. Elastic field of a crack extending non-uniformly under general anti-plane loading. *J. Mech. Phys. Solids*, 17(3):177–199, 1969.

[63] J.D. Eshelby. *in: Dislocations in Solids*, volume 1, Ed. F.R.N. Nabarro, page 167. North-Holland Publ. Co., Amsterdam, 1979.

[64] D. Faken and H. Jonsson. Systematic analysis of local atomic structure combined with 3D computer graphics. *Comput. Mater. Sci.*, 2:279, 1994.

[65] M.L. Falk, A. Needleman, and J. Rice. A critical evaluation of cohesive zone models of dynamic fracture. *J. Phys. IV France*, 11:43–50, 2001.

[66] D. Farkas, H. van Swygenhoven, and P. Derlet. Intergranular fracture in nanocrystalline metals. *Phys. Rev. B*, 66:184112, 2002.

[67] R.P. Feynman. *Feynman Lectures On Physics*. Addison-Wesley, 1970.

[68] J.E. Field. Brittle fracture–its study and application. *Contemp. Phys.*, 12:1–31, 1971.

[69] J. Fineberg, S.P. Gross, M. Marder, and H.L. Swinney. Instability and dynamic fracture. *Phys. Rev. Lett.*, 67(4):457–460, 1991.

[70] J. Fineberg, S.P. Gross, M. Marder, and H.L. Swinney. Instability in the propagation of fast cracks. *Phys. Rev. B*, 45(10):5146–5154, 1992.

[71] M.W. Finnis and J.E. Sinclair. A simple empirical n-body potential for transition metals. *Phil. Mag. A*, 50:45–55, 1984.

[72] N.A. Fleck and J.W. Hutchinson. A phenomenological theory for strain gradient effects in plasticity. *J. Mech. Phys. Solids*, 41:1825, 1993.

[73] A.F. Fossum and L.B. Freund. Nonuniformly moving shear crack model of a shallow focus earthquake mechanism. *J. of Geophysical Research*, 80:3343–7, 1975.

[74] S. Fratini, O. Pla, P. Gonzalez, F. Guinea, and E. Louis. Energy radiation of moving cracks. *Phys. Rev. B*, 66(10):104104, 2002.

[75] L.B. Freund. Crack propagation in an elastic solid subjected to general loading, II. nonuniform rate of extension. *J. Mech. Phys. Solids*, 20:141–152, 1972.

[76] L.B. Freund. A simple model of the double cantilever beam crack proapgation specimen. *J. Mech. Phys. Solids*, 25:69–79, 1977.

[77] L.B. Freund. The stability of a dislocation in a strained layer on a substrate. *J. Appl. Mech.*, 54:553–557, 1987.

[78] L.B. Freund. *Dynamic Fracture Mechanics*. Cambridge University Press, ISBN 0-521-30330-3, 1990.

[79] H.J. Frost and M.F. Ashby. *Deformation-mechanism maps*, page 21. Pergamon Press, Oxford, 1st edition, 1982.

[80] H. Gao. Surface roughening and branching instabilities in dynamic fracture. *J. Mech. Phys. Solids*, 41(3):457–486, 1993.

[81] H. Gao. A theory of local limiting speed in dynamic fracture. *J. Mech. Phys. Solids*, 44(9):1453–1474, 1996.

[82] H. Gao. Elastic waves in a hyperelastic solid near its plane-strain equibiaxial cohesive limit. *Philosphical Magazine Letters*, 76(5):307–314, 1997.

[83] H. Gao, Y. Huang, and F.F. Abraham. Continuum and atomistic studies of intersonic crack propagation. *J. Mech. Phys. Solids*, 49:2113–2132, 2001.

[84] H. Gao, Y. Huang, W.D. Nix, and J.W. Hutchinson. Mechanism-based strain gradient plasticity–I. Theory. *J. Mech. Phys. Solids*, 47:1239–1263, 1999.

[85] H. Gao, B. Ji, I.L. Jäger, E. Arzt, and P. Fratzl. Materials become insensitive to flaws at nanoscale: Lessons from nature. *P. Natl. Acad. Sci. USA*, 100(10):5597–5600, 2003.

[86] H. Gao and P. Klein. Numerical simulation of crack growth in an isotropic solid with randomized internal cohesive bonds. *J. Mech. Phys. Solids*, 46(2):187–218, 2001.

[87] H. Gao, Y. Kong, D. Cui, and C.S. Ozkan. Spontaneous insertion of DNA oligonucleotides into carbon nanotubes. *Nano Letters*, 3:471–473, 2003.

[88] H. Gao, L. Zhang, W.D. Nix, C.V. Thompson, and E. Arzt. Crack-like grain boundary diffusion wedges in thin metal films. *Acta Mater.*, 47:2865–2878, 1999.

[89] E. Gerde and M. Marder. Friction and fracture. *Nature*, 413:285, 2001.

[90] T.C. Germann and A.F. Voter. Accelerating molecular dynamics simulations. *Proc. of Comput. Nanosci. and Nanotech.*, ISBN 0-9708275-6-3:140–143, 2002.

[91] A. Girshick, D.G. Pettifor, and V. Vitek. Atomistic simulation of titanium - II. Structure of $1/3 < \overline{1}2\overline{1}0 >$ screw dislocations and slip systems in titanium. *Phil. Mag. A*, 77:999–1012, 1998.

[92] J.E. Gordon. *The new science of strong materials*. Princeton University Press, Princeton, NJ, 1984.

[93] A.A. Griffith. The phenomenon of rupture and flows in solids. *Phil. Trans. Roy. Soc. A*, 221:163–198, 1920.

[94] W. Gropp, W. Lusk, and A. Skjellum. *Using MPI*. MIT Press, 2nd edition, 1999.

[95] P. Gumbsch. Brittle fracture processes modelled on the atomic scale. *Z. Metallkd.*, 87:341–348, 1996.

[96] P. Gumbsch and G.E. Beltz. On the continuum versus atomsitic descriptions of dislocation nucleation and cleavage in nickel. *Model. Sim. Mat. Science and Engr.*, 3(5):597–613, 1995.

[97] P. Gumbsch and H. Gao. Dislocations faster than the speed of sound. *Science*, 283:965–968, 1999.

[98] P. Gumbsch, S.J. Zhou, and B.L. Holian. Molecular dynamics investigation of dynamic crack instability. *Phys. Rev. B*, 55:3445, 1997.

[99] G.F. Guo, W. Yang, and Y. Huang. Supersonic crack growth in a solid of upturn stress-strain relation under anti-plane shear. *J. Mech. Phys. Solids*, 51:1971–1985, 2003.

[100] C.S. Han, H. Gao, Y. Huang, and W.D. Nix. Mechanism-based strain gradient crystal plasticity - I. Theory. *Submitted for publication*.

[101] A. Hartmaier, M.J. Buehler, and H. Gao. A discrete dislocation model of diffusional creep. *Diffusion and Defect Forum*, 224-225:107–128, 2003.

[102] A.J. Haslam, D. Moldovan, S.R. Phillpot, D. Wolf, and H. Gleiter. Combined atomistic and mesoscale simulation of grain growth in nanocrystalline thin films. *Comput. Mat. Science*, 23:15–32, 2003.

[103] A. Hasnaoui, H. van Swygenhoven, and P.M. Derlet. Dimples on nanocrystalline fracture surfaces as evidence for shear plane formation. *Science*, 300(5625):1550–1552, 2003.

[104] J.A. Hauch, D. Holland, M. Marder, and H.L. Swinney. Dynamic fracture in single crystal silicon. *Phys. Rev. Lett.*, 82:3823–2826, 1999.

[105] J.A. Hauch and M. Marder. Energy balance in dynamic fracture, investigated by a potential drop technique. *Int. J. Fract.*, 1-2:133–151, 1998.

[106] P. Heino, H. Häkkinen, and K. Kaski. Molecular-dynamics study of mechanical properties of copper. *Europhysics Letters*, 41:273–278, 1998.

[107] Hellan. Debond dynamics of an elastic strip, I: Timoshenko-beam properties and steady motion. *Int. Journal of Fracture*, 14(1):91–100, 1978.

[108] K. Hellan. *Introduction to Fracture Mechanics*. McGraw-Hill, Inc., 1984.

[109] J.P. Hirth and J. Lothe. *Theory of Dislocations*. Wiley-Interscience, 1982.

[110] R.G. Hoagland, J.P. Hirth, and P.C. Gehlen. Atomic simulation of dislocation core structure and Peierls stress in alkali-halide. *Phil. Mag.*, 34(3):413–439, 1976.

[111] D. Holland and M. Marder. Ideal brittle fracture of silicon studied with molecular dynamics. *Phys. Rev. Lett.*, 80(4):746, 1998.

[112] D. Holland and M. Marder. Cracks and atoms. *Advanced Materials*, 11(10):793, 1999.

[113] J.D. Honeycutt and H.C. Andersen. Molecular dynamics study of melting and freezing of small Lennard-Jones clusters. *J. Phys. Chem.*, 91:4950, 1987.

[114] M.F. Horstemeyer, M.I. Baskes, V.C. Prandtl, J. Philliber, and S. Vonderheid. A multiscale analysis of fixed-end simple shear using molecular-dynamics, crystal plasticity and a macroscopic internal state variable theory. *Model. Sim. Mat. Science and Engr.*, 11:265–386, 2003.

[115] K. Huang. On the atomic theory of elasticity. *Proc. R. Soc. London*, 203:178–194, 2002.

[116] Y. Huang and H. Gao. Intersonic crack propagation–Part I: The fundamental solution. *Journal of Applied Mechanics*, 68:169–175, 2001.

[117] Y. Huang and H. Gao. Intersonic crack propagation–Part II: The suddenly stopping crack. *Journal of Applied Mechanics*, 69:76–79, 2002.

[118] D. Hull and D.J. Bacon. *Introduction to Dislocations*. Butterworth Heinemann, 2002.

[119] D. Hull and P. Beardmore. Velocity of propagation of cleavage cracks in Tungsten. *In. J. Fract.*, 2:468–488, 1966.

[120] G.R. Irwin. Fracture dynamics. *in: Fracturing of Metals*, pages 147–166, 1948.

[121] K.W. Jacobsen and J. Schiotz. Computational materials science - nanoscale plasticity. *Nature materials*, 1:15–16, 2002.

[122] I. Kaur and W. Gust. *Handbook of Grain and Interface Boundary Diffusion Data*. Ziegler Press, Stuttgart, 1989.

[123] E. Kaxiras. Personal communication.

[124] P. Keblinski, D. Wolf, S.R. Phillpot, and H. Gleiter. Continuous thermodynamic-equilibrium glass transition in high energy grain boundaries? *Phil. Mag. Letters*, 76(3):143–151, 1997.

[125] P. Keblinski, D. Wolf, S.R. Phillpot, and H. Gleiter. Self-diffusion in high-angle fcc metal grain boundaries by molecular dynamics simulation. *Phil. Mag. Letters*, 79(11):2735–2761, 1999.

[126] C. Kelchner, S.J. Plimpton, and J.C. Hamilton. Dislocation nucleation and defect structure during surface-intendation. *Phys. Rev. B*, 58:11085–11088, 1998.

[127] R.-M. Keller, S. P. Baker, and E. Arzt. Stress-temperature behavior of unpassivated thin copper films. *Acta Materialia*, 47(2):415–426, 1999.

[128] C. Kittel. *Einführung in die Festkörperphysik*. Oldenburg, München, 2nd edition, 1999.

[129] P. Klein and H. Gao. Crack nucleation and growth as strain localization in a virtual-bond continuum. *Engineering Fracture Mechanics*, 61:21–48, 1998.

[130] P.A Klein, J.W. Foulk, E.P. Chen, S.A. Wimmer, and H.J. Gao. Physics-based modeling of brittle fracture: Cohesive formulations and the application of meshfree methods. *Theoretical and Applied Fracture Mechanics*, 37:99–166, 2001.

[131] M.J. Kobrinsky, G. Dehm, C.V. Thompson, and E. Arzt. Effects of thickness on the characteristic length scale of dislocation plasticity in Ag thin films. *Acta Materialia*, 49:3597, 2001.

[132] M.J. Kobrinsky and C.V. Thompson. The thickness dependence of the flow stress of capped and uncapped polycrystalline Ag thin films. *Appl. Phys. Letts.*, 73:2429–2431, 1998.

[133] M.J. Kobrinsky and C.V. Thompson. Activation volume for inelastic defomration in polycrystalline Ag thin films. *Acta Materialia*, 48:625, 2000.

[134] S. Kohlhoff, P. Gumbsch, and H.F. Fischmeister. Crack propagation in b.c.c. crystals studied with a combined finite-element and atomistic model. *Phil. Mag. A*, 64:851–878, 1991.

[135] R. Komanduri, N. Chandrasekaran, and L.M. Raff. Molecular dynamics (MD) simulations of uniaxial tension of some single-crystal cubic metals at nanolevel. *Int. J. Mech. Sciences*, 43:2237–2260, 2001.

[136] L. P. Kubin, G. Canova, M. Condat, B. Devincre, V. Pontikis, and Y. Bréchet. Dislocation microstructures and plastic flow: A 3D simulation. *Solid State Phenomena*, 23&24:455–472, 1992.

[137] L. P. Kubin, B. Devincre, G. Canova, and Y. Bréchet. 3-D simulations of dislocations and plasticity. *Key Engineering Materials*, 103:217–226, 1995.

[138] H. Kuppers. The initial course of crack velocity in glass plates. *Int. J. of Fracture Mechanics*, 3:13–17, 1969.

[139] P. Lagarde and M. Biscondi. Intercrystalline creep of oriented copper bicrystals. *Mem. Etud. Sci. Rev. Met.*, 71:121–131, 1974.

[140] A. Laioa and M. Parrinello. Escaping free-energy minima. *P. Natl. Acad. Sci. USA*, 99:12562–12566, 2002.

[141] J. Lambros and A.J. Rosakis. Development of a dynamic decohesion criterion for subsonic fracture of the interface between two dissimilar materials. *Proc. Roy. Soc. Lond. A*, 41:711–736, 1995.

[142] E.H. Lee. Elastic-plastic deformation at finite strains. *Journal of Applied Mechanics*, 1:1, 1969.

[143] M. Legros, K.J. Hemker, A. Gouldstone, S. Suresh, R.-M. Keller-Flaig, and E. Arzt. Microstructural evolution in passivated Al films on Si substrates during thermal cycling. *Acta Materialia*, 50:3435–3452, 2002.

[144] C. Liu, Y. Huang, and A.J. Rosakis. Shear dominated transonic interfacial crack growth in a bimaterial–II. Asymptotic fields and favorable velocity regimes. *J. Mech. Phys. Solids*, 43(2):189–206, 1993.

[145] C. Liu, J. Lambros, and A.J. Rosakis. Highly transient elastodynamic crack growth in a bimaterial interface: higher order asymptotic analysis and experiments. *J. Mech. Phys. Solids*, 41:1887–1954, 1993.

[146] L. Lu, Y. Shen, X. Chen, L. Qian, and K. Lu. Ultrahigh strength and high electrical conductivity in copper. *Science*, 304:422–426, 2004.

[147] R. Madec, B. Devincre, L. Kubin, T. Hoc, and D. Rodney. The role of collinear interaction in dislocation-induced hardening. *Science*, 301:1879–1882, 2003.

[148] M. Marder. Molecular dynamics of cracks. *Computing in Science and Engineering*, 1(5):48–55, 1999.

[149] M. Marder and J. Fineberg. How things break. *Phys. Today*, 49(9):24–29, 1996.

[150] M. Marder and S. Gross. Origin of crack tip instabilities. *J. Mech. Phys. Solids*, 43(1):1–48, 1995.

[151] J.E. Marsden and T.J.R. Hughes. *Mathematical Foundations of Elasticity*. Prentice Hall, Englewood Cliffs, New Jersey, 1983.

[152] D. Marx and J. Hutter. *Ab-initio* molecular dynamics: Theory and implementation. *Modern Methods and Algorithms in Quantum Chemistry, Forschungzentrum Jülich, NIC Series*, 1, 2000.

[153] R. Mikulla, J. Roth, and H.-R. Trebin. Simulation of shear-stress in 2-dimensional decagonal quasi-crystals. *Phil. Mag. B*, 71(5), 1995.

[154] R. Mikulla, J. Stadler, F. Krul, H.-R. Trebin, and P. Gumbsch. Crack propagation in quasicrystals. *Phys. Rev. Lett.*, 81(15), 1998.

[155] Y. Mishin, M.J. Mehl, D.A. Papaconstantopoulos, A.F. Voter, and J.D. Kress. Structural stability and lattice defects in copper: *Ab-initio*, tight-binding and embedded-atom calculations. *Phys. Rev. B*, 63:224106, 2001.

[156] Williams M.L. The stresses areound a fault or crack in dissimilar media. *Bull. Seismol. Soc. America*, 49:199–204, 1959.

[157] D. Moldovan, D.Wolf, S.R. Phillpot, and A.J. Haslam. Mesoscopic simulation of two-dimensional grain growth with anisotropic grain-boundary properties. *Phil. Mag. A*, 82(7):1271–1297, 2002.

[158] F. Montalenti, M.R. Sorensen, and A.F. Voter. Closing the gap between experiment and theory: Crystal growth by temperature accelerated dynamics. *Phys. Rev. Lett.*, 87(12):126101, 2001.

[159] F. Montalenti, A.F. Voter, and R. Ferrando. Spontaneous atomic shuffle in flat terraces: Ag(100). *Phys. Rev. B*, 66:205404, 2002.

[160] P.M. Morse. Diatomic molecules according to the wave mechanics. II-vibrational levels. *Phys. Rev.*, 34:57–64, 1929.

[161] T. Mura. *Micromechanics of Defects in Solids*. Martinus Nijhoff, Dordrecht, 19887.

[162] F.R.N. Nabarro. In: *Report of a conference on strength of solids*, pages 75–90. London: Phys. Soc., 1948.

[163] A. Nakano, M.E. Bachlechner, R.K. Kalia, E. Lidorikis, P. Vashishta, and G.Z. Voyiadijs. Multiscale simulation of nanosystems. *Comp. in Science and Engrg.*, pages 56–66, 2001.

[164] T. D. Nguyen, S. Govindjee, P.A. Klein, and H. Gao. A rate-dependent cohesive continuum model for the study of crack dynamics. *In the press: Computer Meth. in Appl. Mech. and Engrg.*, 2003.

[165] L. Nicola, E. Van der Giessen, and A. Needleman. Discrete dislocation analysis of size effects in thin films. *J. Appl. Phys.*, 93:5920–5928, 2003.

[166] T.G. Nieh and J. Wadsworth. Hall-Petch relation in nanocrystalline solids. *Scripta Met.*, 25(4), 1991.

[167] W.D. Nix. Mechanical properties of thin films. *Metall. Trans. A*, 20:2217–2245, 1989.

[168] W.D. Nix. Yielding and strain hardening of thin metal films on substrates. *Scripta Materialia*, 39:545–554, 1998.

[169] W.D. Nix. Yielding and strain hardening of thin metal films on substrates. *Scripta Mater.*, 39:545–554, 2001.

[170] R.W. Ogden. *Nonlinear Elastic Deformations*. Wiley and Sons, New York, 1984.

[171] R.E. Peierls. The size of a dislocation. *Proc. Pys. Soc.*, 52:256, 1940.

[172] P.J. Petersan, D. Robert, M. Deegan, M. Marder, and H.L. Swinney. Cracks in rubber under tension break the shear wave speed limit. *To appear in Phys. Rev. Letters, preprint available at: http://arxiv.org/abs/cond-mat/0311422.*

[173] S. Plimpton. Fast parallel algorithms for short-range molecular-dynamics. *Journal of Computational Physics*, 117:1–19, 1995.

[174] Y. Qi, A. Strachan, T. Cagin, and W.A. Goddard III. Large-scale atomistic simulations of screw dislocation structure, annihilation and cross-slip in FCC Ni. *Mat. Science and Engrg A*, 145:309–310, 2001.

[175] A. Rahman. Correlations in the motions of atoms in liquid Argon. *Phys. Rev.*, 136:A405A411, 1964.

[176] K. Ravi-Chandar. Dynamic fracture of nominally brittle materials. *International Journal of Fracture*, 90:83–102, 1998.

[177] J.R. Rice. Elastic fracture mechanics concepts for interfacial cracks. *Transactions of the ASME*, 55(1):98–103, 1988.

[178] J.R. Rice. Dislocation nucleation from a crack: an analysis based on the Peierls concept. *J. Mech. Phys. Solids*, 40:239–271, 1992.

[179] J.R. Rice and G.B. Beltz. The activation energy for dislocation nucleation at a crack. *J. Mech. Phys. Solids*, 42:333–360, 1994.

[180] J.R. Rice and G.C. Sih. Plane problems of cracks in dissimilar media. *Transactions of the ASME*, 32(2):418–423, 1965.

[181] J.R. Rice and R.M. Thomson. Ductile versus brittle behavior of crystals. *Phil. Mag.*, 29:73–97, 1974.

[182] A.J. Rosakis. Intersonic crack propagation in bimaterial systems. *J. Mech. Phys. Solids*, 6(10):1789–1813, 1998.

[183] A.J. Rosakis. Intersonic shear cracks and fault ruptures. *Advances in Physics*, 51(4):1189–1257, 2002.

[184] A.J. Rosakis, O. Samudrala, and D. Coker. Cracks faster than the shear wave speed. *Science*, 284(5418):1337–1340, 1999.

[185] J. Roth, F. Gähler, and H.-R. Trebin. A molecular dynamics run with 5.180.116.000 particles. *Int. J. Mod. Phys. C*, 11:317–322, 2000.

[186] C.L. Rountree, R.K. Kalia, E. Lidorikis, A. Nakano, L. van Brutzel, and P. Vashishta. Atomistic aspects of crack propagation in brittle materials: Multimillion atom molecular dynamics simulations. *Annual Rev. of Materials Research*, 32:377–400, 2002.

[187] G.D. Schaaf, J. Roth, and H.-R. Trebin. Dislocation motion in icosahedral quasicrystals at elevated temperatures: Numerical simulation. *Phil. Mag.*, 83(21), 2003.

[188] J. Schiotz, D. DiTolla, and K.W. Yacobsen. Softening of nanocrystalline metals at very small grain sizes. *Nature*, 391:561–563, 1998.

[189] J. Schiotz, T. Leffers, and B.N. Singh. Dislocation nucleation and vacancy formation during high-speed deformation of fcc metals. *Phil. Mag. Lett.*, 81:301–309, 2001.

[190] J. Schiotz, T. Vegge, D. DiTolla, and K.W. Yacobsen. Atomic-scale simulations of the mechanical deformation of nanocrystalline metals. *Phys. Rev. B*, 60:11971–11983, 1999.

[191] G. Schoeck. Dislocation emission from crack tips as a variational problem of the crack energy. *J. Mech. Phys. Solids*, 44(3):413–437, 1996.

[192] K.W. Schwarz. Simulation of dislocations on the mesoscopic scale. I. methods and examples, II. application to strained-layer relaxation. *J. Appl. Phys.*, 85:108–129, 1999.

[193] A. Sharma, R.K. Kalia, and P. Vashishta. Large multidimensional data vizualization for materials science. *Comp. in Science and Engrg.*, pages 26–33, 2003.

[194] E. Sharon and J. Fineberg. Confirming the continuum theory of dynamic brittle fracture for fast cracks. *Nature*, 397:333, 1999.

[195] Y.-L. Shen. Strength and interface-constrained plasticity in thin metal films. *J. Mater. Res.*, 18:2281–2284, 2003.

[196] V. Shenoy, R. Miller, E.B. Tadmor, D. Rodney, R. Phillips, and M. Ortiz. An adaptive methodology for atomic scale mechanics - the quasicontinuum method. *J. Mech. Phys. Sol.*, 73:611–642, 1999.

[197] V.B. Shenoy, R. Miller, E.B. Tadmor, R. Phillips, and M. Ortiz. Quasicontinuum models of interfacial structure and deformation. *Phys. Rev. Lett.*, 80:742, 1998.

[198] J.Y. Shu and N.A. Fleck. The prediction of a size effect in micro-indentation. *Int. J. of Solids and Structures*, 35:1363–1383, 1998.

[199] L.I. Slepyan. *Models and Phenomena in Fracture Mechanics*. Springer, Berlin, 2002.

[200] V.P. Smyshlyaev and N.A. Fleck. The role of strain gradients in the grain size effect for polycrystals. *J. Mech. Phys. Solids*, 44:465–495, 1996.

[201] R. Spolenak, N. Tamura, B. Valek, R. S. Celestre, A.A. MacDowell, T. Marieb, H. Fujimoto, W.L. Brown, J. C. Bravman, H.A. Padmore, B.W. Batterman, and J. R. Patel. Local plasticity of Al thin films as revealed by X-ray microdiffraction. *Phys. Rev. Lett.*, 90:096102, 2003.

[202] M. Springborg. *Density-functional methods in chemistry and materials science*. Wiley research series in Theoretical Chemistry, 1997.

[203] J. Stadler, R. Mikulla, and H.-R. Trebin. Imd: A software package for molecular dynamics studies on parallel computers. *Int. J. Mod. Phys. C*, 8:1131–1140, 1997.

[204] F. Stillinger and T.A. Weber. Computer-simulation of local order in condensed phases of silicon. *Phys. Rev. B*, 31(8):5262–5271, 1985.

[205] Z. Suo and J.W. Hutchinson. Steady-state cracking in brittle substrates beneath adherent films. *Int. J. of Solids and Structures*, 25(11):1337–1353, 1989.

[206] J.G. Swadener, M.I. Baskes, and M. Nastasi. Molecular dynamics simulation of brittle fracture in silicon. *Phys. Rev. Lett.*, 89(8):085503, 2002.

[207] W.C. Swope, H.C. Andersen, P.H. Berens, and K.R. Wilson. A computer-simulation method for the calculation of equilibrium-constants for the formation of physical clusters of molecules - application to small water clusters. *J. Chem. Phys.*, 76(1):637–649, 1982.

[208] E.B. Tadmor, M. Ortiz, and R. Phillips. Quasicontinuum analysis of defects in solids. *Phil. Mag. A*, 73:1529, 1996.

[209] G.I. Taylor. Mechanism of plastic deformation in crystals. *Proc. Roy. Soc. A*, 145:362, 1934.

[210] J. Tersoff. Empirical interatomic potentials for carbon, with applications to amorphous carbon. *Phys. Rev. Lett.*, 61(25):2879–2883, 1988.

[211] H.-R. Trebin, R. Mikulla, J. Stadler, G. Schaaf, and P. Gumbsch. Molecular dynamics simulations of crack propagation in quasicrystals. *Computer Physics Communications*, 121-122, 1999.

[212] D.H. Tsai. Virial theorem and stress calculation in molecular-dynamics. *J. of Chemical Physics*, 70(3):1375–1382, 1979.

[213] B.P. Uberuaga, S.J. Stuart, and A.F. Voter. Introduction to the time scale problem. *Proc. of Comput. Nanosci. and Nanotech.*, ISBN 0-9708275-6-3:128–131, 2002.

[214] B. van Beest, G. Kramer, and R. van Santen. Force-fields for silicas and aluminophosphates based on *ab-initio* calculations. *Phys. Rev. Lett.*, 64(16):1955, 1990.

[215] H. van Swygenhoven and A. Caro. Plastic behavior of nanophase metals studied by molecular dynamics. *Phys. Rev. B*, 58:11246–11251, 1998.

[216] H. van Swygenhoven and P.M. Derlet. Grain-boundary sliding in nanocrystaline fcc metals. *Phys. Rev. B*, 64:224105, 2001.

[217] H. van Swygenhoven, P.M. Derlet, and A. Hasnaoui. Atomic mechanism for dislocation emission from nanosized grain boundaries. *Phys. Rev. B*, 66:024101, 2002.

[218] H. van Swygenhoven, M. Spaczer, and A. Caro. Microscopic description of plasticity in computer generated metallic nanophase samples: A comparison between Cu and Ni. *Acata Mat.*, 47:3117, 1999.

[219] H. van Swygenhoven, M. Spaczer, A. Caro, and D. Farkas. Competing plastic deformation mechanisms in nanophase metals. *Phys. Rev. B*, 60:22–25, 1999.

[220] P. Vashishta, R.K. Kalia, and A. Nakano. Large-scale atomistic simulations of dynamic fracture. *Comp. in Science and Engrg.*, pages 56–65, 1999.

[221] P. Vashishta, R.K. Kalia, and A. Nakano. Multimillion atom molecular dynamics simulations of nanostructures on parallel computers. *Journal of Nanoparticle Research*, 5:119–135, 2003.

[222] R. P. Vinci, E. M. Zielinski, and J. C. Bravman. Thermal strain and stress in copper thin films. *Thin Solid Films*, 262:142–153, 1995.

[223] B. von Blanckenhagen, P. Gumbsch, and E. Arzt. Dislocation sources in discrete dislocation simulations of thin film plasticity and the Hall-Petch relation. *Modelling Simul. Mater. Sci. Eng.*, 9:157–169, 2001.

[224] B. von Blanckenhagen, P. Gumbsch, and E. Arzt. Dislocation sources and the flow stress of polycrystalline thin metal films. *Phil. Mag. Lett.*, 83:1–8, 2003.

[225] A.F. Voter. *Intermetallic Compounds: Principles and Applications,*, chapter The embedded-atom model, page 7790. New York: Wiley.

[226] A.F. Voter. Hyperdynamics: Accelerated molecular dynamics of infrequent events. *Phys. Rev. Lett.*, 78(20):3908–3911, 1997.

[227] A.F. Voter. Parallel replica method for dynamics of infrequent events. *Phys. Rev. B*, 57(22):985–988, 1998.

[228] A.F. Voter and S.P. Chen. Accurate interatomic potentials for Ni, Al and Ni_3Al characterization of defects. *Materials Res. Soc. Symp. Proc.*, 82:175180, 1987.

[229] A.F. Voter, F. Montalenti, and T.C. Germann. Extending the time scale in atomistic simulation of materials. *Ann. Rev. Mat. Res.*, 32:321–346, 2002.

[230] B.Q. Vu and V.K. Kinra. Britle fracture of plates in tension – static field radiated by a suddenly stopping crack. *Engrg. Fracture Mechanics*, 15(1-2):107–114, 1981.

[231] N.J. Wagner, B.L. Holian, and A.F. Voter. Molecular-dynamics simulation of two-dimensional materials at high strain rates. *Phys. Rev. A*, 45:8457–8470, 1992.

[232] P.D. Washabaugh and W.G. Knauss. A reconcilation of dynamic crack velocity and rayleigh-wave speed in isotropic brittle solids. *Int. J. Fracture*, 65:97–114, 1994.

[233] J.J. Weiner. Hellmann-Feynmann theorem, elastic moduli, and the cauchy relation. *Phys. Rev. B*, 24:845–848, 1983.

[234] D. Weiss, H. Gao, and E. Arzt. Constrained diffusional creep in UHV-produced copper thin films. *Acta mater.*, 49:2395–2403, 2001.

[235] D. Wolf, V. Yamakov, S.R. Phillpot, and A.K. Mukherjee. Deformation mechanism and inverse Hall-Petch behavior in nanocrystalline materials. *Z. Metallk.*, 94:1052–1061, 2003.

[236] R. Würschum, S. Herth, and U. Brossmann. Diffusion in nanocrystalline metals and alloys–a status report. *Adv. Engrg. Mat.*, 5(5):365–372, 2003.

[237] K.W. Yacobsen, K.S., and M.J. Puska. Interatomic interactions in the effective-medium theory. *Phys. Rev. B*, 35(14):7423, 1987.

[238] K.W. Yacobsen, P. Stoltze, and J.K. Norskov. A semi-empirical effective medium theory for metals and alloys. *Surf. Sci.*, 366:394, 1996.

[239] B.I. Yakobson, C.J. Brabec, and J. Bernholc. Nanomechanics of carbon tubes: Instabilities beyond linear response. *Phys. Rev. Lett.*, 76(14):2511–2514, 1996.

[240] V. Yamakov, D. Wolf, S.R. Phillpot, and H. Gleiter. Grain-boundary diffusion creep in nanocrystalline palladium by molecular-dynamics simulation. *Acta mater.*, 50:61–73, 2002.

[241] V. Yamakov, D. Wolf, S.R. Phillpot, and H. Gleiter. Deformation mechanism crossover and mechanical behaviour in nanocrystalline materials. *Phil. Mag. Lett.*, 83:385–393, 2003.

[242] V. Yamakov, D. Wolf, S.R. Phillpot, A.K. Mukherjee, and H. Gleiter. Dislocation proceses in the deformation of nanocrystalline aluminium by MD simulation. *Nature Materials*, 1:1–4, 2002.

[243] V. Yamakov, D. Wolf, M. Salazar, S.R. Phillpot, and H. Gleiter. Length scale effects in the nucleation of extended dislocations in nanocrystalline Al by molecular-dynamics simulations. *Acta mater.*, 49:2713–2722, 2001.

[244] W. Yang, Z. Suo, and C.F. Shih. Mechanics of dynamic debonding. *Proc. Roy. Soc. Lond. A*, 433:679–697, 1991.

[245] S. Yip. The strongest size. *Nature*, 391:532–533, 1998.

[246] E.H. Yoffe. The moving griffith crack. *Phil. Mag.*, 42:739–750, 1951.

[247] H.H. Yu and Z. Suo. Intersonic crack growth on an interface. *P. Royal Society London A Mat.*, 456(1993):223–246, 2000.

[248] A.R. Zak and M.L. Williams. Crack point singularities at a bi-material interface. *J. Appl. Mech.*, 30:142–143, 1963.

[249] H.F. Zhang and A.H.W. Ngan. Atomistic simulation of screw dislocation mobility ahead of a mode III crack tip in the bcc structure. *Scripta Materialia*, 41(7):737–742, 2002.

[250] L. Zhang. *A class of strongly coupled elasticity and diffusion problems in thin metal films*. PhD thesis, Stanford University, Stanford, CA, 2001.

[251] L. Zhang and H. Gao. Coupled grain boundary and surface diffusion in a polycrystalline thin film constrained by substrate. *Z. Metallk.*, 93:417–427, 2002.

[252] P. Zhang, P. Klein, Y. Huang, and H. Gao. Numerical simulation of cohesive fracture by the virtual-internal-bond model. *Computer Modeling in Engineering and Sciences*, 3(2):263–277, 1998.

[253] M. Zhou. Equivalent continuum for dynamically deforming atomistic particle systems. *Phil. Mag. A*, 82(13), 2002.

[254] S.J. Zhou, D.M. Beazly, P.S. Lomdahl, and B.L. Holian. Large-scale molecular-dynamics simulations of three-dimensional ductile failure. *Phys. Rev. Lett.*, 78:479–482, 1997.

[255] S.J. Zhou, D.L. Preston, P.S. Lomdahl, and D.M. Beazley. Large-scale molecular-dynamics simulations of dislocation interactions in copper. *Science*, 279:1525–1527, 1998.

[256] S.J. Zhou, P.S. Lomdahl R. Thomson, and B.L. Holian. Dynamic crack processes via molecular-dynamics. *Phys. Rev. Letters 76*, 55:3445, 1996.

[257] J.A. Zimmerman, H. Gao, and F.F. Abraham. Generalized stacking fault energies for embedded atom FCC metals. *Modelling Simul. Mater. Sci. Eng.*, 8:103–115, 2000.

[258] J.A. Zimmerman, C.L. Kelchner, P.A. Klein, J.C. Hamilton, and S.M. Foiles. Surface step effects on nanoindentation. *Phys. Rev. Lett.*, 87(16):165507, 2001.

[259] J.A. Zimmerman, E.B. Webb, J.J. Hoytz, R.E. Jonesy, P.A. Klein, and D.J. Bammann. Calculation of stress in atomistic simulation. *In the press: Model. Sim. Mat. Science and Engr.*, 2004.

[260] J.A. Zimmermann. *Continuum and atomistic modeling of dislocation nucleation at crystal surface ledges*. PhD thesis, Stanford University, 1999.

Part V.

Appendix

A. Virial stress and strain

Definitions of virial stress [212, 253, 259] and strain [260] allow a coupling of the atomistic scale with continuum theories [212, 253]. The correct coupling of quantities like stress or strain still remains an important issue in research. With its limitations understood, the expressions of stress and strain allow for an immediate comparison of the different levels of detail.

A.1. Virial stress

The virial stress is given by [212, 253]

$$\sigma_{ij} = \frac{1}{2} \sum_{\alpha,\beta} \left(-\frac{1}{r} \frac{\partial \phi}{\partial r} r_i r_j \mid_{r=r_{\alpha\beta}} \right) \tag{A.1}$$

where r_i is the projection of the interatomic distance vector $\mathbf{r}$ along coordinate i. We only consider the force part, excluding the part containing the effect of the velocity of atoms (the kinetic part). It was recently shown [253] that the stress including the kinetic contribution is not equivalent to the mechanical Cauchy stress.

The virial stress needs to be averaged over space and time to converge to the Cauchy stress tensor. For further discussion on the virial stress and other definitions of the Cauchy stress tensor (e.g. the Hardy stress) see [259].

A.2. Virial strain

The strain field is a measure of geometric deformation of the atomic lattice [260]. The local atomic strain is calculated by comparing the local deviation of the lattice from a reference configuration. Usually, the reference configuration is taken to be the undeformed lattice. In the atomistic simulations, the information about the position of every atom is readily available, either in the current or in the reference configuration and thus calculation of the virial strain is relatively straightforward.

We define the following tensor for atom l

$$q_{ij}^{l} = \frac{1}{N} \sum_{k=1}^{N} \left(\frac{\Delta x_i^{kl} \Delta x_j^{kl}}{r_0^2} \right), \tag{A.2}$$

were $\Delta x_i^{kl} = x_i^l - x_i^k$ and $\Delta x_j = x_j^l - x_j^k$. The quantity N refers to the number of nearest neighbors considered. The left Cauchy-Green strain tensor is given by

$$b_{ij}^{l} = \frac{N}{\lambda} q_{ij}^{l} = \frac{1}{\lambda} \sum_{k=1}^{N} \left(\frac{\Delta x_i^{kl} \Delta x_j^{kl}}{r_0^2} \right), \tag{A.3}$$

where λ is a prefactor depending on the lattice considered. For a two-dimensional, triangular lattice with nearest neighbor interaction $\lambda = 3$, $\lambda = 2$ for a square lattice with nearest neighbor interaction and $\lambda = 4/3$ for a face-centered cubic lattice.

This definition provides an expression for a measure of deformation defined using continuum mechanics and in terms of atomic positions. The Eulerian strain tensor of atom l is obtained from equation (A.3), $e_{ij}^{l} = \frac{1}{2}\left(\delta_{ij} - b_{ij}^{l}\right)$. One can calculate the engineering strain $\underline{\boldsymbol{\varepsilon}} = \sqrt{\underline{\boldsymbol{b}}} - \underline{\mathbf{1}}$. Unlike the virial stress, the atomic strain is valid instantaneously in space and time. However, the expression is only strictly applicable away from surfaces and interfaces.

B. Asymptotic stress field near a rapidly propagating mode I crack

The functions $\Sigma_{ij}(\Theta, v)$ that appear in equation (6.1) are defined as follows [78].

$$\Sigma_{11}(\Theta, v) = \frac{1}{D}\left\{(1+\alpha_s^2)(1+2\alpha_l^2-\alpha_s^2)\frac{\cos(1/2\Theta_l)}{\sqrt{\gamma_l}} - 4\alpha_s\alpha_l\frac{\cos(1/2\Theta_s)}{\sqrt{\gamma_s}}\right\}, \tag{B.1}$$

$$\Sigma_{12}(\Theta, v) = \frac{2\alpha_l(1+\alpha_s)^2}{D}\left\{\frac{\sin(1/2\Theta_l)}{\sqrt{\gamma_l}} - \frac{\sin(1/2\Theta_s)}{\sqrt{\gamma_s}}\right\}, \tag{B.2}$$

and

$$\Sigma_{22}(\Theta, v) = -\frac{1}{D}\left\{(1+\alpha_s^2)^2\frac{\cos(1/2\Theta_l)}{\sqrt{\gamma_l}} - 4\alpha_d\alpha_s\frac{\cos(1/2\Theta_s)}{\sqrt{\gamma_s}}\right\}. \tag{B.3}$$

Further,

$$\gamma_l = \sqrt{1-(v\sin(\Theta_l/c_l)^2)}, \tag{B.4}$$

$$\tan(\Theta_l) = \alpha_l \tan\Theta, \tag{B.5}$$

$$\gamma_s = \sqrt{1-(v\sin(\Theta_s/c_s)^2)}, \tag{B.6}$$

and

$$\tan(\Theta_s) = \alpha_s \tan\Theta. \tag{B.7}$$

The two factors α_s and α_l are defined as

$$\alpha_s = \sqrt{1-v^2/c_s^2} \tag{B.8}$$

and

$$\alpha_l = \sqrt{1-v^2/c_l^2}. \tag{B.9}$$

The asymptotic stress field in the vicinity of a dynamic crack depends *only* on the ratio of crack speed to the wave velocities in the solid. Similar expressions for the asymptotic field have also been derived for mode II cracks [78].

C. Atomistic simulation procedure for modeling of dynamic fracture

Our simulation tool is classical molecular-dynamics [15] as described in Section 2.3.1. The slab size is chosen large enough such that waves reflected from the boundary do not interfere with the propagating crack.

C.1. Geometry of the model and application of loading

To model weak layers or different interatomic interactions in different regions of the simulation domain, we give atom a virtual type. Based on the type definition of interacting pairs of atoms, we calculate the corresponding interaction. The initial crack is also modeled this way by assuming no atomic interaction. An example for this type decomposition is shown in Figure C.1.

We establish a linear velocity gradient prior to simulation to avoid shock wave generation from the boundaries (see also Figure C.1). To strain the system, we use two approaches. The first is using a constant strain rate applied over a loading time by displacing the outermost rows of atoms (usually we use 10 rows of atoms in the boundary). After the loading time, the boundaries are kept fixed. In the second method, we strain the system prior to simulation in the loading direction, and either keep the boundary fixed during simulation or apply additional loading. In either way, the crack starts to move once a critical strain is applied. The slab is initialized at zero temperature prior to simulation.

The loading in the mode III crack problems is applied in a similar way, with the difference that the atoms in the boundary are moved out and into the plane corresponding to the antiplane shear loading. Similar methods, based on domain decomposition with virtual atom types, are also used in the modeling of thin films.

C.2. Measurement of crack speed

Accurate determination of crack tip velocity is important because we need to be able to measure even smallest changes in the propagation speed. The crack tip position is determined by finding the surface atom with maximum y position in the interior of a search region inside the slab (or, if the crack is oriented in the other direction the atom with maximum x position). This quantity is averaged over a small time interval to eliminate very high frequency fluctuations.

To obtain the steady state velocity of the crack, the measurements are taken within a region of constant stress intensity factor [206]. In addition to checking the velocity

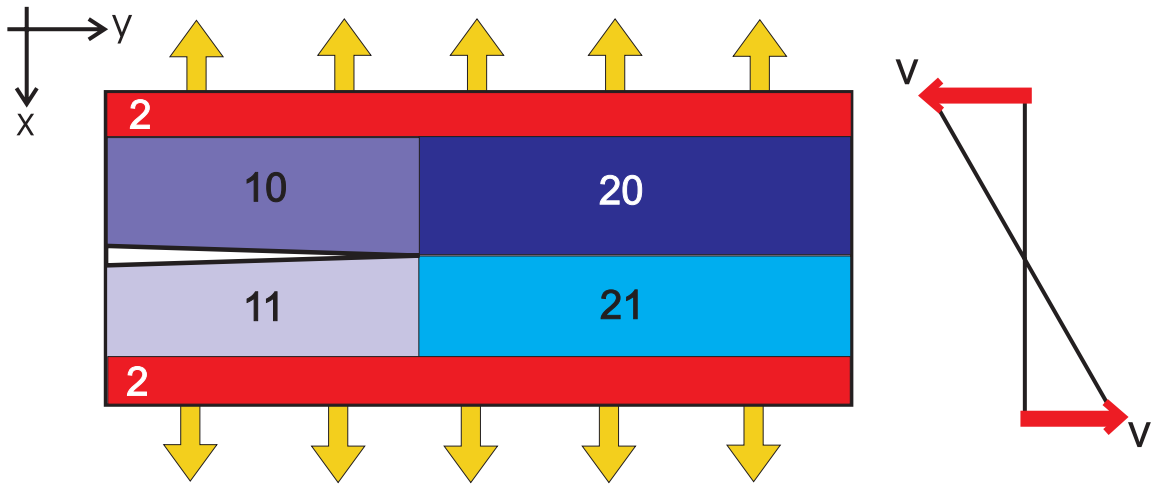

Figure C.1.: Simulation method of domain decomposition via the method of virtual atom types.

history, steady state is verified by path-independency of the energy flux integral.

C.3. Computational method

A FORTRAN molecular-dynamics code parallelized with MPI [94] is used for the simulations. We use the IBM XL FORTRAN Compiler for AIX for compilation of the source code. Most simulations are carried out on IBM Power 4 Regatta nodes in the Max Planck Society Supercomputer Center in Munich. This supercomputer consists of 25 nodes with 32 CPUs each in a shared memory environment, with 64 GByte RAM each. Federation switches are used for internode communication.

Some simulations are carried out on a 84-processor LINUX cluster with INTEL XEON CPUs at the MPI for Metals Research, Stuttgart. The cluster is based on 42 nodes that contain 2 CPUs each, and the nodes are connected via a Gigabit communication network. The total RAM of the system is 42 GByte. We used the PORTLAND GROUP and INTEL C and FORTRAN compilers.

For some of the calculations used in this thesis, we used the ITAP-IMD molecular-dynamics code suitable for large-scale atomistic simulations [185, 203]. This code is written in C and also parallelized with MPI [94].

D. Zusammenfassung (in German)

D.1. Einleitung

Die Kulturgeschichte der Menschheit ist von einem wachsenden Verständnis für Materialien und deren Eigenschaften geprägt. Unsere Vorfahren lernten, aus Stein Faustkeile herzustellen und verbesserten mit diesem neuen Werkzeug ihre Lebensbedingungen entscheidend. Heute ist kaum eine neue technische Errungenschaft ohne moderne Materialwissenschaften möglich. Die Entwicklung der modernen Metallurgie zum Beispiel eröffnete den Weg zu Materialien, die zugleich fest und zäh sind, wie beispielsweise viele Stahllegierungen. Viele technische Systeme enthalten immer kleinere Strukturen, aus der Mikrotechnologie der Halbleiterbranche entwickelt sich allmählich eine Nanotechnologie.

Das wirft die Frage auf, wie solche winzigen Strukturen auf mechanischen Stress reagieren. Wir untersuchen das Materialversagen kleiner Nanokristalle unter extremer Belastung mit Simulationen auf Supercomputern, die einzelne Atome berücksichtigen. Grundlegend wird zwischen zwei Arten von Materialverhalten unterschieden, spröden und duktilen Materialien (siehe Abbildungen 1.1 und 2.2). Spröde Materialien versagen durch die Ausbreitung von Rissen (Beispiel Glas), und duktile Materialien versagen durch die Ausbreitung von Versetzungen und lassen sich meist leicht verformen (Beispiel Kupfer).

In dieser Arbeit sollen verschiedene Aspekte spröden Materialverhaltens sowie das Verhalten von dünnen Schichten aus Kupfer unter mechanischer Belastung untersucht werden.

D.2. Simulationsmethoden

Materialwissenschaftler bezeichnen ein Computermodell, das Materialien bis hinunter zu einzelnen Atome auflöst, als atomistische Simulation. Solche Simulationen haben sich in den vergangen Jahren zu einem unerwartet hilfreichen Werkzeug der Materialwissenschaften entwickelt - nicht zuletzt wegen der rasanten Entwicklung der Supercomputer (siehe Abbildungen 2.1 und 2.2). In solchen Simulationen werden die Newtonschen Bewegungsgleichungen $\mathbf{F} = m\ddot{\mathbf{a}}$ für mehrere Millionen Teilchen gelöst [13, 14, 175, 15, 1, 173].

Die Längen- und Zeitskalen, die wir durch solche "Computerexperimente" studieren können, bleiben bei Mikrostrukturen dem realen Laborexperiment noch weitgehend verschlossen. Das gilt auch für die klassische Lehre von der Verformung von Festkörpern. Diese basiert auf der Kontinuumstheorie, berücksichtigt also nicht einzelne Atome und die Bindungen und Kräfte zwischen ihnen. Klassische Modelle besitzen somit keine in-

ternen Längenskalen, die bei Mikrostrukturen jedoch eine wichtige Rolle spielen können: Sie haben Einfluss darauf, wie das Material bei zu großen mechanischen Spannungen durch Brechen oder Verformen nachgibt. Deshalb sind atomistische Simulationen in solchen Fällen fast der einzige Weg, ein Phänomen des Materialverhaltens grundlegend zu verstehen. Sie erlauben einen fundamentalen Einblick in das Materialverhalten, wie keine andere numerische Methode in der Materialwissenschaft. Um mechanische Eigenschaften zu erforschen, ist es wichtig, dass die simulierten Systeme relativ viele Atome beinhalten. Um Rechnungen mit bis zu 150 Millionen Atomen durchführen zu können, verwenden wir daher klassische Molekulardynamik basierend auf empirischen Potentialen [15, 1].

D.3. Modellierung von sprödem Materialversagen

Atomistische Simulationen stellen aufgrund der Längen- und Zeitskalen eine sehr gut geeignete Methode zur Untersuchung der Rissdynamik dar, denn Risse breiten sich mit einigen Kilometern pro Sekunde in Materialien aus, was einigen Nanometern pro Pikosekunde entspricht (vgl. Abbildung 2.1).

Einige der fundamentalen Aspekte der Rissdynamik sind bis heute überhaupt nicht oder nur unzureichend verstanden. Die wichtigsten Ziele der Arbeit im Bereich der spröden Rissdynamik sind daher:

- Wie können die kontinuumsmechanische Theorie und die atomistische Betrachtungsweise aneinander gekoppelt werden, und wie gut sind die Vorhersagen der Kontinuumstheorie auf atomistischer Ebene?
- Welche Rolle spielen Materialnichtlinearitäten in der Dynamik der Rissausbreitung (vor allem bzgl. der maximal erreichbaren Rissgeschwindigkeit und dynamische Rissinstabilitäten)?
- Wie wirken sich geometrische Einschränkungen auf die Rissdynamik aus (z.B. Grenzflächen oder Risse in sehr dünnen Streifen)?

D.3.1. Ein-dimensionales Modell der Rissdynamik

Wir beginnen die Untersuchungen mit einem einfachen eindimensionalen Modell für dynamische Rissausbreitung, das auf Hellan [107] zurückgeht.

Das eindimensionale Modell der Rissdynamik ist besonders attraktiv, da es erlaubt, einige fundamentale Konzepte der Rissdynamik zu erklären, dabei mathematisch aber recht einfach zu behandeln ist. Außerdem erlaubt es uns, im Gegensatz zu den weit komplizierteren höherdimensionalen Fällen, die Bestimmung einer geschlossenen Lösung für Rissdynamik in nichtlinearen Materialien. Eine wichtige Konsequenz aus dem neu entwickelten nichtlinearen Modell ist, dass Rissausbreitung mit Überschallgeschwindigkeit möglich wird, im Gegensatz zu den klassischen linearen Theorien. Rissausbreitung mit Überschall wird möglich, wenn eine Zone in der Nähe des Risses entsteht, die elastisch härter ist als das umgebende Material und damit eine hohe *lokale* Wellengeschwindigkeit entsteht. Viele Werkstoffe wie Elastomere zeigen ein solches Verhalten.

Der erste Schritt ist die Entwicklung eines atomistischen Modells mit harmonischen Wechselwirkungen zwischen Atomen. Dieses Modell entspricht der linear-elastischen Theorie [107]. Wir zeigen, dass das atomistische Modell die Vorhersagen der Theorie sehr gut widergibt, was in Abbildung 4.5 verifiziert werden kann. Im nächsten Schritt erweitern wir das harmonische atomistische Modell, um Materialnichtlinearitäten zu modellieren. Dies erlaubt es uns, die Spannungs- und Dehnungsfelder in der Nähe eines Risses im nichtlineraren Material mit den Vorhersagen unserer Theorie zu vergleichen. Die Vorhersagen des Modells werden relativ gut von den atomistischen Simulationen wiedergegeben. Die Ergebnisse sind in Abbildung 4.11 dargestellt. Zum ersten Mal war es hier möglich, für Rissausbreitung mit Überschall eine geschlossene Lösung für die Deformationsfelder in der Nähe eines Risses zu finden.

D.3.2. Mechanische Eigenschaften zweidimensionaler Festkörper

Für Risse unter Modus I, Modus II und Modus III Belastung [78] sind zwei- und dreidimensionale atomistische Modelle notwendig. Zunächst konzentrieren wir uns auf die Modellierung von Modus I und Modus II Rissen.

Das Studium der Rissdynamik mit Hilfe atomistischer Simulationen setzt die genaue Kenntnis der mechanischen und physikalischen Eigenschaften der untersuchten Kristalle voraus, sollen die Ergebnisse später mit kontinuumsmechanischen Theorien verglichen werden. Man muss dabei verstehen, wie sich die Wahl des interatomaren Potentials auf mechanische und physikalische Materialeigenschaften auswirkt. Unsere Untersuchungen beziehen sich dabei auf analytische und numerische Methoden, wie schematisch in Abbildung 5.2 dargestellt.

Ein wichtiger Aspekt dieses Teils der Arbeit ist die Entwicklung von "Modellmaterialien". Dabei ist das Ziel nicht die Besonderheiten *eines* bestimmten Werkstoffes zu modellieren, sondern die Eigenschaften einer ganzen *Klasse* von Werkstoffen abzudecken. Die elastischen Eigenschaften für verschiedene Potentiale sind in den Abbildungen 5.3 (LJ), 5.4 (gefaltetes LJ), 5.9 (biharmonisches Potential), 5.5 (harmonisches Potential) und 5.7 sowie 5.8 (harmonisches Potential mit "snapping bonds") gezeigt. Eine detaillierte Analyse des Versagens in verschiedenen Kristallrichtungen liefert wichtige Erkenntnisse bezüglich der Stabilität der Rissausbreitung. Harmonische Potentiale führen zu linear-elastischen Materialeigenschaften, genau so wie sie vielen klassischen Theorien der Rissdynamik zugrunde liegen [78]. Diese Modelle dienen als Referenzsysteme, wobei die anderen nichtlinearen Modellmaterialien dazu verwendet werden um die Änderung der Rissdynamik aufgrund der Variation in den einzelnen Modellen zu studieren. Dadurch lassen sich Erkenntnisse darüber gewinnen, wie sich bestimmte Details der atomistischen Wechselwirkung auf die Dynamik auswirken.

Ferner dient die Berechnung der Rissoberflächenenergie als wichtige Komponente zu Studien der Bedingungen für Rissinitiierung und Risswachstum im Rahmen der Griffith-Theorie der Rissentstehung [93].

D.3.3. Spannungs- und Dehnungsfelder in der Nähe eines Modus I Risses

Hier untersuchen wir, wie die kontinuumsmechanische Theorie und die atomistische Betrachtungsweise aneinander gekoppelt werden können. Unter Verwendung der Konzepte der Virialspannung und der Virialdehnung zeigen wir, dass die Theorie [78] die Deformationsfelder in der Nähe des Risses recht gut vorhersagt. Wir verwenden dabei nur harmonische Potentiale, und eines der Hauptziele dieses Teils der Arbeit ist zu zeigen, dass die linearelastische Theorie die Dynamik und Deformationen gut beschreibt und die Systeme mit harmonischen Wechselwirkungen daher als Referenzsysteme dienen können.

Die Simulationsgeometrie der Simulationen ist in Abbidlung 6.1 dargestellt. Ein Vergleich zwischen Atomistik und kontinuumsmechanischer Theorie ist in den Abbildungen 6.2 bis 6.6 für verschiedene Komponenten des Spannungstensors σ_{ij} gezeigt. In weiteren Untersuchungen haben wir auch die Dehnungsfelder, den Energiefluss, die Dehnungsenergie sowie die Teilchengeschwindigkeit untersucht und gute Übereinstimmung mit der Risstheorie gefunden. Das wichtigste Ergebnis ist, dass die Simulationen mit harmonischen Potentialen und linear-elastischem Verhalten sehr gut durch die linearelastische Kontinuumstheorie beschrieben werden können. In den folgenden Kapiteln werden wir die Stärke der Nichtlinearität schrittweise erhöhen und zeigen, dass die Ergebnisse immer mehr von den Vorhersagen der linearen Theorien abweichen.

D.3.4. Hyperelastizität dominiert die Rissdynamik bei einer kritischen Längenskala

Glas zerbricht, Stahl reißt, Gummi platzt - es gibt vielerlei Arten, wie Materialien bei Überbeanspruchung versagen können. Doch bis heute sind viele der atomaren Ursachen für Materialversagen noch unbekannt. So werden manche Materialien bei großen Dehnungen weich, andere wiederum hart - ein Phänomen, das man als Hyperelastizität bezeichnet.

Das wichtigste Ergebnis der Arbeit ist, dass sich Risse mit Überschallgeschwindigkeit ausbreiten können, wenn Hyperelastizität jenen Bereich um die Rissspitze dominiert, der für den Energietransport wichtig ist. Die Entdeckung dieser neuen und in den bisherigen Theorien bislang fehlenden Längenskala beschreibt jenen Bereich um den Riss, aus dem Energie transportiert werden muss, damit der Riss seine Ausbreitung fortsetzen kann. Diese charakteristische Längenskala ist proportional zur Rissoberflächenenergie und den elastischen Eigenschaften und umgekehrt proportional zum Quadrat der angelegten elastischen Spannung:

$$\chi \sim \frac{\gamma E}{\sigma^2} \tag{D.1}$$

Im Gegensatz zum bisherigen Verständnis ist kein Energietransport von weiter entfernten Regionen zum Riss notwendig, sondern nur von einem kleinen, lokal begrenzten Bereich, der durch die charakteristische Längenskala beschrieben ist! Dieses Skalierungsgesetz wurde durch eine Serie von Simulationen nachgewiesen (Abbildung 7.10).

Unter Anderem haben wir gezeigt, dass sich Modus I Risse mit intersonischen Geschwindigkeiten ausbreiten können (Abbildung 7.6). Diese Ergebnisse stehen in klarem

Widerspruch zur klassischen Theorie [78], nach der die Geschwindigkeit von elastischen Wellen - in Analogie zur Lichtgeschwindigkeit in der Relativitätstheorie - als Höchstgeschwindigkeit für die Rissausdehnung in Materialien gilt. Die Vorhersagen unserer theoretischen Arbeiten [32] wurden kürzlich in Experimenten verifiziert [172]: Dabei wurde ein Modus I Riss in einem hyperelastisch verhärtenden Material mit intersonischer Geschwindigkeit beobachtet.

Die Hyperelastizität dominiert den Energietransport zur Rissspitze, wenn sich die Größe der hyperelastischen Zone der des kritischen Energieflussbereichs nähert. Unter normalen experimentellen Bedingungen sind die Spannungen eine oder zwei Größenordnungen kleiner als in atomistischen Simulationen. In diesen Fällen ist die charakteristische Länge des Energietransports relativ groß, und der Effekt von Hyperelastizität auf die effektive Geschwindigkeit des Energietransports ist klein. Wir haben gezeigt, dass - im Gegensatz dazu - bei nur einem Prozent Dehnung die charakteristische Länge für den Energietransport nur noch einige hundert Atomabstände, also nur einige Dutzend Nanometern groß ist. In diesem Fall treten sofort bedeutende hyperelastische Effekte auf. Von daher vermuten wir, dass Hyperelastizität in nanostrukturierten Materialien wie dünnen Schichten oder bei sehr schnellen Verformungsvorgängen die Rissentwicklung dominiert. Denn in beiden Fällen treten sehr hohe Spannungen auf, so dass die Region, aus der Energie zum Riss fließen muss, relativ klein ist.

D.3.5. Rissinstabilitäten und der Einfluss von Hyperelastizität

In diesem Kapitel geht es um die Beschreibung von Rissinstabilitäten und den Zusammenhang mit Materialnichtlinearitäten. Viele experimentelle und numerische Ergebnisse [5, 70] zeigen eine deutliche Abweichung vom klassischen linearelastischen Model der Rissinstabilität, dem Yoffe Kriterium [246].

Risse breiten sich bei kleinen Geschwindigkeiten gerade aus und zeigen eine perfekte atomar glatte Rissoberfläche. Ab einer gewissen kritischen Geschwindigkeit beginnt die Oberfläche rau zu werden, und der Riss breitet sich nicht mehr strikt gerade aus sondern wächst in einer Zickzack-Bewegung (siehe Abbildung 8.1). Dieses Phänomen wird als dynamische Rissinstabilität bezeichnet.

Es wurde bereits früher vorgeschlagen [5, 81, 82], dass Hyperelastizität eine entscheidende Rolle für die kritische Rissgeschwindigkeit spielt, bei der die Rissinstabilität auftritt. Wir zeigen nun mit Hilfe einer Serie von atomistischen Simulationen, bei der die Potentialeigenschaften systematisch variiert werden, dass Hyperelastizität in der Tat eine bestimmende Rolle spielt. Materialien, die bei großen Dehnungen elastisch weich werden (z.B. Metalle) weisen eine deutlich niedrigere kritische Geschwindigkeit auf, und Materialien, die bei großen Dehnungen elastisch hart werden, breiten sich sogar mit Geschwindigkeiten über die Rayleigh-Wellengeschwindigkeit gerade aus (siehe Abbildung 8.5). Wir erklären diese Phänomene mit Gao's Model der Energieflusslimitierung bei weich werdenden Materialien, und mit Hilfe eines generalisierten Yoffe Kriteriums bei elastisch verhärtenden Stoffen. Diese Behauptung wird durch unsere Simulationsergebnisse untermauert (siehe Abbildungen 8.8, 8.9 und 8.10).

D.3.6. Risse an Grenzflächen

Hier untersuchen wir die Dynamik von Rissen an Grenzflächen von elastisch verschiedenen Materialien. Solche Studien sind sowohl vom Blickwinkel der Geophysik als auch technologisch interessant. In vielen Fällen dienen nämlich gerade die Grenzflächen zwischen Materialien als bevorzugter Risspfad. Nun ist es in solchen Fällen nicht möglich, eine eindeutige Wellengeschwindigkeit zu definieren, da sich die elastischen Eigenschaften und damit auch die Wellengeschwindigkeiten beim Übertritt zwischen den Materialien unstetig verhalten (Geometrie siehe Abbildung 9.1).

Wir konzentrieren uns auf Modus I und Modus II Risse. Ein wichtiges Ergebnis ist die Entdeckung eines Mutter-Tochter Mechanismus bei Modus I Rissen an Grenzflächen. Dabei wird ein Stück vor dem primären Mutterriss ein sekundärer Tochterriss erzeugt, der sich mit Überschallgeschwindigkeit relativ zum weichen Material an der Grenzfläche ausbreitet. Das Phänomen des Mutter-Tochterriss-Mechanismus war bislang nur aus Modus II Rissen bekannt [11]. Die Grenzgeschwindigkeit des Risses ist daher durch die Rayleigh-Wellengeschwindigkeit des elastisch härteren Materials gegeben, und der Riss kann sich mit Überschallgeschwindigkeit relativ zum weichen Material ausbreiten. Bislang wurde angenommen, dass die Rayleigh-Wellengeschwindigkeit des weicheren Materials eine Grenze darstellt. Vorläufige theoretische Überlegungen zeigen, dass solche Phänomene möglich sind [42].

Bei Modus II Rissen an Grenzflächen beobachten wir einen Mutter-Tochter-Enkel-Mechanismus. Die Grenzgeschwindigkeit des Risses ist durch die Longitudinalwellengeschwindigkeit des elastisch härteren Materials gegeben, und der Riss kann sich somit mit Überschallgeschwindigkeit relativ zum weichen Material ausbreiten. Abbildung 9.9 zeigt den Mutter-, Tochter- und Enkelriss. Diese Beobachtung entspricht den Ergebnissen aus experimentellen Arbeiten [182].

D.3.7. Unmittelbar stoppende Risse

Die Dynamik unmittelbar stoppender Risse ist von Interesse bezüglich des Vergleichs von Theorie, Experiment und atomistischer Modellierung.

Das Hauptergebnis dieser Arbeit ist, dass sich Modus I Risse in linear-elastischen Materialien, in Übereinstimmung mit der Theorie [78] und Experimenten [230], wie ein masseloses Teilchen verhalten. Intersonische Modus II Risse, sowie Modus I und Modus II Risse in nichlinearen Materialien (z.B. im Modellmaterial des gefalteten LJ Potentials) verhalten sich dagegen nicht wie ein masseloses Teilchen. Teilweise wurden diese Ergebnisse von kürzlich entwickelten Theorien [117] vorhergesagt. Die Verteilung der Spannung in den verschiedenen Fällen wird mit den experimentellen und analytischen Vorhersagen verglichen und qualitative Übereinstimmung gefunden (siehe beispielsweise Abbildungen 10.7 und 10.16).

D.3.8. Mechanische und physikalische Eigenschaften dreidimensionaler Festkörper

Bislang konzentrierten wir uns auf die Dynamik von Modus I und Modus II Rissen, und dafür waren zweidimensionale Modelle ausreichend. Nun erweitern wir unser Modell und untersuchen auch Modus III Risse, wofür aber dreidimensionale Modelle notwendig werden.

Ebenso wie für die Studien mit zweidimensionalen Rissen ist die Analyse der elastischen und physikalischen Eigenschaften ein wichtiger Aspekt für die Untersuchung von Rissdynamik mit Hilfe drei-dimensionaler Modelle. Die Ergebnisse numerischer und analytischer Studien sind in Tabelle 11.1 und den Abbildungen 11.1, 11.2 sowie 11.3 für verschiedene Belastungsarten zusammengefasst. Ein wichtiger Aspekt ist hier ebenso die Berechnung der Rissoberflächenenergie.

D.3.9. Rissdynamik von Modus III Rissen

Die Belastungsart für Modus III Risse ist in Abbildung 12.1 gezeigt. Der Hauptaugenmerk der Studien in diesem Teil liegt auf der Dynamik von Rissen, die sich in dünnen elastisch harten Streifen eingebettet in einer weichen Matrix ausbreiten (siehe Abbildung 7.9, aber mit Modus III Belastung des Systems). Wir möchten dann diese mit einer kürzlich entwickelten kontinuumsmechanischen Theorie [44] für diesen Fall vergleichen. Die Theorie sagt die Existenz der charakteristischen Längenskala für den Energietransport, die bereits für Modus I Risse beschrieben wurde, auch für Modus III Risse voraus. Daher geht es uns vor allem um den Vergleich der Geschwindigkeit des Risses als Funktion der Materialparameter und der Geometrie.

Zunächst zeigen wir, dass die Grenzgeschwindigkeit homogener harmonischen Systeme der Vorhersage der linear-elastischen Kontinuumstheorie entspricht (siehe Abbildung 12.3). Wie in den vorigen Kapiteln erlaubt uns dies, die harmonischen Systeme als Referenzsysteme zu betrachten. Das Hauptergebnis dieses Kapitels ist der Vergleich von Simulation und Theorie [44], dargestellt in Abbildung 12.5. Die Simulationsergebnisse und die theoretischen Überlegungen beweisen die Existenz der charakteristischen Längenskala auch bei Modus III Rissen, und zeigen zudem eine relativ gute Übereinstimmung der Theorie mit den Simulationsergebnissen. Die Ergebnisse werden genutzt, um die Größe der charakteristischen Längenskala für realistische experimentelle Bedingungen abzuschätzen. Sie liegt für Risse in Metallen unter 0.1 % Scherbelastung bei etwa 1 Millimeter.

D.3.10. Diskussion und Zusammenfassung

Der Hauptaugenmerk der Studien in diesem Teil der Arbeit bezog sich auf die Rolle von Materialnichtlinearitäten in der Rissdynamik. Mit Hilfe von großen Computersimulationen haben wir gezeigt, dass die klassische linear-elastische Theorie versagt, wenn sich das Material mit zunehmender Dehnung nichlinear verhält. Da praktisch alle realen Werkstoffe Nichtlinearitäten aufweisen, scheinen die klassischen Theorien in vielen Fällen zweifelhaft zu sein. In der Tat deuten viele experimentelle Ergebnisse darauf hin, wie

zum Beispiel die stark reduzierte Maximalrissgeschwindigkeiten in vielen Materialien [69].

Ein wichtiger Punkt der Untersuchungen war die Grenzgeschwindigkeit der Risse. Mit Hilfe des neuen Konzepts der charakteristischen Länge für den Energiefluss in der Nähe eines Risses konnten einige experimentelle und numerische Ergebnisse erklärt werden. Die neue Längenskala, in bisherigen Theorien nicht vorhanden, ist in Abbildung 13.1 dargestellt.

Weitere Studien zeigten, dass Hyperelastizität auch eine große Rolle bei der dynamischen Rissinstabilität spielt. Unsere Ergebnisse deuten ferner darauf hin, dass geometrische Einschränkungen und Grenzflächen eine bedeutende Rolle für die Rissdynamik spielt. So kann sich ein Modus I Riss an einer Grenzfläche von weichen und harten Materialien mit Hilfe eines Mutter-Tochter-Mechanismus mit Überschallgeschwindigkeit ausbreiten, im klaren Widerspruch zur klassischen Theorie (siehe Abbildung 9.5).

D.4. Mechanische Eigenschaften ultra-dünner Kupferschichten auf Substraten

In diesem Teil der Arbeit widmen wir uns den mechanischen Eigenschaften dünner Kupferschichten, die auf Substraten (z.B. aus Silizium) aufgebracht sind. Ein solches System ist in Abbildung 14.1 schematisch dargestellt. Dünne Schichten zeigen sehr interessante mechanischen Eigenschaften, die in vielen Fällen als unzureichend verstanden gelten. So zeigen Filme, die dünner sind als 400 nm eine von der Filmdicke unabhängige Festigkeit [25]. Diese Beobachtung steht im Gegensatz zu einigen existierenden Theorien der Eigenschaften dünner Schichten, wie dem Mathews-Freund-Nix Modell [77, 167, 168]. Diese Modelle sagen eine Steigerung der Festigkeit invers proportional zur Filmdicke voraus.

Vor einigen Jahren wurde von Gao ein neues Modell vorgeschlagen [88], welches postuliert, dass in sehr dünnen Schichten Korngrenzendiffusion die Spannungen in der Korngrenze relaxiert, einen rissähnlichen Defekt erzeugt und dann Versetzungen auf Gleitebenen parallel zur Rissoberfläche generiert werden. Dies stellt einen völlig neuen Deformationsmechanismus dar. Dieser neuartige Defekt wird als Korngrenzen-Diffusionskeil (grain boundary diffusion wedge) bezeichnet und steht im Mittelpunkt der Abhandlungen in diesem Teil der Arbeit. Das Gao'sche Modell ist schematisch in Abbildung 14.2 zusammenfasst.

D.4.1. Entwicklung kontinuumsmechanischer Theorien zur Initiierung von Diffusion und Nukleation von Versetzungen an Diffusionskeilen

Als ersten Schritt leiten wir einige neue Aspekte der Kontinuumstheorie her. Ein wichtiges Ergebnis ist die Bestimmung einer kritischen Spannung zur Initiierung von Diffusion. Dieses Kriterium beruht auf der Annahme, dass zumindest *eine* Halbebene von Atomen mit Breite eines Burgers Vektors spontan in die Korngrenze klettert. Dies

führt auf eine von der Filmdicke unabhängige Schwellspannung für das Auftreten von Diffusion.

Weitere Untersuchungen beziehen sich auf Bildspannungen, die auf Versetzungen in extrem dünnen Schichten wirken (Abbildung 15.1). Wir konnten zeigen, dass bei Schichten die nur einige Nanometer dick sind, Bildspannungen von der Größenordnung GPa auftreten.

Das Hauptergebnis ist die Entwicklung eines Modells, welches die kritische Bedingung für Nukleation von Versetzungen von Diffusionskeilen beschreibt. Dabei verwenden wir die klassische Rice-Thomson-Theorie als Ansatz [181]. Das Modell ist schematisch in Abbildung 15.3 gezeigt. Letzlich wird mit Hilfe dieses Modells ein kritischer Spannungsintensitätsfaktor ermittelt (Abbildung 15.4), dessen Wert später mit den Ergebnissen atomistischer Simulationen verglichen wird.

D.4.2. Modellierung thermomechanischer Experimente

Eine wichtige experimentelle Technik zur Untersuchung, auf welche Art und Weise dünne Schichten auf mechanischen Stress reagieren, sind thermomechanische Experimente [234]. Dabei führt die Temperaturänderung aufgrund des Unterschiedes des thermischen Ausdehnungskoeffizienten zu Zug-und Druckspannungen im Film.

Die existierende Theorie der Korngrenzendiffusion in dünnen Schichten nimmt an, dass die Spannung in der Korngrenze komplett relaxiert werden kann [88]. Im Gegensatz dazu findet man in Experimenten und numerischen Simulationen eine Schwellspannung, unterhalb der keine Diffusion stattfindet [132, 133, 131]. Die existierende Theorie des Modells der Korngrenzendiffusion wird daher so abgeändert, dass eine Schwellspannung für das Auftreten von Diffusion eingeführt wird. Im Gegensatz zum klassischen Verständnis [88] kann damit die Spannung an der Korngrenze nicht mehr komplett relaxieren.

Wir nutzen nun das modifizierte Modell, um thermische Zyklenexperimente zu modellieren und die Spannungen als Funktion der Temperatur zu bestimmen. Das neue Modell erlaubt eine Verbesserung der Modellierung insbesondere bei hohen Temperaturen während des Zyklus [234]. Die Ergebnisse sind in den Abbildungen 16.2 und 16.3 dargestellt.

D.4.3. Atomistische Modellierung von Kriechvorgängen in dünnen Schichten

Wir verwenden klassische Molekulardynamik, um den Vorgang des Kriechens in dünnen Schichten näher zu untersuchen. Durch die Limitierung der Simulationszeit auf maximal etwa 10 Nanosekunden in der klassischen Molekulardynamik beschränken wir uns auf Untersuchungen bei erhöhten Temperaturen um die 90 Prozent der Schmelztemperatur sowie sehr hohen Spannungen. Die Berechnungen zeigen, dass Material von der Oberfläche entlang der Korngrenze in Richtung Substrat transportiert wird, in Übereinstimmung mit den Vorhersagen der kontinuumsmechanischen Theorie [88] (Abbildung 17.3).

Ein weiteres wichtiges Ergebnis ist die Beobachtung der Nukleation von Versetzungen die parallel zur Filmoberfläche in der Nähe der Grenzfläche Substrat-Film gleiten (paral-

lel glide dislocations), wie in Abbildung 17.5 gezeigt. Solche Versetzungen wurden auch in Experimenten beobachtet [24, 55], und deuten darauf hin, dass bei sehr dünnnen Kupferschichten diese Art der Deformationsvorgänge dominieren.

Die Ergebnisse der atomistischen Simulationen werden verwendet, um eine kritische Bedingung für die Nukleation solcher Versetzungen abzuleiten. Dabei benutzen wir das Konzept des kritischen Spannungsintensitätsfaktors und vergleichen die Werte der atomistischen Rechnungen mit den Vorhersagen der neu entwickelten Theorie (Tabelle 17.1). Das Kriterium, basierend auf dem Spannungsintensitätsfaktor, konnte auch erfolgreich in mesoskopischen Modellierungsansätzen verwendet werden [101]. Dabei dienen dann die Ergebnisse der molekulardynamischen Rechnungen als Eingabeparameter.

D.4.4. Atomistische Modelle von Korngrenzentrippelpunkten

Hier betrachten wir ein Modell mit drei Körnern, das einen Korngrenzentrippelpunkt enthält (Geometrie siehe Abbildung 18.1). Dabei konstruieren wir unser Modell so, dass zwei verschiedenen Arten von Korngrenzen vorhanden sind: Zum einen hochenergetische Korngrenzen mit homogener Verteilung der Energie, und zum anderen niedrigenergetische Korngrenzen, welche aus Misfit-Versetzungen aufgebaut sind.

Wir konnten zeigen, dass die niedrigenergetischen Korngrenzen gute Quellen für Versetzungen darstellen. Insbesondere beobachten wir, dass misfit Versetzungen selbst als Nukleationspunkt dienen. Im Gegensatz dazu gibt es bei homogenen Korngrenzen keinen intrinschen Nukleationspunkt, und Versetzungen werden an den Stellen höchster Schubspannungskonzentration nukleiert (siehe Abbildung 18.2 und 18.3). Wir beobachten auch, dass in solch kleinen nanostrukturierten Materialien partielle Versetzungen dominieren und eine starke Tendenz zur Ausbildung von Zwillingsgrenzflächen auftritt (siehe Abbildung 18.4). Eine weitere Beobachtung ist die Generierung von Punktdefekten als Reaktionsprodukt verschiedener Versetzungen. Diese Defekte werden dadurch erklärt, dass Versetzungen auf verschiedenen Gleitebenen nukleiert werden und sich bei Schnitt und Vereinigung der Versetzungen Jogs bilden, die eine nichtgleitfähige Komponente enthalten. Diese nichtgleitfähige Komponente der Versetzung kann nur durch Klettern, oder durch Generierung von Punktdefekten bewegt werden und übt im letzteren Fall eine Rückhaltekraft auf die Versetzung aus [109].

D.4.5. Polykristalline Modelle

Wir haben polykristalline Modelle entwickelt, um unsere atomistischen Simulationen an die experimentellen Begebenheiten anzunähern (schematische Geometrie der Modelle siehe Abbildung 19.1).

Ein wichtiges Computerexperiment war die Simulation von Filmen mit und ohne Relaxation der Spannung an der Korngrenze. Es zeigte sich, in Übereinstimmung mit den Ergebnissen der experimentellen Arbeiten [25], dass sogenannte “threading” Versetzungen die Plastizität dominieren, wenn die Korngrenzentraktion nicht relaxiert ist (Abbildung 19.3). Im Gegenzug findet man vorwiegend Versetzungen auf Gleitebenen parallel zur Filmoberfläche, wenn die Korngrenzenspannung z.B. durch Korngrenzendiffusion relaxiert ist (siehe Abbildungen 19.7 und 19.8). Dieses Ergebnis stimmt auch mit

den qualitativen Vorhersagen der Theorie [88] überein.

Neben diesen Untersuchungen haben wir Diffusion in polykristallinen Modellen untersucht. Ein wichtiges Ergebnis ist die Beobachtung der Ausbildung von Diffusionskeilen und die darauffolgende Nukleation von Versetzungen auf Gleitebenen parallel zur Filmoberfläche (Abbildung 19.14). Diese Ergebnisse verdeutlichen noch einmal die wichtige Rolle diffusiver Prozesse in dünnen Kupferschichten und zeigen eine gute Übereinstimmung mit den experimentellen Ergebnissen [24, 55, 25], denn wie im Experiment werden Halbschleifen aus Versetzungen auf Gleitebenen parallel zur Oberfläche nukleiert.

Die Ausbildung der Diffusionskeile ist stark von der Korngrenzenstruktur und der daraus resultierenden Diffusivität abhängig.

D.4.6. Zusammenfassung und Diskussion

Die wichtigsten Ergebnisse dieser Arbeit und die vorhergehender theoretischer und experimenteller Beiträge wurden am Ende in einer grafischen Übersicht zusammengefasst. Diese zeigt die verschiedenen Mechanismen als Funktion der Filmdicke und der angelegten Spannung (siehe Abbildung 20.2).

Wir schlagen vier verschiedene Deformationsmechanismen ultra-dünner Kupferschichten vor. Diese sind: (A) klassische “threading” Versetzungen, (B) Kriechvorgänge (constrained diffusional creep) mit Nukleation von Versetzungen auf Gleitebenen parallel zur Filmoberfläche, (C) Kriechvorgänge ohne Nukleation von Versetzungen und (D) keinerlei Relaxationsmechanismen. Der Bereich (D) tritt bei sehr dünnen Schichten und niedrigen Spannungen auf. Bislang wurde nur der Bereich (A) beschrieben, und dieses Ergebnis zeigt, dass viele neue Effekte auftreten können, wenn die Dimensionen der Materialien den Bereich von Nanometern erreichen. Für die Entwicklung neuer Materialien könnte das Verständnis solcher Effekte aber sehr wichtig werden.

D.5. Zusammenfassung und Diskussion

Es wurden atomistische Computersimulationen zusammen mit Konzepten der Kontinuumsmechanik verwendet, um verschiedene Aspekte des Versagens und Deformation von Materialien zu untersuchen.

Der erste Teil der Arbeit widmete sich der Dynamik spröder Rissausbreitung. Es stellte sich heraus, dass einige der Theorien der Rissdynamik auch auf atomarer Ebene eine recht gute Beschreibung geben, sofern harmonische Wechselwirkungen zwischen Atomen angenommen werden. So ist die Grenzgeschwindigkeit in der Simulation in recht guter Übereinstimmung mit der Vorhersage, und auch die Spannungs- und Dehnungsfelder in der Nähe des Risses sind recht gut durch die Theorie beschrieben. Werden dagegen nichlineare Materialien simuliert, so versagt in vielen Fällen die linear-elastische Theorie und sie muss durch nichtlineare Ansätze ersetzt werden. Dies zeigte sich beispielsweise an Studien zur Grenzgeschwindigkeit von Rissen oder bei den Untersuchungen zur dynamischen Rissinstabilität. Die Simulationsergebnisse halfen bei der Identifizierung einiger wichtiger atomistischer Aspekte, die zum Verständnis der nichtlinearen Rissdynamik wichtig sind. Das wichtigste Beispiel ist die Entdeckung einer neuen

charakteristischen Längenskala für den Energiefluss zur Rissspitze.

Im zweiten Teil der Arbeit wurden die mechanischen Eigenschaften dünner Kupferfilme untersucht. Im Mittelpunkt stand dabei ein neuer Materialdefekt, ein rissähnlicher Diffusionskeil. Atomistische Simulationen wurden durchgeführt, um die Entstehung von Versetzungen an solchen Diffusionskeilen näher zu untersuchen. Unsere Ergebnisse deuten darauf hin, dass solche Defekte in der Tat in sehr dünnen Kupferschichten unter 400 nm eine wichtige Rolle spielen. Unsere Ergebnisse sind in Übereinstimmung mit experimentellen und theoretischen Arbeiten [24, 55, 25, 88] und schließen daher die Lücke zwischen Experiment und Theorie. Während wir im ersten Teil der Arbeit die Kontinuumsmechanik vorwiegend mit Hilfe der Virialspannung und der Virialdehnung gekoppelt haben, benutzten wir im zweiten Teil das Konzept des Spannungsintensitätsfaktors. Die Ergebnisse zeigen damit exemplarisch Methoden auf, wie atomistische Konzepte mit Methoden der Kontinuumsmechanik gekoppelt werden können.

Index